

NORTHWESTERN UNIVERSITY

Heat Conduction in Defective and Complex Crystals:  
Phonon Scattering and Beyond

A DISSERTATION

SUBMITTED TO THE GRADUATE SCHOOL IN PARTIAL FULFILLMENT OF THE  
REQUIREMENTS

for the degree

DOCTOR OF PHILOSOPHY

Field of Materials Science & Engineering

by

Riley Hanus

EVANSTON, ILLINOIS

December 2019

©Copyright by Riley Hanus 2019

All rights reserved

## Abstract

The flow of heat through solids is a topic of technological importance for microelectronics and energy materials such as thermoelectrics. In simple, defect-free crystals the thermal conductivity is generally well understood. However, in materials containing defects and/or in those with very complex crystal structures there is a lack of basic understanding which inhibits technological progress. In this thesis, a combined experimental, theoretical, and computational approach is used to establish a basic understanding of thermal transport in defective and complex crystals. Particular focus is given to the influence of interfaces, dislocations, and point defects and the transition between crystalline-like and amorphous-like heat conduction. Additionally, a more targeted materials design approach is applied to thermoelectric skutterudite material systems where thermal and electronic properties are optimized by the controlled use of defects.

## Notation conventions

The notation convention used in this thesis is summarized as follows. Deviations from this convention will be noted.

Vectors and tensors are denoted with italic sub/superscripts, where  $i, j, k = 1, 2, 3$  (the three Cartesian directions  $x$ ,  $y$ , and  $z$ ) unless otherwise noted. Subscripts that are roman font are simply for labeling. For example,  $\kappa^{ij}$  denotes the 3x3 thermal conductivity tensor, and  $\kappa_{\text{ph}}^{ij}$  denotes the 3x3 phonon-gas channel thermal conductivity tensor. It is common to drop the tensor subscripts, in particular when treating a cubic crystal since each diagonal component is equal to the scalar  $\kappa_{\text{ph}}$  and off diagonal components are zero. Additionally,  $v_g^i$  and  $v_p^i$  denote the group and phase velocity vectors of a phonon. Similarly, dropping the vector superscript will imply that we are referring to the magnitude of the vector.

Vectors may also be denoted by bold font. This specifically applies to the position vector,  $\mathbf{r}$ , and wavevector,  $\mathbf{k}$ . The non-bold version of these variable stands for the magnitude of the vector. For example,  $k$  stands for the magnitude of  $\mathbf{k}$ . An integral over  $\mathbf{r}$  denotes an integral over the three dimensions of  $\mathbf{r}$ ,

$$\int_{-\infty}^{\infty} d^3 \mathbf{r} = \int_{-\infty}^{\infty} \int_{-\infty}^{\infty} \int_{-\infty}^{\infty} dx dy dz. \quad (1)$$

Likewise for integrals over  $\mathbf{k}$ .

Phonon calculations often involve the sum of over all phonon modes in the system, each of which has a distinct wavevector  $\mathbf{k}$  and branch index  $s$ . This will often be expressed by the shorthand  $\mathbf{k}s$ , such that  $C(\mathbf{k}s)$  denotes the heat capacity of a phonon at  $\mathbf{k}$  in branch  $s$ .

This thesis will consider theoretical treatments which are ‘mode specific’ and ‘spectral’. Mode specific means that the phonon properties at of each mode  $\mathbf{k}s$  are considered. A spectral treatment means that phonon properties are expressed function of frequency  $\omega$ . The mode specific phonon properties are therefore contained ‘under the hood’ of a spectral model. We designate the mode specific and spectral phonon properties by the variables argument. For example, the mode specific and spectral heat capacity,  $C(\mathbf{k}s)$  and  $C(\omega)$  respectively, have different definitions. Specifically,  $C(\omega)$  contains the phonon density of states and  $C(\mathbf{k}s)$  does not.

Einstein summation convention will be used, where repeated indices within a term are summed. A tensor denoted by  $a_{ij}$ , multiplied into a vector  $b_i$ , written as  $a_{ij}b_j$  implies summation over  $j$ ,

$$a_{ij}b_j = \sum_{j=1,2,3} a_{ij}b_j. \quad (2)$$

In this convention the dot product between two vectors,  $b_i$  and  $c_i$  is simply written as  $b_i c_i$ .

## Nomenclature

$\kappa^{ij}$	total thermal conductivity tensor .....	[W m <sup>-1</sup> K <sup>-1</sup> ]
$\kappa_{\text{vib}}^{ij}$	vibrational thermal conductivity tensor .....	[W m <sup>-1</sup> K <sup>-1</sup> ]
$\kappa_{\text{ph}}^{ij}$	phonon-gas channel thermal conductivity tensor, phonon-gas channel thermal conductivity is more commonly called the lattice thermal conductivity $\kappa_{\text{ph}} = \kappa_L = \kappa_{\text{lat}}$ ...	[W m <sup>-1</sup> K <sup>-1</sup> ]
$\kappa_{\text{diff}}^{ij}$	diffusion channel thermal conductivity tensor .....	[W m <sup>-1</sup> K <sup>-1</sup> ]
$j^i$	heat flux vector .....	[J m <sup>-2</sup> s <sup>-1</sup> ]
$C$	phonon heat capacity .....	[J K <sup>-1</sup> m <sup>-3</sup> ]
$g$	density of phonon states .....	[s m <sup>-3</sup> ]
$v_g^i$	group velocity vector .....	[m/s]
$v_p^i$	phase velocity vector .....	[m/s]
$v_s$	speed of sound .....	[m/s]
$v_{\text{L,T}}$	longitudinal and transverse sound speed .....	[m/s]
$W_{\mathbf{k},\mathbf{k}'}$	scattering probability from state $\mathbf{k}$ into state $\mathbf{k}'$ .....	[s <sup>-1</sup> ]
$\Gamma$	scattering rate .....	[s <sup>-1</sup> ]
$\tau$	relaxation time .....	[s]
$\hbar$	reduced Plank's constant $h/2\pi$ .....	[J s]
$k_B$	Boltzmann's constant .....	[J K <sup>-1</sup> ]
$\mathcal{H}$	Crystal Hamiltonian .....	[eV]
$\mathcal{T}$	Crystal kinetic energy .....	[eV]
$U$	Crystal potential energy .....	[eV]
$\mathbf{k}$	phonon wavevector .....	[m <sup>-1</sup> ]
$s$	phonon branch index .....	[unitless]

$\omega$	phonon angular frequency .....	[s <sup>-1</sup> ]
$\Phi_{ijk}^{\alpha\beta\gamma}$	3rd order interatomic force constants. Read, the force on atom $\alpha$ in the $i$ direction when atoms $\beta$ and $\gamma$ are displaced in the $j$ and $k$ directions, respectively. .....	[eV Å <sup>-3</sup> ]
$\Phi_{ij}^{\alpha\beta}$	2nd order interatomic force constants. Read, the force on atom $\alpha$ in the $i$ direction when atom $\beta$ is displaced in the $j$ direction. .....	[eV Å <sup>-2</sup> ]
$n_{\text{BE}}$	Bose-Einstein distribution function .....	[unitless]
$m_\alpha$	Mass of atom $\alpha$ in the crystal .....	[kg]
$u_i^\alpha$	Atomic displacement vector of atom $\alpha$ in the crystal .....	[m]
$\theta_D$	Debye temperature .....	[T]
$\theta_{\text{GB}}$	grain boundary angle .....	[°]
$\gamma$	Grüneisen parameter .....	[unitless]
$\gamma_{\text{GB}}$	grain boundary energy .....	[J m <sup>-2</sup> ]
$\gamma_{\text{st}}$	grain boundary strain energy .....	[J m <sup>-2</sup> ]
$\gamma_{\text{core}}$	grain boundary core energy .....	[J m <sup>-2</sup> ]
$\epsilon_{ij}$	symmetric strain tensor .....	[unitless]
$R_{ij}$	anti-symmetric rotation tensor .....	[radians]
$R_\kappa$	thermal boundary resistance .....	[m <sup>2</sup> K W <sup>-1</sup> ]
$h_B$	thermal boundary conductance, $h_B = R_\kappa^{-1}$ .....	[W m <sup>-2</sup> K <sup>-1</sup> ]

Pursuing a PhD in Materials Science and Engineering has been the most challenging, fulfilling, and fun experience of my life. I owe much of this to the patience, flexibility, knowledge and intuition of my mentors, for which I am most grateful. I would like to thank my family and friends for providing social and emotional guidance during this sometimes taxing endeavor.

If one allows curiosity to triumph over the fear of failure or of what might be found, they will find life and the universe ever amazing.

# Contents

<b>1</b>	<b>Introduction</b>	<b>12</b>
1.1	Thermal management of microelectronics . . . . .	14
1.2	Thermoelectrics . . . . .	14
1.3	Thesis overview . . . . .	16
<b>2</b>	<b>Background</b>	<b>18</b>
2.1	Thermal conductivity . . . . .	18
2.2	Phonons in perfect crystals . . . . .	21
2.2.1	Lattice dynamics . . . . .	21
2.2.2	Phonon thermal conductivity . . . . .	23
2.3	Phonons in defective crystals . . . . .	29
2.3.1	Phonon defect scattering . . . . .	30
<b>3</b>	<b>Phonons and interfaces</b>	<b>42</b>
3.1	Diffraction and dimensionality crossover . . . . .	42
3.1.1	Scattering from an infinite array of linear defects . . . . .	45
3.1.2	Grain boundary strain and rotation field scattering . . . . .	47
3.1.3	Low-T thermal conductivity of polycrystals . . . . .	53
3.1.4	Discussion . . . . .	58
3.2	Thermal boundary resistance and GB strain energy . . . . .	59
3.2.1	Si twist grain boundaries . . . . .	59
3.2.2	$R_\kappa$ correlated with interfacial strain energy . . . . .	60

<b>4 Lattice softening</b>	<b>63</b>
4.1 Chemical lattice softening in SnTe . . . . .	64
4.1.1 Microstructural analysis . . . . .	64
4.1.2 Defect chemistry and thermal conductivity . . . . .	64
4.2 Microstructural lattice softening . . . . .	70
4.2.1 Results . . . . .	73
4.2.2 Discussion . . . . .	77
4.2.3 Conclusion . . . . .	82
4.2.4 Methods . . . . .	82
4.2.5 Elastic properties . . . . .	87
<b>5 Phonons in complex crystals: beyond the phonon gas model</b>	<b>90</b>
5.1 Introduction . . . . .	91
5.2 Methods . . . . .	94
5.2.1 Computational methods . . . . .	94
5.2.2 Synthesis . . . . .	95
5.2.3 Inelastic neutron scattering . . . . .	96
5.3 Results and discussion . . . . .	96
<b>6 Optimizing thermoelectric transport of CoSb<sub>3</sub> through the controlled use of defects</b>	<b>100</b>
6.1 Graphene modified grain boundary complexions . . . . .	101
6.1.1 Material synthesis . . . . .	102
6.1.2 Structural characterization . . . . .	102
6.1.3 Electric transport . . . . .	104
6.1.4 Thermal transport . . . . .	104
6.1.5 <i>zT</i> and module performance . . . . .	108
6.1.6 Discussion . . . . .	109
6.2 CoSb <sub>3</sub> electronic band structure . . . . .	109

6.2.1	Experimental and computational methods . . . . .	110
6.2.2	Results and discussion . . . . .	114
6.2.3	Discussion . . . . .	122
<b>A</b>	<b>Reciprocal space and the first Brillouin zone</b>	<b>143</b>
<b>B</b>	<b>Lattice dynamics</b>	<b>145</b>
<b>C</b>	<b>Phonon Boltzmann transport equation</b>	<b>148</b>
<b>D</b>	<b>Analytical models for phonon properties</b>	<b>151</b>
D.1	Dispersion relation approximations . . . . .	151
D.2	Heat capacity . . . . .	151
D.3	Phonon thermal conductivity at high- $T$ . . . . .	152
<b>E</b>	<b>Measurements of the speed of sound and Debye temperature</b>	<b>155</b>
E.1	Pulse-echo ultrasound . . . . .	155
E.2	Low temperature heat capacity . . . . .	156
<b>F</b>	<b>Grüneisen parameters and tensors</b>	<b>158</b>
F.0.1	Relating phonon and thermodynamic Gruneisen parameters . . . . .	159
<b>G</b>	<b>Phonon scattering theory</b>	<b>161</b>
G.1	Three phonon scattering . . . . .	161
G.2	Elastic defect scattering . . . . .	162
G.2.1	One-dimensional defects . . . . .	163
G.2.2	Zero-dimensional defects . . . . .	165
G.2.3	Two-dimensional defects . . . . .	166
G.3	Defining $\tau(\omega)$ for non-isotropic defect scattering . . . . .	167
G.4	Scattering from an infinite array of linear defects . . . . .	168
G.4.1	Conservation laws . . . . .	169

G.4.2 Specular scattering: long wavelength limit . . . . .	169
G.4.3 Phonon-dislocation strain scattering: short wavelength limit . . . . .	170
G.5 Useful Fourier transforms and identities . . . . .	171
<b>H Thermal boundary conductance</b>	<b>173</b>

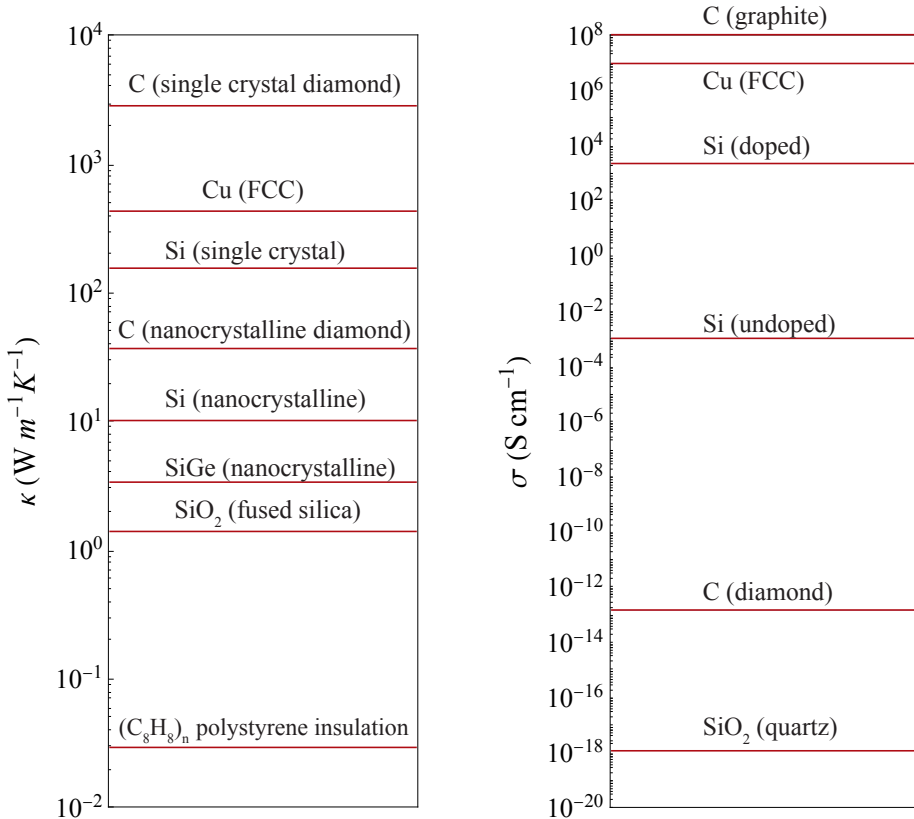
# Chapter 1

## Introduction

Thermal energy and the thermal properties of materials impact our daily lives, and the society in which we live, in many direct and indirect ways. Direct impacts include domestic, commercial, and automotive climate control, the overheating of a computer or device, thermal runaway explosions of Li-ion batteries, and of course cooking. However, there are many indirect impacts which are equally, if not more, important. Indirect impacts include thermal limitations in computer processing speed (clock rate), maximum power and range of wireless networks, and power production in the space industry and exploration (radio isotope thermoelectric generators, RTGs). Additionally, 60 to 70% of the energy consumed in the United States is wasted, the majority in the form of waste heat [1]. Controlling the thermal properties of materials is critically important for mitigating and/or reusing the heat wasted during energy production, conversion, and utilization. Thermal transport science plays an integral role in the development of next generation electronic devices, and clean and sustainable energy solutions.

Comparing the overall landscape of thermal and electrical transport of solids provides a nice perspective when analyzing the challenges facing thermal science. Figure 1.1 shows the range of thermal and electrical conductivity for all solids. The electrical conductivity of all solids ranges over about 26 orders of magnitude, and can span approximately 6 orders of magnitude within a material system such as silicon. In contrast, the thermal conductivity of all solids ranges over 5 orders of magnitude, and can span approximately 1.5 orders of magnitude within a material system such as silicon. The main reason for this dramatic difference is that the number of carriers for electronic conductivity (the electron or hole carrier concentration) can be shifted by orders of magnitude relatively easily by chemical doping. The analog to carrier concentration for thermal conductivity is a material's heat capacity. There is no straight forward way to dramatically change a material's heat capacity.

Imagine for a moment that we had the scientific knowledge and technological capability to tune thermal conductivity of solids by 26 orders of magnitude, or the capability to tune the thermal conductivity of a given material system by 6 orders of magnitude. Thermal limitations are so



7

Figure 1.1: The general ranges of thermal ( $\kappa$ ) and electrical ( $\sigma$ ) conductivity for solids. Thermal conductivity spans approximately 5 orders of magnitude while electrical conductivity spans approximately 26. Within a material system, such as silicon (Si), thermal and electrical conductivity can be changed by approximately 1.5 and 6 orders of magnitude, respectively.

ingrained in our intuition, that imagining the world in this way may not be an easy task. If we had such capabilities, energy consumption would likely plummet, computer processing speed would likely skyrocket, wireless network speed and coverage would be dramatically increased, and electronic devices and vehicles would charge in minutes (possibly even seconds). Unfortunately, it would still take approximately five minutes to boil a four liter pot of water.

Due to the physical limitations of materials, mainly on a materials heat capacity, such a dramatic technological achievement is unlikely. In practice the thermal sciences, like most fields, tend to progress with continuous and moderate improvements in understanding and capability. This thesis aims to contribute to this progress by establishing materials design principles for controlling thermal transport in defective and complex crystals. The materials systems studied here are most directly relevant to microelectronic and thermoelectric technologies, which we now introduce.

## 1.1 Thermal management of microelectronics

Since the first experimental demonstration of the field effect transistor in 1947 and its rapid commercialization in the early 1950s, microelectronics have become rapidly integrated into the world economy and culture. Transistors are the basic building block for a computers central processing unit (CPU) and its processing speed is set by the speed at which the transistors can switch between their on and off state (clock rate). Switching the state of the transistor requires pushing electrons through the integrated circuit and often dumping this charge to ground producing heat which raises the operating temperature of the device. In fact, nearly all of the energy used to operate a CPU, is converted to heat which must be removed. The device's maximum operating temperature sets the maximum operating power and computing speed. The faster the heat removal, the lower the operating temperature for a given operating power. This is the concept of the integrated circuits thermal design power, or the power at which the device can be run at without exceeding the maximum transistor junction temperature [2].

Field effect transistors inherently have many interfaces. The volumetric density of transistors and material interfaces in CPU has dramatically increased over the past decades. The thermal resistance of transistor devices is strongly influenced, and sometimes dominated, by internal thermal boundary resistances. Beyond CPUs, the electrification of transportation and the development of an electrical grid which can cope with intermittent power supplies from renewal energy sources, requires advancement in power electronics and wide band gap semiconductors. The maximum temperature of Si based electronics is approximately 100 °C. Above this temperature carriers have enough energy to jump silicons band gap and the electronic device loses functionality. Wide band gap semiconductors can be operated at much higher temperature, making them suitable for the high power levels required by electric vehicles and the energy grid. The thermal properties of the microelectronic devices discussed above are strongly influenced by their crystalline defects and interfaces. Many of these defects and interfaces are required for the operation of the device, meaning that finding engineering solutions to simply remove them is not a valid solution. Therefore, advancement in many microelectronic technologies requires the development of materials design principles for controlling thermal transport with defects [3, 4, 5].

## 1.2 Thermoelectrics

Thermoelectrics (TEs) are a class materials which convert heat directly to electricity and vice versa. TE energy conversion is a solid state process, with no moving parts, which operates through the Seebeck (or Peltier) effect. When the heat flow of the entire TE system is optimized (i.e. thermal load matching between the TE module and heat exchangers) the maximum possible conversion

efficiency is given by

$$\eta = \frac{T_h - T_c}{T_h} \frac{\sqrt{1 + ZT} - 1}{\sqrt{1 + ZT} + T_c/T_h} \quad (1.1)$$

which depends on the hot and cold side temperature ( $T_h$  and  $T_c$ ), and the device figure of merit  $ZT$ . The device figure of merit  $ZT$  (denoted with an upper case  $Z$ ), is set by the temperature dependent material figure of merit  $zT$  (denoted with a lower case  $z$ ), as well as  $T_h$  and  $T_c$ . The material figure of merit is given by

$$zT = \frac{\alpha^2 \sigma}{\kappa} T, \quad (1.2)$$

where  $\alpha$  is the Seebeck coefficient,  $\sigma$  is the electrical conductivity,  $\kappa$  is the thermal conductivity,  $T$  is the absolute temperature. The materials power factor,  $\alpha^2 \sigma$ , characterizes the electrical aspects of TE transport.  $ZT$  and the average value of  $zT$  over a given temperature can be very different, especially when  $zT$  varies significantly across the temperature range.  $ZT$ , for a desired  $T_h$  and  $T_c$ , can be easily calculated from temperature dependent  $zT$  with an algorithm provided by Snyder and Snyder [6]. Nonetheless, a higher  $zT$  will inevitably result in a larger  $ZT$ . Therefore, if the thermal design of entire TE system can be optimized (i.e. TE leg geometry, hot and cold side heat exchangers etc.), then  $zT$  provides a metric for the maximum efficiency a device can achieve using this specific TE material. It is important to note that there are applications which contain engineering limitations prohibiting optimal thermal design (e.g. wearable TEs). In these cases heat exchanger design is likely a more pressing concern than TE material improvement.

Each material parameter in  $zT$  depends on the material's carrier concentration. If the band structure of a material is known, the optimum carrier concentration for the material can be calculated. Therefore, when exploring different TE material systems, it makes more sense to examine the materials quality factor,  $B$ , which is carrier concentration independent [7]

$$B = \left( \frac{k_B}{e} \right)^2 \frac{\sigma_{E_0}}{\kappa_{vib}} T. \quad (1.3)$$

$\kappa_{vib}$  is the thermal conductivity carried by atomic vibrations (often referred to as the lattice thermal conductivity), and  $\sigma_{E_0}$  is a transport coefficient with units of electric conductivity which characterizes how well a material conducts electricity at a given carrier concentration. If the materials carrier concentration can be optimized,  $B$  gives the maximum  $zT$  that could be achieved in that material system. By examining  $B$ , one sees the TE material optimization problem boils down to maximizing the ratio  $\sigma_{E_0}/\kappa_{vib}$ . Utilizing microstructural defects to reduce  $\kappa_{vib}$  while leaving electrical transport and  $\sigma_{E_0}$  unchanged is a major focus in the field of TEs.  $\sigma_{E_0}$  can be improved by increasing the 'complexity' of the electronic band structure at the Fermi level [8], which is sometimes parameterized as a valley degeneracy or the number of distinct carrier pockets  $N_V$ . Most of this thesis will focus on developing materials design principles for optimizing  $\kappa_{vib}$ . Electronic band structure properties,

which impact  $\sigma_{E_0}$ , will be discussed in Chapter 6.2.2.

To summarize, minimizing  $\kappa_{\text{vib}}$ , while keeping electronic transport constant, will maximize a materials  $B$ , which determines the maximum achievable  $zT$  if the carrier concentration can be optimized.  $zT$  gives the maximum  $\eta$  a device can achieve using this material, if the systems level thermal transport can be optimized (e.g. if sufficiently large heat exchangers can be used).

### 1.3 Thesis overview

Heat transport is generally well understood in simple, defect free crystals [9]. However, the technologies reviewed in Sections 1.1 and 1.2, as well as many others, are limited by thermal properties of materials which contain defects. The structure of these defects is also generally well understood and many concepts extend from the well established field of metallurgy. One main challenge facing the thermal sciences is to explain the influence of defects on the thermal conductivity. Additionally, our basic understanding of phonon transport is typically grounded in the phonon-gas model. Within the phonon-gas model phonon wave packets are defined which can be viewed as quasi-particles propagating through the solid. A growing body of work has shown that the phonon-gas model is incomplete for solids exhibiting a thermal conductivity in lower 2 to 3 orders of magnitude shown in Figure 1.1. However, a detailed understanding of the breakdown of the phonon-gas model has not yet been established. The work in this thesis aims to address these limitations and is summarized as follows.

Chapter 2 reviews the fields current theoretical understanding. It starts by defining the thermal conductivity, highlighting that there are theoretically two channels for phonon conduction. One is the standard phonon-gas model and usually dominates in simple crystals. The second one we term the diffuson-channel since it is mathematically the same conduction channel through which diffusons were defined [10], and becomes important in highly defective and/or complex crystals, as well as amorphous materials. Chapters 3 and 4 only explicitly consider the phonon-gas channel. The diffuson-channel is considered in Chapter 5. Chapter 2 proceeds to review the standard theory of phonons and simulations for phonon transport through the phonon-gas channel in perfect crystals. Next, general concepts of phonon-defect scattering are reviewed and several modeling procedures for explaining phonon transport across interfaces are reviewed and compared. In Chapter 3 phonon grain boundary interactions are examined. We present the concept of a dimensionality crossover which we find to be essential for explaining phonon grain boundary scattering. The concept of a dimensionality crossover acknowledges that long wavelength phonons see the interface as a two dimensional plane, while shorter wavelength phonons see the atomic structure of the interface. The results presented suggest that shorter wavelength phonons see clean low-energy grain boundaries as a collection of linear defects, and that phonon interactions with the localized grain boundary strain

field dominate. In Chapter 4 we theoretically and experimentally demonstrate the importance of defect induced lattice softening, or the reduction of phonon frequencies, elastic moduli, and speed of sound. This is a fundamentally different mechanism through which defects can reduce a materials thermal conductivity. It is shown to be important in nanocrystalline Si, PbTe, and SnTe systems and can be achieved through chemical and/or microstructural means. In Chapter 5 we turn to the breakdown of the phonon-gas model by examining the  $\text{Yb}_{14}MSb_{11}$  material system (where  $M$  is Mg or Mn) which has a very complex crystal structure containing 104 atoms per unit cell. By examining the lattice dynamics computationally and experimentally we show that this material system is expected to conduct heat through the diffuson-channel similar to an amorphous material even though it is indeed a crystal. This case study reveals a mechanism for the break down of the phonon-gas model and the transition from crystalline-like to amorphous-like thermal conduction. Chapters 2 through 5 focus on establishing general physical principles and the materials studied are treated as model systems through which a basic understanding can be established. In Chapter 6 a more targeted materials design strategy is adopted where the thermoelectric properties of the  $\text{CoSb}_3$  system are improved through the controlled use of defects. This is achieved by controlling thermal properties by the modification of grain boundary with two-dimensional graphene, and controlling the electrical band structure with point defects and chemical doping.

## Chapter 2

### Background

#### 2.1 Thermal conductivity

Consider that one side of a homogeneous solid is brought into contact with a heat source raising its temperature to  $T_H$  and that the heat is removed from the other side by use of a heat sink setting its temperature to  $T_C < T_H$  and establishing a temperature gradient,  $\nabla^i T$  (Figure 2.1). When steady state is reached, a flux of heat,  $j^i$ , will be established which is constant in time and space. The value of  $j^i$  in the solid is set by the material's thermal conductivity  $\kappa^{ij}$  which is defined using Fourier's law

$$j^i = -\kappa^{ij} \nabla^j T. \quad (2.1)$$

Given a designated  $\nabla^i T$ , a material with a low thermal conductivity will have a low heat flux  $j^i$ , and vice versa.  $\kappa$  is the sum of the thermal conductivity due to each heat conduction channel. The most common channels considered are atomic vibrations ( $\kappa_{\text{vib}}$ ) and electrons ( $\kappa_e$ ) (omitting the tensor superscripts)

$$\kappa = \kappa_{\text{vib}} + \kappa_e + \dots \quad (2.2)$$

$\kappa_e$  is set by the electrical conductivity ( $\sigma$ ) and Lorenz number ( $L$ ), as  $\kappa_e = L\sigma T$ . Most of this thesis will focus on the heat carried by atomic vibrations  $\kappa_{\text{vib}}$ .

In a solid, where the forces between atoms are assumed to be harmonic and periodic boundary conditions are upheld, the normal modes of vibration are called phonons. Describing vibrational modes as phonons is common in crystalline materials. However, when periodic boundary conditions are applied to simulations of amorphous materials the phonon description rigorously holds as well. This approximation seems to maintain much of the essential physics and has provided many valuable insights.

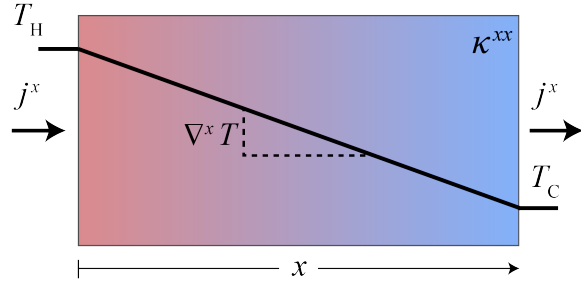


Figure 2.1: An illustration of a solid in which heat is flowing. A source has injected heat on the left side, and on the right side there exists a sufficiently large heat sink. When steady state is reached a thermal gradient  $\nabla^x T$  has been established. The magnitude of the heat current  $j^i$  is set by the materials thermal conductivity  $\kappa^{ij}$  through Fourier's law, Eq. 2.1.

The heat flux due to phonon transport is given by [11, 12]

$$j^i = \sum_{\mathbf{k}ss'} a_{\mathbf{k}s}^\dagger a_{\mathbf{k}s'} j^i(\mathbf{k}ss') \quad (2.3)$$

$$j^i(\mathbf{k}ss') = \frac{\hbar}{V} \frac{(\omega(\mathbf{k}s) + \omega(\mathbf{k}s'))}{2} v^i(\mathbf{k}ss'). \quad (2.4)$$

The meaning of these equations will become more clear as they are formulated further below. We will come to find that the diagonal ( $s = s'$ ) and off-diagonal ( $s \neq s'$ ) terms in the sum in Eq. 2.3 have very different physical interpretations. Following the conventional phonon representation, each phonon mode is designated by its wavevector  $\mathbf{k}$  and branch (polarization) index  $s$ .  $j^i(\mathbf{k}ss')$  is the heat current matrix with rows  $s'$  and columns  $s$ . The phonon creation and annihilation operators are given by  $a_{\mathbf{k}s}$  and  $a_{\mathbf{k}s}^\dagger$ , respectively.  $v^i(\mathbf{k}ss')$  is a term with units of m/s for which we adopt different names for diagonal and off-diagonal elements. For diagonal elements,  $v^i(\mathbf{k}ss) = v_g^i(\mathbf{k}s)$  is the phonon group velocity. For off-diagonal elements,  $v^i(\mathbf{k}ss')$  is a normal mode mixing parameter.

One way in which phonons can conduct heat is by constructing wave packets which propagate at a speed equal to the magnitude of the phonon group velocity vector,  $v_g$ . Since these wave packets behave like particles and obey essentially the same transport physics as gas particles, we call this mechanism phonon transport through the phonon-gas channel, or simply phonon transport<sup>1</sup>  $\kappa_{ph}$ . The thermal flux and conductivity due to the phonon-gas channel are given by (see Appendix C

---

<sup>1</sup>The term lattice has a specific meaning in crystallography and is simply an array of points in space. Lattice thermal conductivity refers to the thermal conductivity through a crystal which is defined using a crystallographic lattice. A lattice, being simply an array of points in space, can not have a thermal conductivity, however a crystal defined using this lattice can. Therefore, phonon thermal conductivity  $\kappa_{ph}$  is a more precise term.

and Eq. 2.17)

$$j_{\text{ph}}^i = \frac{1}{V} \sum_{\mathbf{k}s} n(\mathbf{k}s) \hbar\omega(\mathbf{k}s) v_g^i(\mathbf{k}s) \quad (2.5)$$

$$j_{\text{ph}}^i = -\kappa_{\text{ph}}^{ij} \nabla^j T. \quad (2.6)$$

By recognizing that  $a^\dagger(\mathbf{k}s)a(\mathbf{k}s)$  becomes the number of phonons in the state  $\mathbf{k}s$ ,  $n(\mathbf{k}s)$ , it is clear that  $j_{\text{ph}}^i$  is simply diagonal portion of  $j^i$ . This mechanism is very effective at conducting heat and typically dominates in simple crystals.

Another mechanism through which phonons can conduct heat is by transferring thermal energy from one mode to another due to normal mode mixing. This results in heat being transferred diffusely in a random walk type manner and normal modes conducting heat in this way have therefore been named diffusons [10]. We call this phonon transport through the diffuson channel,  $\kappa_{\text{diff}}$ . The thermal flux and conductivity due to the diffuson channel are given by

$$j_{\text{diff}}^i = \frac{1}{V} \sum_{\mathbf{k}s s'}^{s \neq s'} a_{\mathbf{k}s}^\dagger a_{\mathbf{k}s'} \frac{\hbar(\omega(\mathbf{k}s) + \omega(\mathbf{k}s'))}{2} v^i(\mathbf{k}s s') \quad (2.7)$$

$$j_{\text{diff}}^i = -\kappa_{\text{diff}}^{ij} \nabla^j T. \quad (2.8)$$

These two channels contribute additively to the vibrational thermal conductivity [11]

$$\kappa_{\text{vib}} = \kappa_{\text{ph}} + \kappa_{\text{diff}}. \quad (2.9)$$

The diffuson channel is in principle present in all solids, but tends to become important in amorphous materials [10] and crystalline materials that are anharmonic [13] and/or have very complicated crystals structures with many atoms per unit cell (Chapter 5). As defects are introduced, it is expected that the phonon-gas channel will be suppressed and the diffuson channel will be promoted [14]. The transition between  $\kappa_{\text{ph}}$ - and  $\kappa_{\text{diff}}$ -dominated heat conduction with increasing crystal complexity, anharmonicity, and defect concentration is an important avenue of ongoing research. The current paradigm of understanding is that in crystals the phonon-gas channel is so large it dominates  $\kappa_{\text{vib}}$  making it common to assert that  $\kappa_{\text{vib}} = \kappa_{\text{ph}}$ . In Chapters 3 and 4, and Section 6.1 we consider the suppression of the phonon-gas channel due to the introduction of defects. We consider thermal conduction through the diffuson channel in Chapter 5. First, we review phonon thermal conductivity in perfect crystals.

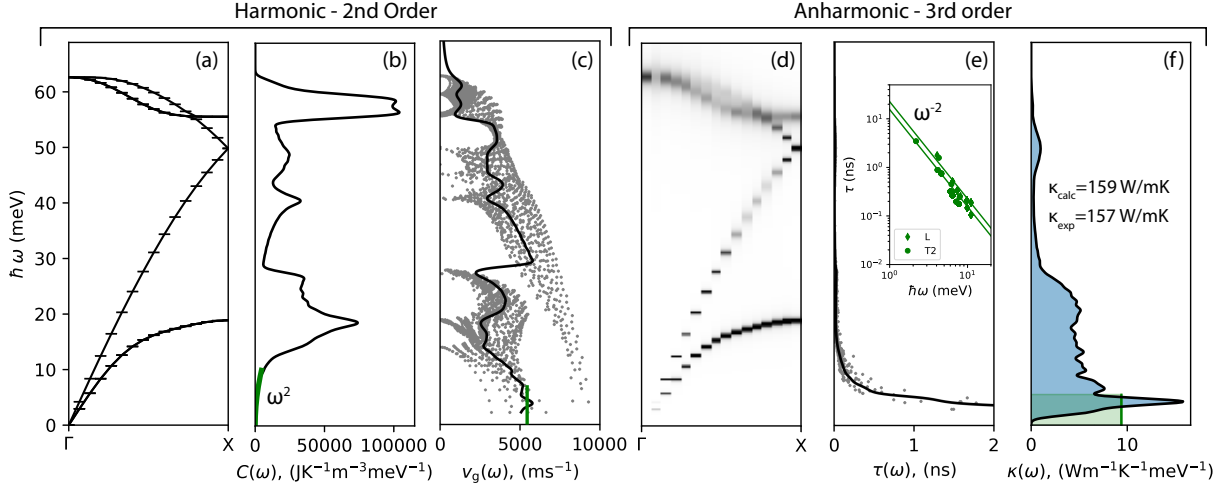


Figure 2.2: Phonons and phonon thermal conductivity of perfect, single crystalline Si computed using *ab initio* based lattice dynamics and the phonon Boltzmann transport equation at 300K. The green lines show analytical expressions which hold at low- $\omega$ , and highlight numerical artifacts which commonly accompany this type of mode specific simulation. a) The phonon dispersion relation along  $\Gamma - X$  calculated from 2nd order interatomic force constants (Appendix B). b) The spectral heat capacity (Eq. 2.18). c) Mode dependent phonon group velocity,  $v_g(\mathbf{k}\omega)$  (dots) and the isotropic average group velocity at a given frequency  $v_g(\omega)$  (line, Eq. 2.19). d) The phonon dispersion relation with phonon line broadening defined by the phonon-phonon scattering relaxation time. The discrete behavior in  $\mathbf{k}$  is not physical and represents the discrete nature of the uniform  $\mathbf{k}$ -mesh. Note that we use a relatively dense mesh of  $30 \times 30 \times 30$ . e) The mode dependent relaxation time due to phonon-phonon scattering  $\tau(\mathbf{k}\omega)$  (dots), and the isotropic average relaxation time at a given frequency  $\tau(\omega)$  (line, Eq. 2.20). The inset shows a  $\tau \propto \omega^{-2}$  fit to the computational data at low- $\omega$ . f) The spectral thermal conductivity computed using the data points shown in panels a, c, and e. The peak at 5 meV is artificial and is due to poor sampling of  $\mathbf{k}$ -space below 10 meV. From analytical consideration (green lines),  $\kappa(\omega)$  should converge to a constant value as  $\omega \rightarrow 0$  rather than go to zero.

## 2.2 Phonons in perfect crystals

Before examining how crystalline defects will influence heat conduction by phonons, we first must understand phonons in perfect crystals. This will be achieved by mathematically describing how atoms vibrate in crystals. This field of study is often referred to as lattice dynamics and McGaughey *et al.* provide a nice tutorial [9]<sup>2</sup>.

### 2.2.1 Lattice dynamics

We begin with the end in mind, which is shown in Figure 2.2. Phonons can be mathematically defined by solving the equations of motion of a crystal, assuming harmonic coupling between all

<sup>2</sup>Note, we use  $i, j, k$  for Cartesian directions, and  $\alpha, \beta, \gamma$  for atomic labels to keep consistent with the tensor notation used in this thesis. McGaughey *et al.* flip this.

atoms (read  $F = m\ddot{x}$ , with  $F = kx$ ). These solutions are often visualized in a phonon dispersion relation (Figure 2.2a), or a plot of the phonons inverse wavelength or wavevector,  $\mathbf{k}$ , versus its energy,  $\hbar\omega$  ( $\hbar$  is the reduced Plank's constant and  $\omega$  is the phonon frequency). The phonon dispersion relation is, in essence, a Fourier transform of the interatomic force constants weighted by the atomic mass, and naturally contains information about the symmetry of the lattice.

The basis of lattice dynamics starts with the crystal Hamiltonian  $\mathcal{H}$  which describes the energy of the system as the sum of the kinetic energy  $\mathcal{T}$  and the potential energy  $U$  of all of the atoms in the crystal

$$\mathcal{H} = \mathcal{T} + U. \quad (2.10)$$

The kinetic energy of a single atom in a crystal on lattice site  $\alpha$  moving in the Cartesian direction  $i$  is given by  $m_\alpha(\dot{u}_i^\alpha)^2/2$ . Here,  $m_\alpha$  is the mass of the atom,  $u_i^\alpha$  is the time varying atomic displacement vector, and  $\dot{u}_i^\alpha$  is its velocity (the dot denotes the derivative with respect to time). The total kinetic energy is then given by summing over all lattice sites and directions

$$\mathcal{T} = \frac{1}{2} \sum_{\alpha} \sum_i m_\alpha(\dot{u}_i^\alpha)^2. \quad (2.11)$$

The potential energy is treated as a Taylor expansion about the equilibrium atomic position ( $u_i^\alpha = 0$ ) where the first non-zero term is the harmonic potential energy

$$U = \frac{1}{2!} \sum_{\alpha\beta} \sum_{ij} \Phi_{ij}^{\alpha\beta} u_i^\alpha u_j^\beta + \frac{1}{3!} \sum_{\alpha\beta\gamma} \sum_{ijk} \Phi_{ijk}^{\alpha\beta\gamma} u_i^\alpha u_j^\beta u_k^\gamma + \dots, \quad (2.12)$$

or simply

$$U = U_{2\text{nd}} + U_{3\text{rd}} + \dots. \quad (2.13)$$

$\Phi_{ij}^{\alpha\beta}$  and  $\Phi_{ijk}^{\alpha\beta\gamma}$  are the second and third order derivatives of the potential energy with respect to atomic displacements, and are often referred to as the 2nd and 3rd order interatomic force constants (IFCs).  $\Phi_{ij}^{\alpha\beta}$  can be read as the force on atom  $\alpha$  in the  $i$  direction when atom  $\beta$  is displaced in the  $j$  direction.  $\Phi_{ijk}^{\alpha\beta\gamma}$  can be read as the force on atom  $\alpha$  in the  $i$  direction when atoms  $\beta$  and  $\gamma$  are displaced in the  $j$  and  $k$  directions, respectively. These constants can be readily calculated in perfect single crystals using density functional theory (DFT) with various computational suites (VASP [15], QuantumExpresso [16], Phonopy [17]). Additionally, there are databases containing IFCs of many compounds to 2nd [18] and even 3rd order [19]. It seems that for many materials treating  $U$  to 3rd order is sufficient [9]. In some very anharmonic materials such as NaCl 4th order IFCs become important and play the role of renormalizing the phonon dispersion relation and opening up additional scattering phase space [20]. In this thesis we will only consider  $U$  up to 3rd order.

Within this treatment we can write the lattice Hamiltonian truncated to 3rd order as

$$\mathcal{H} = \mathcal{T} + U_{\text{2nd}} + U_{\text{3rd}}. \quad (2.14)$$

This expression, together with Eqs. 2.11 and 2.12, is useful when determining how a given defect will perturb phonons, and we will return to this in later sections.

If we only consider  $\mathcal{H}$  to 2nd order, the following equation of motion can be written

$$-\sum_{j\beta}\Phi_{ij}^{\alpha\beta}u_j^\beta = \ddot{u}_i^\alpha m_\alpha. \quad (2.15)$$

This equation is simply Newton's 2nd law stating that the force on atom  $\alpha$  in the  $i$  direction due to all other atoms in the crystal  $\beta$ ,  $-\sum_{j\beta}\Phi_{ij}^{\alpha\beta}u_j^\beta$ , is equal to its acceleration in that direction,  $\ddot{u}_i^\alpha$ , times its mass  $m_\alpha$ . This differential equation can be solved by transforming to reciprocal space (Appendix A) and assuming plane wave solutions for  $u_i^\alpha$  (Appendix B). These solutions are shown for Si in Figure 2.3a. The data points (horizontal dashes) show the  $\mathbf{k}$ -points for which the phonon properties were calculated, lying on a  $30 \times 30 \times 30$  uniform  $\mathbf{k}$ -mesh within the first Brillouin zone (Appendix A). Note that phonon properties below 10 meV are sampled very poorly with this uniform  $\mathbf{k}$ -meshing procedure, even when we use a relatively dense grid. This point will become important when considering the spectral phonon properties. First we will examine how phonons conduct heat.

## 2.2.2 Phonon thermal conductivity

The phonon thermal conductivity,  $\kappa_{\text{ph}}$ , determines the amount of heat carried by phonons when a material is put under a temperature gradient (Figure 2.1). This transport property is a  $3 \times 3$  tensor,  $\kappa_{\text{ph}}^{ij}$  where  $i$  and  $j$  are the three Cartesian directions.  $\kappa_{\text{ph}}^{ij}$  denotes how much heat is conducted in direction  $i$  due to a temperature gradient in direction  $j$ . However, in cubic crystals all off diagonal terms are zero and the three diagonal terms are equal, such that  $\kappa_{\text{ph}}^{ij}$  reduces to a scalar  $\kappa_{\text{ph}}$ , times the Kronecker  $\delta_{ij}$ .

It is important to note that the energy scale of phonons is small compared to electrons. The maximum phonon frequency shown in Figure 2.3 is approximately 65 meV, where  $k_B T = 25$  meV at room temperature ( $T = 300$  K). Therefore, all the phonons in Si will be populated at around 2.5 times room temperature. This is one intrinsic material property that the Debye temperature ( $\theta_D$ ) strives to quantify, the temperature at which all vibrations in a material are active. The Debye temperature of Si is  $\theta_D = 660$  K which is 2.2 times room temperature. There are many ways to measure and compute  $\theta_D$ , and one should only compare the magnitude of  $\theta_D$  values that are determined by a consistent method. Several methods for quantifying  $\theta_D$  are reviewed in Appendix

E. Important relations are

$$k_B\theta_D = \hbar\omega_D = \hbar v_s \left( \frac{6\pi^2}{V} \right)^{1/3}, \quad (2.16)$$

where  $\omega_D$  is the Debye frequency,  $v_s$  is the average speed of sound (Eq. E.1.1), and  $V$  is the volume per atom.

Another important feature that distinguishes phonons from electrons is that they are bosons rather than fermions, meaning that they do not obey the Pauli exclusion principle and they are governed by Bose-Einstein statistics rather than Fermi-Dirac statistics. Practically, this means that the whole spectrum of phonons contributes to transport. In stark contrast, only electrons near the Fermi level contribute to transport. Consequently, for phonon transport there is, in essence, an averaging effect. By this, we mean that subtle features and changes to a band structure tend to have much more of an impact on electron transport than they do on phonon transport. Additionally, the concept of adding and removing carriers does not exist for phonons in the same manner as for electrons. One can dope a semiconductor and dramatically change the number of charge carriers. The analog to electron charge for atomic vibrational energy is the heat capacity, and the heat capacity of a solid is more or less fixed since it is closely tied to the number density of atoms.

These important features in phonon transport are reflected in the formula for  $\kappa_{ph,ij}$  which is obtained by solving the Peirels Boltzmann transport equation (BTE), in the relaxation time approximation (see details in Appendix C)

$$\kappa_{ph}^{ij} = \sum_{\mathbf{k}s} C(\mathbf{k}s) v_g^i(\mathbf{k}s) v_g^j(\mathbf{k}s) \tau(\mathbf{k}s). \quad (2.17)$$

$C(\mathbf{k}s)$  is the heat capacity of the specific phonon mode (Eq. C.0.9), where we use a short hand for identifying a phonon mode by denoting its wavevector  $\mathbf{k}$  and its branch index  $s$  with the compound label  $\mathbf{k}s$ .  $v_g^i(\mathbf{k}s) = d\omega(\mathbf{k}s)/dk_i$  is the component of the phonon group velocity vector pointing in the  $i$  direction.  $\tau(\mathbf{k}s)$  is the lifetime of the phonon, or its time between collisions.

The quantities present in Eqs. 2.17 can be readily computed using *ab initio* based lattice dynamics and the results for a perfect, infinite (i.e. no crystal boundary scattering), Si crystal is shown in Figure 2.2a, c, and e. For these calculations, the 2nd and 3rd order IFCs from the almaBTE database were used [19], along with the associated computational suite for computing phonon energies and lifetimes. To gain physical insight into the phonon thermal conductivity, and to prepare for the modeling of complex systems, which can not be simulated in such detail, we will reduce this ‘mode specific’ model with  $\mathbf{k}s$  specific properties to a ‘spectral’ model with  $\omega$  dependent properties, in the following sections.

## Spectral phonon thermal conductivity

Often times it is informative to analyze the spectral behavior of Eq. 2.17. by defining the spectral phonon heat capacity

$$C(\omega) = \sum_{\mathbf{ks}} C(\mathbf{ks}) \delta(\omega - \omega(\mathbf{ks})), \quad (2.18)$$

and the average group velocity and relaxation time at a given frequency

$$v_g(\omega) = \frac{\sum_{\mathbf{ks}} v_g(\mathbf{ks}) \delta(\omega - \omega(\mathbf{ks}))}{\sum_{\mathbf{ks}} \delta(\omega - \omega(\mathbf{ks}))}, \quad (2.19)$$

$$\tau(\omega) = \frac{\sum_{\mathbf{ks}} \tau(\mathbf{ks}) \delta(\omega - \omega(\mathbf{ks}))}{\sum_{\mathbf{ks}} \delta(\omega - \omega(\mathbf{ks}))}. \quad (2.20)$$

Note that by omitting the Cartesian index in  $v_g(\mathbf{ks})$  we are implicitly referring to the magnitude of the group velocity of phonon mode  $\mathbf{ks}$ . Since

$$\sum_{\mathbf{ks}} \delta(\omega - \omega(\mathbf{ks})) = g(\omega), \quad (2.21)$$

is the phonon density of states (pDOS), Eqs. 2.19 and 2.20 are simply pDOS weighted averages of  $v_g(\mathbf{ks})$  and  $\tau_g(\mathbf{ks})$ .

With the definitions given in Eqs. 2.18, to 2.20 we can write down a spectral decomposition of Eq. 2.17

$$\kappa_{\text{ph}} = \frac{1}{3} \int_0^{\omega_{\text{max}}} C(\omega) v_g(\omega)^2 \tau(\omega) d\omega. \quad (2.22)$$

This equation is commonly called the single mode isotropic approximation, since it can be envisioned as describing all the phonons in the system with a single isotropic phonon branch. It is also possible, and sometimes useful to not make the single mode approximation. In this case the sum over  $s$  would be omitted in Eqs. 2.18, to 2.20, and one would be included outside of the integral over  $\omega$  (Eq. 2.23).

Alternative to computing  $v_g(\omega)$  and  $\tau(\omega)$  using Eqs. 2.19 and Eqs. 2.20, one can define them analytically using approximations for the phonon dispersion relation and semi-empirical expressions for the phonon relaxation time. Unlike the mode dependent treatment with uniform  $\mathbf{k}$ -mesh described above (Eq. 2.17, and Fig. 2.2), this analytic treatment is effective at describing acoustic phonons particularly at low- $\omega$ . This procedure is commonly called Callaway-Klemens type modeling of phonon transport, and can be useful when interpreting emergent phenomena in the thermal transport of complex, defective systems in which a mode resolved treatment (Eq. 2.17) is either exceedingly difficult or impossible.

Using the information shown in Figures 2.2b, c, and e, the spectral thermal conductivity ( $\kappa_{\text{ph}}(\omega) = C(\omega) v_g(\omega)^2 \tau(\omega)/3$ ) can be computed and is shown in Figure 2.2f. It can be seen that the majority of the heat is carried by acoustic phonons, below 25 meV, due primarily to their very long relaxation times. While optical phonons indeed have a lower  $v_g(\omega)$ , they carry much less heat primarily due to their very low  $\tau$ , due to a large phase space for phonon scattering.

Now we take a closer look at the behavior of low- $\omega$  phonons (below 10 meV). Understanding the behavior of  $\kappa_{\text{ph}}(\omega)$  as  $\omega \rightarrow 0$  is particularly important when considering the impact of extended defects such as grain boundaries, interfaces, and dislocation strain fields since they will influence low- $\omega$  phonons (Section 2.3). From examining the computational results in Figure 2.2f (black line) it may seem that phonons below 2 meV do not carry heat. This conclusion may even seem intuitive since there are very few phonon modes at this low energy; i.e. the pDOS, and  $C$  go to 0 as  $\omega \rightarrow 0$ . However, this attribute is a computational artifact and through analytical considerations one can show that low- $\omega$  phonons are indeed important for thermal conductivity. We start by recalling that at low- $\omega$  and/or at  $T > \omega_D$ ,  $C(\omega) \approx 3k_B g(\omega)$ . At low- $\omega$ ,  $v_g(\omega) = v_s$  and  $g(\omega) \propto \omega^2$ . These  $\omega$  dependencies are shown as the green lines in 2.2b and c. Next, the inset of Figure 2.2e shows that  $\tau \propto \omega^{-n}$  with  $n = 2$  at low- $\omega$ . In Section 2.2.2 we discuss the physics of intrinsic phonon-phonon scattering and justify this analytical form. By comparing the  $\omega$ -dependence of  $C(\omega)$ ,  $v(\omega)$ , and  $\tau(\omega)$  at low- $\omega$  it can easily be seen that we expect  $\kappa_{\text{ph}}(\omega)$  to approach a constant value as  $\omega \rightarrow 0$  (green line), and not go to zero (black line). If  $\kappa(\omega)$  truly approaches zero as  $\omega \rightarrow 0$ , then  $\tau$  must scale as  $\omega^{-n}$  with  $n < 2$ . In reality  $\tau$  typically scales with  $n = 2$  to 3. Recall that a uniform  $\mathbf{k}$ -mesh is used to approximate the Brillouin zone integration and phonon relaxation times are not computed at the  $\Gamma$ -point ( $\mathbf{k} = 0$ ). Therefore the phonon properties below 10 meV are sampled very poorly (see Figure 2.2a), even when a relatively dense (30x30x30) mesh is used.

This analysis provides an important physical insight. First we define the amount of heat carried by phonons within a small band of frequency  $d\omega$  centered around  $\omega$  as  $\kappa_{\text{ph}}(\omega) d\omega$ . Therefore, since  $\kappa_{\text{ph}}(\omega)$  is constant at low frequencies, phonons within  $d\omega$  approaching the  $\Gamma$ -point,  $\hbar\omega \approx 1$  meV, carry as much heat as phonons within  $d\omega$  at higher frequencies,  $\hbar\omega \approx 10$  meV. This analysis highlights that it is important to ensure that not only the magnitude of the thermal conductivity is converged, but also that the spectral thermal conductivity is converged, with respect to  $\mathbf{k}$ -mesh density, especially when phonon properties near the  $\Gamma$ -point are important. Extended crystal defects such as phonon-dislocation and phonon-interface scattering are known to influence low frequency phonons, as we discuss in Section 2.3. Therefore, this misrepresentation of the near  $\Gamma$ -point phonons will likely cause errors if one were to use this uniform  $\mathbf{k}$ -mesh treatment as the basis of a multiscale model. Before discussing phonon-defect interactions we must first understand intrinsic phonon-phonon scattering which arises from the natural anharmonicity of a crystal.

## Anharmonicity

When anharmonicity is introduced, i.e.  $U_{3\text{rd}}$  is included, phonons interact. One intuitive way for conceptualizing anharmonicity, is that now when atoms are displaced from their equilibrium lattice positions (i.e. strain is introduced) the forces between the atoms are changed with respect to what they would have been in the harmonic approximation. Simply put, the spring constants change when strain is present. The larger the strain the larger the change in the spring constants. This change in force constants changes the phonon energy which can induce a scattering event, and can change the speed at which the phonon travels. These atomic displacements can arise from other phonons or from static strain fields in a crystal which are induced by crystal defects (e.g. dislocations, interfaces, point defects).

One can understand anharmonic interactions in the context of Eqs. 2.12 and 2.14 as follows. The energy of a phonon associated with the atomic displacement vector  $u_i^\alpha(\mathbf{r}, t)$  is changed by the atomic displacement field  $u_j^\beta(\mathbf{r}, t)$  and is then scattered into a new phonon associated with the displacement vector  $u_k^\gamma(\mathbf{r}, t)$ . Note, the assignment of  $i, j, k$  and  $\alpha, \beta, \gamma$  is arbitrary and  $u$  can be a function of position  $\mathbf{r}$  and/or time  $t$ . If  $u_j^\beta$  is associated with another phonon containing vibrational energy, then the interaction changes the energy of the incident phonon, meaning the incident ( $u_i^\alpha$ ) and scattered phonons ( $u_k^\gamma$ ) will have different energies. Therefore, this interaction is commonly referred to inelastic, phonon-phonon scattering. If  $u_j^\beta$  is associated with a static strain field which contains no vibrational energy ( $u_j^\beta$  only a function of  $\mathbf{r}$ ), the energy of  $u_i^\alpha$  and  $u_k^\gamma$  will be equal and we call this elastic strain field scattering. If anharmonicity is not included, the interaction of phonons with other phonons, as well as static strain fields induced by crystal defects will be neglected.

In terms of the phonon dispersion relation of Si shown in Figure 2.2a, the introduction of anharmonicity will introduce a broadening in energy of the phonon states shown in Figure 2.2d. This broadening is commonly described as a Lorentzian peak with a full width half maximum equal to twice the phonon scattering rate,  $2\Gamma(\mathbf{k}s) = 2/\tau(\mathbf{k}s)$  [21, 22]. The discrete nature of the dispersion relation in the  $\mathbf{k}$  direction of Figure 2.2a and d is not physical, but represents the space between wave vectors computed on a uniform  $\mathbf{k}$ -mesh. A broadening in the  $\mathbf{k}$ -direction of a phonon dispersion relation is related to the phonon coherence length in real space [23] and no information about this quantity is explicitly contained within this theoretical framework. In Figure 2.2, we only consider the phonon scattering and line width due to intrinsic phonon-phonon interactions, which arise from the crystal's natural anharmonicity.

## Intrinsic phonon-phonon scattering

The scattering from other phonons in three-phonon processes can be computed if 2nd and 3rd order IFCs are known. It is now common place to compute these IFCs using DFT, and several open

source codes are available which compute the three phonon scattering rate using Fermi's Golden Rule Eq. G.0.1. The tutorial provided by McGaughey *et al.* reviews this method (Eq. 26 of [9]), and we briefly outline it in Appendix G.1. We will apply Fermi's Golden Rule to phonon-defect scattering in Section 2.3. Here we will attempt to build physical insight for three phonon scattering processes and present a semi-emperical analytical form which can capture some of this physics.

We start by considering an interesting question which has historically received much debate [24, 25, 26, 27]: Will a defect free, infinite crystal have infinite thermal conductivity? In such a case the only phonon scattering mechanism would be scattering off of other phonons due to the natural anharmonicity of the crystal. While this question may seem academic at first glance, a conclusive answer would bring with it an accurate prediction of how extended defects such as interfaces will influence the thermal conductivity, which is a topic of technological importance.

One can understand this problem by examining the spectral decomposition of the thermal conductivity (note we do not make the single mode approximation as we did in Eq. 2.22, and therefore maintain the branch index  $s$ )

$$\kappa_{\text{ph}} = \frac{1}{3} \sum_s \int_0^{\omega_{\text{max}}} C(\omega, s) v_g(\omega, s)^2 \tau(\omega, s) d\omega. \quad (2.23)$$

To see where the proposed question arises, we examine the lower bound of the integral over  $\omega$ . First, we assign  $\tau(\omega)$  the general form

$$\tau(\omega, s) = A(T, s)\omega^{-n}, \quad (2.24)$$

which contains a temperature dependent constant  $A(T, s)$  and an arbitrary frequency dependence  $n$ . As  $\omega \rightarrow 0$ ,  $v_g(\omega, s) = v_s(s)$ , and the spectral heat capacity becomes  $C(\omega, s) = k_B\omega^2/(2\pi^2 v_s(s)^3)$ . With these low- $\omega$  approximations Eq. 2.23 becomes

$$\kappa_{\text{ph}} = \frac{k_B}{6\pi^2} \sum_s \frac{A(T, s)}{v_s(s)} \int_0^{\omega_{\text{max}}} \omega^{2-n} d\omega. \quad (2.25)$$

From this representation one can easily see that the exponent in the power law dependence of the lifetime,  $n$ , is the critical parameter. If any of the branches  $s$  contain phonons exhibiting a power law dependence with  $n \geq 3$ , then  $\kappa_{\text{ph}}$  will diverge to infinity if there are no other phonon scattering mechanisms. Consequently, the power law dependence of the phonon lifetime at low- $\omega$  is critical for determining the strength at which extended defects, such as interfaces and dislocations, will reduce  $\kappa_{\text{ph}}$ . Early theories predicted phonon lifetimes at low  $\omega$  would exhibit  $n = 4$ , therefore several theories indeed predicted that the thermal conductivity would diverge to infinity if the materials were infinite and defect free [27]. There are several consequences of phonons exhibiting  $n \geq 3$ . First, the thermal conductivity of very clean crystals would continue to increase as crystal size

increases. Second, computationally the thermal conductivity would not converge with increasing  $\mathbf{k}$ -mesh density. It seems that neither of these attributes are observed in bulk crystals, suggesting that in most cases  $n < 3$ .

C. Herring provides a nice discussion about this and tabulates  $n$  for various crystal classes [27]<sup>3</sup>. The work shows that when phonon dispersion anisotropy is included when deriving the form of  $\tau$ , at low- $\omega$  where the dispersion relation is linear  $n$  is often between 2 and 3.

We now compare the semi-empirical form in Eq. 2.24 to the DFT based results for  $\tau$  given in Figure 2.2e. Silicon has the space group Fd $\bar{3}$ m and is in the O<sub>h</sub> crystal class. According to Table II of Herring [27],  $n = 2$  when the dispersion is linear. The inset of Figure 2.2e shows a  $\tau \propto \omega^{-2}$  fit to the simulated results.

While the mode dependent treatment (Eq. 2.17) is tractable for perfect single crystalline systems, there are limitations when utilizing this approach to predict the thermal conductivity of defective systems. Several cases do exist demonstrating that DFT based lattice dynamics and Boltzmann transport can capture the influence of certain point defects. Utilizing this mode dependent approach to describe large systems with extended defects such as interfaces and dislocations often requires some level multi-scale modeling. We will use the analytical treatment provided in Eq. 2.22 to identify the dominant mechanisms which reduce  $\kappa_{\text{ph}}$  in defective systems.

## 2.3 Phonons in defective crystals

Two fundamentally different mechanisms through which defects influence the phonon thermal conductivity are phonon scattering and lattice softening. Both are illustrated in Figure 2.3. In the phonon scattering picture the energy of the phonon branches, and therefore the elastic moduli and speeds of sound are assumed to be unchanged. The defect introduces an additional scattering parameter  $\tau_i$  (note  $i$  is not a Cartesian index here) and the phonon linewidth is broadened, Figure 2.3b to c. The decrease in  $\tau$  is often modeled using Matthiessen's rule

$$\tau^{-1} = \sum_i \tau_i^{-1}. \quad (2.26)$$

By lattice softening we refer to the mechanism in which the defects can modify the elastic moduli, speeds of sound, and energy of the phonon branches, Figure 2.3b and d. Since, in this case the phonon dispersion is changed, the maximum phonon frequency  $\omega_{\text{max}}$ , heat capacity  $C(\omega)$ , and phonon propagation (group) velocity  $v_g$  are changed. Additionally, the intrinsic phonon-phonon

---

<sup>3</sup>Only 3-phonon scattering processes are considered. Other effects contributing to  $\tau$  can be important at very low frequency MHz, such as thermoelastic and Akhieser damping [28]. The phonon spectrum extends up to the THz scale, therefore in the context of the thermal transport of phonons we only consider 3-phonon processes.

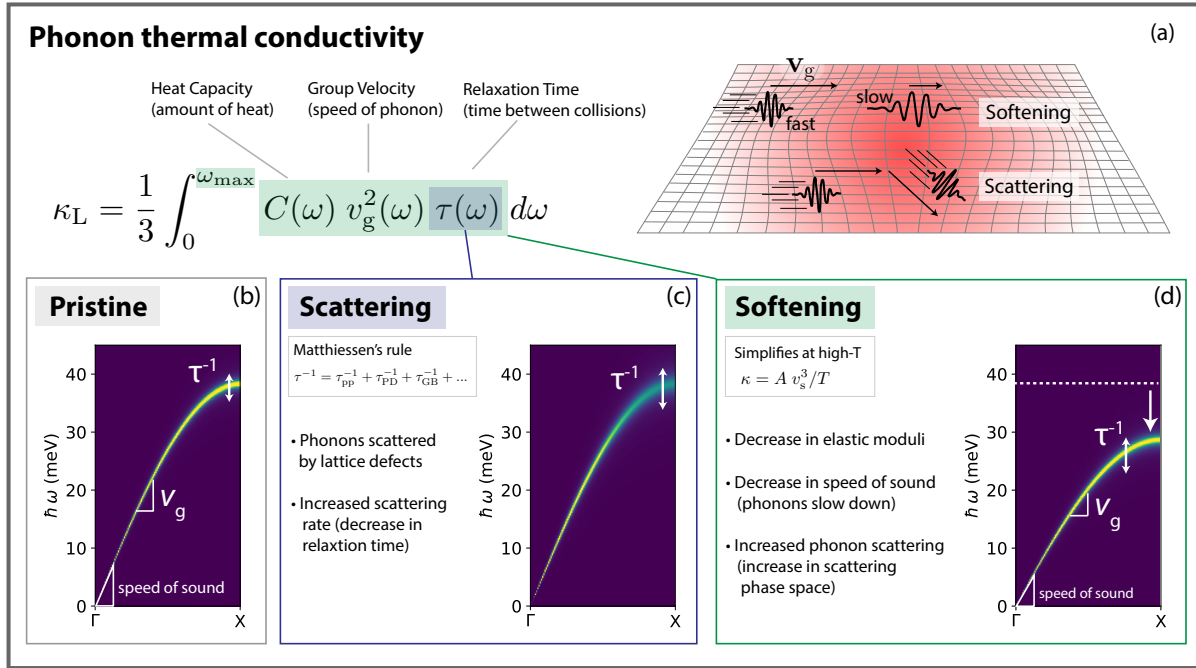


Figure 2.3: Schematic representations of phonon scattering and lattice softening. a) A real space depiction of phonon scattering and lattice softening. b) The phonon dispersion and linewidth of a pristine crystal. c) Phonon scattering due to the introduction of crystal defects. d) Lattice softening, reduced elastic moduli and speed of sound due to the introduction of crystal defects.

scattering is changed as well since the phase space for 3-phonon scattering has changed. At high temperatures, when phonon-phonon scattering dominates, we can analytically show that  $\kappa_{ph} = A/v_s^3 T$ . Therefore,  $\kappa_{ph}$  is very sensitive to lattice softening.

Figures 2.3b through d represent these effects in reciprocal space. Figure 2.3a schematically represents this in real space. The phonon scattering picture shows the phonon changing propagation direction while its frequency is unchanged. The lattice softening picture shows a decrease in phonon frequency and propagation speed. In the following sections we will examine the theoretical and experimental implications of these two distinct mechanisms.

### 2.3.1 Phonon defect scattering

Here we review analytical aspects of phonon-defect scattering. We attempt to build physical intuition which may guide materials design strategies in technologies where thermal conductivity is important. These fundamental aspects of phonon-defect scattering are important when controlling thermal conductivity with materials chemistry, nano/microstructure, and synthesis procedures. Additionally, they are important to consider when analyzing computational simulations. The an-

alytical treatment reviewed here illustrates expected behavior, and deviations from this behavior may reveal interesting physics which has been captured computationally. Further, the analytical theory reviewed here can be used to identify the limitations of a particular simulation method.

When crystal defects are introduced they will couple to the phonons in the material by perturbing the lattice Hamiltonian,  $\mathcal{H}$ , given in Eq. 2.14. If this perturbation varies in space or time, it can induce phonon scattering. In this section we capture a spatially varying perturbation by considering the defects as introducing a scattering potential,  $V(\mathbf{r})$ , and the resulting phonon scattering process is computed in the context of Fermi's Golden Rule perturbation theory (i.e. under the Born approximation). We consider only elastic interactions<sup>4</sup>, meaning the incident and scattered phonon have the same energy. The theory is formulated to capture first order physics, and therefore makes several approximations to achieve closed form expressions which help establish physical intuition.

### Effect of defect dimensionality

We start by considering the effect of just the dimensionality of the scattering defect on the  $\omega$ -dependence of the phonon lifetime. We follow the basic precepts of the theory of phonon scattering and its contribution to lattice thermal conductivity as laid out, for example, by Ziman [29]. By applying these precepts to elastic scattering from a defect with scattering potential  $V(\mathbf{r})$  (described in more detail in Section G.2), the scattering rate or inverse relaxation time ( $\Gamma(\mathbf{k}) = \tau(\mathbf{k})^{-1}$ ) of a phonon with wavevector  $\mathbf{k}$  and frequency  $\omega$  may be written as a product of three factors,

$$\Gamma(\mathbf{k}) = n_{\bar{n}d} g_{\bar{n}d}(\omega) \overline{|M_{\bar{n}d}|^2}. \quad (2.27)$$

The three factors  $n$ ,  $g$ , and  $\overline{|M|^2}$  are, respectively, the spatial density of the defect in the crystal, the phonon density of states (pDOS), and a term containing the squared magnitude of a scattering matrix element

$$\langle \mathbf{k}' | \mathcal{H}' | \mathbf{k} \rangle = (L_x L_y L_z)^{-1} \int d^3 \mathbf{r} V(\mathbf{r}) e^{i(\mathbf{k}-\mathbf{k}') \cdot \mathbf{r}}, \quad (2.28)$$

where  $V(\mathbf{r})$  is the scattering potential and  $L_x L_y L_z$  is the volume of the crystal containing the defect. It can be seen in Eq. 2.28 that the matrix element can be thought of as the Fourier transform of the scattering potential  $V(\mathbf{r})$ . The bar in  $\overline{|M|^2}$  indicates that the magnitude of the matrix element squared has been weighted by the forward scattering parameter and summed over possible final states  $\mathbf{k}'$ . The essential point, indicated by the subscript ‘ $\bar{n}d$ ’, is that all three factors depend on  $\bar{n}$ , the codimension of the defect. That is,

$$\bar{n} = 3 - d_d \quad (2.29)$$

---

<sup>4</sup>The defect can also introduce additional vibrational states which can in principle change the energy of the incident phonon, inducing inelastic scattering. While it is possible that inelastic phonon-defect interactions may be important, we have (to date) not seen sufficient experimental evidence to support the argument that they are important in the context of thermal transport.

with  $d_d$  being the dimensionality of the defect. Thus, for a one-dimensional defect such as a dislocation line,  $d_d = 1$  and  $\bar{n} = 2$ , for a point defect  $d_d = 0$  and  $\bar{n} = 3$ , and so on.

We can understand Eq. 2.27 as follows. For example consider a line defect, so  $\bar{n} = 2$ . Suppose the defect is parallel to the  $z$  axis. Then, in addition to the energy, the  $z$  component of the phonon wavevector must also be conserved in the scattering event. This results in the phonon scattering onto a circle in  $k$  space, and when summing over all possible final state wavevectors the density of accessible phonon states is effectively that of a system with two real spatial dimensions, written as  $g_{2d}$ . At the same time, the matrix element of the perturbation reduces to an integral over the coordinates perpendicular to the defect,  $x$  and  $y$ , and since this is now a two-dimensional integral, we write it as  $M_{2d}$ . Finally, the density of line defects  $n_{2d}$  is an areal density, or a number per unit area with dimensions  $(length)^{-2}$ .

It is easy to see that the same reasoning applies to planar ( $\bar{n} = 1$ ) and point ( $\bar{n} = 3$ ) defects. All three cases are illustrated in Figure 2.4 where the scattering diagram is shown on top (analogous to an Ewald sphere) and the corresponding density of final states,  $g_{\bar{n}d}$ , is given on the bottom which for acoustic phonons obeys the following relation,

$$g_{\bar{n}d} \propto \omega^{\bar{n}-1}. \quad (2.30)$$

A phonon interacting with a point defect scatters onto a shell in  $k$  space, a phonon interacting with a line defect scatters onto a circle, and one interacting with a planar defect scatters onto two states (forward and backward scattering) on a line in  $k$  space.

Our objective in writing the rate as a product of  $n_{\bar{n}d}$ ,  $g_{\bar{n}d}$ , and  $\overline{|M_{\bar{n}d}|^2}$ , is to highlight those aspects of the answer that are most important for practical purposes. It is useful to refer to the quantities  $g_{\bar{n}d}$  and  $\overline{|M_{\bar{n}d}|^2}$  as the ‘phase-space’ and ‘matrix-element’ contributions, respectively. It may also be useful to examine Eq. 2.27 by simple dimensional analysis. Denoting the dimensions of any quantity  $X$  by  $[X]$ , we have,

$$[n_{\bar{n}d}] = \frac{1}{(length)^{\bar{n}}}, \quad [g_{\bar{n}d}] = \frac{time}{(length)^{\bar{n}}}, \quad \left[ \overline{|M_{\bar{n}d}|^2} \right] = \frac{(length)^{2\bar{n}}}{(time)^2}, \quad (2.31)$$

and  $\Gamma(\mathbf{k})$  correctly has dimensions of  $(time)^{-1}$ . It is important to note that, while the isotropic approximation is implied in Figure 2.4, where the constant energy surface is represented as the shell of perfect sphere, these dimensionality and phase space arguments hold even when anisotropy in the phonon dispersion is considered.

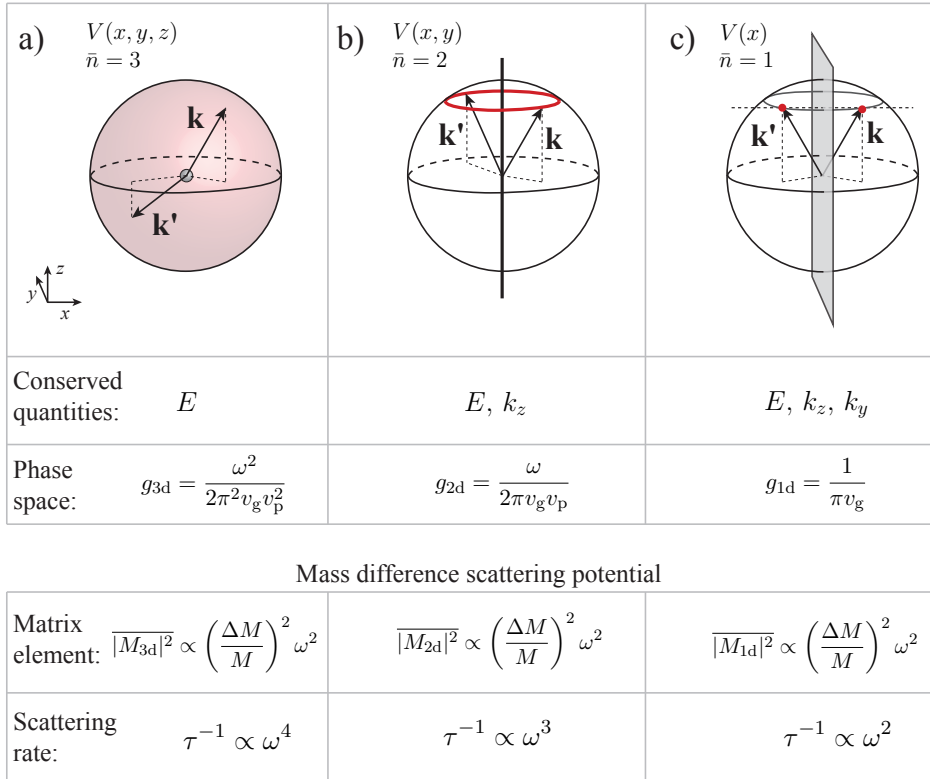


Figure 2.4: Phonon scattering diagrams for defects with different dimensionality. a) A phonon scattered elastically by a point defect scatters into the 3d phonon density of states (pDOS). b) A phonon scattered by a linear defect (scattering potential,  $V(x, y)$ ) conserves phonon momentum in the  $z$ -direction and thus scatters into the 2d pDOS, contributing  $\omega$  to the phonon scattering rate. c) A phonon scattered by planar defect ( $V(x)$ ) conserves phonon momentum within the defect plane ( $yz$ -plane) and scatters into the 1d pDOS which is  $\omega$ -independent.  $v_g$  and  $v_p$  are the phonon group and phase velocities. The bottom panel shows this dimensionality argument for the  $\omega$  power law applied to the scattering rate due to mass fluctuation scattering.

### Mass contrast scattering

Now that we have established the kinematic and phase space effects that arise from considering a scattering potentials dimensionality, we consider the nature of the scattering potential itself. It is instructive to first consider the effect of a change in atomic mass. By examining the two terms in  $\mathcal{H}$  (Eq. 2.10), it can be seen that a change in mass will perturb the phonon states through the lattice kinetic energy,  $\mathcal{T}$  (Eq. 2.11). A change in atomic mass locally changes the crystals kinetic energy. Later we will consider changes in the interatomic bond strength which will change the crystals potential energy  $U$ . Within the formalism provided in Appendix G.2, the scattering potential due

to a change in atomic mass at point  $\mathbf{r}$  in a crystal is

$$V(\mathbf{r}, \omega) = \frac{1}{2} \left( \frac{\Delta M}{M} \right) \hbar \omega V_0 \delta(\mathbf{r}). \quad (2.32)$$

This describes the scattering potential due to mass difference of a point defect or isotope, and is shown graphically in Figure 2.4a.  $\delta(\mathbf{r})$  is the three-dimensional  $\delta$ -function and  $V_0$  is the volume that the mass fluctuation occupies<sup>5</sup>. Care must be taken to ensure that  $V_0$  and the mass fluctuation parameter  $\Delta M/M$  are defined consistently. One theoretically consistent method is to define  $V_0$  as the volume of the primitive unit cell ( $V_0 = V_{\text{PUC}}$ , equation A.0.1), and  $\Delta M = M_{\text{def}} - M$  where  $M_{\text{def}}$  is the mass of a unit cell containing the defect, and  $M$  is the average mass of all unit cells in the crystal.

The Fourier transform of Eq. 2.32 is trivial given the presence of  $\delta(\mathbf{r})$ , and with Eq. G.2.24 we can define the matrix element contribution to  $\tau^{-1}$  as

$$\overline{|M_{3d}|^2} = \frac{V_0^2 \pi}{2} \left( \frac{\Delta M}{M} \right)^2 \omega^2. \quad (2.33)$$

This, combined with the phase space contribution  $g_{3d} \propto \omega^2$ , gives the familiar  $\tau^{-1} \propto \omega^4$  dependence, which is often referred to as Rayleigh scattering. The resulting expression, using Eqs. G.2.25, 2.33, and G.2.23 is

$$\tau(\omega)^{-1} = \frac{n_{3d} V_0^2}{4\pi v_g v_p^2} \left( \frac{\Delta M}{M} \right)^2 \omega^4. \quad (2.34)$$

This is identical to the formula provided by Klemens [30], and the analytical expression provided by Tamura (Eq. 23 of [31]).

Now suppose the mass fluctuation is arranged as a line through the crystal at  $x = y = 0$  (Figure 2.4b) rather than localized at a point. Klemens proposed that the dislocation core could be modeled as a line of vacancy defects. For such a case we can define the scattering potential

$$V(x, y, \omega) = \frac{1}{2} \left( \frac{\Delta M}{M} \right) \hbar \omega A_0 \delta(x) \delta(y). \quad (2.35)$$

$A_0$  is the cross-sectional area the line defect occupies. Using the primitive cell based convention above, one could define  $A_0 = V_{\text{PUC}}^{2/3}$ . The matrix element contribution to  $\tau^{-1}$  for this case is

$$\overline{|M_{2d}|^2} = \frac{A_0^2 \pi}{2} \left( \frac{\Delta M}{M} \right)^2 \omega^2 \sin(\theta)^2, \quad (2.36)$$

---

<sup>5</sup>Recall that  $\delta(\mathbf{r})$  has units of  $1/(volume)$ , so the quantity  $V_0 \delta(\mathbf{r})$  is unitless.  $V$  therefore has the correct units of energy.

which along with the phase space contribution,  $g_{2d} \propto \omega$  (Eq. G.2.14), gives

$$\tau(\mathbf{k})^{-1} = \frac{n_{2d} A_0^2}{4v_g v_p} \left( \frac{\Delta M}{M} \right)^2 \omega^3 \sin(\theta)^2. \quad (2.37)$$

Note that for this case  $\tau^{-1}$  depends on the direction of the incident phonon rather than just the frequency, as was the case for a point defect scattering. This equation is equivalent to that given by Klemens except for a numerical factor<sup>6</sup>. Once we choose which component of  $\kappa_{ph,ij}$  we are interested in, the appropriate  $\tau(\omega)$  for use in Eq. 2.22 can be defined (Section G.3). If we are interested in the direction perpendicular to the linear defect, than using Eqs. 2.37 and G.3.2, it can be found that  $\tau(\omega)^{-1} = (2/3)\tau(\mathbf{k})^{-1}$ .

Now imagine a planar defect, where on the atoms lying on the plane at  $x = 0$  are a different mass, Figure 2.4c. In a similar way we can define the scattering potential as

$$V(x, \omega) = \frac{1}{2} \left( \frac{\Delta M}{M} \right) \hbar\omega L_0 \delta(x). \quad (2.38)$$

Following a similar procedure, we can find  $\overline{|M_{1d}|^2}$  (Eq. G.2.33). This along with  $g_{1d}$ , which is independent of frequency (Eq. G.2.30), gives

$$\tau(\mathbf{k})^{-1} = \frac{n_{1d} L_0^2}{2v_g} \left( \frac{\Delta M}{M} \right)^2 \omega^2 \frac{k_x^2}{k^2}. \quad (2.39)$$

If we are again interested in  $\kappa_{ph,xx}$ , we find  $\tau(\omega)^{-1} = (1/3)\tau(\mathbf{k})^{-1}$ . Eq. 2.39 has the same form as the expression given by Turk and Klemens (Eq. 19 of [32]), which was derived for platelet-like coherent precipitates.

The treatment for mass difference scattering given above demonstrates how defect dimensionality effects the phonon scattering rate. In each case the matrix element contribution contributes  $\omega^2$  to  $\tau^{-1}$ . This stems from the fact that the mass fluctuations considered are localized in spatial extent and are therefore well described using  $\delta$ -functions. This is illustrated and tabulated in the top portion of Figure 2.4. When the dimensionality of the defect is changed from a point, to a line, to a plane, the phase space into which the phonon can scatter is changed. This changes the phase space contribution to  $\tau^{-1}$ , which follows the expression provided in Eq. 2.30, and is tabulated in the bottom portion of Figure 2.4. These phase space effects hold for all types of phonon-defect scattering. However, we will find in the next section that when the scattering potential is a more

---

<sup>6</sup>Eq. 2.37 is a factor of 3 smaller than Klemens' expression, Eq. 65 of [30] (which is given for  $\theta = \pi/2$ ). This may be due to differences in assumptions regarding mode conversion when computing the scattering phase space. If one assumes a phonon can scatter into any three of the acoustic branches, than the phase space contribution would be  $3g_{2d}$ . Since in full detail the matrix element will contain a dot product between the incident phonon eigenvector (polarization vector), and the scattered phonon eigenvector, we use  $g_{2d}$ .

complex function in real space, the matrix element contribution is less straightforward.

### Strain and rotation scattering

Atomic displacement fields, which are induced by crystal defects, can also scattering phonons. To describe this mathematically we first define a displacement vector field,  $u_i(\mathbf{r})$ , which defines the displacement of an atom at location  $\mathbf{r}$  from its equilibrium position. There are several ways in which one can theoretically compute the influence of  $u_i(\mathbf{r})$  on phonons. The method which allows for greatest physical insight starts by reducing the information contained in  $u_i(\mathbf{r})$  into a symmetric strain tensor [33]

$$\epsilon_{ij}(\mathbf{r}) = \frac{1}{2} \left( \frac{du_i(\mathbf{r})}{dx_j} + \frac{du_j(\mathbf{r})}{dx_i} \right) = \epsilon_{ji}(\mathbf{r}), \quad (2.40)$$

and an anti-symmetric rotation tensor

$$R_{ij}(\mathbf{r}) = \frac{1}{2} \left( \frac{du_i(\mathbf{r})}{dx_j} - \frac{du_j(\mathbf{r})}{dx_i} \right) = -R_{ji}(\mathbf{r}). \quad (2.41)$$

Imagine an infinitesimal unit volume of a material at position  $\mathbf{r}$ , in the shape of a cube. One can interpret  $\epsilon_{ij}(\mathbf{r})$  as describing the change in the shape of this cube, and  $R_{ij}(\mathbf{r})$  as describing its rotation.  $R_{12}$  gives the angle of rotation about the  $x_3$  axis (in radians),  $R_{13}$  gives rotation about  $x_2$  and so on. Additionally, it is evident that if  $\epsilon_{ij}$  and  $R_{ij}$  are known, one can obtain  $u_i$  by

$$u_i = (u_0)_i + R_{ij}x_j + \epsilon_{ij}x_j, \quad (2.42)$$

where  $(u_0)_i$  is a rigid body translation vector, which corresponds to someone picking up and moving the sample. For theoretical treatments we set  $(u_0)_i = 0$ .

In order to define how this atomic displacement field changes the phonon energy, and in turn induces scattering, we define the generalized, mode specific, Grüneisen tensor (Eq. 11.75 of Wallace [34])

$$\gamma_{ij}(\mathbf{ks}) = -\frac{d \ln \omega(\mathbf{ks})}{d \epsilon_{ij}}. \quad (2.43)$$

This definition provides a scalar value for every mode  $\mathbf{ks}$ , describing how sensitive it is to the  $ij$  component of the strain tensor,  $\epsilon_{ij}$ . Therefore it captures how anharmonic a crystal is to hydrostatic and shear (deviatoric) strain. One can conceptualize hydrostatic strain as a change in volume of a crystal and shear strain as a change in its shape (at constant volume). Consequentially, shear strain breaks crystal symmetry. A more commonly used metric for describing crystal anharmonicity is the hydrostatic mode specific Grüneisen parameter, commonly referred to as simply the mode specific

Grüneisen parameter

$$\gamma(\mathbf{ks}) = \gamma_{ii}(\mathbf{ks}) = -\frac{d \ln \omega(\mathbf{ks})}{d \ln V}. \quad (2.44)$$

The relationship between Eq. 2.43 and 2.44 is made by recalling that the change in volume of a material is given by the trace of the strain tensor,  $\epsilon_{ii}$ . An overview and derivation of several common Grüneisen parameters and tensors is given in Appendix F. Using Eq. 2.43 one can define a scattering potential due to an internal strain field (analogous to Eq. 6.4.2 of Ziman [29])

$$V(\mathbf{r}, \mathbf{ks}) = \hbar \omega(\mathbf{ks}) \gamma_{ij}(\mathbf{ks}) \epsilon_{ij}(\mathbf{r}). \quad (2.45)$$

By inserting Eq. 2.43 into 2.45, one can see that it reduces to simply  $\hbar d\omega$  or the change in phonon energy due to the strain field.

### Phonon-dislocation strain scattering

Phonon dislocation strain scattering is formally treated in Sections 3.1.1 and G.4.3, and the final expression obtained within this theoretical framework can be found in Eq. G.4.22. Here we highlight the main points needed for a conceptual understanding.

Perhaps the most characteristic features of dislocations is their long range strain field which falls off as  $1/r$  when moving away from a dislocation core located at  $r = 0$  (with  $r = (x^2 + y^2)^{1/2}$  for a dislocation pointing in the  $z$ -direction). This results in a scattering potential which also falls off as  $1/r$ , rather than the simple  $\delta$ -functions we had for mass difference scattering above. The 2D Fourier transform of  $1/r$  is  $1/q$  (with  $q = (q_x^2 + q_y^2)^{1/2}$ , Eq. G.5.3). By recalling that  $q \propto k$  and  $k = \omega/v_p$ , one can see that the Fourier transform of the strain field from a dislocation will produce a  $1/\omega$  dependence. This  $1/\omega$  dependence cancels with the  $\omega$  dependence in  $V$  and results in an  $\omega$ -independent matrix element contribution,  $\overline{|M_{2d}|^2}$ . We can show this in a simple way by writing the scattering potential in a concise form, neglecting angular dependencies and coefficients for the time being

$$V(r) = \hbar \omega \gamma \left( \frac{1}{r} \right), \quad (2.46)$$

$$M_{2d} = \tilde{V}(r) \propto \hbar \omega \gamma \left( \frac{1}{k} \right) = \hbar \omega \gamma \left( \frac{v_p}{\omega} \right) = \hbar \gamma v_p. \quad (2.47)$$

This Fourier analysis shows that we do not expect any explicit  $\omega$  dependence in  $M_{2d}$  (Section 6.4 of Ziman [29]). Therefore, the classic  $\tau^{-1} = n_{2d} g_{2d} \overline{|M_{2d}|^2} \propto \omega$  for dislocation strain scattering stems from the phase space contribution  $g_{2d} \propto \omega$ , and a  $\omega$  independent matrix element contribution  $\overline{|M_{2d}|^2} \propto \omega^0$  [35, 36, 30]. From an analytical perspective, if there is a frequency dependence in the matrix element of dislocation strain scattering observed computationally, we would expect it to

come from an  $\omega$ -dependence in  $\gamma$  or  $v_p$ , or from the fact that the  $1/r$  strain field was not faithfully captured.

### Acoustic mismatch scattering

Now let us consider phonon scattering due to a change in the elastic properties in the material. This case can be solved within the formalism of classical wave mechanics, and has been termed the acoustic mismatch model (AMM). Here, we provide a quantum mechanical derivation which achieves an essentially analogous result to the classical treatment (equivalent at  $\Delta v_s/v_s < 0.2$  where  $v_s$  is the speed of sound). Crystals have anisotropic elastic properties, speeds of sound, phonon dispersion relations even in cubic systems, such that acoustic mismatch can arise due to adjacent grains of the same material having different orientations, i.e. the rotation of a crystal lattice across a grain boundary (GB). Alternatively, acoustic mismatch can occur at the interface between two materials with different elastic properties, even if they are aligned in the same crystallographic orientation.

We can describe the change in phonon energy across a grain boundary in the  $yz$  plane at  $x = 0$  due to acoustic mismatch in a general way

$$V(x) = \hbar \Delta\omega \Theta(x) = \hbar k \Delta v_p \Theta(x) \quad (2.48)$$

where  $\Delta\omega$  is the change in phonon frequency of a phonon with wavevector  $k$ .  $\Delta v_p$  is its phase velocity and  $\Theta(x)$  is a step function defined in Eq. G.5.4. To compute the scattering rate,  $\tau^{-1}$  for this planar perturbation we require the 1d matrix element

$$M_{1d} = \tilde{V}(x) = -\hbar k \Delta v_p \left( \frac{i}{q_x} \right) = \frac{\hbar \Delta v_p}{2} \left( \frac{i}{\sin \theta \cos \phi} \right) \quad (2.49)$$

recalling that only specular back scattering contributes to the scattering rate ( $k'_x = -k_x$ ,  $k'_y = k_y$ , and  $k'_z = k_z$ , such that  $q_x = -2k_x = -2k \sin \theta \cos \phi$ ). By following the procedure outlined in Appendix G.2.3, we find

$$\tau(\omega)^{-1} = \frac{2v_s}{3L_x} \left( \frac{\Delta v_s}{v_s} \right)^2. \quad (2.50)$$

Note that we have made the Debye approximation ( $v_s = v_g = v_p$ ) for comparison with the analytical treatment of the classical AMM, which is given in the next section. As can be seen from Eq. 2.50, there is no explicit frequency dependence from this planar, step-function type perturbation.

## Models for the thermal conductivity of systems with interfaces

There are several ways to model the phonon thermal conductivity  $\kappa_{\text{ph}}$  of systems containing interfaces. Here we will examine the two most common. In both treatments, each frequency  $\omega$  is considered an independent conduction channel. In Appendix H we provide a mode ( $\mathbf{k}s$ ) specific treatment. The thermal conductivity of the, bulk, interface free system is given by Eq. 2.22 with only phonon-phonon scattering  $\tau(\omega) = \tau_{\text{pp}}(\omega)$ . Here we will focus on the thermal conductivity of one channel with frequency  $\omega$

$$\kappa_{\text{bulk}}(\omega) = \frac{1}{3}C(\omega)v_g(\omega)^2\tau_{\text{pp}}(\omega), \quad (2.51)$$

and its corresponding thermal resistivity  $\kappa_{\text{bulk}}(\omega)^{-1}$ .

The first method we examine is based on the Landauer method, which simply computes the conductance of particles encountering an interface when each particle is assigned a transmissivity  $t(\omega)$  [37]. When the Landauer approach is applied to phonons, each channel carries a heat capacity  $C(\omega)$ , at a speed equal the group velocity  $v_g(\omega)$ . Within this formulation the thermal boundary conductance is given by

$$h_B = \int h_B(\omega)d\omega, \quad (2.52)$$

$$h_B(\omega) = \frac{1}{4}C(\omega)v_g(\omega)\frac{t(\omega)}{1-t(\omega)}. \quad (2.53)$$

Since  $h_B$  is the thermal boundary conductance,  $h_B^{-1}$  is the thermal boundary resistance. Additionally, it will be convenient to define the thermal boundary resistivity  $(L_z h_B(\omega))^{-1}$  where  $L_z$  is the linear spacing between boundaries as shown in Figure 2.5. Since the bulk material and interfaces are in series in this model, the total thermal resistivity of the conduction channel  $\omega$  is given by the sum of the resistivities

$$\kappa_{\text{ph}}(\omega)^{-1} = \kappa_{\text{bulk}}(\omega)^{-1} + (L_z h_B(\omega))^{-1}. \quad (2.54)$$

If the spectral properties, or mode specific properties of the thermal boundary resistance and bulk thermal conductivity are neglected one can write the total thermal conductivity simply as

$$\kappa_{\text{ph}}^{-1} = \kappa_{\text{bulk}}^{-1} + (L_z h_B)^{-1}. \quad (2.55)$$

The second method is to consider the interface as introducing an additional scattering mechanism which can reduce the phonon lifetime. The relaxation time due to this scattering mechanism can be calculated using the scattering theory presented in Section 2.3.1. The total thermal resistivity is calculated as the sum of the resistivity due to phonon-phonon scattering and the resistivity due

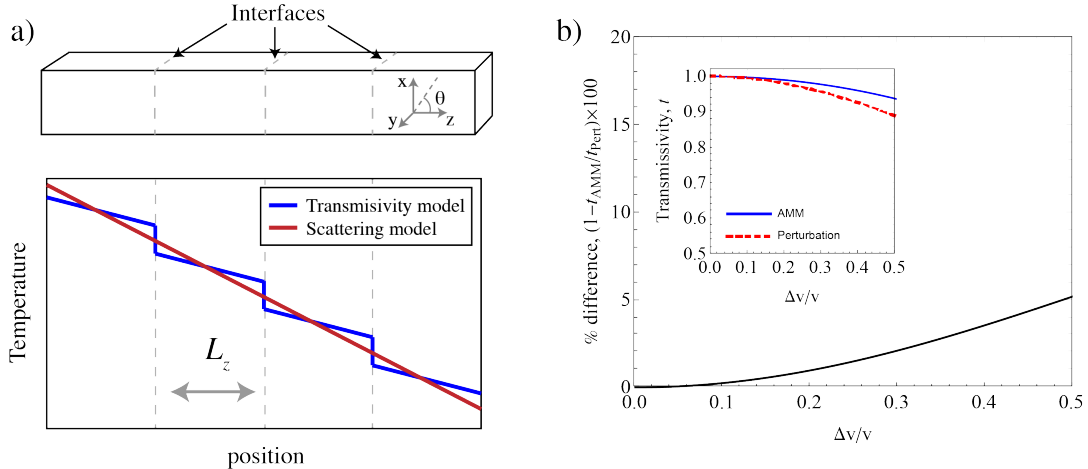


Figure 2.5: a) A schematic illustration of two common models used to describe heat conduction in materials with interfaces. The vertical can be interpreted as temperature of a specific conduction channel, which can be either a specific phonon mode  $\mathbf{k}s$  or frequency  $\omega$  depending on the level of detail of the model. The blue line depicts the Landauer based model where a thermal boundary resistance arising from the conduction channel having a interfacial transmission probability  $t(\mathbf{k}s) > 1$  (or  $t(\omega) > 0$ ), induces an instantaneous drop in temperature. The red line depicts a model based on phonon scattering theory and Matthiessen's rule, where each scattering mechanism contributes a scattering rate ( $\tau(\mathbf{k}s)^{-1}$  or  $\tau(\omega)^{-1}$ ) and thermal resistance to the conduction channel. b) A comparison between the transmissivity calculated using classical acoustic mismatch (AMM) theory and quantum perturbation theory (Eq. 2.50 and 2.59). The two differ no more than 5% across the entire range.

to boundary scattering,  $\kappa_B = C(\omega)v_g(\omega)^2\tau_B(\omega)/3$

$$\kappa_{\text{ph}}(\omega)^{-1} = \kappa_{\text{bulk}}(\omega)^{-1} + \kappa_B(\omega)^{-1}, \quad (2.56)$$

or equivalently

$$\kappa_{\text{ph}}(\omega) = \frac{1}{3}C(\omega)v_g(\omega)^2\tau(\omega), \quad (2.57)$$

with  $\tau(\omega)$  having the familiar form (Eq. 2.26)

$$\tau(\omega)^{-1} = \tau_{\text{ph}}(\omega)^{-1} + \tau_B(\omega)^{-1}. \quad (2.58)$$

Since this relaxation time is derived by considering perturbations to the crystal Hamiltonian, this method has the capacity for capturing materials physics which may be missed by the Landauer approach. In the perturbation theory approach, the effects of defect dimensionality and spatial extent of the scattering potential, as well as the physical origin of the phonon scattering are naturally built into the theoretical framework (e.g. anharmonicity, elastic anisotropy, local changes in atomic mass or interatomic force constants etc.).

However, the two approaches can be related by equating Eqs. 2.55 and 2.56

$$t(\omega) = \frac{\tau_B(\omega)}{\frac{3}{4} \frac{L_z}{v_g(\omega)} + \tau_B(\omega)}. \quad (2.59)$$

Using this equation with the acoustic mismatch perturbation theory given in Eq. 2.50, we obtain

$$t_{\text{Pert}} = \frac{1}{\frac{1}{2} \left( \frac{\Delta v_s}{v_s} \right)^2 + 1} \quad (2.60)$$

In the classical AMM theory, the transmissivity is given by [38]

$$t_{\text{AMM}} = \frac{4Z_1 Z_2}{(Z_1 + Z_2)^2} \quad (2.61)$$

where  $Z_i = \rho_i v_{s,i}$  is the acoustic impedance of side  $i$ , and  $\rho_i$  is its mass density. For direct comparison with the perturbation theory approach derived here we set  $v_{s,1} = v_s + \Delta v_s/2$ ,  $v_{s,2} = v_s - \Delta v_s/2$ , and  $\rho_1 = \rho_2$ . The two are compared in Figure 2.5b, where Eq. 2.50 is converted to a transmissivity using Eq. 2.59. The two are identical at  $\Delta v/v > 0.2$  and differ no more than 5% across the entire range.

## Chapter 3

### Phonons and interfaces

#### 3.1 Diffraction and dimensionality crossover<sup>1</sup>

Thermal resistance at interfaces and grain boundaries is important in a range of fields from microelectronics to energy materials. Standard models treat interfaces as structureless even though at the nanoscale they are often better described as arrays of linear defects. Here, we examine several characteristics of heat transport that arise when considering such a structure at the interface. When heat carrying phonons scatter off linear defect arrays, diffraction of phonons occurs. Furthermore, a dimensionality crossover is observed in diffusive transport. Phonons transition from seeing a structureless planar defect when their wavelength is longer than the defect spacing,  $\lambda \gtrsim D$ , to seeing the interface as a collection of independently scattering linear defects when  $\lambda \lesssim D$ . By applying this theory to grain boundary strain-field scattering, we show that this dimensionality crossover can explain the frequency dependence of grain boundary scattering and transmissivity, which results in the  $T^2$  temperature dependence observed in the low- $T$  thermal conductivity of poly/nanocrystalline materials.

The current standard models for describing phonon-interface interactions are the acoustic and diffuse mismatch models (AMM and DMM)[40], which define the interface as a structureless planar defect where the transmissivity or scattering rate is determined by the bulk properties on either side of the interface. Specifically, within the AMM phonons interact with interfaces through an acoustic analogue to the refraction of light, where a change in elastic properties (i.e. acoustic impedance) determines the probability that an incident phonon will reflect or transmit across the interface [41, 38]. In the DMM every phonon scatters randomly or diffusely at the interface and the probability of transmission is determined by the density of phonon states on either side of the boundary [38]. The commonly used gray model also assumes diffuse scattering and simply limits the phonon mean free path (MFP) to the average grain size of a polycrystal. This is essentially an extension of the

---

<sup>1</sup>The content in this section was published by Hanus, Garg, and Snyder in Ref. [39].

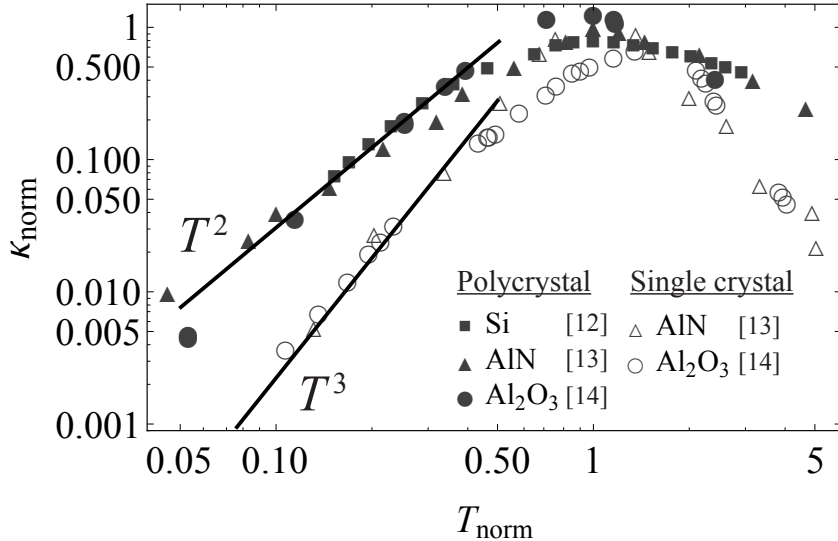


Figure 3.1: The low temperature lattice thermal conductivity ( $\kappa_L$ ) of polycrystalline samples compared to that of single crystals. In polycrystals where the phonon scattering is dominated by grain boundary interactions,  $\kappa_{\text{ph}}$  scales as  $T^2$ . In single crystals where scattering is dominated by phonon sample surface interactions,  $T^3$  behavior is observed. The  $\kappa_{\text{ph}}$  and  $T$  values are normalized for comparison. Un-normalized data are shown in Figure 3.7.

Casmir limit which was initially proposed for single crystals where the MFP was limited to the size of the sample [42]. Each of these models predicts frequency independent scattering of phonons at low temperatures, and thus predicts a  $T^3$  temperature dependence in the phonon thermal conductivity,  $\kappa_{\text{ph}}$ , stemming from the temperature dependence of the heat capacity.

In contrast, studies of the low- $T$   $\kappa_{\text{ph}}$  of polycrystals provided by Wang et al. [43], Watari et al. [44], and Berman [45] show a  $\kappa_{\text{ph}} \propto T^2$  temperature dependence (Figure 3.1) which is characteristic of a grain boundary (GB) scattering rate that is linear in frequency,  $\tau^{-1} \propto \omega$ . An empirical expression for the spectral transmissivity function of phonons at GBs with the form  $t(\omega) = (1 + \alpha\omega/\omega_{\text{max}})^{-1}$ , (where  $\alpha$  is a constant on the order of unity, and  $\omega_{\text{max}}$  is the maximum phonon frequency), was presented to account for the observed  $\kappa_{\text{ph}} \propto T^2$  ( $\tau^{-1} \propto \omega$ ) behavior in polycrystals [43] and has been used in a number of computational and experimental studies [46, 47, 48]. Additionally, Hua *et al.* have recently measured the spectral phonon transmissivity of an Al-Si interface and experimentally showed that the interface of dissimilar materials can have a transmissivity function which is  $\omega$ -independent at the lowest frequencies and decrease above some critical crossover frequency [49]. Providing mechanistic explanations for these phenomena is a key step in understanding phonon-interface interactions at a fundamental level.

The frequency independence of the phonon scattering in the AMM, DMM, and grey models stems (in

part) from their definition of the interface as a structureless planar defect. However, real interfaces between similar (GBs) and dissimilar (phase boundaries) materials are not structureless at the nanoscale but are better described as arrays of linear defects of various types (Refs. [50, 51, 52, 53, 54, 55] and Section 2.3 of [56]). In fact, prevailing models of GB defect energies and structure have essentially extended the classic Read-Shockley model [55], which defines the GB structure as an array of lattice dislocations, to many GB types (including GBs at high angle) despite the complexity and variety of GB structures [57, 58, 59]. Furthermore, interfaces between dissimilar materials are known to accommodate the mismatch in lattice parameter by the formation of arrays of misfit dislocations spaced periodically (e.g. GaAs heterostructures [60, 61]). X-Ray and electron diffraction peaks arising from the periodic dislocation structures in semi-coherent phase boundaries and GBs have been experimentally observed and can be used to study interfacial structure [62, 63]. We note that the wavelength of X-Rays and electrons used in these studies are comparable to the wavelengths of heat carrying phonons. The interface between two crystalline materials with structural periodicity will tend to have structural periodicity itself. We propose that the description of phonon-interface scattering should be grounded in a definition which contains this structural information.

Phonon diffraction conditions arising from periodically spaced dislocations have been discussed previously by authors such as Klemens [30], Carruthers [36], and are formally considered by Omini and Sparavigna [64]. Previous works, however, have not examined the dimensionality crossover effects that diffraction engenders. We have previously suggested that dislocation strain may dominate phonon-GB scattering processes [65]. Here we develop a rigorous theory for this and identify several interesting phenomena that arise from treating the GB dislocation arrays collectively. This study focuses only on phonon-interface interactions, and does not consider electron-phonon interactions which can be important at metal semiconductor interfaces.

To that end, we first discuss the general effect of defect dimensionality on phonon scattering in order to establish concepts that will be used to interpret the theory that follows. We then derive a general formula to calculate the phonon lifetime due to an array of linear defects, where by analyzing the conservation laws and kinematics of this system, diffraction conditions and a crossover in defect dimensionality can be observed. Next, this general formula is applied to the specific case of phonon-GB strain field scattering by defining the linear defects as the strain field from edge dislocations which collectively define a symmetric tilt grain boundary. A simple, semi-empirical expression is provided as an excellent approximation of the full analytical theory which embodies the crossover in defect dimensionality observed in this calculation. Finally, this scattering theory is applied to standard phonon transport models, where the phonon-GB strain field scattering and inherent dimensionality crossover provide a mechanistic explanation for the experimentally observed  $\kappa_{\text{ph}} \propto T^2$  of polycrystalline and nanocrystalline materials [43, 44, 45]. This power law analysis provides evidence that the dominate phonon-GB scattering mechanism is through GB strain fields. It may also provide an explanation for crossover effects in the frequency dependence of phonon

transmissivity at phase boundary interfaces [49].

### 3.1.1 Scattering from an infinite array of linear defects

The derivation and analysis below will build on the concepts presented in Section 2.3.1. Special attention should be given to the effects of defect dimensionality on phonon scattering which are shown in Figure 2.4 and derived in Appendix G.2. The case considered here is the phonon scattering from an interface described by array of linear defects. In general, the results can be conceptualized as a phonon scattering process which transitions from scattering off a 2D defect (Figure 2.4c) to a collection 1D defects (Figure 2.4b), with decreasing wavelength and increasing frequency.

#### Kinematics & diffraction conditions

Due to the wavelike nature of phonons, their interaction with periodic perturbations leads to diffraction conditions which depend on the wavelength of the phonon and the spacing of the perturbations. We now consider the case of linear defects parallel to the  $z$  axis periodically spaced by a distance  $D$ . The  $x$  and  $y$  coordinates of the defects are

$$x = 0, \quad y = jD \quad (j = 0, \pm 1, \pm 2, \dots). \quad (3.1)$$

Defect arrays fitting this definition describe a variety of interfaces, such as grain boundaries and semi-coherent phase boundaries which can be defined as arrays of linear dislocations [57, 58, 66].

Scattering from such an array will conserve phonon energy and momentum in the  $z$ -direction,  $k_z$ . In addition, diffraction conditions will be observed from the periodic structure in the  $y$  direction, such that  $k_y$  will change by integer multiples of  $2\pi/D$ . This in turn means that for any incident phonon wavevector  $\mathbf{k}$ , the scattered phonon wave vector  $\mathbf{k}'$  will take only a discrete set of values. Then, with the definition

$$q_m = \frac{2\pi}{D}m, \quad (3.2)$$

we can solve for the final phonon states by casting the constraints on  $\mathbf{k}'$  as

$$k' = k, \quad k'_z = k_z, \quad k'_y = k_y - q_m \quad (m = \text{integer}). \quad (3.3)$$

The condition  $k' = k$  is equivalent to  $k'^2 = k^2$ , or,  $k'^2_x = k_x^2 + k_y^2 - q_m^2$ , which leads to

$$k'_x = k'_{x,m\pm} \equiv \pm(k_x^2 + 2k_y q_m - q_m^2)^{1/2}. \quad (3.4)$$

However,  $k'_x$  must be real, so only a limited number of values of  $m$  are allowed for any given  $\mathbf{k}$ , i.e. only a finite number of final phonon states ( $\mathbf{k}'$ ) exist.

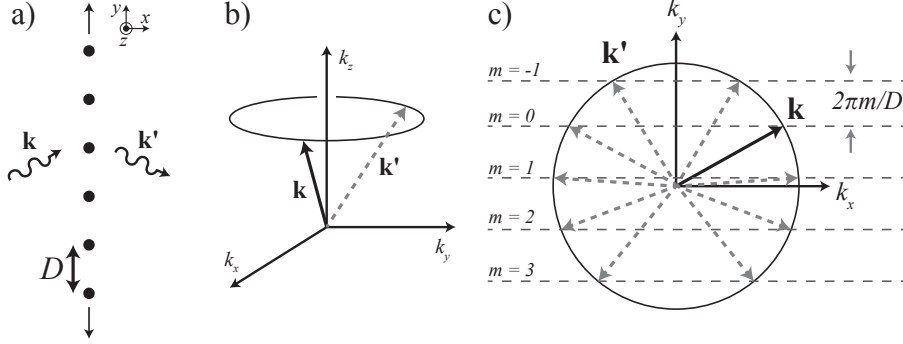


Figure 3.2: Kinematics and conservation laws leading to diffraction conditions and dimensionality crossover. a) An illustration of the array of linear defects which scatters a phonon  $\mathbf{k}$  into a state  $\mathbf{k}'$ . b) Scattering from linear defects requires the conservation of momentum in the  $k_z$  direction,  $k_z = k'_z$ . This results in a scattering circle that lies parallel to the  $xy$ -plane. c) Because of further conservation laws arising from the periodic nature of the scattering potential (given in Eq. 3.3 in the text), only intersections of this circle with the dashed lines are valid. For small  $|\mathbf{k}|$ , only the  $m = 0$  line will give valid solutions (and a phonon density of states (pDOS),  $g_{1d}$ ). When  $|\mathbf{k}|$  is large, the entire circle is essentially accessible (pDOS  $g_{2d}$ ).

Figure 3.2 provides a visualization of the conservation laws given in Eq. 3.3. Figure 3.2b illustrates the conservation of  $k_z$ , meaning the incident phonon will scatter onto a circle in  $k$  space. Figure 3.2c shows this scattering circle. Due to the conservation of  $k_y$  (as well as the conservation of energy,  $k' = k$ ), only intersections of this scattering circle with the dashed lines give valid final wavevectors. As  $|\mathbf{k}|$  increases (i.e. phonon frequency increases), the size of the circle increases, while the spacing between the dashed lines is fixed. When  $|\mathbf{k}|$  becomes large enough such that another term in the sum over  $m$  becomes available, a diffraction event is encountered. These diffraction peaks will be observed in our calculation of GB strain field scattering.

### Dimensionality crossover

When  $|\mathbf{k}|$  is smaller than  $\pi/D$ , the only allowed solution is  $m = 0$ , for which  $k'_y = k_y$ ,  $k'_z = k_z$ , and  $k'_x = \pm k_x$ . In other words, only forward scattering and specular reflection are allowed, and only the latter contributes to  $\tau^{-1}$ . This is the solution found by Klemens when solving for phonon scattering at GBs (Eq. 73 of [30]). In this case, the interface behaves like a structureless planar defect, and  $k_y$  is conserved just as  $k_z$ , making the final pDOS one-dimensional ( $g_{1d}$ ). When  $|\mathbf{k}|$  is much larger than  $2\pi/D$ , on the other hand, much of the scattering circle is accessible and there is effectively no constraint on  $k'_y$ . Now the interface behaves like a collection of independently scattering line defects, and the density of final phonon states is two-dimensional ( $g_{2d}$ ). The transition between these two

limits gives rise to a ‘dimensionality crossover’ and has important implications for the lifetime and thermal conductivity.

We show in Appendix G.4.1 that the expression for the phonon scattering rate from an array of linear defects takes the form,

$$\Gamma(\mathbf{k}) = \frac{n_{1d}}{\hbar^2 v_g D^2} \sum_{m,\sigma=\pm} |\tilde{V}_1(q_{x,m\sigma}, -q_m)|^2 (1 - \hat{\mathbf{k}} \cdot \hat{\mathbf{k}}') J(\mathbf{k}, m), \quad (3.5)$$

where  $q_{x,m\sigma} = k'_{x,m\sigma} - k_x$ ;  $\tilde{V}_1$  is the Fourier transform of the scattering potential associated with one line defect at  $(x, y) = (0, 0)$ , i.e.,

$$\tilde{V}_1(q_x, q_y) = \iint dx dy V_1(x, y) e^{-i(q_x x + q_y y)}; \quad (3.6)$$

and  $J(\mathbf{k}, m) = k(k_x^2 + 2k_y q_m - q_m^2)^{-1/2}$  is a Jacobian or volume rescaling factor associated with re-expressing the conservation laws (Eq. 3.3) in terms of  $q_x$ ,  $q_y$ , and  $q_z$ . The sum in Eq. 3.5 is over accessible final wavevectors as shown in Figure 3.2c, and each term in the sum corresponds to a separate diffraction peak.

### 3.1.2 Grain boundary strain and rotation field scattering

In this section we consider the specific problem of scattering from the strain field of grain boundaries, using the concepts illustrated in Figures 2.4 and 3.2. An edge dislocation array (Burger’s vector  $b\hat{\mathbf{x}}$ ) with the geometry shown in Figure 3.3a is considered. This array describes a symmetric tilt grain boundary (STGB) with a misorientation angle  $\theta_{GB}$  such that,

$$2 \sin\left(\frac{\theta_{GB}}{2}\right) = \frac{b}{D}. \quad (3.7)$$

This is the same microscopic picture behind the extended Read-Shockley model which is used to describe the GB energy of many types of GBs, and has been extended to GBs at high angle [57, 59]. Figure 3.3a schematically illustrates this interfacial defect next to its strain fields which are shown in Figure 3.3b.

The displacement field  $\mathbf{u}(\mathbf{r})$  is then independent of  $z$ , and the strain state can be formulated in terms of the quantities  $\epsilon_\Delta = \epsilon_{ii}$ , and  $\epsilon_S = \epsilon_{12}$ , which describe the dilation and shear strain. The rotation of the crystal orientation across the GB is represented by  $\epsilon_R = 2R_{12}$  [58]. Each type of deformation constitutes an independent scattering channel, which contributes additively to the scattering rate.

For the perturbation  $V$  due to this strain and rotation, we employ the same form as that used by Ziman (Section 6.4 of [29]). We will take the perturbation from the array of dislocations as the

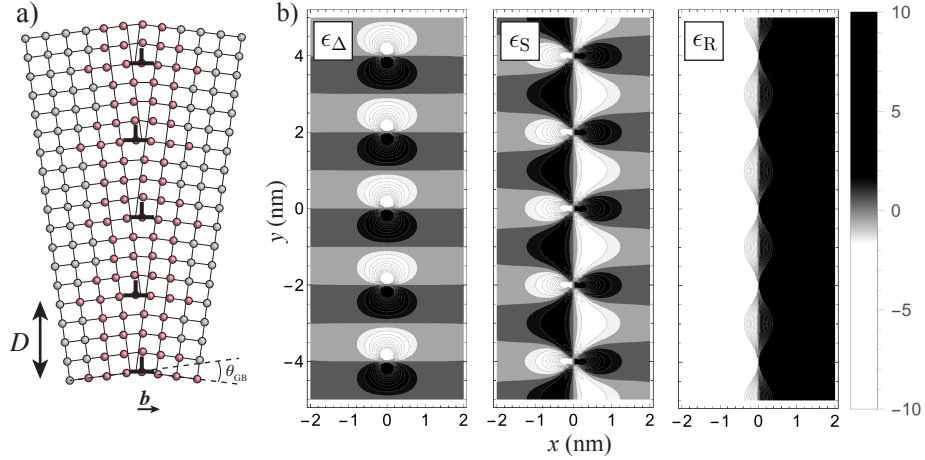


Figure 3.3: A periodic array of edge dislocations describing the structure of a symmetric tilt grain boundary. a) Schematic illustration of an array of edge dislocations ( $\perp$ ) periodically spaced by  $D$  with Burger's vector  $b\hat{x}$  forming a grain boundary of angle  $\theta_{\text{GB}}$ . Careful examination of the atoms highlighted in red reveals that they are displaced. b) Grain boundary strain maps of hydrostatic strain  $\epsilon_{\Delta}$ , pure shear strain  $\epsilon_S$ , and rotation  $\epsilon_R$ , calculated via Eq. 3.11 with parameters given in Table 3.1. Scale bar shows the percent strain ( $10^{-2}$ ).

sum of contributions from each individual dislocation for each deformation type. More specifically, denoting the contribution from a single dislocation along the line  $x = y = 0$  by a subscript ‘1’ as in Eq. 3.5,

$$V_{1,a} = \hbar\omega\gamma_a\epsilon_a(x,y), \quad (a = \Delta, S, R), \quad (3.8)$$

so that the total perturbation from each type of deformation is

$$V_a = \hbar\omega\gamma_a \sum_{n=-\infty}^{\infty} \epsilon_a(x, y - nD). \quad (3.9)$$

Here,  $\omega$  is the phonon angular frequency, and  $\gamma_a$  is a coefficient relating the type of strain or rotation  $a$  to a change in phonon energy. The change in phonon energy with strain,  $\gamma_\Delta$  and  $\gamma_S$ , is defined through the generalized Grüneisen parameter (Eq. 11.75 of [34]). The change in phonon energy with a rotation of the lattice,  $\gamma_R$ , is determined by the anisotropy of the phonon dispersion and elastic properties.

In this work, we use a single averaged Grüneisen parameter,  $\gamma = \gamma_\Delta = \gamma_S = \gamma_R$  instead a full phonon-mode and deformation specific representation, which is in line with historical treatments of Ziman [29], Klemens [30], and Carruthers [36], and more recent ones by Meng *et al.* [67], for example.

With this perturbation defined, we can now use the formalism developed in Section G.4 and Eq.

3.5 to calculate the phonon lifetime. It can be seen from Eq. 3.5 that this will require the Fourier transform of the single dislocation perturbation which can be found for each deformation type to equal

$$\tilde{V}_{1,a} = \hbar\omega\gamma\tilde{\epsilon}_a(\mathbf{q}). \quad (3.10)$$

The explicit forms of these deformations are (Section 3-4 of [58])

$$\epsilon_{\Delta} = \frac{-b}{2\pi} \frac{(1-2\nu)}{(1-\nu)} \frac{y}{(x^2+y^2)}, \quad \epsilon_S = \frac{b}{4\pi(1-\nu)} \frac{x(x^2-y^2)}{(x^2+y^2)^2}, \quad \epsilon_R = \frac{b}{\pi} \frac{x}{(x^2+y^2)}, \quad (3.11)$$

and thus their Fourier transforms are given by

$$\tilde{\epsilon}_{\Delta}(\mathbf{q}) = ib \frac{(1-2\nu)}{(1-\nu)} \frac{q_y}{q^2}, \quad \tilde{\epsilon}_S(\mathbf{q}) = -ib \frac{1}{(1-\nu)} \frac{q_x q_y^2}{q^4}, \quad \tilde{\epsilon}_R(\mathbf{q}) = -2ib \frac{q_x}{q^2}, \quad (3.12)$$

where  $b$  is the Burgers vector for one dislocation, and  $\nu$  is the Poisson ratio. Note that because all forms of  $\tilde{\epsilon}_a$  scale as  $1/q$ , and since  $q$  (the momentum transfer) scales as  $k = \omega/v_p$ , the  $\omega$  dependence cancels in  $\tilde{V}_{1,a}$  from Eq. 3.10 (at low  $\omega$ ). This results in a matrix-element contribution that is essentially  $\omega$  independent for phonon-strain field scattering. When the three channels are added together, we get

$$\Gamma_{\text{gbs}}(\mathbf{k}) = \frac{n_{1d}\gamma^2}{v_g D^2} \sum_{m,\sigma} \omega_k^2 \left[ |\tilde{\epsilon}_{\Delta}|^2 + |\tilde{\epsilon}_S|^2 + |\tilde{\epsilon}_R|^2 \right] (1 - \hat{\mathbf{k}} \cdot \hat{\mathbf{k}}') J(\mathbf{k}, m). \quad (3.13)$$

This expression will be averaged over incident phonon direction (Eq. G.3.2) and be applied to Eq. 2.22 to examine its implications on  $\kappa_{\text{ph}}$ .

## Rotation and specular reflection

It leads to greater physical insight to examine the  $m = 0$  (specular) term in the sum in (3.13) separately from the  $m \neq 0$  (nonspecular) terms. For the  $m = 0$  term,  $q_y = 0$ , and we see from Eq. 3.12 that  $\tilde{\epsilon}_{\Delta} = \tilde{\epsilon}_S = 0$ , so only rotation is nonzero (see the inset of Figure 3.4). Thus, for  $k < \pi/D$ , only specular reflection survives and only rotational deformation contributes to scattering. This deformation arises because the crystals on the two sides of the grain boundary are rotated with respect to each other, and the deformation is long-ranged for the same reason (see  $\epsilon_R$  in Figure 3.3b). The coupling coefficient for rotation is determined by the anisotropy of the crystal and is only a function of the second order force constants [68]. Thus, the  $m = 0$  term is analogous to the AMM (Section 2.3.1), and  $\gamma_R$  should be interpreted as an anisotropy factor. In Appendix G.4.2 the AMM is derived by analytically solving Eq. 3.13 in the low-frequency limit.

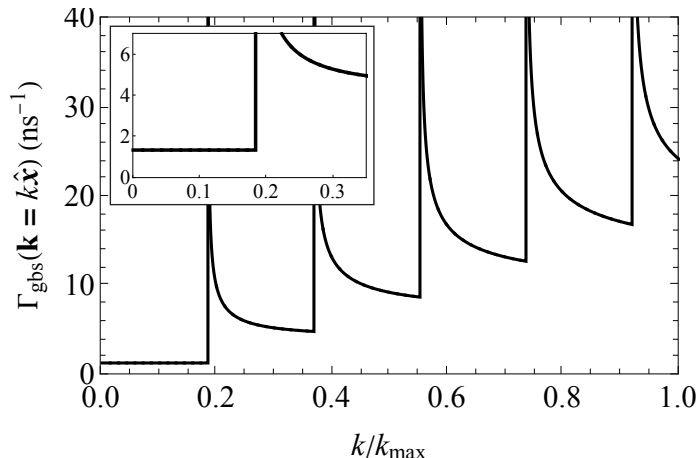


Figure 3.4: Phonon diffraction peaks arising from the periodic nature of a grain boundary strain field. The scattering rate is calculated from Eq. 3.13 for a phonon at normal incidence ( $\mathbf{k} \parallel \hat{\mathbf{x}}$ ) at different magnitudes of the phonon wavevector,  $k = |\mathbf{k}|$ . Scattering at low  $k$  is non-zero as shown in the inset, and diffraction peaks are observed as singularities at  $2\pi m/D$ , where  $m$  is an integer.

### Phonon diffraction from GB strain fields

Scattering of wave-like phonons from the GB strain fields shown in Figure 3.3 with material values of Si (given in Table 3.1 and 3.2) are calculated using Eq. 3.13 and the results for phonons at normal incidence ( $\mathbf{k} \parallel \hat{\mathbf{x}}$ ) are shown in Figure 3.4. Diffraction events for normal incidence occur when  $k = 2\pi m/D$  where  $m$  is an integer and these events appear as singularities in  $\Gamma_{\text{gbs}}$ . The exact position of the diffraction peaks depends on the phonon angle of incidence. This diffraction may be observable for ballistic phonons if the periodic structure of the interface is maintained for a length scale longer than the wavelengths of the phonons considered. In a real system where the GB structure is not infinitely periodic, one would expect these diffraction peaks to broaden in a manner analogous to Scherrer-broadening of X-Ray diffraction peaks due to particle size effects [69].

### Dimensionality crossover in diffuse heat conduction

For diffuse (bulk) thermal conduction, a dimensionality crossover is observed as phonons transition from seeing the GB as a 2d plane, to a collection of individually scattering linear defects. In bulk thermal conduction, phonons transport diffusively, arriving at the interface in random directions rather than one specific angle of incidence. Thus, the diffraction observed for one specific  $\mathbf{k}$  (Figure 3.4) is washed out when all the possible directions of incidence are included. We define  $\tau(\omega)$  in Eq. G.3.2 as a lifetime averaged over incident direction which can be directly applied to Eq. 2.22. By setting  $\Gamma(\mathbf{k})$  to  $\Gamma_{\text{gbs}}(\mathbf{k})$ , we obtain a directionally averaged GB strain scattering rate  $\tau_{\text{gbs}}(\omega)^{-1}$  which is shown in Figure 3.5. This can be used to describe the  $\omega$ -dependence of phonon-GB scattering in

diffuse heat conduction, and thus be used to interpret the temperature dependence of the lattice thermal conductivity of bulk polycrystalline and nanocrystalline materials.

The change in slope, or crossover in  $\omega$ -dependence, observed in Figure 3.5 is an important result of this study. When the phonon wavelength is larger than the microscopic structure of a GB ( $D$  in this work), the phonon will see it as planar defect and the phase space contribution to the phonon lifetime will be  $\omega$ -independent ( $g_{1d}$ ). When the wavelength is smaller than the microscopic structure of the GB, the phonon lifetime will obtain  $\omega$ -dependence through the phase space contribution ( $g_{2d}$ ). In the case shown above for GB strain field scattering, the matrix-element contribution is  $\omega$ -independent so the  $\omega$ -dependence of the phonon lifetime comes exclusively from phase-space contributions. We note that, while the diffraction conditions shown in Figure 3.4 require structural periodicity of the GB structure, the dimensionality crossover discussed here is purely a phase-space effect and is thus expected to be preserved even if perfect periodicity is not maintained in a real GB structure.

By recognizing the dimensionality crossover behavior, the following semi-empirical expression can be inferred through careful analysis<sup>2</sup>

$$\frac{1}{\tau_{\text{gbs}}(\omega)} = A n_{1d} v_s \gamma_R^2 \left( \frac{b}{D} \right)^2 + B \left( \frac{n_{1d}}{D} \right) \gamma^2 b^2 (\omega - \omega^*) \Theta(\omega - \omega^*), \quad (3.14)$$

where

$$\omega^* = \frac{4\pi v_s}{3D}, \quad (3.15)$$

is the dimensionality crossover frequency (averaged over the incident phonon direction) and  $\Theta(x)$  is the Heaviside step function. The best fit of Eq. 3.14 to Eq. 3.13 is obtained with  $A = 8/3$  and  $B = 0.93K_\nu$ , where

$$K_\nu = 1 + \frac{(1-2\nu)^2}{4(1-\nu)^2} + \frac{1}{32(1-\nu)^2}, \quad (3.16)$$

and  $\nu$  is Poisson's ratio. Eq. 3.14 provides an excellent approximation (dashed lines in Figure 3.5 and 3.6) for the numerical solution of the full analytical expression in Eq. 3.13 (solid lines). We note that the first term in Eq. 3.14 is the  $m = 0$  (specular) term in the sum in Eq. 3.13. It is  $\omega$ -independent and proportional to the linear density of interfaces  $n_{1d}$ , a misorientation factor  $b/D$  (Eq. 3.7), and a coefficient characterizing the crystal anisotropy  $\gamma_R$ . The second term in Eq. 3.14 contains  $m \neq 0$  (nonspecular) terms and is proportional to the areal density of grain boundary dislocations  $n_{1d}/D$  and the Burger's vector squared  $b^2$ , and a coefficient characterizing the anharmonicity of the crystal  $\gamma$ . These dependencies stem directly from the dimensionality arguments presented in Figure 2.4

---

<sup>2</sup>At high frequencies,  $1/\tau$  should vary as  $\omega$ , and at low frequencies it can be rigorously argued that it should be frequency-independent. Thus a piecewise continuous interpolation formula where the high frequency part turns on at some crossover value  $\omega^*$ , is superior to one where the high and low frequency parts are simply added together or smoothly transition from one to the other. The reason the best fit value for the constant  $B \neq K_\nu$  is that the frequency-independent term will raise the overall value of  $1/\tau$ , so a fit is expected to give  $B \lesssim K_\nu$ .

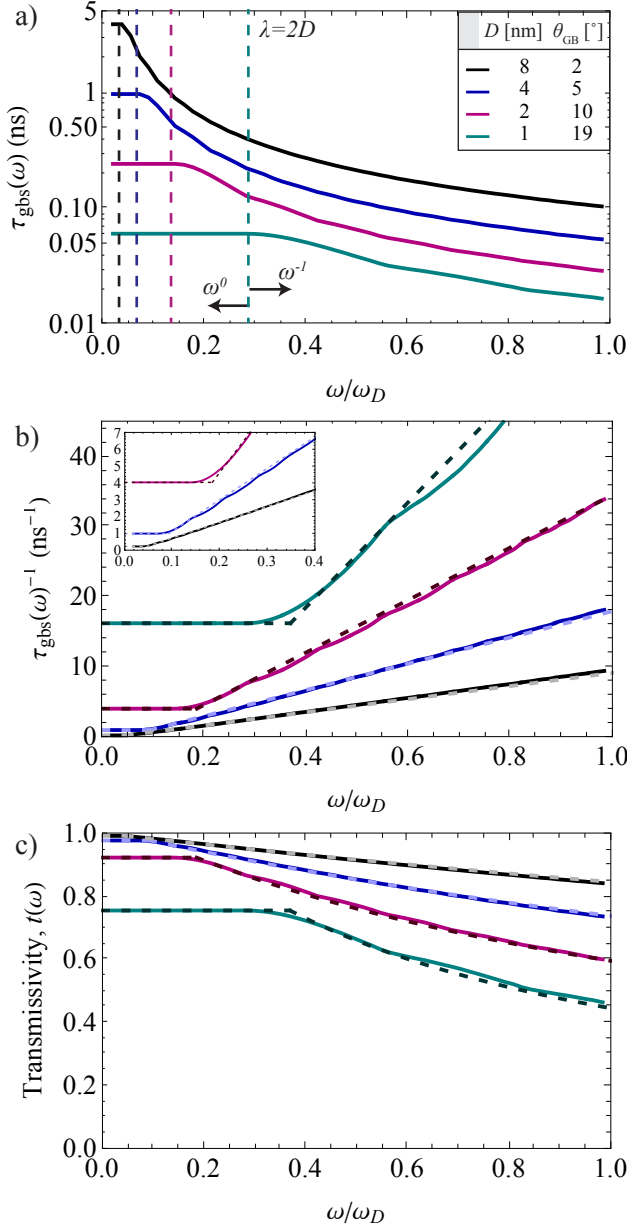


Figure 3.5: Dimensionality crossover effects observed in phonon-GB strain field scattering in diffuse heat conduction. a) The vertical dashed line denotes the crossover frequency, below which the phonon scatters off the GB as a 2d defect ( $\omega$  independent,  $\tau \propto \omega^0$ ), and above which scatters off the grain boundary as an array of 1d defects ( $\tau \propto \omega^{-1}$ ).  $D$  is the linear defect spacing (Figure 3.3a), and  $\theta_{\text{GB}}$  can be interpreted as the magnitude of angular deviation from a special boundary [57]. b) The spectral scattering rate is shown where the dashed line compares the approximate formula given in the main text (Eq. 3.14) to the exact formula (solid line). c) Phonon-GB strain field scattering cast in terms of a spectral transmissivity function (Eq. 3.17) shows a frequency independent transmissivity at low- $\omega$  and a decrease above the crossover frequency.

and 3.2. As discussed in ‘Rotation and specular reflection’, the first term in Eq. 3.14 depends only on rotation, while the second term depends on rotation, hydrostatic, and shear strain. Thus, if the scattering coefficients of each deformation type ( $a = \Delta, S, R$ ) are treated separately the relative magnitudes of the first and second term will change and thus the dependence of  $\tau_{\text{gbs}}^{-1}$  with GB angle will also change.

The scattering theory presented here characterizes the phonon GB interaction as a phonon lifetime  $\tau(\omega)$  and is a convenient means to observe dimensionality and phase space effects. In Figure 3.5c we cast our results into the form of a spectral phonon transmissivity using the expression provided by Dames and Chen [70], and derived in the text preceding Eq. 2.59

$$t(\omega) = \frac{v_g n_{1d} \tau(\omega)}{\frac{3}{4} + v_g n_{1d} \tau(\omega)}. \quad (3.17)$$

This demonstrates how the dimensionality crossover of the phonon-interface interaction results in a transmissivity that is  $\omega$ -independent at low  $\omega$ , and decreases above the critical frequency  $\omega^*$ , which is a function of the linear defect spacing.

### 3.1.3 Low-T thermal conductivity of polycrystals

Now, we discuss how GB strain scattering influences thermal transport in polycrystalline materials. Specific analysis is given for polycrystalline Si, AlN and  $\text{Al}_2\text{O}_3$ . We use the Callaway model for phonon thermal conductivity (Eq. 2.22) and modeling procedure given by Wang *et al.* [43, 71] wherein the net relaxation rate is given by

$$\tau^{-1} = \tau_{\text{pp}}^{-1} + \tau_{\text{pd}}^{-1} + \tau_{\text{gbs}}^{-1}. \quad (3.18)$$

The three contributions are due to phonon-phonon ( $\tau_{\text{pp}}$ ), intrinsic point defect ( $\tau_{\text{pd}}$ ) and grain boundary strain ( $\tau_{\text{gbs}}$ ) scattering. We take  $\tau_{\text{pp}}^{-1} = C_1 \omega^2 T e^{-C_2/T}$  (same form as that given by Slack [72]),  $\tau_{\text{pd}}^{-1} = C_3 \omega^4$ , but account for GB scattering in polycrystalline materials using Eq. 3.14. Since  $\tau_{\text{pp}}^{-1}$  and  $\tau_{\text{pd}}^{-1}$  are considered intrinsic to a given crystal system, the coefficients  $C_1$ ,  $C_2$ , and  $C_3$  are fit to single crystal data (Table 3.1) and fixed for subsequent modeling. The parameters for Si are the same as those of Wang *et al.* [43].

In Figure 3.6, we show the temperature dependence of  $\kappa_{\text{ph}}$  that results from the modeling procedure described above for the specific case of Si. This dependence is shown for various values of  $D$ , the GB dislocation spacing (Figure 3.3a) with the remaining material parameters for Si given in Table 3.2. The central point of the figure is that depending on  $D$ , the  $T$  dependence of  $\kappa_{\text{ph}}$  at low temperature (below the temperature of maximum  $\kappa_{\text{ph}}$ ) can vary from  $T^2$  to  $T^3$ . At such temperatures the dominant scattering in this model is from GB strain and therefore, the variation from  $T^2$  to  $T^3$

Table 3.1: Intrinsic scattering parameters entering  $\tau_{\text{pp}}^{-1}$ ,  $\tau_{\text{pd}}^{-1}$ , and  $\tau_{\text{Casimir}}^{-1}$  obtained by fitting to single crystal data [73, 44, 45]. For each material, parameters are given based on both Debye and Born von Karman (BvK) phonon dispersions.

<b>Material Parameter</b>	<b>Value</b>		
	<b>Si</b> (Debye, BvK)	<b>AlN</b> (Debye, BvK)	<b>Al<sub>2</sub>O<sub>3</sub></b> (Debye, BvK)
$C_1 [\times 10^{-19} \text{ s/K}]$	2.69, 1.53 [43]	2.2, 1.3	30, 15
$C_2 [\text{K}]$	167, 140 [43]	270, 250	350, 320
$C_3 [\times 10^{-45} \text{ s}^3]$	1.81, 1.69 [43]	0, 0	1, 1
Single crystal size, $L_{\text{sc}}$ [mm]	–	6	2.4

stems directly from the dimensionality crossover argument embedded in our semi-empirical formula for  $\tau_{\text{gbs}}$  (Eq. 3.14, Figure 3.5). As GB dislocation spacing decreases, the crossover frequency  $\omega^*$  (Eq. 3.15) increases. For reference, the peak in the phonon occupation number at  $\sim 50$  K occurs at  $\omega/\omega_D \simeq 0.2$ . For the case of  $D = 1$  nm,  $\omega^*/\omega_D = 0.37$ , so below 50 K most phonons see the GB as a planar defect with  $\bar{n} = 1$  ( $\tau$  independent of  $\omega$ ) resulting in  $\kappa_{\text{ph}} \propto T^3$  (see lower most curve in Figure 3.6). For larger dislocation spacings the crossover shifts downward in frequency and a significant number of phonons see the GB as a collection of linear defects with  $\bar{n} = 2$  and  $\tau^{-1} \propto \omega$ , leading to  $\kappa_{\text{ph}} \propto T^2$ . This crossover in  $\tau^{-1}$  also means that for any fixed  $D$  there is a transition from  $\kappa_{\text{ph}} \propto T^2$  to  $\kappa_{\text{ph}} \propto T^3$  at a crossover temperature which is related to  $\omega^*$ .

We now wish to compare our model for GB strain scattering with experimental thermal conductivity data of real materials. We choose polycrystalline Si [43], AlN [44] and Al<sub>2</sub>O<sub>3</sub> [45] as model systems. The data for AlN given by Watari *et al.* is specifically included because the sample was synthesized with clean GBs with almost no GB oxide phase. The intrinsic phonon scattering parameters are given in Table 3.1 as before. In addition, material parameters related to GB strain scattering are required to calculate  $\tau_{\text{gbs}}$ . These parameters are given in Table 3.2 and are obtained as follows. Literature values are used for the average speed of sound, Grüneisen parameter, and Poisson’s ratio. When applied to a bulk polycrystal,  $\tau_{\text{gbs}}$  in Eq. 3.14 is meant to embody phonon scattering off an ensemble of GB structures within the polycrystal. Thus, one may interpret  $D$  as the characteristic length scale of GB structure in the polycrystal and  $b$  as an average GB dislocation Burger’s vector. Recognizing the energetic considerations which require dislocations to have Burger’s vectors which are integer multiples of a primitive unit cell vector (see Figure 9-2 in Ref. [58]), a good approximation (and lower bound) for the average GB Burger’s vector is  $b_{\text{GB}} = (VN)^{1/3}$ , where  $V$  is the volume per atom and  $N$  is the number of atoms in the primitive unit cell. When chosen in this way,  $b_{\text{GB}}$  is fixed and the only adjustable parameters are  $D$ , and the average grain size  $\bar{d}$ . The latter is related to the linear density of interfaces by calculating the GB area over volume assuming cubic grains,

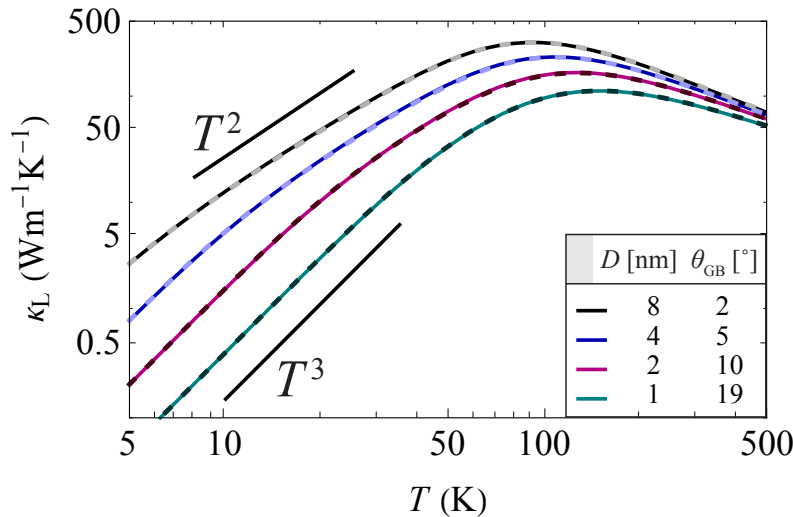


Figure 3.6: General features of the influence of phonon-grain boundary (GB) strain-field scattering on low temperature lattice thermal conductivity. The figure is based on parameters appropriate for Si with a Debye dispersion as described in the text. Curves are shown for several values of GB dislocation spacing ( $D$ ), corresponding to GB angles ( $\theta_{GB}$  shown in the legend). When  $D$  is small, phonons see the grain boundary as a planar defect ( $\bar{n} = 1$ ) resulting in  $\omega$ -independent scattering and  $\kappa_{ph} \propto T^3$ . When  $D$  is large the phonons see the grain boundary as an array of independently scattering line defects ( $\bar{n} = 2$ ) which gives  $\tau_{gbs}^{-1} \propto \omega$ , leading to  $\kappa_{ph} \propto T^2$  behavior at low- $T$ . The full and dashed lines are calculated using the full summation (Eq. 3.13 and G.4.13) and the semi-empirical formula (Eq. 3.14), respectively.

i.e.,  $n_{1d} = 3/\bar{d}$ . The agreement between the experimental grain sizes and the values used in this modeling study is reasonable, as can be seen in Table 3.2.

The results of this comparison are shown in Figure 3.7. The figure includes data for both single and polycrystalline materials. The single crystal data of AlN and Al<sub>2</sub>O<sub>3</sub> show classic  $T^3$  power laws at low- $T$ , indicative of Casimir scattering from crystal surfaces. Thus, in the theoretical modeling,  $\omega$ -independent Casimir scattering is incorporated by adding a term  $\tau_{\text{Casimir}}^{-1} = v_g/L_{sc}$  in the total scattering rate. Here,  $L_{sc}$  is the size of the single crystal (Table 3.1). By contrast, all polycrystalline data show  $T^2$  dependence at low- $T$ . This dependence is captured by our GB strain scattering model and demonstrates the importance of defect dimensionality considerations. The figures also show a comparison of the data with the commonly used gray model, where instead of using  $\tau_{gbs}^{-1}$  in Eq. 3.18 we use  $\tau_{\text{gray}}^{-1} = v_g/\bar{d}$ . As discussed in the 3.1  $\tau_{\text{gray}}$  is  $\omega$ -independent (like the AMM and DMM at low temperatures) since it is a direct extension of Casimir scattering to polycrystals and thus predicts a  $T^3$  power law which is not seen. In addition, the low- $T$  magnitude of  $\kappa_{ph}$  given by the gray model is too low by several orders of magnitude. We note that the value of  $\bar{d}$  used to produce the dashed lines in Figure 3.7 is adjusted to match the magnitude of the roll-over  $\kappa_{ph}$ . This value differs from that shown in Table 3.2 by at most a factor of two. Were this adjustment not made the comparison with experimental data would be worse. We note here that for the theoretical modeling we have

Table 3.2: Material parameters used for grain boundary strain scattering,  $\tau_{\text{gbs}}^{-1}$ . \*Grain size distribution having a standard deviation of 48% of the average grain size,  $0.55\mu\text{m}$ .

Material Parameter	Value		
	Si	AlN	Al <sub>2</sub> O <sub>3</sub>
Average speed of sound, $v_s$ [m/s]	6084 [43]	6976 [74]	7011 [75]
Grüneisen parameter, $\gamma$	1 [76]	1.1 [77]	1.3 [78]
Poisson's ratio, $\nu$	0.27 [79]	0.2 [74]	0.23 [75]
Volume of per atom, $V$ [ $\text{\AA}^3$ ]	20	10.4	8.5
Atoms per primitive unit cell, $N$	2	4	10
GB Burger's vector, $b_{\text{GB}} = (VN)^{1/3}$ [ $\text{\AA}$ ]	3.4	3.5	4.4
Characteristic length of GB structure, $D$ [nm] ( <i>model</i> )	3	8	5.5
Average grain size, $\bar{d}$ [ $\mu\text{m}$ ] ( <i>model</i> )	0.35	1	1
Average grain size, $\bar{d}$ [ $\mu\text{m}$ ] ( <i>experimental</i> )	0.29 to 0.8*	8	5 to 30

used both Debye and Born-von Karman (BvK) dispersions (Appendix D) and as can be seen the differences are not significant except for the softest material considered here, Si. In particular the low- $T$  power law behavior is not affected when dispersive phonons are considered.

The characteristic length scale parameter  $D$  deserves further discussion. We can understand the values used in our theoretical model by considering the case of Si. The modeling results show that GBs with characteristic lengths of  $D \gtrsim 3\text{ nm}$  will display  $\kappa_{\text{ph}} \propto T^2$  like behavior above  $\sim 15\text{ K}$ , as is observed experimentally. By relating  $D$  to a GB angle using Eq. 3.7, we can estimate that GBs within  $5$  to  $10^\circ$  of a special boundary should have spacings larger than  $\sim 3\text{ nm}$ . This includes low-angle GBs, as well as GBs in the vicinity of special GBs at higher angle (e.g.  $\Sigma 5$  at  $36.9^\circ$  for symmetric tilt and twist boundaries in cubic materials) [50, 52, 51]. Given that this window spans a significant range of possible GB angles, and that such GBs are low in energy [57], we argue that a sufficient proportion of GBs that occur naturally in a polycrystalline material would scatter with  $\tau^{-1} \propto \omega$ , and result in  $\kappa_{\text{ph}} \propto T^2$ . While the results of this modeling study agree with the experimental data available, controlled computation and experimental studies containing spectral information of the phonon-GB interaction would help further validate the effects discussed here.

Structural information of interfaces can indeed be included when calculating the thermal boundary resistance by computational methods such as molecular dynamics [80] or Green's function methods [81, 82], and much progress has been made regarding these approaches in recent years [4]. These detailed methods are invaluable for progress in the field of heat transfer as the interfacial structure can

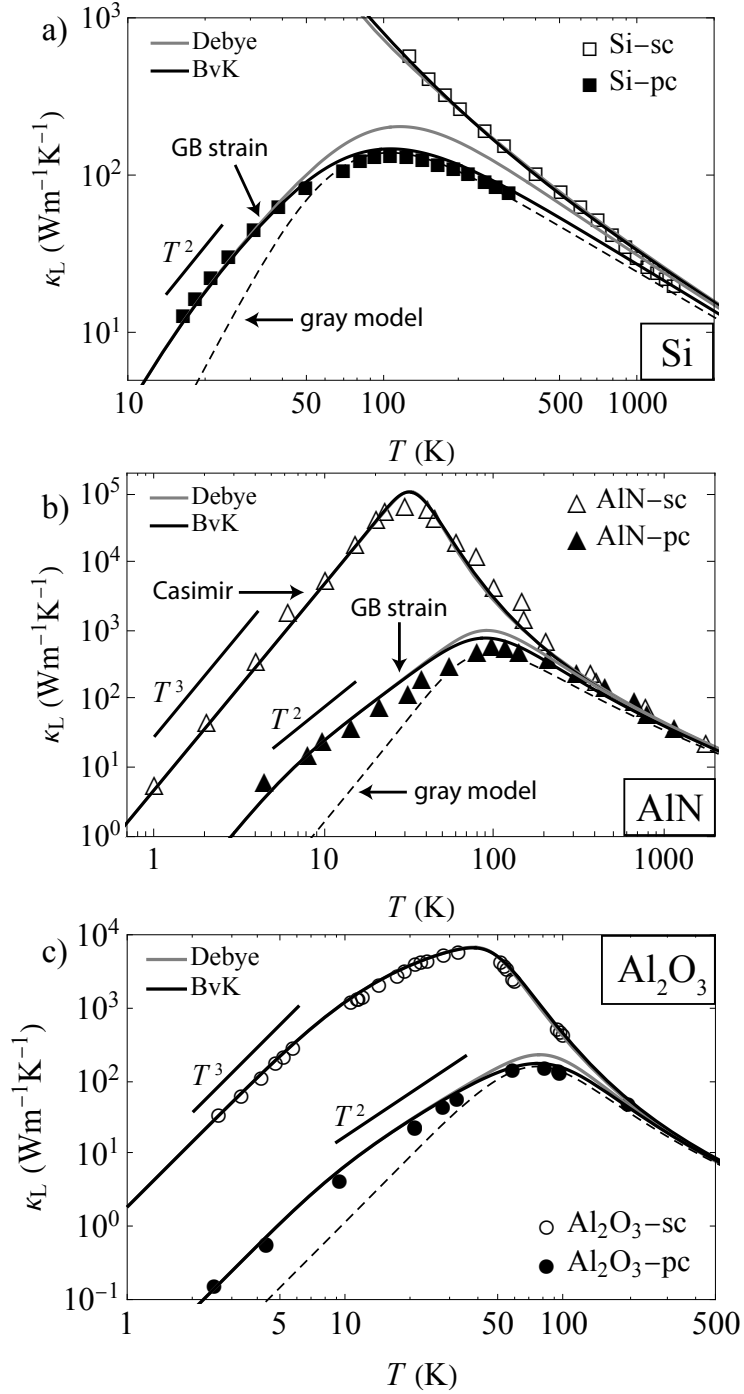


Figure 3.7: Thermal transport modeling of polycrystalline (pc) a) Si, b) AlN, and c)  $\text{Al}_2\text{O}_3$ . Data for these materials is taken from Refs. [43, 44, 45]. The intrinsic scattering parameters are fit to single crystals (sc) and have the values shown in Table 3.1. The solid lines follow from the theoretical modeling as described in the text. The data for polycrystals shows a clear  $T^2$  power law in accord with our GB strain field scattering theory and defect dimensionality arguments. The dashed lines show a comparison of the data with the gray model. The error in the literature data is smaller than size of the data points on this logarithmic scale.

be defined and systemically controlled, and spectral information can be obtained which is difficult to obtain experimentally [83]. Due to the inevitable complexity of interfaces in real materials (e.g. the grain boundary character distribution in a bulk polycrystal), detailed theoretical and computational treatments should be used to establish engineering design principles which are generalizable and can thus be applied to real systems. This work shows, through standard scattering theory, that general kinematic arguments can explain measurable phenomena which emerge from this complexity. We hope this work can help guide more detailed computational simulations and experiments.

Phonon-dislocation interactions have also been studied using molecular dynamics [84], and even *ab initio* methods [85]. The *ab initio* technique of Wang *et al.* extends the **T**-matrix formalism to phonon scattering on an array of dislocation quadrupoles, with the periodicity imposed by periodic boundary conditions [85]. The structure calculated in Ref. [85] however eliminates the long range ( $1/r$ ) strain field [86] which is characteristic of dislocations and is known to be the dominant phonon-dislocation interaction [87, 29, 88, 89, 35, 68]. This long range strain field is required to give the  $\tau^{-1} \propto \omega$  and thus  $\kappa_{\text{ph}} \propto T^2$ , so it is not surprising that this study does not find  $\kappa_{\text{ph}} \propto T^2$ . We emphasize that the dislocation configuration considered in Ref. [85] does not describe a GB, and since it does not contain the  $1/r$  strain field it does not describe isolated lattice dislocations.

### 3.1.4 Discussion

Phonon scattering at interfaces is an inherently complex phenomenon where many physical processes are at play simultaneously. This work focuses specifically on effects that arise when considering interfacial structure at the nanoscale by defining the interface as an array of linear defects, rather than treating the interface as a structureless planar defect. This definition is sufficiently general such that it includes many types of grain boundaries (particularly those of low energy) and semi-coherent phase boundaries. Indeed the interface between two materials with structural periodicity will tend to have structural periodicity itself, and we suggest that the standard model for phonon-interface scattering should not assume perfect disorder at the interface. Several emergent phenomena arise from this analysis stemming directly from this structural definition. These include phonon diffraction conditions arising from the periodic structure of the interface and the wavelike nature of phonons, as well as a crossover in the  $\omega$  dependence of the phonon lifetime stemming from dimensionality and phase space considerations. The general analytical expression derived was applied to the specific case of a symmetric tilt grain boundary where the linear defects were defined as the strain field from edge dislocations. The result is a phonon-grain boundary strain lifetime ( $\tau_{\text{gbs}}$ ) that is independent of  $\omega$  below a critical frequency  $\omega^* \simeq 4\pi v_s/3D$  which depends on the GB dislocation spacing  $D$ , and  $\tau_{\text{gbs}}^{-1} \propto \omega$  above  $\omega^*$ . A simple semi-empirical expression is provided as an excellent approximation of the full analytical expression, which embodies this dimensionality crossover effect. This scattering theory is applied to standard phonon transport models and is shown

to explain the  $\kappa_{\text{ph}} \propto T^2$  temperature dependence of polycrystalline and nanocrystalline materials at low temperatures. This power law analysis provides evidence that the dominant phonon GB scattering mechanism is through GB strain fields and that interfacial structure and strain energy are important.

## 3.2 Thermal boundary resistance and GB strain energy<sup>3</sup>

One common challenge when establishing physical mechanisms which control thermal transport across interfaces, is that experimental data usually probes transport across many grain boundaries. Most commonly, the thermal conductivity of a polycrystalline material is measured as a function of temperature (Figure 3.7). Changes in the thermal conductivity with modifications to either the grain size or grain boundary complexion are then used to probe the thermal transport behavior across the interfaces. Therefore, one must model the behavior of the ensemble of grain boundaries present in the material. It is well accepted that the interfacial thermal resistance  $R_\kappa$  (or equivalently the phonon-GB relaxation time) of a GB has a strong dependence on the detailed interfacial atomic structure, including the misorientation between two grains and GB dislocations. The theory and power law analysis presented in Section 3.1 provide evidence that phonon GB interactions are dominated by the GB strain fields which arise from the GB dislocation structure. While the data analyzed supports this physical picture, detailed measurements across single grain boundaries can provide additional insight that bulk measurements on polycrystals cannot.

In this section, measurements of  $R_\kappa$  of single Si twist GBs, with varying misorientation angles are presented. A super-flexible 70 nm thick Si thin film was hot pressed onto a Si wafer to represent a twist GB. The  $R_\kappa$  of the film-wafer interface was measured as a function of the rotation angle between the film and the wafer. The experimental data were further compared with an analytical model to interpret the twist angle dependence of the measured  $R_\kappa$ .

It was found that the strain part of the grain-boundary energy is correlated with the measured twist angle-dependent  $R_\kappa$ .

### 3.2.1 Si twist grain boundaries

Thermal investigation of twist GBs was performed with a 70-nm-thick (100) Si thin film hot pressed onto a (100) Si wafer. Details on the synthesis of these samples are provided in Ref. [90]. The high-quality interfaces achieved via film-wafer bonding were confirmed by transmission electron microscopy (TEM) studies and enabled thermal studies of GBs across a large range of misorientation angles,  $3.4^\circ \leq \theta_{\text{GB}} \leq 86.5^\circ$ . Figure 3.8 shows the  $\theta_{\text{GB}} = 3.4^\circ$  GB as an example. This angle is

---

<sup>3</sup>The content in this section was published by Xu and Hanus *et al.* in Ref. [90].

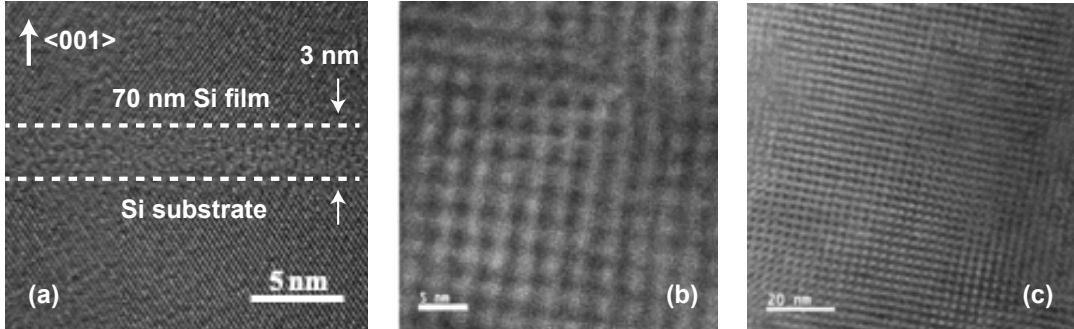


Figure 3.8: Transition electron microscopy images of Si twist GBs. a) Image of the GB with the electron beam perpendicular to the GB plane normal vector  $<001>$ . The GB structure seems to be amorphous when observed from this angle. b) Image of GBs with the electron beam parallel to the GB plane normal vector. When viewed from this angle the GB dislocation structure can be observed, confirming that this procedure produces clean GBs in their low energy configuration. Notice that the GB strain field thickness (3nm) shown in panel a is approximately equal to GB dislocation spacing in panel b. c) A lower magnification image of panel b.

chosen since the clean, low energy configuration is theoretically known (Figure 19-16 of Ref. [58]) and should be observable with TEM. When viewed with the electron beam perpendicular to the plane normal (Figure 3.8a), the GB looks to have an amorphous structure approximately 3 nm in thickness. However, when viewed with the electron beam parallel to the plane normal (Figure 3.8b), the expected GB dislocation structure can be observed: two orthogonal arrays of screw dislocations forming a grid structure. The spacing between dislocations observed in Figure 3.8b is approximately equal to the GB ‘thickness’, or the size of the interfacial strained layer, observed in Figure 3.8a, 3 nm. This falls inline with the conventional understanding of the structure and local strain field of GBs.

### 3.2.2 $R_\kappa$ correlated with interfacial strain energy

Although GBs are varied and complex, the GB energy  $\gamma_{\text{GB}}$  is a useful single parameter that correlates with many properties. The widely used Read-Shockley model [55] effectively describes the structure of a GB as an array of dislocations [57, 59], as shown in Fig. 3.8b and c. In general,  $\gamma_{\text{GB}}$  is split into two parts: the core energy  $\gamma_{\text{core}}$  and the strain energy  $\gamma_{\text{strain}}$ . The Read-Shockley model was generalized by Wolf [57] into what is now called the extended Read-Shockley model, where the core energy due to broken bonds across the interface ( $E_c/b$ ) and the GB strain energy ( $E_{\text{st}}/b$ ) are treated

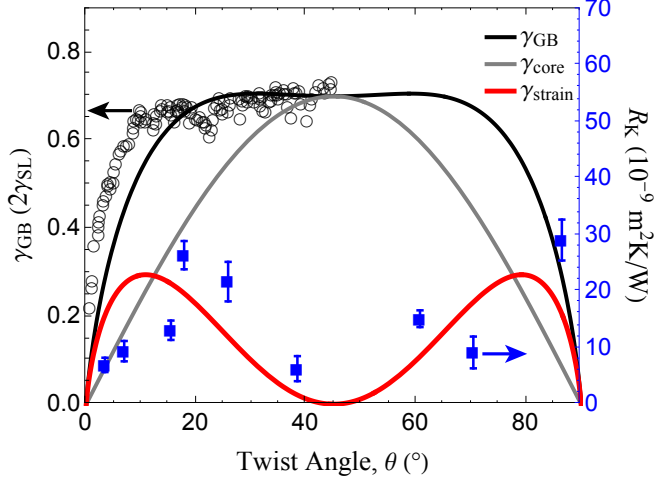


Figure 3.9: Experimental data of the GB energy ( $\gamma_{\text{GB}}$ ) and thermal boundary resistance ( $R_{\kappa}$ ) of Si twist GBs. Open circles (left axis) are data from Otsuki [91]. Blue squares (right axis) are  $R_{\kappa}$  data from this study for samples after annealing. The lines are associated with the left axis and show the extended Read-Shockley model for GB energies, where the core energy ( $\gamma_{\text{core}}$ ) and the strain energy ( $\gamma_{\text{strain}}$ ) sum to give  $\gamma_{\text{GB}}$ .

as fitting parameters

$$\gamma_{\text{GB}} = \gamma_{\text{strain}} + \gamma_{\text{core}} = 2 \sin(2\theta_{\text{GB}}) \left[ \frac{E_c}{b} - \frac{E_{\text{st}}}{b} \ln(\sin 2\theta_{\text{GB}}) \right]; \text{ with } 0^\circ \leq \theta_{\text{GB}} \leq 90^\circ. \quad (3.19)$$

We now apply this model to experimental data of  $\gamma_{\text{GB}}$  for (100) Si twist boundaries provided by Otsuki [91]. This early study on Si-Si bicrystals was made using a solid-state bonding method at 1473 K for 10 hr. The boundary was wetted with a liquid Sn-Al alloy at 1473 K for three days in Ar. Grooves were formed on the surface at the GB to satisfy the energy balance between the GB energy ( $\gamma_{\text{GB}}$ ) and the solid-liquid interfacial energy ( $\gamma_{\text{SL}}$ ). The dihedral angle of the groove is thus a measure of  $\gamma_{\text{GB}}$  normalized by  $2\gamma_{\text{SL}}$ , which is taken to be a constant. A comparison of the GB energy model in Eq. 3.19 to the experimental data is shown in Figure 3.9 with  $E_c/b = 0.35(2\gamma_{\text{SL}})$  and  $E_{\text{st}}/b = 0.4(2\gamma_{\text{SL}})$ . As  $\theta_{\text{GB}}$  increases, the spacing between GB dislocations decreases. As can be seen in Figure 3.9,  $\gamma_{\text{strain}}$  peaks between  $\theta_{\text{GB}} = 10$  and  $15^\circ$  and decreases at higher  $\theta_{\text{GB}}$  due to interaction between individual GB dislocations.

Watanabe et al. have analyzed the thermal boundary resistance data of diamond obtained via MD simulations [59]. They concluded that the Kapitza length, which is directly proportional to  $R_{\kappa}$ , is correlated with the  $\gamma_{\text{GB}}$ . In MD studies of two-dimensional polycrystalline graphene [92] or a twist Si GB [93], a larger  $\gamma_{\text{GB}}$  was also found to lead to a higher  $R_{\kappa}$ . Comparing our experimental data of  $R_{\kappa}$  of annealed Si twist GBs to the extended Read-Shockley model, it seems that  $R_{\kappa}$

may be correlated with  $\gamma_{\text{strain}}$ , the interfacial strain energy of the twist GB, instead of the total energy  $\gamma_{\text{GB}}$ . To accurately capture the phonon-strain-field interaction in an MD simulation, the anharmonicity and Grüneisen parameters of the material need to be accurately represented by the interatomic potential employed. Because the transverse Grüneisen parameters of the Stillinger-Weber and Tersoff potentials are significantly underestimated, the correlation between  $R_\kappa$  and  $\gamma_{\text{strain}}$  may be missed in existing MD simulations [94].

We note that this GB energy model neglects energy cusps that occur at special GBs, i.e. the  $\Sigma 3$  boundary at  $\theta_{\text{GB}} = 36.9^\circ$ , and the non-zero  $\gamma_{\text{GB}}$  at  $\theta_{\text{GB}} = 90^\circ$ . While the measured  $\gamma_{\text{GB}}$  does indeed show cusps in GB energy at special boundaries, the experimental data available show that they are relatively shallow. Although there will be additional complexities and variations from this model when special boundaries are considered, we argue that the general trend of GB energy captured by the extended Read-Shockley model may hold.

## Chapter 4

### Lattice softening

As discussed in detail in Chapters 2.3.1 and 3, crystal defects induce phonon scattering and reduce thermal conductivity by decreasing the phonon lifetime and mean free path. In this paradigm of understanding the speeds of sound are assumed to be fixed when describing thermal transport. Here, we present an often overlooked but important mechanism through which defects can decrease thermal conductivity, which we refer to as lattice softening. Figure 2.3d illustrates lattice softening in a k-space representation, where the phonon energies decrease (soften) upon the introduction of defects. This phonon softening expresses itself through experimentally accessible material parameters such as a decrease in the materials speed of sound, Debye temperature, and elastic moduli. These experimental metrics are particularly important because they probe the properties of the acoustic phonon branches near the  $\Gamma$ -point. As discussed in Section 2.2.2, the acoustic branches are typically the dominant heat carriers and the behavior of the properties at the  $\Gamma$ -point is expected to reflect the behavior of the phonon modes up the acoustic branch. Other experimental probes which are valuable in studying lattice softening include: Raman spectroscopy which can measure the energy of optical phonon modes at the  $\Gamma$ -point (given that the symmetry allows it to be Raman active), and inelastic neutron and X-ray scattering which can measure phonon dispersion relations and density of states.

In this chapter we show several cases where defect induced lattice softening is critically important when explaining the materials reduction in thermal conductivity. We first provide an example of chemically induced lattice softening. Then we demonstrate a perhaps less intuitive effect, whereby lattice softening can be induced by microstructural defects at constant chemical composition. We demonstrate, in several important thermoelectric and microelectronic materials systems, how lattice softening seems to have been a missing piece which is key for explaining the defect induced reduction of thermal conductivity. The cases treated here also provide a ‘best practices’ for spectral phonon transport modeling (Callaway-Klemens type models for  $\kappa_{\text{ph}}$ , Eq. 2.22).

## 4.1 Chemical lattice softening in SnTe<sup>1</sup>

The  $(\text{SnTe})_{1-x}(\text{AgSbTe}_2)_x$  system exhibits a much higher thermoelectric figure of merit ( $zT$ ) than its parent compound SnTe. One main reason is a dramatically reduced phonon thermal conductivity,  $\kappa_{\text{lat}}$ . Substituting Ag and Sb on the Sn site in SnTe is known to decrease  $\kappa_{\text{lat}}$  by  $\sim 75\%$ . In an early study on this material system nanoprecipitates were observed via high-resolution transmission electron microscopy [96]. It was suggested that phonon scattering off of these nanoprecipitates was the origin of the dramatically reduced  $\kappa_{\text{lat}}$ . Here,  $(\text{SnTe})_{1-x}(\text{AgSbTe}_2)_x$  solid solutions were synthesized with no evidence of nanoprecipitates present. However, the dramatic reduction in  $\kappa_{\text{lat}}$  was still observed. We reveal, through a combined theoretical, computational, and experimental approach, that substitution of Ag and Sb on the Sn site promotes cation vacancy formation. These cation vacancies act as strong phonon scattering centers and significantly soften the materials lattice. The combined effect results in the 75% reduction in  $\kappa_{\text{lat}}$ , and is a main reason for the 300% improvement in the thermoelectric figure of merit  $zT$  over its parent compound SnTe.

### 4.1.1 Microstructural analysis

Powder X-ray diffraction (PXRD) patterns for samples of  $\text{AgSn}_m\text{SbTe}_{2+m}$  (where  $x = (1 + m)^{-1}$ ) after densification using spark plasma sintering (SPS) can be indexed to single-phase compounds with a rock-salt SnTe crystal structure (synthesis and PXRD analysis are given in the Supplemental Information of Ref. [95]). The variation of the lattice parameters for  $\text{AgSn}_m\text{SbTe}_{2+m}$  follows Vegard's law between two end members SnTe and  $\text{AgSbTe}_2$ , implying continuous solid solution, Figure 4.1a. The backscattered electron image and corresponding elemental maps from energy-dispersive X-ray spectroscopy are shown in Figure 4.1b and c, respectively. Moreover, transmission electron microscopy (TEM) indicates single-phase compounds and absence of second phases for  $\text{AgSn}_5\text{SbTe}_7$ , Figure 4.1d. The  $\text{AgSn}_m\text{SbTe}_{2+m}$  samples in this study therefore are considered complete solid solutions.

### 4.1.2 Defect chemistry and thermal conductivity

The earliest study on the thermoelectric properties of  $(\text{SnTe})_{1-x}(\text{AgSbTe}_2)_x$  can be traced back to the 1960s [97]. Perhaps the most striking feature in the  $(\text{SnTe})_{1-x}(\text{AgSbTe}_2)_x$  system is the dramatic reduction in  $\kappa_{\text{lat}}$ , which is far greater than is predicted from a simple mass difference scattering model (Eq. 2.34). This reduction was again seen in the solid-solution samples of this study.

---

<sup>1</sup>The content in this section was published in [95].

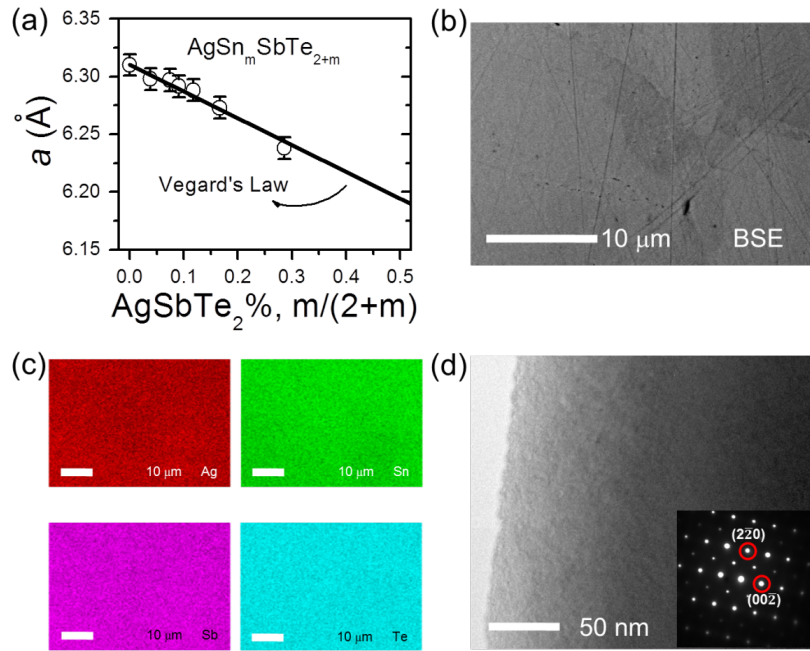


Figure 4.1: (a) Room temperature lattice parameters of SnTe as a function of AgSbTe<sub>2</sub> content. The linear change in lattice parameter through the entire composition range suggests a full solid solution. (b) Backscattered electron image, (c) corresponding elemental maps obtained from energy dispersive X-ray spectroscopy. (d) Transmission electron microscopy image as well as selective area diffraction pattern (lower left inset image in (d)) for the sample AgSn<sub>5</sub>SbTe<sub>7</sub>. There is no evident phase separation at either the micro- or nano scale, which suggests a solid solution behavior between SnTe and AgSbTe<sub>2</sub>.

Here, it is experimentally observed that the substitution of Sb and Ag on the Sn site simultaneously increases the p-type carrier concentration (from Hall effect measurements, Table 1 of Ref. [95]), decreases the average speed of sound (from pulse echo ultrasound and low temperature heat capacity, Figure 4.2b) and decreases  $\kappa_{\text{lat}}$  (from laser flash analysis diffusivity). To understand the origin of this decreased  $\kappa_{\text{lat}}$ , we first must understand the defect chemistry of the  $(\text{SnTe})_{1-x}(\text{AgSbTe}_2)_x$  system.

Since Ag has an ionic charge of +1 and Sb has one of +3, a co-doping of Ag and Sb on the Sn<sup>2+</sup> site is expected to be charge neutral and the carrier concentration should not change, if no other defects are induced. However, the p-type carrier concentration increased, suggesting an increase in the cation vacancy concentration. SnTe is known to naturally exist as Sn-deficient, and the p-type carrier concentration of SnTe can be changed from 1.5 to  $6 \times 10^{20} \text{ cm}^{-3}$  by simply changing the Sn content. In this study it was observed that Ag and Sb substitution can increase the p-type carrier concentration to as high as  $14 \times 10^{20} \text{ cm}^3$ .

To understand this effect further, density functional theory (DFT) calculations were conducted to examine the defect formation energies of pristine SnTe, and SnTe containing (Ag,Sb) co-substitution

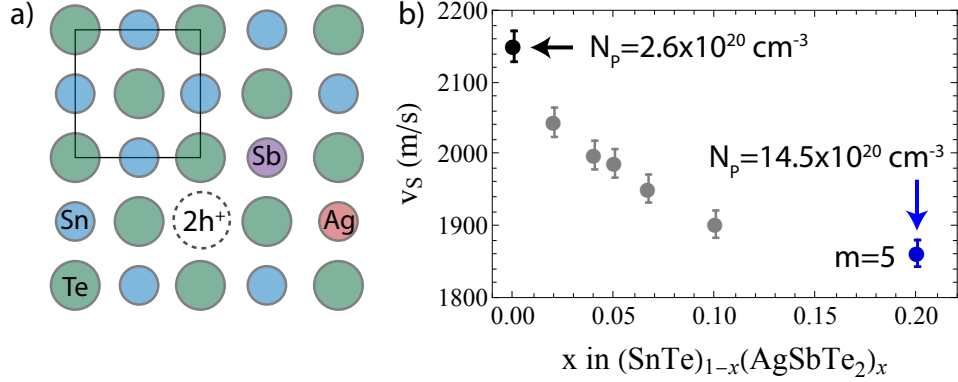


Figure 4.2: a) Schematic diagram summarizing the results of the DFT defect energy study. Ag and Sb prefer to reside as nearest neighbors on the metal sublattice and promote Sn-vacancy formation. Each Sn-vacancy contributes two holes to the valence band. b) Experimental measurements of the average speed of sound. The measured Hall carrier concentration for the end members are labeled. Ag and Sb promote cation vacancy formation which increases the carrier concentration and decreases the average speed of sound.

on the Sn site. First, a single Sn vacancy in a pure  $\text{Sn}_{27}\text{Te}_{27}$  54 atom unit cell was calculated. To compare the changes in Sn vacancy formation energy upon Ag and Sb addition, we also calculated various Ag and Sb substitutions on Sn in  $\text{AgSn}_{25}\text{SbTe}_{27}$  before adding a vacancy. We found that Ag and Sb are more favorable residing as first nearest neighbors in the metal sublattice. On the basis of the most favorable  $\text{AgSn}_{25}\text{SbTe}_{27}$  configuration, we considered all possible Sn vacancy positions around Ag and Sb. We found that  $V_{\text{Sn}}$  prefers to reside on an Sb side, which is schematically shown in Figure 4.2a. The relative  $V_{\text{Sn}}$  formation energy is calculated by  $E_{\text{VSnAgSb}} - E_{\text{AgSb}} - (E_{\text{VSn}} - E_{\text{pure}})$ . Here  $E_{\text{VSnAgSb}}$  is the total energy of the Sn vacancy in Ag and Sb codoped SnTe ( $\text{Ag}\square\text{Sn}_{24}\text{SbTe}_{27}$ ,  $\square$  represents a vacancy),  $E_{\text{AgSb}}$  is the total energy of the most favorable Ag and Sb codoped SnTe ( $\text{AgSn}_{25}\text{SbTe}_{27}$ ),  $E_{\text{VSn}}$  is the total energy of the Sn vacancy in pure SnTe ( $\text{Sn}_{26}\square\text{Te}_{27}$ ), and  $E_{\text{pure}}$  is the total energy of pure SnTe ( $\text{Sn}_{27}\text{Te}_{27}$ ). We found that the single Sn vacancy formation energy decreases by 0.58 eV for the Ag and Sb codoped case relative to pure SnTe. The decreased formation energy suggests that the Sn vacancies in Ag and Sb substituted system are even more favorable than those in SnTe and hence accounts for the higher hole carrier concentration, as experimentally observed (Table 1 of [95]). In addition, the increased cation vacancy concentrations have a dramatic impact on thermal properties, as will be discussed below.

To understand the effect of alloying on thermal conductivity and its link to lattice softening, we measured the longitudinal ( $v_L$ ) and transverse ( $v_T$ ) speeds of sound. We found that the measured  $v_L$  and  $v_T$  for the  $m = 5$  sample reduce by 10 and 14%, respectively, compared to those of the parent SnTe composition (Table S1 of [95]). The calculated average speed of sound is shown in Figure 4.2. Furthermore, the Debye temperatures ( $\theta_D$ ) derived from the low-temperature heat

capacity measurements showed a systematic decrease from 175 to 160 K with increasing  $\text{AgSbTe}_2$  concentration (Figure S2 of Ref. [95]). This again confirms the lattice softening of SnTe upon  $\text{AgSbTe}_2$  addition.

To explain the observed lattice softening upon  $\text{AgSbTe}_2$  alloying indicated by the sound velocity and heat capacity data, we need to consider the role of defects in the system. It is important to note here that the cation vacancy concentration in SnTe increases from 0.7 to 4.6% upon alloying with  $\text{AgSbTe}_2$  ( $m = 5$ ) by estimating that each vacancy generates two holes that are solely responsible for the carriers observed in the system. To distinguish the role of the  $\text{Ag}_{\text{Sn}}$  and  $\text{Sb}_{\text{Sn}}$  substitutional defects in the solid solution from that of the increasing cation vacancy concentration, we calculated the isotropic speeds of sound from the elastic modulus tensor of  $\text{Sn}_{1-x}\text{Te}$  and  $\text{SnTe} - \text{AgSbTe}_2$  (Figure S3 of Ref. [95]). We found that the speed of sound for SnTe stays approximately constant, with Ag-Sb alloying on the Sn site. On the other hand, we found significant reduction in speeds of sound with increasing Sn vacancies ( $V_{\text{Sn}}$ ). The longitudinal ( $v_L$ ) and transverse ( $v_T$ ) speeds of sound decreased by 9 and 16%, respectively, in the structure containing 6% vacant Sn sites in comparison with stoichiometric SnTe. These calculations are in reasonable agreement with our experimentally measured speeds of sound. We presume that the lattice softening observed both experimentally and computationally is due to removal of electrons occupying bonding states with the formation of cation vacancies. Thus, we demonstrate that the reduction in speeds of sound must stem from the formation of cation vacancies accompanying the alloy formation instead of atom substitutions on the Sn site.

Now, we conduct a systematic modeling study to determine the mechanisms through which  $\kappa_{\text{lat}}$  is being reduced, recognizing the defect chemistry discussed above. A Callaway-type (Eq. 2.22) model is constructed which can capture the influence of the Sn-vacancies on thermal conductivity. The experimentally measured speed of sound for each sample was used when setting the phonon dispersion relations. In this way, the significant experimentally observed lattice softening could be incorporated into the thermal transport model without the use of fitting parameters or literature values. The model uses the isotropic phonon branches because the speed of sound was measured on polycrystalline samples with averaged crystallographic orientations. Both Debye and Born-von Karman acoustic branches were used for the phonon dispersion relation, giving nearly equivalent results (primarily because we are analyzing  $\kappa_{\text{lat}}$  above the Debye temperature). The lattice thermal conductivity was calculated by Eq. 2.22, where the total phonon relaxation time was calculated by Mattiessen's rule (Eq. 2.26).

To decouple phonon-phonon  $\tau_{\text{pp}}$ , phonon-grain boundary  $\tau_{\text{GB}}$ , and phonon-vacancy scattering times, data from a SnTe single crystal (sample a of Damon [98]) was modeled along with the polycrystalline SnTe and  $m = 5$  samples of this study by the following procedure. The phonon-phonon scattering

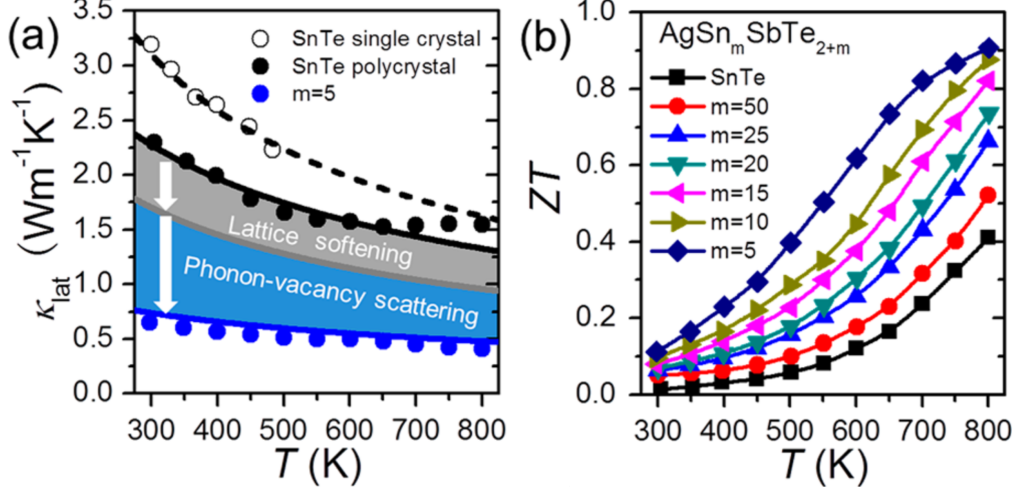


Figure 4.3: (a) Lattice thermal conductivity modeling. Data from a SnTe single crystal from Damon [98] was modeled along with the polycrystalline SnTe sample and  $m = 5$  sample,  $\text{AgSn}_m\text{SbTe}_{2+m}$  of this study. The gray shaded region shows the reduction in  $\kappa_{\text{lat}}$  from SnTe to  $\text{AgSn}_m\text{SbTe}_{2+m}$  solely due to lattice softening because of decreased sound velocity, which is measured using ultrasound. The further reduction from gray to blue (blue shaded region) is due to increased  $[\text{V}_{\text{Sn}}]$  and phonon-vacancy scattering. (b) ZT values as a function of temperature for  $\text{AgSn}_m\text{SbTe}_{2+m}$  system. (ZT here is the material figure of merit.)

was accounted for using the following expression

$$\tau_{\text{pp}}^{-1} = A \frac{\omega^2 T}{v_p^2 v_g} \quad (4.1)$$

and the phonon micro-structural scattering was accounted for by the simple phenomenological expression

$$\tau_{\text{GB}}^{-1} = \frac{v_g}{d}. \quad (4.2)$$

Note that the phonon-phonon scattering parameter  $A$  includes material parameters such as the Grüneisen parameter  $\gamma$  (which we measured to be approximately constant throughout the sample series, Figure S4 of Ref. [95]), the average atomic volume and mass, but not the phonon velocity. This is important because the speed of sound was observed to change with increasing Ag and Sb content, and the dependence of  $\tau_{\text{pp}}$  on phonon velocity should be embedded in the model. The average grain size,  $d$ , can be considered a phenomenological fitting parameter accounting for different phonon-microstructure scattering processes. The model is relatively insensitive to this parameter in this case (in contrast to the case shown in Figure 3.7), making a more sophisticated model unnecessary. Because SnTe has a large intrinsic Sn vacancy concentration ( $[\text{V}_{\text{Sn}}]$ ) phonon-vacancy

scattering was included for all samples with the following expression [99]

$$\tau_{\text{vac}}^{-1} = f \frac{3V\omega^4}{\pi v_p^2 v_g} s^2 \quad (4.3)$$

where  $V$  again is the volume per atom. The phonon-vacancy scattering strength of  $s^2 = 0.89$  for Sn vacancies in SnTe was determined by Ratsifaritana and Klemens [99] by analyzing the lattice thermal conductivity of SnTe single crystals with different  $[V_{\text{Sn}}]$  and is used in this model. Sn vacancy concentration was estimated using the simplified charge-neutrality equation:  $2[V_{\text{Sn}}] = N_p = f/V$ . In this way,  $\tau_{\text{vac}}$  was not fit but was set to experimental results. The results of this modeling procedure are shown in Figure 4.3a (Debye approximation) and Figure S5 of Ref. [95] (Born-von Karman approximation). To summarize,  $\tau$  for the SnTe single crystal includes  $\tau_{\text{vac}}$  and  $\tau_{\text{pp}}$ , where  $A$  was fit to single crystal data and fixed and  $f$  was set to the experimentally measured values.  $\tau$  for the two polycrystalline samples of this study included  $\tau_{\text{pp}}$ ,  $\tau_{\text{vac}}$ , and  $\tau_{\text{GB}}$ , where one value of  $d$  was used for both samples because the hand milling and pressing procedure was the same for each sample. The experimentally determined  $[V_{\text{Sn}}]$  and  $v_s$  for these samples and all values used are compiled in Table 4.1. Note that no fitting parameters were used to model the reduction in  $\kappa_{\text{lat}}$  from SnTe polycrystal to  $m=5$ . Figures 4.3a shows that the dramatic reduction of  $\kappa_{\text{lat}}$  in SnTe with the addition of AgSbTe<sub>2</sub> can be explained by the increased number of Sn vacancies. These vacancies soften the lattice, resulting in a reduced speed of sound, which accounts for a significant reduction of  $\kappa_{\text{lat}}$ . This is indicated by the gray line and shaded region where  $[V_{\text{Sn}}]$  is kept constant and only the phonon velocity is changed. The remaining  $\kappa_{\text{lat}}$  reduction (blue shaded region) is attributed to the strong phonon scattering from the increase in Sn vacancy concentration.

One important attribute of this model is that phonon-vacancy scattering is inherently much stronger than the commonly used phonon-isotope scattering with the relative change in atomic mass  $\Delta M/M = 1$ . For example, Eq. 4.3 can be converted to the phonon-isotope scattering expression by the following relation,  $12s^2 = (\Delta M/M)^2$ , meaning  $s^2 = 0.08$  for  $\Delta M/M = 1$ . This is more than an order of magnitude smaller than the value used in this model ( $s^2 = 0.89$ ), which was determined experimentally in the literature for Sn vacancies in SnTe [99]. The reason for this discrepancy stems from the fact that phonon-isotope scattering with  $\Delta M/M = 1$  accounts for only the change in kinetic energy of the lattice ( $\mathcal{T}$  in 2.10) and neglects changes in the potential energy upon the removal bonds when an atom is removed ( $U$ ). This result demonstrates the importance of tracking the lattice stiffness experimentally (e.g., pulse echo ultrasound, resonant ultrasound spectroscopy, low-temperature heat capacity) and incorporating these changes into the transport modeling when studying the thermal properties of materials.

While this simple model reproduces the majority of the reduction in  $\kappa_{\text{lat}}$ , the experimental data are still slightly lower than what the model predicts. We suspect that this could be attributed to the

Table 4.1: Parameters for  $\kappa_{\text{lat}}$  modeling.

sample	$A (10^{-8} \text{ m}^3 \text{K}^{-1} \text{s}^{-2})$		$d (\mu\text{m})$		$[\text{V}_{\text{Sn}}] (10^{20} \text{ cm}^{-3})$	$v_s (\text{m/s})$
	Debye	BvK	Debye	BvK		
single crystal	4	2.3	-	-	0.8	2151
m = 0 polycyrstal	4	2.3	2	5	1.3	2151
m=5 polycrystal	4	2.3	2	5	7.3	1862

fact that we took the Hall carrier concentration to be a direct measurement of  $[\text{V}_{\text{Sn}}]$ , while in reality holes may come from other defects such as Ag vacancies (contributing one hole per vacancy), which would result in higher vacancy concentrations. Additionally, the effects of Ag and Sb on the Sn site were neglected because of the negligible mass difference of these atoms. However, there will still be bond strength disorder, which may introduce non-negligible scattering contributions.

We further increased maximum ZT to  $\sim 1.2$  at 800 K by properly doping  $\text{AgSn}_5\text{SbTe}_7$  with iodine to optimize the electronic transport properties, Figure S6 of Ref. [95]. This value represents a 300% improvement over SnTe.

## 4.2 Microstructural lattice softening<sup>2</sup>

The influence of micro- and nano-structure on thermal conductivity is a topic of great scientific interest and of particular technological importance to thermoelectrics and microelectronics. In the previous section we discussed how when chemical composition and defect chemistry changes, the materials average speed of sound should change as well which has an important impact on the phonon thermal conductivity. However, at constant chemical composition it is typically assumed that the materials speed of sound does not change, and the materials elastic properties are usually held constant when examining the thermal conductivity. In this section, by examining PbTe and Si model systems, we show how microstructure can soften a materials lattice, at constant chemical composition. Spectral thermal conductivity modeling shows that microstructural lattice softening can play an important, and sometimes dominant, role when describing the defect induced reduction in the phonon thermal conductivity. In practice, many engineering materials will exhibit both softening and scattering effects, as is shown in silicon. This work shines new light on studies of thermal conductivity in fields of energy materials, microelectronics, and nano-scale heat transfer.

Pushing the thermoelectric figure of merit beyond two ( $zT > 2$ ), has been a milestone achievement in the field of energy science. In PbTe, this high  $zT$  has been achieved by significantly reducing the

---

<sup>2</sup>The content in this section was published by Hanus *et al.* in [100].

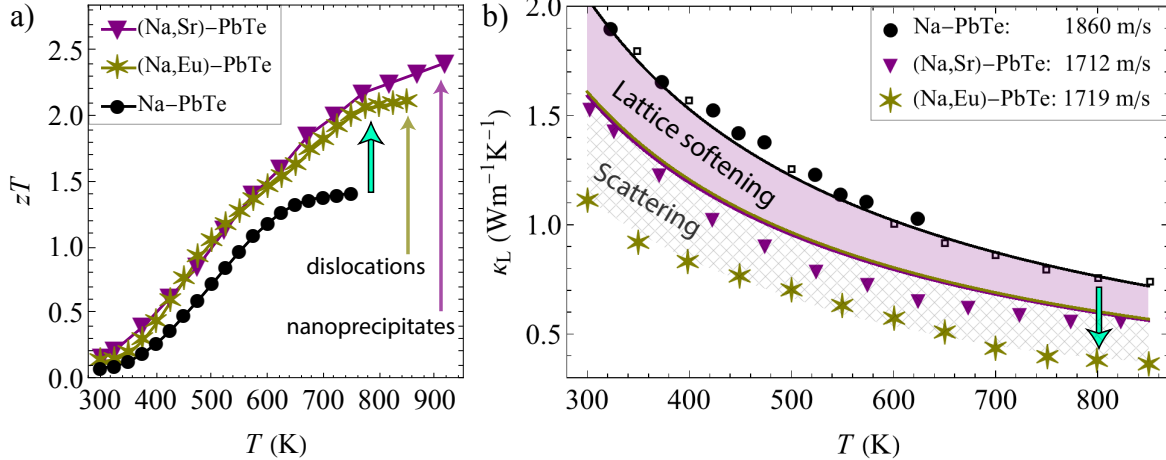


Figure 4.4: Milestone improvements in the figure of merit ( $zT$ ) of Na-doped PbTe due to reductions in lattice thermal conductivity ( $\kappa_L$ ) (a) The improved  $zT$  was previously attributed solely to phonon scattering from micro/nanostructural defects. Data for (Na,Sr)-PbTe ( $Pb_{0.98}Na_{0.02}Te$ -10%SrTe) are from [101], (Na,Eu)-PbTe ( $Na_{0.025}Eu_{0.03}Pb_{0.945}Te$ ) from [102], and Na-PbTe from [103]. (b) A reduction of  $\kappa_L$  upon the introduction of micro/nanostructural defects. The lines show the  $\kappa_L = Av_s^3 T^{-1}$  model describing phonon thermal conductivity in the high-T limit where the only scattering mechanism is phonon-phonon scattering.  $A$  is normalized to the Na-PbTe sample and fixed. The shaded region shows the reduction in  $\kappa_L$  expected from lattice softening alone, without assuming an increase in phonon-defect scattering centers. Phonon scattering mechanisms could account for the remaining reduction in  $\kappa_L$ , depicted by the cross-hatched region. The speed of sound ( $v_s$ ) reduction, measured in this study, is given in the legend. The circles are data for a Na-doped (0.75% Na) sample synthesized and measured in this study. The square data points are a low dislocation density sample from Ref. [104] ( $Na_{0.015}Eu_{0.03}Pb_{0.955}Te$ ).

lattice thermal conductivity ( $\kappa_L$ ) at high temperatures [101, 102] (Figure 4.4a and b). The reduction of  $\kappa_L$  in PbTe, and many other thermoelectric and systems, has been realized by controlling the material's micro/nanostructure. This reduced  $\kappa_L$  has been rationalized by assuming the lattice defects introduce additional scattering centers which reduces the phonon mean free path (and relaxation time) while the speeds of sound and phonon dispersion are assumed to be fixed (present authors included). However,  $\kappa_L$  is very sensitive to changes in the phonon dispersion and thus a materials speed of sound ( $v_s$ ). This can be demonstrated by considering a spectral analysis of the phonon thermal conductivity given in Eq. 2.22. At high temperatures ( $T > \theta_D$ ), when phonon-phonon scattering dominates ( $\tau = \tau_{pp}$ ) Eq. 2.22 becomes (details given in Section D.3) [105, 72]

$$\kappa_L = \frac{(6\pi^2)^{2/3} \bar{M}}{V^{2/3} 4\pi^2 \gamma^2} \frac{\langle v_g^3 \rangle}{T} = A \frac{v_s^3}{T}. \quad (4.4)$$

This simple expression produces the same results as the spectral Callaway model (Eq. 2.22) when  $T > \theta_D$  and  $\tau = \tau_{pp}$  (Eq. D.3.2), and is consistent with the model used by Tan *et al.* [95]. We express it this way to demonstrate the sensitivity of  $\kappa_L$  on lattice stiffness which is reflected in the

cubic dependence of  $\kappa_L$  on phonon velocity. We denote the average group velocity over the Brillouin zone as  $\langle v_g^3 \rangle$  which is defined in Eq. D.3.4. Additionally, we consolidate the numerical constant and factors of the average atomic mass  $\bar{M}$ , atomic volume  $V$ , and Grüneisen parameter  $\gamma$  into the coefficient  $A$ . In practice,  $A$  will be normalized to a pristine (control) sample and the change in speed of sound will be used as an estimate for the change in average group velocity ( $\langle v_g^3 \rangle \propto v_s^3$ ). Thus, if the speed of sound (i.e. lattice stiffness) can be engineered in a material it is expected to be an effective parameter for controlling  $\kappa_L$ . In fact, tuning the lattice stiffness is expected to have a larger impact on  $\kappa_L$  than micro/nanostructural scattering in some cases. Specifically, at high temperatures, when phonon-defect scattering in anharmonic materials is competing with an intrinsic phonon-phonon mean free path which is already very short. For example, 75% of the heat in intrinsic PbTe is carried by phonons with a mean free path less than approximately 10 nm (at room temperature), compared to 1000 nm (at room temperature) for Si [106]. This means only lattice defects that are spaced on the order of 10 nm should significantly influence  $\kappa_L$  in PbTe [107], and this length decreases with increasing temperature.

Internal-strain fields, which are induced by lattice defects such as dislocations and nanoprecipitates, will locally change phonon frequencies within the material and can, in principle, lead to lattice softening. This simultaneously changes phonon speed and induces phonon scattering. The two distinctly different effects are illustrated in Figure 2.3a. Again, the importance of each effect on the lattice thermal conductivity depends on intrinsic material properties and the nature (e.g. length scale) of the internal-strain fields. Specifically, when phonon-phonon scattering is strong (in anharmonic materials and at high temperatures) phonon-strain field scattering is expected to be less important and lattice softening is expected to dominate. Therefore, lattice softening provides a promising avenue for engineering the high temperature thermal conductivity of anharmonic materials, such as thermoelectrics.

Several cases have been presented where an improvement in thermoelectric efficiency is attributed to chemical lattice softening due to alloying or the introduction of vacancies [95, 108]. Additionally, there has been much discussion about the connection between the chemical bonding, and a materials intrinsic lattice stiffness and anharmonicity [109]. Due to the unique bonding characteristics of IV-VI compounds, such as PbTe, they are likely sensitive to the introduction of microstructural defects and in particular lattice strain.

Here, we show a different lattice softening effect where the speed of sound is engineered in stoichiometric PbTe, by changing the amount of internal-strain induced by lattice defects. Astonishingly, in PbTe the observed reduction in speed of sound completely accounts for the reduced  $\kappa_L$ . Additionally, internal-strain induced lattice softening is shown to be a major reason for the reduced  $\kappa_L$  in high efficiency ( $zT > 2$ ) compositions of Na-doped PbTe [101, 102]. Establishing internal-strain softening as a mechanism for engineering thermal conductivity is not only of critical importance

to the field of thermoelectrics, but is also valuable to the fields of nanoscale heat transfer [40], microelectronics [3, 110], and thermal barrier coatings [111, 112].

#### 4.2.1 Results

##### Lattice softening and thermal conductivity of PbTe

To determine the influence of microstructure and internal-strain on thermal conductivity, stoichiometric PbTe samples were synthesized with varying amounts of internal-strain induced by high energy ball milling (Section 4.2.4). The low Debye temperature of PbTe ( $\theta_D \approx 150$  K) means that room temperature measurements are within the ‘high temperature’ limit and Eq. 4.4 is applicable. Since the focus of this study is the lattice thermal conductivity ( $\kappa_L$ ), the samples were left undoped and were analyzed at temperatures where bipolar effects are negligible (below 400 K). The electronic contributions to the total thermal conductivity were found to be less than 1% of the total (i.e.,  $\kappa \simeq \kappa_L$ ). The internal-strain of each pellet sample was measured via XRD peak broadening by the Williamson-Hall method. The thermal and elastic properties of each pellet were measured by the laser flash method (Section 4.2.5) and pulse-echo ultrasound (Section E.1), respectively. The time delay between ultrasound reflections was accurately determined via the maximization of the cross-correlation such that the largest source of error was the measurement of the sample thickness [113]. The error of the pulse-echo measurement was determined to be approximately 1%.

Bulk PbTe pellets containing increasing amounts of internal-strain showed significantly decreased speeds of sound, and this lattice softening was found to completely account for the observed reductions in  $\kappa_L$  (Figure 4.5). Quantitatively, we use Eq. 4.4 and normalize the coefficient  $A$  to the nominally unstrained sample (green squares in Figure 4.5). This value,  $A = 1.09 \times 10^{-7} \text{ Ws}^3\text{m}^{-4}$ , is held constant so that  $v_s$  is the deciding parameter of the model. Thus, since  $v_s$  is a measurable, there are no additional free parameters in this model. We note that the experimentally determined value of  $A$  is within a factor of three of the theoretical value found for PbTe ( $A = 2.6 \times 10^{-7} \text{ Ws}^3\text{m}^{-4}$ ). This agreement is comparable to models used to predict  $\kappa_L$  with semi-empirical models or even *ab initio* calculations [114, 115].

The reduction in  $\kappa_L$  measured in these samples can be completely accounted for by lattice softening effects alone (see Eq. 4.4 and Fig. 4.5a,b). It is important to recognize that small changes in  $v_s$  correspond to large changes in  $\kappa_L$ . For example, the 7% reduction in  $v_s$  observed in stoichiometric PbTe results in a 20% reduction in  $\kappa_L$ , without introducing additional scattering parameters.

To verify the  $\kappa_L \propto v_s^3$  relationship, a second series of samples were synthesized and measured, and the results are displayed in Figure 4.5b, 4.5c, and Figure S4 of Ref. [100]. The agreement between this reproducibility study and the primary study is shown in Figure 4.5b. Care was taken to ensure

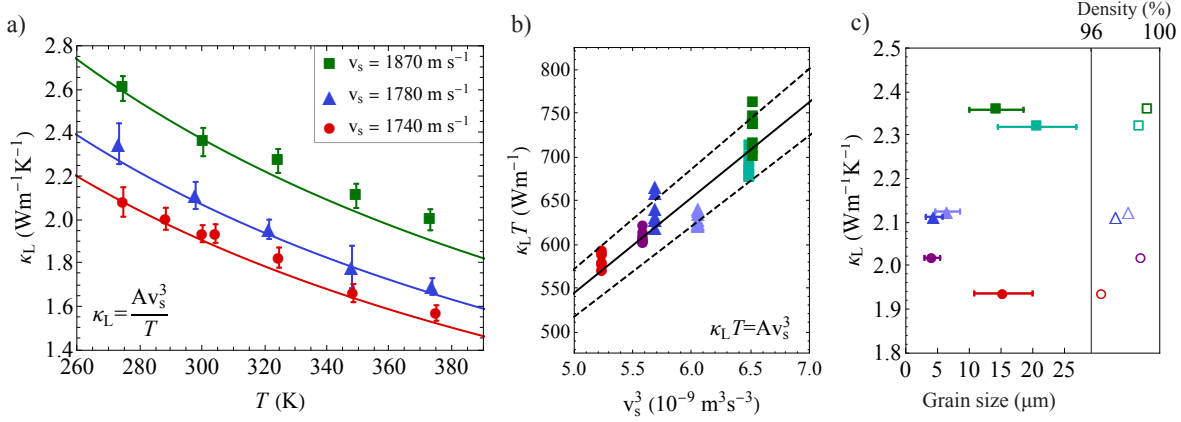


Figure 4.5: Lattice thermal conductivity of PbTe samples with different amounts of internal strain and average speeds of sound ( $v_s$ ). (a)  $\kappa_L$  vs.  $T$  of three characteristic samples. The lines are applications of the  $\kappa_L = Av_s^3T^{-1}$  model where, since the coefficient  $A = 1.09 \times 10^{-7}\text{Ws}^3\text{m}^{-4}$  is normalized to the unstrained sample (squares) and held constant, there are no adjustable parameters and only difference in the model between samples is the measured  $v_s$ . (b) A different representation of Eq. 4.4, showing the data in panel (a) in comparison to a reproducibility study containing three independently synthesized samples (Figure S4 of [100]). The dashed lines show a 5% error in  $\kappa_L$ . This data shows that the reduction in lattice thermal conductivity in stoichiometric PbTe is fully accounted for by lattice softening. (c) The measured grain size (filled data points) and density (empty data points) of each sample versus its room temperature  $\kappa_L$  showing that all samples have a density between 97 and 99% of the theoretical density, are large grained, and that there is no systematic trend of  $\kappa_L$  with grain size or density.

that there was no systematic relationship between  $\kappa_L$  and grain size or density. Figure 4.5c shows that all sample had a density above 97% of the theoretical density (confirmed by both the geometric and Archimedes method), and that there is no systematic trend of  $\kappa_L$  with grain size measured via scanning electron microscopy (Figure 4.12). Since the speed of sound measured ultrasonically is sensitive to sample density, the lattice softening measured was confirmed by low- $T$  heat capacity measurements and is shown in Figure 4.6. The 10% reduction in the Debye temperature,  $\theta_D \propto v_s$ , agrees with the 7% reduction of  $v_s$  measured via ultrasound. Since PbTe is a soft material, the Debye level is only observed below 2.5 to 3 K, making the ultrasound measurement more accurate than this low- $T$  heat capacity analysis. When analyzing the elastic properties of soft materials, it can be important to validate softening effects with multiple experimental methods, but ultrasound is recommended for obtaining quantitative values.

### Lattice softening and internal strain

The reductions in speed of sound and lattice thermal conductivity correspond to an increase in internal-strain. As can be seen in Figure 4.7, the speed of sound decreases linearly with an increase in internal-strain measured via XRD peak broadening. The open diamond data point corresponds to

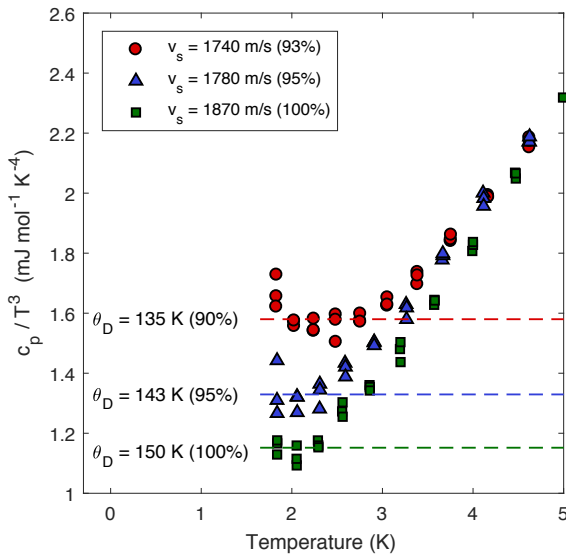


Figure 4.6: Experimentally measured heat capacity plotted as  $C_p/T^3$  vs  $T$  in order to illustrate the horizontal Debye level,  $\beta$ , in the  $T \rightarrow 0$  K limit. Corresponding Debye model fits of  $\beta$ , from which Debye temperature  $\theta_D$  can be calculated, are shown for each data set. Inside parenthesis,  $\theta_D$  and  $v_s$  are shown as a percentage of the nominally unstrained sample (green). The reduction in  $\theta_D$  is in excellent agreement with the reduction measured by pulse-echo ultrasound.

the isotropic average speed of sound of PbTe calculated from the components of the elastic tensor measured on a single crystal [116, 117], and shows this linear trend of  $v_s$  extends down to zero internal strain.

Figure 4.7a shows the measurement of internal-strain of the pellet samples by Williamson-Hall analysis of XRD peak broadening.  $\beta$  is the broadening (integral breadth) of the diffraction peak at angle  $\theta$  after correcting for instrument broadening. Figure 4.7b shows the peak fits of samples containing small and large amounts of internal strain. Peak shape asymmetry can be observed, particularly in samples with large amounts of internal strain, where the peak broadening is more significant on the low  $2\theta$  (larger d-spacing) side of the peak maximum. This indicates that the state of inhomogeneous internal-strain of these samples has a tendency to increase the lattice plane spacing distribution. An increase in lattice plane spacing (d-spacing) most commonly corresponds to a decrease in phonon frequencies and speeds of sound through considerations of the Grüneisen tensor [118, 34]. From a chemical perspective, bond stiffness is inversely proportional to bond length. A number of extended lattice defects are known to cause peak shape assymetry, including dislocations and coherency strains [119].

The slope of the plots shown in Figure 4.7a is a measure of  $C\epsilon_{XRD}$ , where  $\epsilon_{XRD}$  is the internal strain determined via the Williamson-Hall method, and  $C$  is a constant related to the nature of the strain

and details of the analysis method [120, 121, 122]. The full peak broadening analysis, given in Section 4.2.4, shows that the strain state of the PbTe samples is consistent with dislocations having Burger's vectors in the  $\langle 110 \rangle$  direction [58], in agreement with the analysis of Chen *et al.* [104]. Since the spot size of the X-ray beam is approximately  $10 \text{ mm}^2$ , this method for characterizing strain is a bulk measurement. While transmission electron microscopy provides detailed strain information about specific defects it is limited to a small field of view and is often limited to nanoscale observations. While grain boundaries and interfaces can be a means to introduce internal strain, they do not appear to be the primary cause of internal-strain in the stoichiometric PbTe system (Figure 4.5c and Figure 4.7).

The present study also characterized the speed of sound and internal-strain of the  $zT > 2$  samples shown in Figure 4.4 reported by Tan *et al.* [101] and Chen *et al.* [102]. Remarkably, these measurements follow the same trend as that measured in stoichiometric PbTe synthesized for this study (Figure 4.7). These data indicate that the same softening mechanism observed in the stoichiometric PbTe samples of this study is also present in the high- $zT$  (Na,Eu)-PbTe and (Na,Sr)-PbTe systems. The measured  $v_s$  in these two samples suggests that a large percentage of the reduction in  $\kappa_L$  is due to lattice softening alone (Figure 4.4b).

The relationship between strain and phonon frequency (and thus the speed of sound) is described through the Grüneisen tensor Eq. 2.43 which at small strains can be written as

$$\omega = \omega_0(1 - \gamma_{ij}\epsilon_{ij}), \quad (4.5)$$

where  $\omega_0$  is the phonon frequency at zero strain. Recognizing that  $\omega \propto v_s$  at low  $\omega$ , it is possible to define an engineering Grüneisen parameter  $\gamma_{\text{int}}$ , which is associated with the internal-strain state of PbTe measured via XRD. Then,

$$v_s = v_{s,0}(1 - \gamma_{\text{int}}\epsilon_{\text{XRD}}). \quad (4.6)$$

This expression is consistent with the experimental observation of a linear dependence of speed of sound on strain. From a fit of Eq. 4.6 to the experimental data in Figure 4.7c using  $C = 4$  [122, 121, 120], we estimate that  $\gamma_{\text{int}} = 5$ , which is of the same order as the thermodynamic Grüneisen parameter of PbTe ( $\gamma = 2.2$ , Ref. [116]). The order of magnitude agreement between  $\gamma_{\text{int}}$  and  $\gamma$  for PbTe strongly supports the argument that internal-strain is the origin of lattice softening, reduced  $\kappa_L$  and improved  $zT$ . It should be noted that the analysis shown in Figure 4.7a determines relative changes in internal-strain, and that the absolute magnitude of internal strain depends on the value of  $C$ . Thus,  $\gamma_{\text{int}}$  is an experimental parameter that is expected to be consistent when the analysis method is consistent between samples. Several other theories predict softening with increasing strain and/or dislocation density [123, 124, 125, 126]. Theories that relate lattice softening explicitly to strain energy give a quadratic dependence on strain, rather than the linear

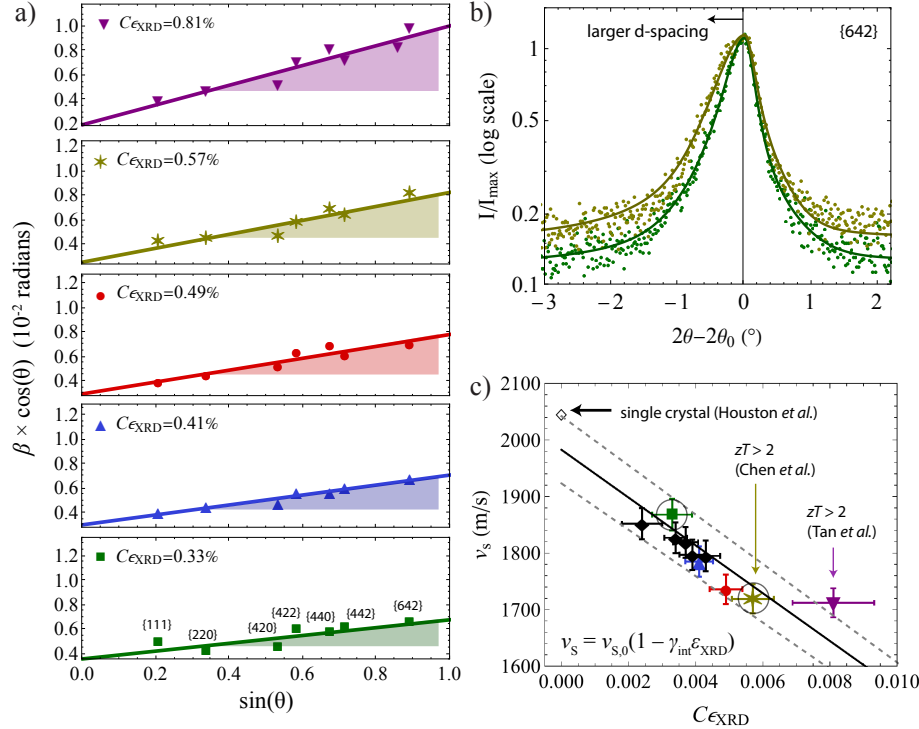


Figure 4.7: Speed of sound decreases linearly with increasing internal-strain in PbTe based materials. a) Williamson-Hall strain analysis of stoichiometric PbTe, as well as Na-doped, high  $zT$ , compositions (colors are consistent with Figure 4.4 and 4.5).  $\beta$  is the integral breadth (peak area/height) of a diffraction peak at  $\theta$ . The slope of the plots ( $C\epsilon_{XRD}$ ) are proportional to the average internal-strain in the material (details in Section 4.2.4). b) Example peak fits of a low and high internal-strain samples (circled in panel (c)). Diffraction peaks in samples with large amounts of internal-strain show peak shape asymmetry where the peak has a larger broadening on the low  $2\theta$  (larger d-spacing) side of the peak maximum. c) The speed of sound ( $v_s$ ) measured by pulse-echo ultrasound versus the internal-strain ( $C\epsilon_{XRD}$ ) as measured in panel (a). The increase in internal-strain is correlated with a linear decrease in the speed of sound, a reduction in the lattice thermal conductivity, and improved thermoelectric efficiency.

dependence observed in this study [124, 125, 126].

#### 4.2.2 Discussion

##### Temperature dependence of $\kappa_L$ reduction: scattering vs. softening

Lattice softening is fundamentally different than phonon-defect scattering as a mechanism to reduce  $\kappa_L$ . Thus, softening and defect scattering have distinguishing features in the temperature dependence of  $\kappa_L$ . This difference stems from the fact that phonon-phonon scattering has a  $\tau_{pp}^{-1} \propto T$  temperature dependence above the Debye temperature, whereas all elastic phonon-defect scattering mechanisms ( $\tau_{defect}$ ) are independent of temperature, given that the defect concentration is approx-

imately constant with temperature (Table I of Klemens [127]). Consequently, phonon-defect scattering should be proportionally more effective at lower temperatures than at higher temperatures. Lattice softening is effective at all temperatures since it reduces thermal conductivity regardless of scattering mechanisms. This is demonstrated in the schematic model shown in Figure 4.8, which is based on Eqs. 2.22, 2.18, and D.3.2. The black line indicates a pristine sample with speed of sound  $v_{s,1}$  (e.g. a single crystal, or nominally unstrained and large grained polycrystal). The dashed line represents a defective material where the speed of sound stays constant at  $v_{s,1}$  and  $\kappa_L$  is reduced by defect scattering (i.e. temperature independent  $\tau_{\text{defect}}$ ). The dark red line illustrates a reduction in  $\kappa_L$  through lattice softening (i.e. a reduction in speed of sound,  $v_{s,2} < v_{s,1}$ ) without changing scattering mechanisms. When analyzing thermal conductivity as  $\kappa_L$  vs.  $T$  (as in Figure 4.8a) it may be difficult to determine if scattering or softening is the primary mechanism of  $\kappa_L$  reduction. However, the difference in the temperature dependence can be more clearly seen by normalizing the thermal conductivity of the defective sample by that of the pristine sample ( $\kappa/\kappa_0$ ). A positive slope of  $\kappa/\kappa_0$  with temperature is characteristic of phonon-defect scattering. In contradistinction, if lattice softening dominates,  $\kappa/\kappa_0$  is expected to be constant with temperature (Figure 4.8b). To verify lattice softening effects are present, elasticity, low- $T$  heat capacity, and/or phonon density of states measurements are required.

Lattice softening has been observed by low- $T$  heat capacity in Si, where the measured  $v_s$  reduces from  $5830 \text{ m s}^{-1}$  in a Si single crystal [128] and  $5700 \text{ m s}^{-1}$  in a polycrystal, to  $4440 \text{ m s}^{-1}$  in a nanocrystalline material [129]. However, the phonon-phonon mean free path in Si is large at room temperature, with 75% of the heat being transported with a mean free path ( $\Lambda = v_g\tau$ ) larger than approximately 100 nm. Therefore, nanocrystalline Si is still expected to have significant phonon scattering effects at room temperature due to grain boundary scattering. Figure 4.9a shows the lattice thermal conductivity of single crystal [73] and nanocrystalline Si with an average grain size of 42 nm [129]. The lines show a transport model constructed to estimate the relative importance of lattice softening and phonon-scattering in this system. This Callaway-type model has been used previously for Si [130, 39], but did not consider changes in speed of sound. In these studies,  $\tau_{\text{pp}}$  is calibrated to single crystalline data and fixed. Here,  $\tau_{\text{pp}}$  is parameterized to capture the experimentally observed lattice softening effects, such that the explicit dependence of  $\tau_{\text{pp}}$  on the phonon velocity is left intact (Eq. 4.15). In the previous studies [130, 39], this dependence was buried in the numerical constants. Thus, the model used herein is able to capture lattice softening effects. It is not surprising, then, that the 24% reduction in  $v_s$  going from single- to nano-crystalline Si coincides with a large predicted reduction in  $\kappa_L$  (red shaded region in Fig. 4.9a). To account for grain boundary scattering in the nanocrystalline material, the relaxation time due to phonon interactions with lattice rotation and localized strain fields at grain boundaries ( $\tau_{\text{gbs}}$ ) is applied (Eq. 3.14, [39]). All parameters associated with the nanoscale structure of the grain boundaries are fixed to those that were used in the low- $T$   $\kappa_L$  model in Figure 3.7, and the grain size was set to

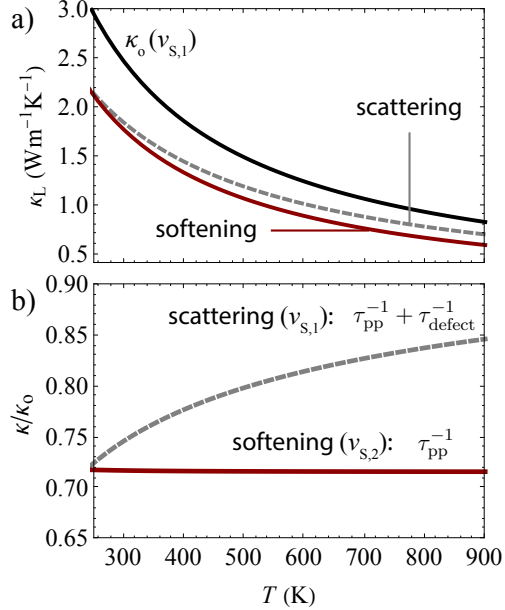


Figure 4.8: A schematic transport model demonstrating the characteristics features of defect scattering and lattice softening mechanisms in the reduction of lattice thermal conductivity ( $\kappa_L$ ). a) The  $\kappa_L$  of a pristine sample ( $\kappa_o$ ) compared to the  $\kappa_L$  of defective samples where the reduction in  $\kappa_L$  is induced by phonon-defect scattering and lattice softening. In the pristine sample ( $\kappa_o$ ), and the case of lattice softening (dark red),  $\tau^{-1} = \tau_{pp}^{-1} \propto T$ . For the case of phonon-defect scattering (dashed),  $\tau^{-1} = \tau_{pp}^{-1} + \tau_{defect}^{-1} \propto T + \text{constant}$ . b) The ratio of  $\kappa_L$  for the defective sample over that for the pristine sample. A positive slope of  $\kappa/\kappa_o$  indicates significant phonon scattering effects, and no slope indicates softening effects.

42 nm, which was measured experimentally [129]. Therefore, the model captures the entire reduction of  $\kappa_L$  from single- to nano-crystalline samples using experimentally measured speed of sound and grain size, without any additional fitting parameters (black and teal lines in Figure 4.9a). This model indicates that at room temperature, phonon-grain boundary scattering and lattice softening are equally important, whereas at high temperatures ( $> 1000$  K) lattice softening dominates. The dashed line shows a predicted  $\kappa_L$  if lattice softening is not included. Phonon scattering on point impurities and free charge carriers in the Si-nc were determined to be negligible and are discussed in Section 4.2.5.

In Figure 4.9b and c, we show the  $\kappa_L$  of the defective samples normalized by that of the pristine sample (Si single crystal, and large grain unstrained Na-PbTe). Indeed, a positive slope in  $\kappa/\kappa_o$  vs.  $T$  is observed in Si near room temperature, where significant scattering is present (compare to Figure 4.8b). In PbTe, however,  $\kappa/\kappa_o$  vs.  $T$  is relatively flat which is consistent with the lattice softening measured in Figure 4.7. This analysis of Si and PbTe demonstrates that lattice softening and scattering effects can both contribute to the reduction of  $\kappa_L$  in engineering materials. However, the relative contribution of each effect depends on the specific material and microstructure. Here, it

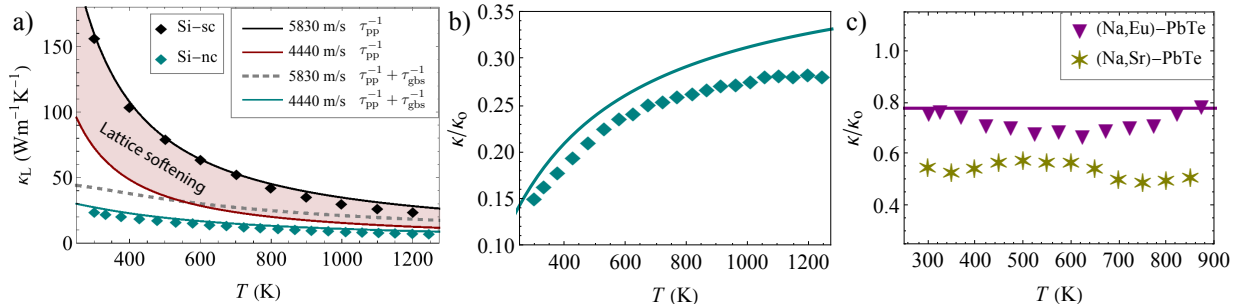


Figure 4.9: The temperature dependent reduction of lattice thermal conductivity ( $\kappa_L$ ) in Si and PbTe. a) A Callaway-type thermal transport model used to estimate the effects of lattice softening and phonon-grain boundary scattering in reducing  $\kappa_L$  from single crystal (sc, [73]) to nanocrystalline (nc, [129]) Si, with average grain size of 42 nm. The red shaded region shows the reduction in lattice thermal conductivity expected from measured lattice softening alone. Phonon-grain boundary scattering was included using the expression derived by Hanus *et al.* [39],  $\tau_{\text{gbs}}$ , where the only parameter changed from Ref. [39] to this study is the grain size. Therefore, the only parameters in the model changed from Si-sc to Si-nc are the experimentally measured  $v_s$  and grain size. The dashed line shows the predicted  $\kappa_L$  if lattice softening is not included. b) The normalized  $\kappa_L$  of Si-nc showing a positive slope with  $T$  around room temperature indicates phonon scattering effects are important. c) The normalized  $\kappa_L$  of high- $zT$  Na-doped PbTe samples showing a flat temperature dependence indicating that lattice softening is important.

is shown that lattice softening can account for over 50% of the reduction in  $\kappa_L$ , and is consequently a primary mechanism with which to engineer thermal conductivity.

### The connection between speed of sound and heat carrying phonons

The speed of sound is a measure of the slope of the phonon dispersion relation near the center of the Brillouin zone ( $\Gamma$ -point). Acoustic measurements of speed of sound and elastic properties are typically made in the kHz to MHz frequency range. Measurement of the speed of sound at higher frequencies can be obtained from the Debye level found from low- $T$  heat capacity ( $\approx 10^2$  GHz) or phonon density of states ( $\approx 1$  THz). Phonons which carry significant amounts of heat are in the THz frequency range. However, speed of sound is inherently a measurement of bond stiffness which is governed by the interatomic force constants.

Interatomic force constants simultaneously govern the speed of sound as well as the frequency and group velocity of phonons throughout the Brillouin zone [34] (see Appendix B and Figure 2.2a). Consequently, acoustic measurements can be used as a gauge for the general behavior of the full phonon dispersion. One justification for this is that the speed of sound has been shown to be an accurate predictor for the average phonon frequency across material systems [131]. Additionally, it is known that Raman-active optical modes typically have a linear strain dependence that can also be characterized by a Gruneisen parameter [132, 133]. From theoretical considerations, this optical Gruneisen parameter is  $\approx 6.5$  for ionic materials and  $\approx 3$  for covalently bonded materials [133].

The phonon mode dependent Grüneisen parameter has been computed for PbTe and values for the optical branches are of similar sign and magnitude [134]. The thermal conductivity of homogeneously strained PbTe has also been computed by Murphy et al. [135]. The results show that positive tensile strain, indeed, strongly reduced the transverse optical  $\Gamma$ -point frequency and the magnitude of reduction in  $\kappa_L$  with increasing strain generally agrees with the experimental results presented here. Therefore, speed of sound measurements are very useful in probing the bond stiffness and in turn the general behavior of heat carrying phonons in defective systems where direct measurement or calculation of THz phonons is prohibitively difficult or impossible (e.g. polycrystalline and heavily strained materials).

### **Engineering thermal conductivity through lattice softening**

Internal-strain induced lattice softening has been demonstrated as a promising method to reduce thermal conductivity. Therefore, methods of introducing and maintaining large amounts of internal-strain should be considered, rather than methods which increase the spatial density of defects, particularly in anharmonic materials. The PbTe study presented here utilized high-energy ball milling in conjunction with a rapid hot-pressing procedure developed to minimize the annealing out of internal-strain. Other processing techniques such as high pressure torsion [136], hot deformation [137], and liquid phase sintering [65] may be optimized to maximize the amount of internal-strain in the material. The softening effects in Si and Si-Ge alloys by Caudio *et al.* [129, 138], and in  $\text{Bi}_2\text{Te}_3$  and  $\text{Sb}_2\text{Te}_3$  based materials by Klobes *et al.* [139] were seen with decreasing grain size. While decreasing grain size often correlates with an increased amount of internal-strain, this is not always the case (as we show in Figures 4.5 and 4.7). Nevertheless, given that microstructural defects contribute to both lattice softening and scattering, it is no surprise that good thermoelectric materials with low thermal conductivity are highly defective. However, lattice softening is a particularly promising avenue for thermoelectrics as it allows for a reduction in  $\kappa_L$  without the requirement of a large spatial density of defects which likely induce electron scattering as well.

Beyond semiconductors, lattice softening has been measured in metallic [124] and ionic materials [140] with increased point defect concentrations. The magnitude of such effects could be assessed with similar experimental methods as those presented here. The totality of these reports indicates that elastic softening should be important in many engineering materials other than PbTe. It is interesting to note that the internal-strain softening effect described here may even be taken to the limit of amorphous materials, which have been theoretically described as fully defective crystals, and whose elastic moduli are nearly universally lower than their crystalline analogues [141].

### 4.2.3 Conclusion

Here, in a PbTe model system, we experimentally established the importance of lattice softening effects on thermal transport. Significant reductions in the thermal conductivity of polycrystalline PbTe were completely accounted for by reductions in the materials average speed of sound, without invoking additional phonon scattering terms. In nanocrystalline Si, both softening and scattering effects were necessary to describe the thermal conductivity reduction. These results demonstrate that monitoring the elasticity of a material throughout a study is of critical importance.

The reduction in speed of sound is found to be linearly related to the increase in the internal-strain of a material. This can be described by defining an engineering Grüneisen parameter which behaves like a material property of PbTe,  $\gamma_{\text{int}} \approx 5$ . With this new understanding of lattice softening, and its implications on thermal transport, it is not surprising that materials processing methods which create and maintain large amounts of internal-strain tend to improve thermoelectric efficiency. Or, more specifically, that these methods are effective at reducing the lattice thermal conductivity at high temperatures, even in very anharmonic materials where the intrinsic phonon-phonon mean free path is already very small.

### 4.2.4 Methods

#### Synthesis

Ingots (between 20 to 40 g) of nominally stoichiometric PbTe were prepared from elemental Pb (Alfa Aesar, lead rod, 6.35 mm diameter, 99.999%) and Te (Alfa Aesar, Tellurium lump, 99.999+%) by melt reaction under vacuum ( $\sim 10^{-4}$  torr) in a carbon-coated quartz ampule (12 mm inside diameter x 16 mm outside diameter) at 1000 °C for 4 to 6 hours and quenched in ice water. Each ingot was independently pulverized by mortar and pestle and sieved to have an initial particle size distribution between 20 to 120  $\mu\text{m}$ . This material was considered to be nominally un-strained. Plastic deformation was introduced via high-energy ball milling for varying durations (5 to 120 min). The ball milling process was standardized such that 2.0 g of unstrained powder was loaded into a stainless steel jar (with inner dimensions of 36.7 mm in diameter and 57 mm in height) along with the same size and number of grinding media (2 stainless steel balls 12.7 mm in diameter and 15 stainless steel balls 6.3 mm in diameter) and sealed in an argon atmosphere. All powders were consolidated by uniaxially hot pressing in a high density graphite die under argon atmosphere. The maximum pressure of  $\sim 45$  MPa and maximum temperature of 550 °C were held concurrently for 20 min. As the temperature ramped from room temperature to 550 °C, the pressure was applied stepwise in 10 MPa intervals. Both temperature and pressure reached their maximum value in 10 min. After consolidating for 20 min, the samples were furnace cooled under a nominal pressure

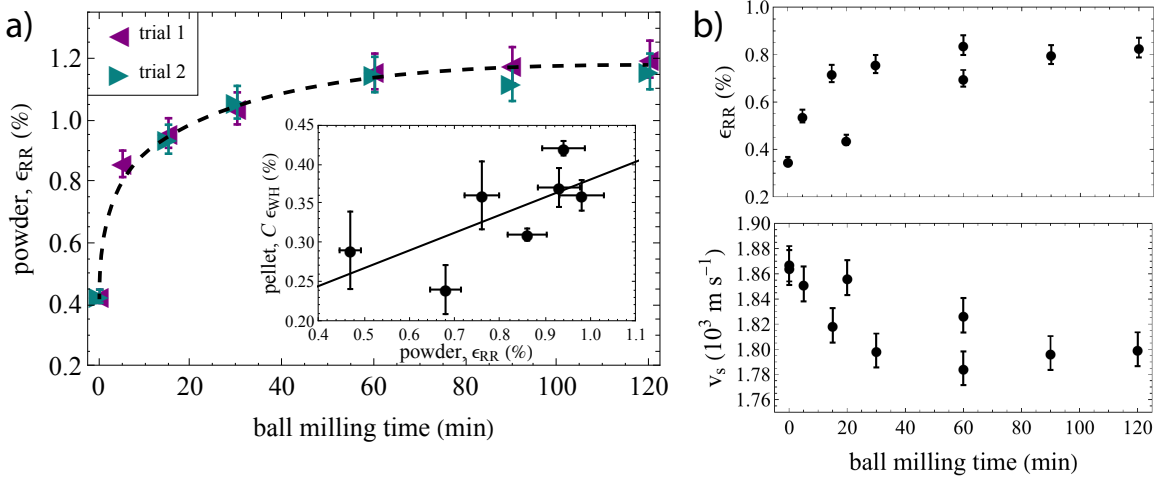


Figure 4.10: a) Internal strain of precursor powder versus ball milling time. High energy ball milling can be used to systematically control internal strain energy, however there is a saturation of the internal strain which depends on the details of the ball milling procedure (60 minutes in this case). The amount of internal strain is only reproducible if: (1) the initial particle size distribution (2) amount of material being ball milled (3) type of milling media and (4) the ball milling time are consistent, as can be seen by comparing the two trials. The inset shows that the internal strain in the powder is roughly proportional to the internal strain of the resulting pressed pellet. b) Powder internal strain and pellet speed of sound when all of the previously mentioned experimental parameters are not controlled.

of 5 MPa. All pellets had a density  $> 97\%$  theoretical density ( $8.16 \text{ g cm}^{-3}$ ), measured by both geometric and Archimedes methods. To minimize error introduced in speed of sound and thermal diffusivity measurements, all samples were sanded and polished to be parallel such that the thickness variation was within 1% of the mean, measured with a micrometer.

Figure 4.10 shows the internal-strain (measurement described in Section 4.2.4) as a function of high energy ball milling time. The amount of internal-strain induced during ball milling can vary with many experimental factors. We found that if the initial particle size distribution is controlled by sieving, the amount of powder being ball milled is kept constant, as well as the milling media and size of the ball milling vial, the internal-strain versus ball milling time trend can be reproduced within experimental uncertainty, as can be seen by comparing the two trials in Figure 4.10.

Figure 4.10 shows the variability seen if all of the mentioned experimental parameters are not controlled. Nevertheless, the speeds of sound correlate with measured internal strain regardless of ball milling conditions (Figure 4.7b).

Figures 4.10a and b also show that internal-strain increases with ball milling time until a plateau is reached at approximately one to two hours depending on previously mentioned details regarding the ball milling procedure. This type of plateau is commonly observed in powder metallurgy, and

is sometimes followed by a decrease in internal strain [142].

## X-Ray diffraction and analysis

**X-Ray data collection.** X-Ray diffraction was conducted on a STOE STADI-MP with pure Cu K- $\alpha 1$  radiation (Figure 4.11). Pre-pressed powders were measured in transmission mode (Debye-Scherrer geometry) and pressed pellets were measured in reflection mode (Bragg-Brentano geometry). A NIST 640e silicon standard was used to calibrate the peak position, and NIST 660c LaB<sub>6</sub> standard was used to characterize the instrumental peak broadening. The instrumental broadening is shown in relation to the peak broadening of a typical PbTe sample in the inset of Figure 4.11a, where the  $2\theta = 71.8^\circ$  LaB<sub>6</sub> peak is normalized in intensity and position for comparison to the PbTe peak. This shows that the instrument resolution in peak width is sufficient for particle size and internal-strain analysis. Since strain information is contained primarily in high angle reflections, data was collected up to  $2\theta = 110^\circ$  for powders in transmission mode and  $2\theta = 130^\circ$  for pellets in reflection, with sufficient counting time to fully resolve the high angle peaks.

**Reitveld refinement and evidence of  $\langle 110 \rangle$  dislocations.** GSAS II was used to conduct Reitveld refinements [143]. An instrument parameter file was constructed in GSAS II by refining the LaB<sub>6</sub> standard, with no sample size or microstrain broadening included. The instrument parameter file was not changed during refinement of PbTe samples. When refining PbTe ( $Fm\bar{3}m$ ) samples, the lattice parameter and sample position were first refined separately and then together. Then the particle size was set to its maximum ( $10\mu m$ ) and microstrain was refined. Since significant anisotropic peak broadening was observed in all samples (peak width is not a smooth function of  $\theta$ ) the generalized anisotropic strain model was used in GSAS II to describe the internal strain, analogous to that used by Christensen et al. [144] in JANA2006. This model allows for two independent strain parameters,  $S_{400}$  and  $S_{220}$ , and a typical result is shown as a strain surface plot in Figure 4.11b. This strain model shows that the crystal is less strained in the principle crystallographic directions, as observed by the ‘dimples’ along the  $x$ ,  $y$ , and  $z$  directions of Figure 4.11b. Additionally, this is reflected in the raw peak fits shown in Figure 4.11c, as well as the anisotropic strain parameters in which all samples show,  $2S_{400} < S_{220}$ . This type of strain state is consistent with that of a dislocation with a Burgers vector in the  $\langle 110 \rangle$  direction, as shown in Figure 4.11d. This dislocation line points into the page and the Burgers vector is rotated  $45^\circ$  from the principle directions, such that there is a zero strain node in the  $\sigma_{yy}$  and  $\sigma_{xy}$  components of the stress tensor in the principle crystallographic directions [58]. This data suggests that the dominant defects inducing the internal strain are dislocations with Burgers vector equal to  $(a/2)\langle 110 \rangle$ , which are known to be a low energy dislocation type in PbTe [58]. Finally, the size was refined separately and then together with strain resulting in no significant contribution to peak broadening from particle size effects. Then all previously refined parameters were refined together (instrument parameters

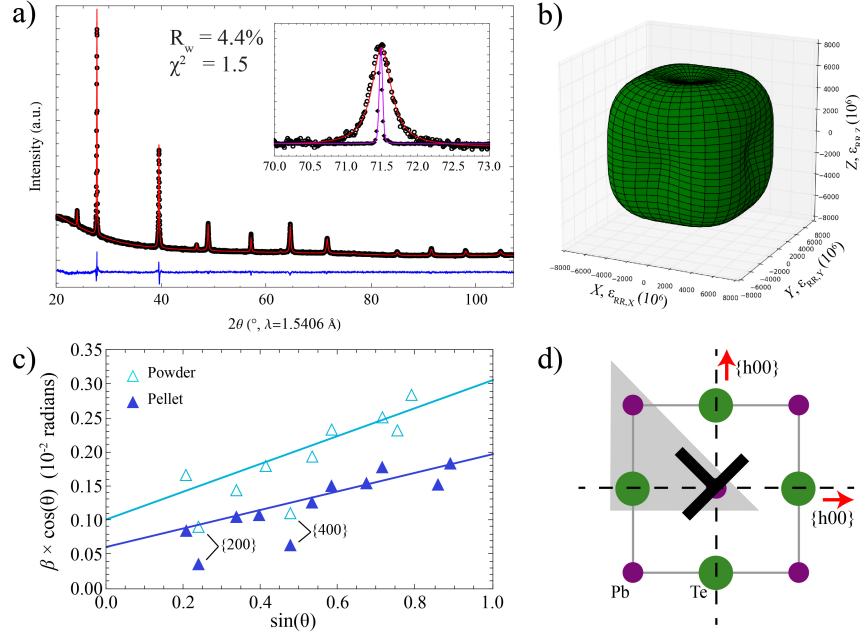


Figure 4.11: a) Characteristic example of X-ray diffraction data and Reitveld refinement results. Circles are observed data of the PbTe sample, the red line is the calculated intensity obtained via refinement with GSAS II, and the blue line is the difference of the two. The inset shows a detailed view of a high angle peak, where the diamonds are data from the LaB<sub>6</sub> 660c NIST standard and the purple line the calculated fit. This shows that the instrument line width resolution is sufficient for strain analysis, and verifies the quality of the refinement specifically in the context of peak broadening. b) Strain contour plot resulting from the generalized strain model, which accounts for the anisotropic peak broadening. c) Single peak fits showing how the h00 type peaks are sharp compared to the rest of the reflections. d) Illustration of a dislocation with a Burger's vector of  $\frac{a}{2} \langle 110 \rangle$ . The extra half plane is shaded in grey, and the dashed lines show nodes in the  $\sigma_{yy}$  and  $\sigma_{xy}$  components of the stress tensor.

still fixed) and the resulting fit is shown in Figure 4.11. The reproducibility of internal strain analysis was verified by refining five independent X-ray scans on the same batch of powder. The standard deviation of internal strain measurements had a value that was 3% of the mean. No change in the lattice parameter was measured.

**Williamson-Hall peak broadening analysis.** To analyze the internal strain of the pressed pellets, select peaks were fit using a split psuedo-Voigt function

$$I(2\theta) = I_{hkl}[\eta L(2\theta - 2\theta_0)) + (1 - \eta)G(2\theta - 2\theta_0)]. \quad (4.7)$$

The Lorenzian full width half max ( $\sigma$ ) was allowed to be different on the left and right side of the

peak maximum,

$$L(2\theta - 2\theta_0) = \frac{(\sigma/2)^2}{(2\theta - 2\theta_0)^2 + (\sigma/2)^2} \cdot \begin{cases} \sigma = \sigma_L, & 2\theta \leq 2\theta_0 \\ \sigma = \sigma_R, & 2\theta > 2\theta_0 \end{cases} \quad (4.8)$$

The Gaussian peak shape function is given by

$$G(2\theta - 2\theta_0) = \exp\left(-\frac{\pi(2\theta - 2\theta_0)^2}{\beta_G^2}\right), \quad (4.9)$$

where  $\beta_G$  is the Gaussian peak width. The  $\theta$  dependence of the peak width was analyzed via the Williamson-Hall method. While the same conclusions can be made by analyzing Reitveld refinement results of the pressed pellets, the Williamson-Hall method was used because it resulted in a lower analysis related error (presumably because of the asymmetric peak shapes which are captured by our peak fits and are not in GSAS II). Additionally, while the results presented in Figure 4.11 suggest that the primary strain inducing defect is a dislocation with Burgers vector  $(a/2)\langle 110 \rangle$ , the Williamson-Hall approach used on the pellets is model *non*-specific and no conclusion about the microscopic origin of the internal strain is required.

Individual peaks were fit using the split pseudo-Voigt profile function (Eq. 4.7) the integral breadth (area/height) of the fitted peak is given by  $\beta_{\text{meas}}$ . The instrument integral breadth,  $\beta_{\text{inst}}$  was determined by conducting the same fitting procedure on a NIST 660c LaB<sub>6</sub> standard. The sample full width at half maximum was then calculated by  $\beta^2 = \beta_{\text{meas}}^2 - \beta_{\text{inst}}^2$  and converted from degrees into radians for analysis. The Williamson-Hall function was used to determine the relative amounts of internal strain in each pellet sample

$$\beta \cos \theta = (C\epsilon_{\text{XRD}}) \sin \theta + \frac{\lambda}{d_{\text{XRD}}}, \quad (4.10)$$

where  $\beta$  is the instrument corrected full width half maximum (in radians),  $\theta$  is the angle of the diffraction peak,  $\lambda$  is the wavelength of the radiation,  $C = 4$  is a constant related to the nature of the internal strain [122, 121, 120], and  $\epsilon_{\text{XRD}}$  and  $d_{\text{XRD}}$  are the internal strain and crystallite domain size determined via this Williamson-Hall method. As can be seen in Figure 4.11c, the  $\{h00\}$  type peaks were significantly sharper than the other peaks [130, 144] and were thus excluded from the Williamson-Hall analysis. The resulting least squares fits are shown as lines in Figures 4.7a and 4.11c.

Table 4.2: Elasticity data for the samples shown in Figure 4.5. Samples can be identified by the labeled  $v_s$  values.

$v_S$ (m s $^{-1}$ )	$v_L$ (m s $^{-1}$ )	$v_T$ (m s $^{-1}$ )	$B$ (GPa)	$\mu$ (GPa)	$\nu$
1870	3031	1676	44.1	22.8	0.28
1780	2877	1603	38.6	20.4	0.27
1740	2738	1562	33.4	19.2	0.26
1860	3026	1673	43.4	22.4	0.28
1820	2935	1637	39.8	21.1	0.27
1770	2738	1599	31.7	19.8	0.24

#### 4.2.5 Elastic properties

The elastic constants are computed with the assumption that the material measured can be described as an isotropic elastic solid, as explained in Hirth and Lothe section 2-4 [58]. This assumption holds since PbTe is cubic and the polycrystal is randomly oriented, as determined from XRD measurement. The bulk modulus is thus given by [145]

$$B = \rho \left( v_L^2 - \frac{4}{3} v_T^2 \right), \quad (4.11)$$

where  $\rho$  is the mass density of the material. It is recommended that this is measured geometrically rather than the Archimedes method which is known to over estimate the materials density. The shear modulus is calculated as

$$\mu = v_T^2 \rho. \quad (4.12)$$

The Young's modulus is calculated as

$$E = \frac{9B\mu}{3B + \mu}. \quad (4.13)$$

The Poisson's ratio is calculated as

$$\nu = \frac{E - 2\mu}{2\mu}. \quad (4.14)$$

Table 4.2 shows elastic properties characterized by ultrasound, bulk density measurements and Eqs. 4.11 to 4.14.

#### Thermal diffusivity and conductivity

Thermal diffusivity was measured using a Netzhc laser flash analysis (LFA) system. The diffusivity measurements,  $D_\kappa$  [m $^2$ s $^{-1}$ ], were combined with the heat capacity of PbTe [103],  $c_p$  [JK $^{-1}$ m $^{-3}$ ] =  $NR\{3.07 + 4.07 \times 10^{-4}(T - 300)\}/M$  (where  $N$  is the number of atoms per primitive unit cell,  $R$  [J K $^{-1}$ mol $^{-1}$ ] is the gas constant, and  $M$  [kg mol $^{-1}$ ] is the molar mass of the primitive unit cell),

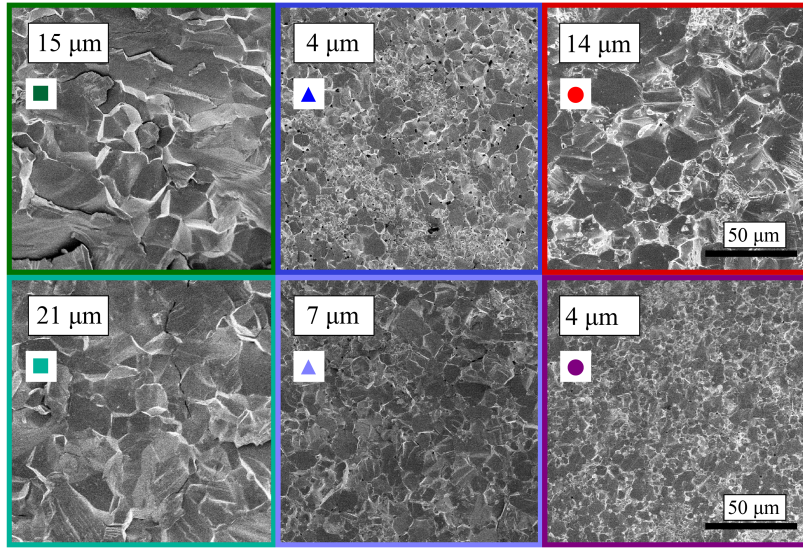


Figure 4.12: Scanning electron microscopy images of fracture surfaces, with the average grain size determined via the linear intercept method indicated. Data points are consistent with Figures 4.5 and S4 of [100], and the scale is the same for all six images. The thermal conductivity measured does not systematically trend with the materials grain size.

and the sample density,  $\rho$  [ $\text{kg m}^{-3}$ ], to calculate the thermal conductivity,  $\kappa = D_\kappa c_p \rho$  [ $\text{W m}^{-1} \text{K}^{-1}$ ]. Electrical conductivity measurements confirmed that the electronic thermal conductivity is less than 1% of  $\kappa$ , so the thermal conductivity measured is essentially equal to the lattice thermal conductivity,  $\kappa \simeq \kappa_L$  (bipolar thermal conduction is negligible in the temperature range considered for undoped PbTe).

### Grain size from SEM

Figure 4.12 shows scanning electron microscopy (SEM) images of three samples, which were used to determine the grain size via the lineal intercept method [146]. The images were obtained on a Hitachi S-4800 in the secondary electron mode, with a beam voltage of 2 kV. This method gives an estimate of the grain size which is accurate to approximately 25%.

### Thermal transport model for nanocrystalline Si

The thermal transport model shown Figure 4.9a is identical to that shown in Figure 2 of Ref. [43] and Figure 8a of Ref. [39] except that the phonon-phonon relaxation time was formulated to maintain its dependence on phonon velocity [72],

$$\frac{1}{\tau_{\text{pp}}(\omega)} = \frac{c_1 \omega^2 T}{v_s^3} e^{-c_2 v_s / T}. \quad (4.15)$$

Table 4.3: Material parameters used in the thermal transport model shown in Figure 4.9a, based on Eqs. 2.22, 2.18, 4.15, and 3.14.

Material Parameter	Value
$c_1$ [m <sup>3</sup> K <sup>-1</sup> s <sup>-2</sup> ]	$5.3 \times 10^{-8}$
$c_2$ [K s m <sup>-1</sup> ]	$2.9 \times 10^{-2}$
Grüneisen parameter, $\gamma$	1
Poisson's ratio, $\nu$	0.27
Volume of per atom, $V$ [Å <sup>3</sup> ]	20
Atoms per primitive unit cell, $N$	2
GB Burger's vector, $b = (VN)^{1/3}$ [Å]	4.07
Characteristic length of GB structure, $D$ [nm]	3
Average grain size [129], $\bar{d} = 3/n_{1d}$ [nm]	42

The coefficients here are related to the coefficients in Ref. [39] as  $C_1 = c_1/v_s^3$  and  $C_2 = c_2 v_s$ . Phonon-grain boundary scattering was included using the relaxation time derived in Ref. [39] which describes a phonon being perturbed by the grain boundary rotation and localized strain field and is given in Eq. 3.14. The total relaxation time is calculated according to Matthiessen's Rule:  $\tau^{-1} = \tau_{pp}^{-1} + \tau_{gbs}^{-1}$ .

The speed of sound for a Si single crystal is slightly different here than that used in Ref. [39] because we are utilizing speeds of sound obtained by low-T heat capacity rather than elastic moduli. Intrinsic phonon-point defects scattering (natural vacancies and isotopes), as well extrinsic point defect scattering due to mass contrast and localized strain fields (P substituted on a Si site) were determined to be negligible [147]. From the measured carrier concentration of the nanocrystalline Si sample [129], the fraction of P on Si sites was only  $f = 0.002$ , and the mass difference and change in atomic radii of P and Si are relatively small. Additionally, phonons scattering on conduction electrons, which mainly effects low frequency phonons, was neglected since the relaxation time of low frequency phonons is already dominated by phonon GB scattering [148]. The material parameters utilized for the model are shown in Table 4.3.

## Chapter 5

### Phonons in complex crystals: beyond the phonon gas model

Thus far we have focused on phonon heat conduction within the phonon-gas channel. However, there is a growing body of theoretical and experimental work which suggests that in amorphous materials the phonon-gas model is incomplete and that contributions from the diffuson channel are important [11, 12, 14]. As we show here the phonon-gas model falls short even in crystalline materials with complex crystal structures.

Due to the open debate regarding the language surrounding vibrational thermal conductivity, phonon and ‘other than phonon’ heat conduction (i.e. propagons, diffusons, and locons), we explicitly state our nomenclature as follows. We refer to phonons as all types of harmonic normal modes of vibration. More explicitly, phonons are solutions to the equation of motion when harmonic interatomic forces are assumed (Eq. 2.15). These phonon eigenstates are often visualized using a phonon band structure (Figure 2.2a). Usually in simple crystals, at a given wavevector  $\mathbf{k}$  the phonon branches (polarizations)  $s$  are sufficiently separated in energy that they don’t interact, even after the lines are broadened due to perturbations such as phonon-phonon interactions (Figure 2.2d). In this case, phonons can be viewed as wave-packets *propogating* at their group velocity  $v_g(\mathbf{ks})$ , carrying an energy  $\hbar\omega(\mathbf{ks})$ . This is the common phonon gas-model, and we will refer to this as phonon conduction through the phonon-gas channel  $\kappa_{ph}$  (Eq. 3.30 of Hardy [11]). However, this is not the only channel through which phonons can conduct heat. If at a given wavevector  $\mathbf{k}$  the phonon branches  $s$  are packed closely together in energy, after broadening the normal modes will overlap in  $\mathbf{k}$ -space and energy and begin to mix. This mixing of normal modes opens up another conduction channel where thermal energy can conduct through a *diffusive* random walk process (Eq. 3.31 of Hardy [11]). Normal modes conducting heat through this channel in harmonic glasses have therefore been termed ‘diffusons’ [10]. We will refer to this as phonon conduction through the diffuson channel  $\kappa_{diff}$ .

## 5.1 Introduction

The foundation for the theory of thermal transport due to atomic vibrations was established in 1963 by Robert J. Hardy [11]. His formulation of the heat current vector,  $j^i$ , is very general and captures all conduction channels for the thermal conductivity due to atomic vibrations  $\kappa_{\text{vib}}$ . One main result of his work is an expression for  $j^i$  which requires only the positions, velocities, and potential energy of all atoms in the system (Eq. 2 of DeAngelis *et al.* [14]). This form of  $j^i$  is commonly implemented with molecular dynamics (MD) simulations and, together with the Green-Kubo formula, gives an expression for the material's thermal conductivity due to atomic vibrations,  $\kappa_{\text{vib}}$  (Eq. 1 of DeAngelis *et al.* [14]). This combination of molecular dynamics, Hardy's expression for  $j^i$ , and the Green-Kubo formula is particularly effective at studying the thermal conductivity of amorphous and defective materials. However, since the results of this methodology comes, in essence, directly from time dependent atomic displacements, velocities, and potential energies, it can be difficult to interpret results, build intuition, and establish materials design principles for amorphous, defective and complex solids. Consequently, this methodology acts more as a computational experiment than a mechanistic model.

There has been considerable progress in analyzing MD results and classifying the nature of heat carrying vibrational modes in a descriptive manner. In the pioneering work of Allen and Feldman [12, 10] the taxonomy of propagons, diffusons, and locons was provided after detailed examination of amorphous silicon simulations. More recently, the method of Green-Kubo modal analysis has been developed which allows one to extract mode specific information contained in a molecular dynamics simulation [149, 150, 14]. These simulations strongly suggest that in amorphous materials, thermal conductivity should be dominated by the diffuson conduction channel, and the phonon-gas model is largely incomplete.

There have been many analytical models proposed for the thermal conductivity of amorphous and disordered materials [151, 131, 152]. Many of them are essentially based on random walk theory, which requires a step distance, attempt frequency, probability of a successful energy transfer, and an amount of heat being transferred during the step. The main difference between models is treatment of the jump distance, and/or the attempt frequency. It seems that these analytical models were attempting to find an expression which captures to behavior of heat conduction through the diffuson channel, as defined in Eq. 2.7.

We approach the same problem, determining limitations of the phonon-gas model, by examining the vibrational properties of complex crystals. In a crystal, there are always 3 acoustic phonon branches and  $3(N - 1)$  optical branches, where  $N$  is the number of atoms in the primitive unit cell. Here, we define an acoustic branch as one whose energy goes to zero,  $\hbar\omega \rightarrow 0$ , as the magnitude of its wavevector goes to zero,  $k \rightarrow 0$ , and an optical branch is one that has non-zero energy as

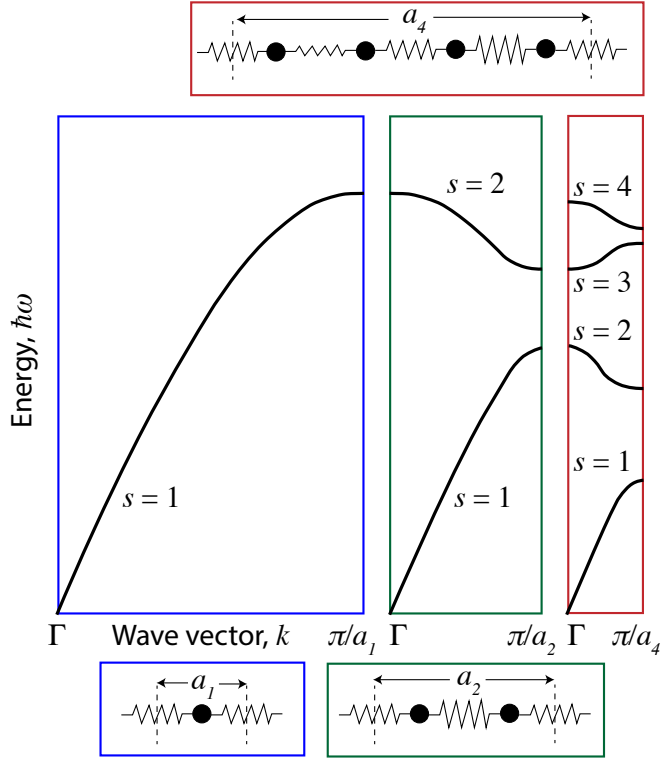


Figure 5.1: Brillouin zone folding promotes phonon conduction through the diffuson channel. Schematic illustration of the folding of one phonon branch when the number of atoms per unit cell is increased from one to two and four. A commonly cited effect of zone folding is that it reduces the average phonon group velocity,  $v_g = d\omega/dk$ , of the phonon-gas channel. However, when the diffuson conduction channel is considered, in addition to the phonon-gas, one recognizes that zone folding increases the number of branches  $s$  and decreases their energy separation. Upon the broadening of these phonon branches this will promote normal mode mixing, and in turn increase thermal conduction through the diffuson channel.

$k \rightarrow 0$ . The rule stated above, which governs the number of acoustic and optical phonon branches can be understood through the concept of Brillouin zone folding which is schematically illustrated in Figure 5.1. For simplicity we show the one dimensional case which has 1 acoustic and  $N - 1$  optical branches. When considering only the phonon-gas conduction channel (Eq. 2.5), the primary effect of zone folding is a reduction of the phonon group velocity  $v_g$ , aside from any phonon scattering phase space effects. However, as discussed in Chapter 2.1 (Eqs. 2.5 and 2.7) the phonon-gas channel is not the only avenue in which phonons can conduct heat. Additionally, when the phonon modes become very close, or overlap, in energy and  $\mathbf{k}$ -space they can conduct heat diffusely through a normal mode mixing (tunneling) processes. In a perfectly harmonic solid, we typically think of phonon modes as non-interacting (though this isn't explicitly true when the material is under a temperature gradient [12]). Mathematically this can be expressed as  $\epsilon_i^\alpha(\mathbf{ks})\epsilon_i^\alpha(\mathbf{ks}') = 0$  for  $s \neq s'$ , where  $\epsilon_i^\alpha(\mathbf{ks})$  is the

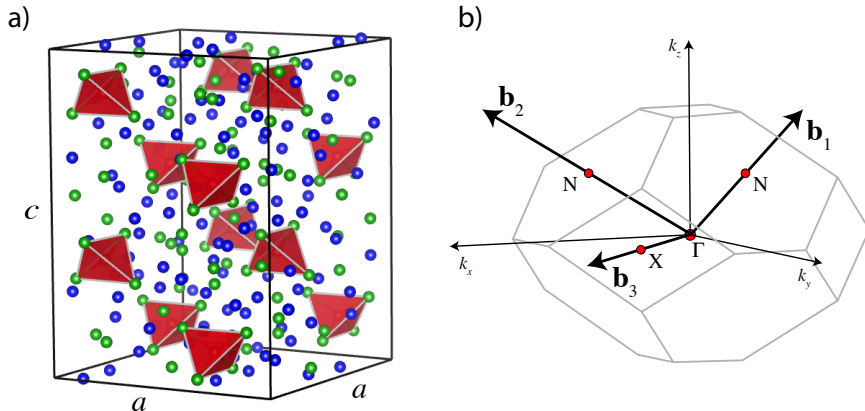


Figure 5.2: a) The body centered  $\text{Yb}_{14}MSb_{11}$  tetrahedral crystal structure containing 208 atoms ( $I4_1/acd$ , no. 142). There are 104 in the primitive unit cell. Yb is shown in blue, Sb in green and  $M = \text{Mn}, \text{Mg}$  are contained in the red  $\text{Sb}_4$  tetrahedra. b) The reciprocal lattice and first Brillouin zone. The harmonic vibrational band structure is shown along the  $\Gamma - \text{N}$  and  $\Gamma - \text{X}$  high symmetry lines.

eigenvector of phonon mode  $\mathbf{k}s$  (Eq. B.0.11). However, anharmonicity will broaden the phonon line widths causing modes that are not necessarily orthogonal to overlap. In most simple crystals this effect is negligible because non-orthogonal phonon modes are typically spaced in energy such that they do not mix, even after anharmonic broadening. However, in complex crystals and amorphous materials non-orthogonal modes can lie close together in energy resulting in a non-negligible amount of normal mode mixing after anharmonic line broadening, resulting in heat conduction through the diffuson channel. In practice, when this model is implemented computationally the phonon modes, which are theoretically  $\delta$ -functions in energy, must be given some width regardless of anharmonicity being included or not. Allen, Feldman *et al.* achieve this by utilizing a Lorentzian peak with a width of 0.043 meV (10 GHz) which is larger than the typical inter-mode spacing ( $\omega(\mathbf{k}s) - \omega(\mathbf{k}s')$  where  $s' = s \pm 1$ ) [12, 153]. If there is no means to transfer thermal energy between phonon eigenstates, local thermodynamic equilibrium can not be achieved, and temperature and therefore a thermal conductivity (as defined through Fourier's law) cannot be defined.

The  $\text{Yb}_{14}MSb_{11}$  system where  $M = \text{Mg}, \text{Mn}$  is a prime candidate to study normal mode mixing and non-phonon-gas type thermal conduction, due to its very complex crystal structure with 104 atoms per primitive unit cell (Figure 5.2a). Additionally, there are detailed studies of the vibrational thermal conductivity, which show a very low magnitude of 1 W/mK near room temperature and a unique temperature dependence for crystalline materials [154, 155, 156]. In crystalline materials around room temperature if the phonon-gas channel dominates one would expect a  $\kappa_{\text{vib}} \propto 1/T$  temperature dependence, however in the  $\text{Yb}_{14}MSb_{11}$  system  $\kappa_{\text{vib}}$  is approximately T-independent which one might suspect is due to a  $\kappa_{\text{diff}}$ -dominated thermal conductivity. This system has a very complex crystal structure with 104 atoms in its primitive unit cell . Additionally, its has a

low vibrational thermal conductivity with a very unusual temperature dependence for crystalline materials.

The  $\text{Yb}_{14}\text{MSb}_{11}$  material system has a high thermoelectric figure of merit and is being considered by NASA-JPL for next generation radio-isotope thermoelectric generators for space exploration [154]. Additionally, this system is a rare case of a dilute ferromagnetic semiconductor making it of potential interest to spintronic technologies [157].

Here, we compare DFT-based lattice dynamics simulations and inelastic neutron scattering experiments which suggest that heat conduction in this system should indeed have a considerable contribution from the diffuson channel. In doing so we provide an intuitive physical picture for diffuson conduction which is important for material's design of complex, amorphous and highly defective systems.

## 5.2 Methods

### 5.2.1 Computational methods

The computation of harmonic interatomic force constants was executed<sup>1</sup> using density functional theory (DFT) in the Vienna Ab initio Simulation Package (VASP) and Phonopy. First, the optimization of the electronic and ionic structures of  $\text{Yb}_{14}\text{MgSb}_{11}$  and  $\text{Yb}_{14}\text{MnSb}_{11}$  were performed with periodic DFT in VASP [158] with strict convergence criteria. For electronic and structural optimization, a criterion of  $\Delta E < 10^{-7}$  and  $\Delta E < 10^{-5}$  eV per cell was used, respectively. The projector augmented-wave method [159] with a plane-wave cutoff of 520 eV and the Perdew–Burke–Ernzerhof (PBE) functional were used during these calculations [160]. Furthermore, the optimizations of the primitive unit cells were performed with a 4x4x4 k-point mesh. Since Mn in this structure is expected to exhibit magnetic properties, we utilized a ferromagnetic model for  $\text{Yb}_{14}\text{MnSb}_{11}$  during the optimization with magnetic moments on all Mn atoms in the primitive unit cell.

Once the optimized ionic and electronic stuctures were obtained, the harmonic interatomic force constants (IFCs) were computed using the finite displacement method as implemented in Phonopy [161, 162]<sup>2</sup>, with a displacement of 0.01 Å and with the help of the conventional cell as the supercell. The forces for this evaluation were calculated at the  $\Gamma$ -point. Again, a ferromagnetic model was used for  $\text{Yb}_{14}\text{MnSb}_{11}$ .

These harmonic IFCs were implemented in a lattice dynamical approach (Appendix B) to obtain the phonon band structure. For the computation of the vibrational density of states, an 8x8x8 uniform

---

<sup>1</sup>DFT obtained harmonic IFCs were provided by J. George and G. Hautier of Université catholique de Louvain. Post-DFT computations were conducted by the author.

<sup>2</sup><https://atztogo.github.io/phonopy/>

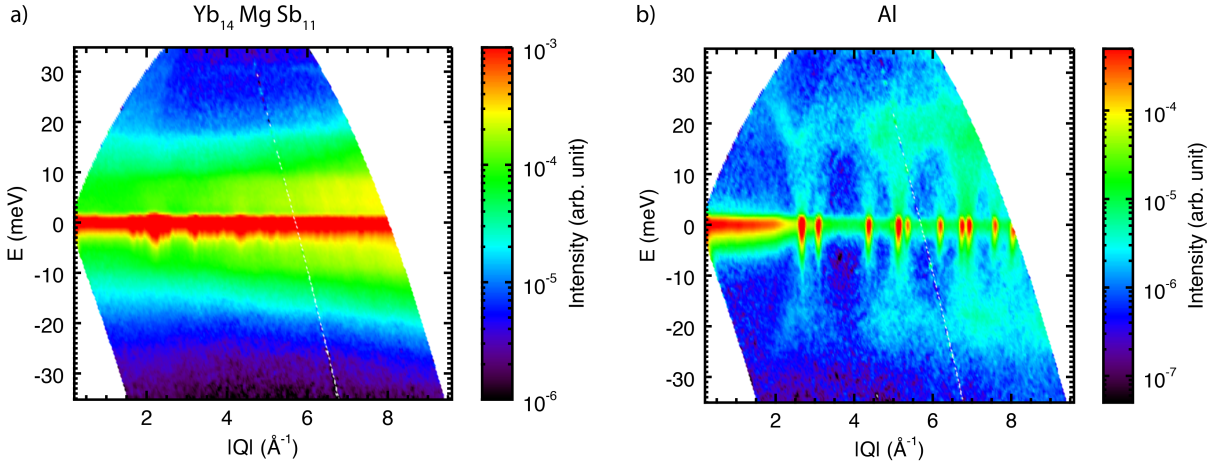


Figure 5.3: The dynamic structure factor (scattering function) shown as a function the magnitude of the scattering wave-vector ( $|\mathbf{Q}|$ ) and energy ( $E$ ),  $S(|\mathbf{Q}|, E)$ . Polycrystalline samples of  $\text{Yb}_{14}\text{MgSb}_{11}$  with 104 atoms per primitive unit cell, and Al with one atom per primitive unit cell are shown for comparison. In polycrystalline Al, clear phonon branches are observed that originate from the diffraction peaks at  $E = 0$  meV. These isolated phonon branches are not easily observed in  $\text{Yb}_{14}\text{MgSb}_{11}$ , and through this qualitative comparison one may suspect that the character of atomic vibrations in  $\text{Yb}_{14}\text{MgSb}_{11}$  is not consistent with the phonon-gas picture. The isolated and distinguished branches in Al indicate that the phonon-gas picture holds.

$\mathbf{k}$ -mesh and the tetrahedron method was used to approximate the integration over the Brillouin zone. Additionally, the DOS was convoluted with a 1.5 meV full width half max Gaussian function which is consistent with the instrument resolution of the inelastic neutron scattering experiments.

### 5.2.2 Synthesis

Cylindrical pellets of polycrystalline  $\text{Yb}_{14}\text{MgSb}_{11}$  and  $\text{Yb}_{14}\text{MnSb}_{11}$  with final dimensions of approximately 12 mm in diameter and 15 mm in height were synthesized as follows. Raw elements were weighed in stoichiometric amounts in an Ar filled glove box and sealed in a ball mill vial. High purity Mn, Mg, and Sb were used as received from suppliers. However, the Yb was arc melted five times to further purify it prior to synthesis. This step was critical to achieve phase pure samples. These raw elements were ball milled together for 5 hours, re-mixing the constituents in the glove box every hour. The resulting powder was pressed at 900 C for 20 minutes under 45 MPa of pressure in a uniaxial hot press.

### 5.2.3 Inelastic neutron scattering

Inelastic neutron scattering experiments were conducted on the ARCS spectrometer at the Spallation Neutron Source (SNS), with incident neutron energies of 45 meV and a sample temperature of 300 K. The samples were dense polycrystalline cylindrical pellets approximately 12 mm in diameter and 15 mm in height. All data are first represented as a function of neutron energy transfer,  $E$ , and momentum transfer,  $|\mathbf{Q}|$ , where  $|\mathbf{Q}| = 4\pi \sin(\theta)/\lambda$ , where  $\theta$  is the scattering angle and  $\lambda$  is the neutron wavelength. The energy resolution is approximately 1.5 meV. An example of the scattering function (dynamic structure factor)  $S(|\mathbf{Q}|, E)$  data obtained via the program Mslice in the Data Analysis and Visualization Environment (DAVE) [163] is shown in Figure 5.3. Due primarily to the large neutron scattering cross-section of Yb, neutron absorption corrections were included in the analysis as implemented by Mslice. This data was used to compute the vibrational density of state by first integrating  $S(|\mathbf{Q}|, E)$  from  $|\mathbf{Q}| = 4$  to  $8 \text{ \AA}^{-1}$ , obtaining  $S(E)$ . Data at the highest scattering angles, from 120 to 136° were masked and data above 36 meV were removed to avoid any instrument related artifacts in  $S(|\mathbf{Q}|, E)$ . The background was subtracted from  $S(E)$  and the data was converted from arbitrary units to counts by recognizing that the intensity and error bars obtained from Mslice are  $An$  and  $A\sqrt{n}$ , where  $n$  is counts and  $A$  is an arbitrary scaling factor. After these corrections,  $S(E)$  was converted to the vibrational density of state  $g(E)$  by removing the elastic scattering peak and multi-phonon contributions in the program isdos10.

## 5.3 Results and discussion

The phonon band structures of  $\text{Yb}_{14}\text{MgSb}_{11}$  and  $\text{Yb}_{14}\text{MnSb}_{11}$ , obtained from DFT based lattice dynamics are shown in Figure 5.4. The many crossing points and close proximity of bands suggests that there should indeed be a significant diffuson channel contribution to  $\kappa_{\text{vib}}$ . Here, we examine the computed vibration density of states and compare this to inelastic neutron scattering data.

The atom projected and total vibrational density of states (DOS) are shown next to the band structures which have been convoluted with a 1.5 meV Gaussian which is consistent with the instrument broadening observed in the inelastic neutron scattering experiments. Starting at the top,  $\text{Yb}_{14}\text{MgSb}_{11}$  is expected to have very flat high energy optical modes at around 30 meV, which are dominated by Mg character with a small amount of Sb character. This can be attributed to the Mg atoms oscillating within their  $\text{Sb}_4$  tetrahedron cage at a high frequency with little interaction with the rest of the atoms. The same type of behavior is expect in  $\text{Yb}_{14}\text{MnSb}_{11}$ , except for a shift in energy to around 23 meV and the modes have been split in energy due to the ferromagnetic properties of the Mn atom. Between approximately 3 and 17 meV, there are expected to be many flat optical modes spaced very closely in energy. The modes of lower energy are dominated by Yb

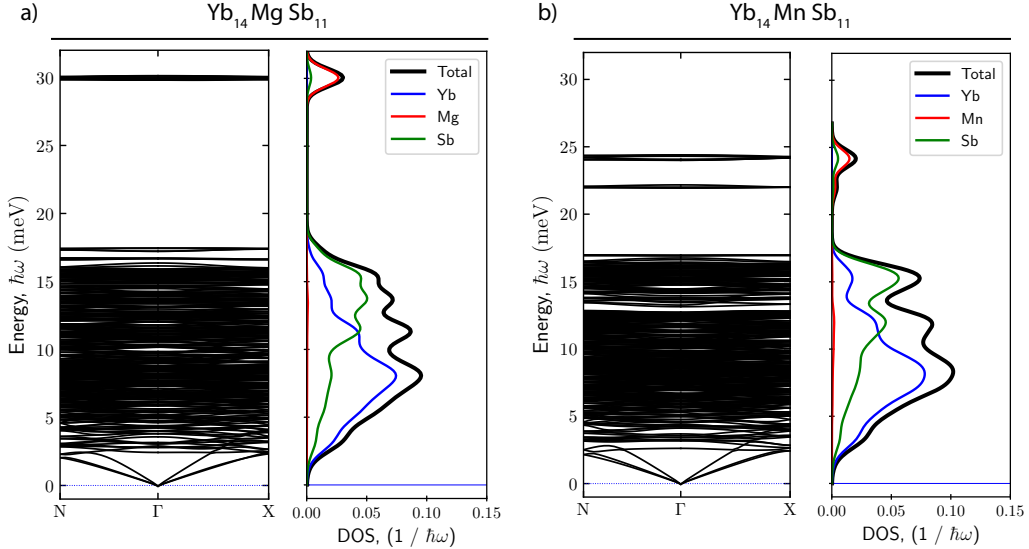


Figure 5.4: The phonon band structure, and vibrational density of states (DOS) computed from DFT-based lattice dynamics for a)  $\text{Yb}_{14}\text{MgSb}_{11}$  and b)  $\text{Yb}_{14}\text{MnSb}_{11}$ . For the DOS, an  $8 \times 8 \times 8$  uniform  $\mathbf{k}$ -mesh and the tetrahedron method was used to approximate the integration over the Brillouin zone. Additionally the DOS was convoluted with a 1.5 meV full width half max Gaussian function which is consistent with the instrument resolution seen in the inelastic neutron experiments.

character and the modes near 17 meV are dominated by Sb character, which may have been expected from atomic mass considerations. The number of optical branches can be expected from the concept of zone folding shown in Figure 5.1. With 104 atoms per primitive unit cell,  $\text{Yb}_{14}\text{MSb}_{11}$  has 309 optical modes. What may not have been obvious without the DFT-based lattice dynamics simulations is their close proximity in energy, which as we discuss above is important for diffuson channel conduction. Finally, the acoustic modes (as defined in this context) only extend up to 2.5 to 3 meV.

These results are now compared to inelastic neutron scattering. However, before a direct comparison can be made the atom projected density of states ( $g_i(E)$ ) must be weighted by their neutron scattering strength, resulting in the neutron weighted density of states

$$g_{n^0}(E) = \frac{\sum_i N_i(\sigma_i/M_i) g_i(E)}{\sum_i N_i(\sigma_i/M_i)}. \quad (5.1)$$

where  $N_i$  is the number of atom of species  $i$  in the formula unit,  $\sigma_i$  is its neutron scattering cross-section, and  $M_i$  is its atomic mass. The results of this comparison are shown in Figure 5.5. The experimental data and computational predictions are normalized and the energy axis is scaled for direct comparison. The shift in energy is expected due to the use of the PBE functional which is known to slightly over estimate lattice parameters and slightly under-estimate elastic moduli and

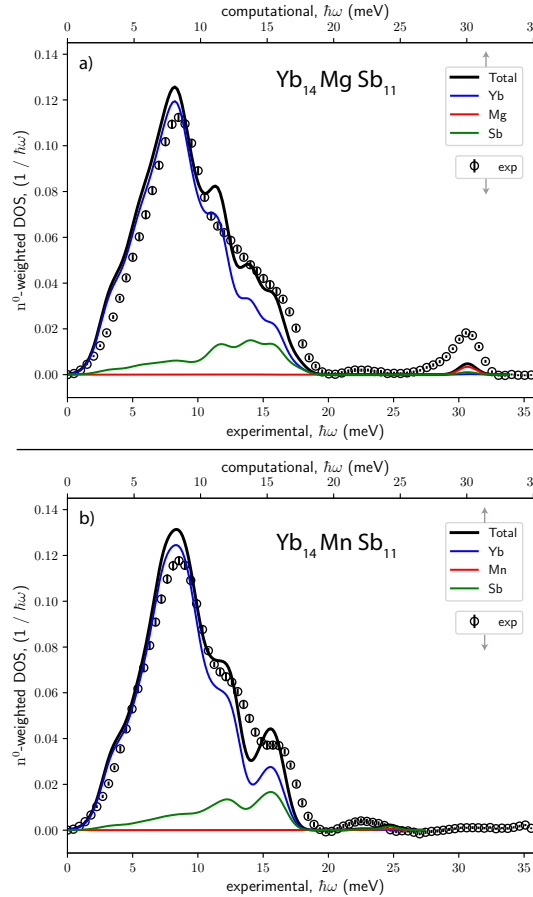


Figure 5.5: Neutron weighted density of states in a)  $\text{Yb}_{14}\text{MgSb}_{11}$  and b)  $\text{Yb}_{14}\text{MnSb}_{11}$  measured via inelastic neutron scattering at 300K on the ARCS spectrometer at the SNS. The experimental data and computational predictions have been normalized and the energy axis has been shifted for comparison. The computation predictions shown here are based on the results shown in Figure 5.4. As can be seen the simulations agree well experimental results, particularly for phonon modes below 20 meV.

vibrational mode energy. We also note that temperature was not included in the lattice dynamics simulations and the experimental data was taken at 300 K. The standard error for the experimental data is shown by the error bars, which is equal to or smaller than the data point size. The data agree well with the computational prediction, especially below 20 meV. In particular we note the agreement in the magnitude and shape of the peak at around 8 meV and modes higher in energy. While the Mg peak seems to be stronger than the prediction, the relative position in energy seems to be well represented. The position of the Mn peaks is approximately 2.5 meV lower in energy than the prediction, which is presumably related to the ferromagnetic model used. Regardless, of these relatively minor discrepancies we believe this result supports the computational results. The density of states analysis lends confidence in the band structure results shown in Figure 5.4, which suggest

that the dense optical modes between 3 meV and 17 meV will exhibit significant heat conduction through the diffuson conduction channel. The typical energy spacing between the optical phonon modes is on the order of 0.05 meV meaning that significant normal mode mixing after anharmonic broadening is expected, which will enable heat conduction through the diffuson conduction channel.

In some cases, materials can behave qualitatively differently in terms of crystallographic and vibrational properties. We conclude that in complex crystalline materials with many atoms per unit cell, the phonon-gas model alone is not expected to fully explain the thermal properties. After examining the vibrational properties of the  $\text{Yb}_{14}MS\text{b}_{11}$  system in detail by computational and experimental methods, we suggest that phonon band proximity should be used as a metric to predict the importance of the diffuson conduction channel. This provides a simple and useful material design metric which can be used to predict the breakdown of the phonon-gas model, and the transition from crystalline-like (phonon-gas channel) to amorphous-like (diffuson channel) heat conduction.

## Chapter 6

### Optimizing thermoelectric transport of CoSb<sub>3</sub> through the controlled use of defects

The previous chapters in this thesis have focused on the materials physics of heat conduction in defective and complex crystals. The materials systems examined were treated mainly as case studies to test our understanding of underlying physical mechanisms. This chapter contains a more applied materials design strategy, where thermal and electrical transport of the CoSb<sub>3</sub> Skutterudite system is optimized by the controlled use of defects. Skutterudites are one of the most promising material systems for TE power generation applications in the intermediate temperature range of 600–800 K, which is a common temperature for industrial and automotive waste heat sources.

Skutterudite materials have a crystal structure built up of CoSb<sub>6</sub> octahedra and Sb<sub>4</sub> rings which together form a caged structure as shown in Figure 6.1. In addition they are semiconductors which can be doped in a controlled manner, often by filling the Sb-icosahedron cages. For a more in-depth structural discussion, the reader is referred to a review by Uher [164]. In brief, Sb forms polyanionic Sb<sub>4</sub> rings. Using a Zintl description, each Sb has a formal charge of -1 forming two covalent bonds and giving the ring a formal charge of Sb<sub>4</sub><sup>4-</sup>. The Sb<sub>4</sub> ring is not necessarily a square, having two longer and two shorter bonds of a rectangle. The remaining two Sb lone pairs coordinate to Co<sup>3+</sup> to form CoSb<sub>6</sub> octahedra. These octahedra either share their vertices via one Sb atom or via one bond of the Sb<sub>4</sub> ring.

The vibrational and thermal properties of CoSb<sub>3</sub> have received much attention. The relatively complex crystal structure is effective at scattering high frequency phonons, which along with the relatively low speed of sound (average speed of sound of approx. 2900 m/s) results in CoSb<sub>3</sub> having low intrinsic vibrational thermal conductivity. Additionally, filling the cage is known to result in a profound reduction in  $\kappa_{\text{ph}}$ . Further reduction of thermal conductivity requires grain boundary engineering beyond simply reducing the grain size. In Section 6.1 it is experimentally demonstrated that modifying n and p type CoSb<sub>3</sub> grain boundaries with graphene dramatically increases thermal

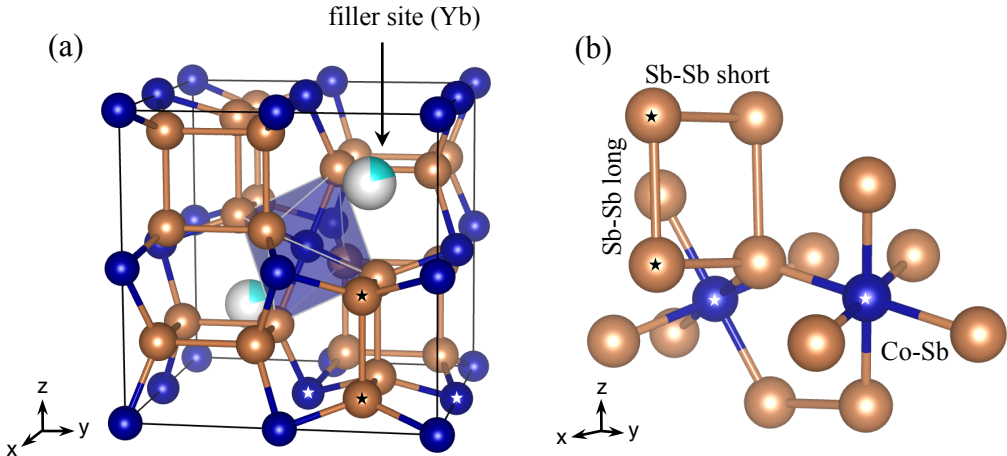


Figure 6.1: Structural representation of Yb-filled CoSb<sub>3</sub> (shown with the origin shifted by -1/4[111]) with Co in blue, Sb atoms in gold, and Yb atoms (filler) in light blue. Sb forms Sb<sub>4</sub> rings that coordinate to Co. (b) Structural motif of CoSb<sub>3</sub>. Two octahedra share either one Sb or an edge of an Sb-Sb ring. Star labeled atoms represent the motif (b) in context within the structure (a).

boundary resistance with negligible effects on electric transport, resulting in improved  $zT$  and device conversion efficiency.

N-type CoSb<sub>3</sub> is known to exhibit superb electrical transport and high TE power factors ( $\sigma\alpha^2$ ). While this material has a long history, it has only recently been shown that its high power factor stems from a complex electronic band structure resulting in a Fermi surface with many valleys at high doping [165]. In Section 6.2, we reveal that this complex electronic band structure arises from the unique bonding chemistry in CoSb<sub>3</sub>. Additionally, extrinsic doping with point defects is shown to promote the convergence of the many valleys in the electronic band structure which promotes thermoelectric power factor.

## 6.1 Graphene modified grain boundary complexions<sup>1</sup>

The reduction of lattice thermal conductivity by grain boundary engineering, without deterioration of electron transport, is an effective strategy to increase thermoelectric efficiency. Grain boundaries add additional degrees of freedom when engineering materials; their structure and chemical composition become critically important when explaining a materials transport properties. We show here that not all grain boundaries are the same, and not only can one engineer grain size but also orientation and coherency of the interfaces. Even more possibilities arise as one considers that the grain boundary region, or complexion, can also be modified with impurity atoms. Being only a single

<sup>1</sup>The content in this section was published by Zong\* and Hanus\* *et al.* in Ref. [166] (\* contributed equally).

atomic layer, graphene (or another two-dimensional material) that coats or wraps grains can modify grain boundary complexions in ways fundamentally different than traditional grain boundary phases.

Here, we show that reduced graphene oxide (rGO) increases the grain boundary thermal resistivity by a factor of 3 to 5 compared to grain boundaries without graphene. Wrapping even micron sized grains with graphene leads to such a significant reduction in the thermal conductivity that a high thermoelectric figure of merit  $zT = 1.5$  was realized in n-type  $\text{Yb}_y\text{Co}_4\text{Sb}_{12}$ , while a  $zT$  of 1.06 was achieved in p-type  $\text{Ce}_y\text{Fe}_3\text{CoSb}_{12}$ . A 16 leg thermoelectric module was made by using n- and p-type skutterudite-graphene nanocomposite that exhibited conversion efficiency 24% higher than a module made without graphene. Engineering grain boundary complexions with 2-D materials introduces a new strategy for advanced thermoelectric materials.

### 6.1.1 Material synthesis

$\text{CoSb}_3$  based skutterudite materials with rGO modified grain boundary complexions were synthesized by a solution based powder processing procedure, followed by densification into sample pellets using spark plasma sintering (SPS). We provide a general description of the procedure used to produce both n- and p-type material and refer the reader to Refs. [167] (n) and [166] (p) for further details.

The composition of the p-type material is  $\text{Ce}_{0.85}\text{Fe}_3\text{CoSb}_{12}/y$ , where  $y$  represents the vol% of rGO ( $y = 0, 0.56, 1.4, 2.8$ ). The composition of the n-type samples is  $\text{Yb}_{0.27}\text{Co}_4\text{Sb}_{12}/y$  vol% rGO ( $y = 0, 0.72, 1.8, 3.6$ ). High purity elements were used as raw material, which were stoichiometrically weighed in an Ar atmosphere glove box and sealed in carbon coated quartz tubes. The sealed quartz tubes were then heated to 1373 K and held for 24 h and quenched followed by a 7 day anneal at 923 K. The obtained ingots were crushed into fine powders. Purified natural graphite (SP-1, Bay Carbon) was used to synthesize graphene oxide (GO) according to the improved Hummers method. Next, 1.5 g of powder was dispersed in 200 ml deionized water, then added with 0.05 mg/ml GO water suspension solution dropwise, followed by ultrasonic mixing for 30 min. The mixture then underwent vacuum filtering and drying at 363 K in Ar-5 vol%  $\text{H}_2$  gas flow for 4 h. The resultant material was regrinded into fine powder. The composite powders were then loaded into a graphite die and consolidated by spark plasma sintering (Sumitomo SPS-2040) in vacuum at 873 K for 15 minutes under a pressure of 55 MPa, yielding fully densified bulk disk-shaped samples.

### 6.1.2 Structural characterization

Powder X-ray diffraction patterns of the rGO-wrapped samples at room temperature are indexed on the  $\text{CoSb}_3$  structure with no rGO or other impurity phase observed within detectability limits

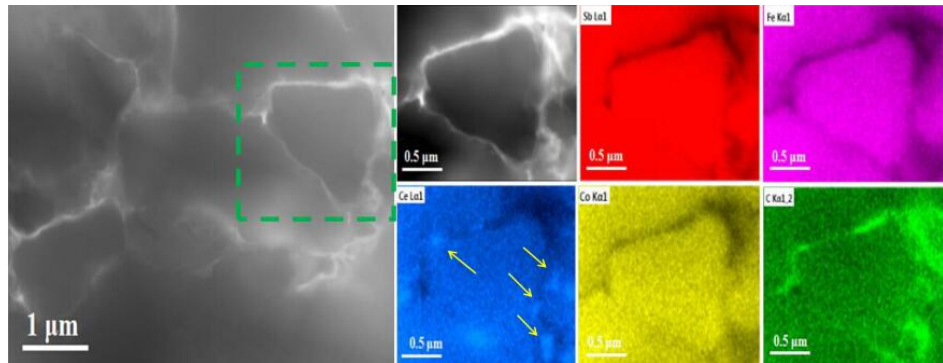


Figure 6.2: High angle annular dark-field, scanning transmission electron microscopy (HAADF-STEM) image of the p-type  $\text{Ce}_{0.85}\text{Fe}_3\text{CoSb}_{12}/0.56$  vol% rGO sample. Right Insets: local energy spectrum analysis for Sb, Fe, Ce, Co and C respectively.

(see Figure S1 of [166]). Raman spectroscopy analysis before and after the SPS procedure shows an increase in the average size of carbon  $\text{sp}^2$  domains, indicating an *in-situ* reduction form GO to rGO during the SPS procedure (see Figure S2 of [166]). To obtain relatively high resolution composition data, high angle annular dark-field scanning transmission electron microscopy was conducted on the rGO wrapped skutterudite samples. Figure 6.2 show the results for the  $\text{Ce}_{0.85}\text{Fe}_3\text{CoSb}_{12}/0.56$  sample and reveals that the rGO was indeed incorporated into the grain boundaries. The yellow arrows in the Ce local energy spectrum show Ce rich precipitates. This observation along with electron energy dispersive X-ray spectroscopy (EDS) analysis (Figure S6 of [166]) indicates that the oxygen from the GO likely reacts with Ce during the SPS process forming  $\text{CeO}_2$  precipitates.

In another study by Tang, Hanus *et al.* the solubility limits of Ce in  $\text{CoSb}_3$  are examined by experimental phase boundary mapping [168]. To validate the bulk composition within the grains of the polycrystalline samples, a nano-tip sample was extracted which contained a grain boundary for atom probe tomography (APT) analysis. The  $\sim 100$  nm diameter needle-like sample was prepared using a dual-beam focused-ion ( $\text{Ga}^+$ ) beam microscope (FEI Helios Nanolab) equipped with a micromanipulator (similar to the lift-out method) [169]. APT experiments were conducted on a Cameca LEAP-4000X Si equipped with a picosecond ultraviolet laser (wavelength 355 nm). Futher details on the sample preparation and exmpmental procedure can be found in Ref. [168]. APT has the unique capability of determining the precise composition at a nm scale resolution. Figure 6.3 reveals that in Ce filled  $\text{CoSb}_3$ , Ce atoms accumulate at the grain boundaries. This APT observation, along with the HAADF-STEM observations in Figure 6.2 (yellow arrows), suggests that excess Ce at the grain boundaries reacts with the O during the reduction of GO to rGO, forming  $\text{CeO}_2$  nanoprecipitates.

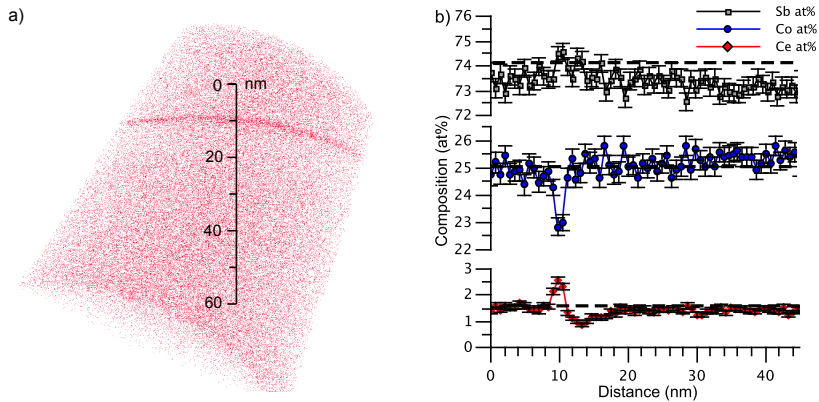


Figure 6.3: Atom probe tomography (APT) analysis of the most heavily doped sample  $\text{Ce}_{0.2}\text{Co}_4\text{Sb}_{12}$ . (a) 3D reconstruction of microtip containing a grain boundary. Ce atoms are displayed in red; Sb and Co atoms omitted for clarity. (b) Concentration profile across the grain boundary and in the grain. The black dashed lines show values measured by electron probe micro analysis (EPMA), and the error bars represent the standard error,  $\sqrt{c(1 - c)/n}$ , where  $c$  is the concentration and  $n$  is the number of atoms detected in each data point bin.

### 6.1.3 Electric transport

The electrical conductivities ( $\sigma$ ) of samples containing small amounts of rGO ( $y = 0.56$  and  $1.4$  for p-type and  $y = 0.72$  for n-type) are only slightly decreased (Fig. 6.4) compared to the samples without graphene, indicating that thin layers of rGO (and potentially  $\text{CeO}_2$  precipitates) at grain boundaries have minimal effect on electronic properties. This minimal effect on charge carrier mobility ( $\mu$ ) is confirmed in Fig. 6.4b. Further increasing the rGO content leads to more noticeable reduction in mobility when rGO content reaches 2.8 vol%. Likewise, the Seebeck coefficients ( $S$ ) and power factors ( $PF = \sigma S^2$ ) as a function of temperature (Fig. 6.4) are essentially unchanged for small contents of rGO. This is consistent with Hall effect measurements (Table S1 of Ref. [166]). The p-type  $\text{Ce}_{0.85}\text{Fe}_3\text{CoSb}_{12}$  shows only a slight increase in hole concentration, which should result from the generation of the small amount of  $\text{CeO}_2$  nano-precipitates.

### 6.1.4 Thermal transport

In order to determine the effect of the three-dimensional rGO network, a phenomenological model for thermal conduction in these composite systems was constructed. This model was used to extract a metric capturing the ensemble average interfacial thermal resistance,  $R_\kappa$ , for materials without rGO and those containing an rGO network.

The total thermal conductivity ( $\kappa$ ) contains contributions from charge carriers through electronic ( $\kappa_e$ ) and bipolar ( $\kappa_{BP}$ ) conduction, and from atomic vibrations which we assume here to be dom-

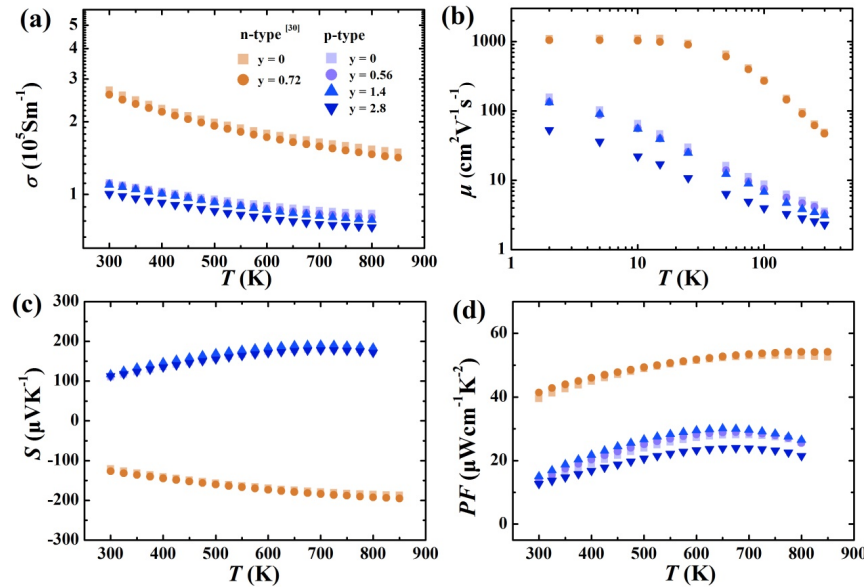


Figure 6.4: Temperature dependence of the (a) electrical conductivity, (b) carrier mobility, (c) Seebeck coefficients, (d) power factors of p-type  $\text{Ce}_{0.85}\text{Fe}_3\text{CoSb}_{12}/y$  vol% rGO samples ( $y = 0, 0.56, 1.4, 2.8$ ) and n-type  $\text{Yb}_{0.27}\text{Co}_4\text{Sb}_{12}/y$  vol% samples ( $y = 0, 0.72$ ) from Ref. [167]

inated by phonons (which here is denoted as  $\kappa_{\text{lat}}$  instead of  $\kappa_{\text{ph}}$ ), whereby,  $\kappa = \kappa_e + \kappa_{\text{BP}} + \kappa_{\text{lat}}$ . We use room temperature data to extract  $R_\kappa$  where  $\kappa_{\text{BP}}$  is negligible. The Wiedemann–Franz law is used to compute  $\kappa_e = L\sigma T$ , with experimental  $\sigma$  values and  $L = 2 \times 10^{-8} \text{ W}\Omega\text{K}^{-2}$ . Using this procedure we measure the vibrational thermal conductivity  $\kappa_{\text{lat}}$  of the composite system which we denote more explicitly as  $\kappa_{\text{comp}}$ . This contains thermal conductivity through the bulk grain  $\kappa_{\text{bulk}}$  as well as the boundary resistance  $R_\kappa = 1/h_B$ , where  $h_B$  is the interfacial thermal conductance. We think of  $R_\kappa$  as including all aspects of the GB complexion for transport perpendicular to the interface including effects between the skutterudite and graphene (interface effects) as well as thermal resistance across the graphene. Below we present a simple thermal circuit model for extracting  $R_\kappa$ . More characterization on this GB complexion (e.g. thermal transport across single GBs) would be required justify a more detailed, mechanistic model.

First, we establish  $R_\kappa$  for regular  $\text{CoSb}_3$  GBs, both n- and p-type. The bulk thermal conductivity  $\kappa_{\text{bulk}}$  is fit empirically along with a constant  $R_\kappa$  for samples without graphene of various grain sizes. This  $\kappa_{\text{bulk}}$  will then include all the relevant phonon-phonon, electron-phonon, point defect scattering processes, and potentially a contribution from the diffuson conduction channel. The complex crystal structure and the presence of rattling interstitial point defects prevent a more sophisticated model for  $\kappa_{\text{bulk}}$ . Here, we use a model of cubic grains with edge length  $\bar{d}$  where the linear density of interfaces is the inverse of the average grain size,  $1/\bar{d}$ . The method used here for determining  $R_\kappa$  is similar to that used in by Yang *et al.* on yttria-stabilized zirconia (see Eq. 5 in Ref. [112]). The

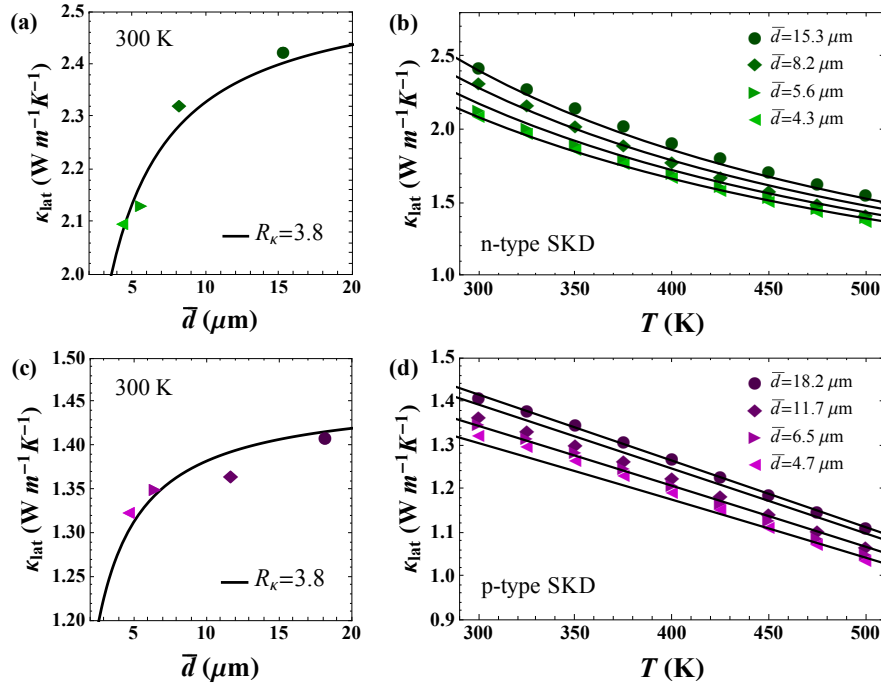


Figure 6.5: Determination of interfacial thermal resistance ( $R_\kappa$ ) from grain boundaries in polycrystalline skutterudite samples (without rGO). The uncertainty in the grain-size is 20%. (a) and (c) show room temperature lattice thermal conductivity with varying grain size.  $R_\kappa$  is in units of  $10^{-7}\text{ m}^2\text{K W}^{-1}$ ; (b) and (d) show  $\kappa_{\text{lat}}$  with temperature for n and p-type skutterudite samples. Lines in all figures are calculated from Eq. 6.1.

lattice thermal conductivity of polycrystalline samples is then fit to

$$\kappa_{\text{poly}}^{-1} = \kappa_{\text{bulk}}^{-1} + R_\kappa/\bar{d}. \quad (6.1)$$

Fig. 6.5 shows the results of modeling the grain size dependent data sets. As can be seen in Fig. 6.5a and c, n-type and p-type skutterudite materials in this study have the same value of  $R_\kappa = 3.8 \times 10^{-7}\text{ m}^2\text{K W}^{-1}$  (without graphene) as could be expected from similarities in crystal structure, chemical species, and processing methods.

For the system with multi-layer graphene, thermal transport through the in-plane direction of the graphene layer of thickness,  $t$ , must be included due to the high thermal conductivity of graphite:  $5\text{ W m}^{-1}\text{K}^{-1}$  in the c-direction and  $2000\text{ W m}^{-1}\text{K}^{-1}$  in the a and b-directions at  $300\text{ K}$  [170].

Using the parallel conductance model depicted in Fig. 6.6a the thermal conductivity of the composite system, for  $t \ll \bar{d}$ , is given by

$$\kappa_{\text{comp}} = \kappa_{\text{poly}} + \frac{2t}{\bar{d}}\kappa_g. \quad (6.2)$$

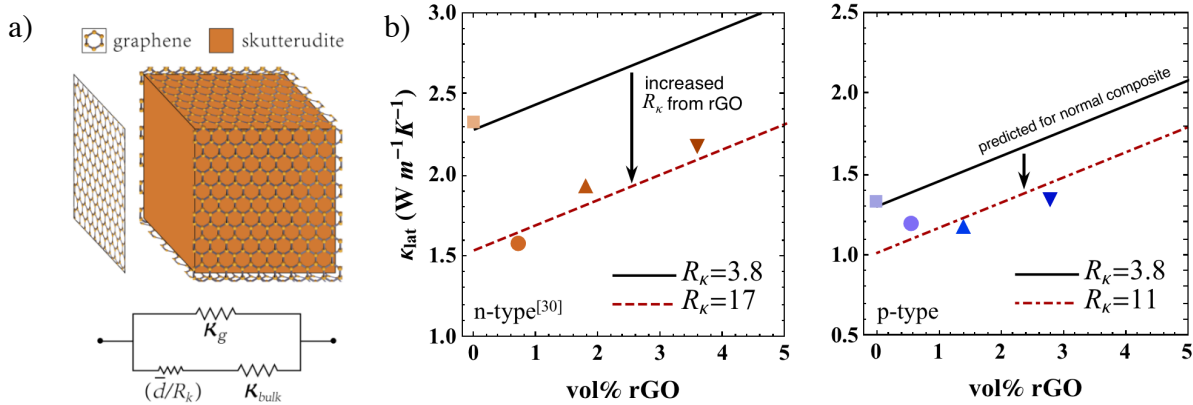


Figure 6.6: a) Diagram of the thermal circuit representing the thermal resistance of grain boundaries wrapped in graphene with the resistance elements labeled by their respective thermal conductivities. b) Lattice thermal conductivity ( $\kappa_{lat}$ ) at 300 K with varying amounts of rGO for both n and p-type skutterudite/rGO composite (solid symbols). Data for n-type material are from Ref. [167]. The solid lines represent the model (Eq. 6.2) when thermal boundary resistance is unchanged  $R_k = 3.8 \times 10^{-7} \text{ m}^2\text{KW}^{-1}$ . The dashed lines represent the model when the thermal boundary resistance is increased to  $17 \times 10^{-7} \text{ m}^2\text{KW}^{-1}$  for n-type and  $11 \times 10^{-7} \text{ m}^2\text{KW}^{-1}$  for p-type, due to graphene modification.

Here,  $\kappa_g$  is an effective in-plane thermal conductivity of graphene, which was treated as a fitting parameter. A value of  $\kappa_g = 23 \text{ Wm}^{-1}\text{K}^{-1}$  at 300 K was used in Figure 6.6b, which is between the extreme values for graphite mentioned above. The rGO thickness used in this equation was determined from the volume fraction,  $y$ , of rGO and  $\bar{d}$  of the samples ( $t = \bar{d} \times y/3$ , again for  $t \ll \bar{d}$ ). While TEM images give a measurement of rGO thickness, this is a very local measurement and the geometrical approach is thought to embody a more average representation of the composite system.

The interfacial thermal resistance,  $R_k$ , of skutterudite with rGO can now be determined by fitting the data in Fig. 6.6b. The resultant value of  $R_k$  at 300 K was increased by nearly a factor of 3 for p-type and 5 for n-type samples containing rGO. From Fig. 6.6b, it is clearly seen that the rise in thermal conductivity for higher volume fractions of rGO is explained by the parallel thermal conductance of graphene around the grains. Thicker multi-layer graphene causes thermal shorting around the skutterudite grains, increasing the thermal conductivity as the volume fraction of rGO increases. This ‘shorting’ effect was not observed in electrical conductivity measurements because the in-plane electrical conductivity of graphite ( $2.26 \times 10^4 \text{ Scm}^{-1}$ , [171]) is smaller than that of n-type and p-type SKD in this study. For the most reduction in thermal conductivity of the composite, thinner graphene layers should be used.

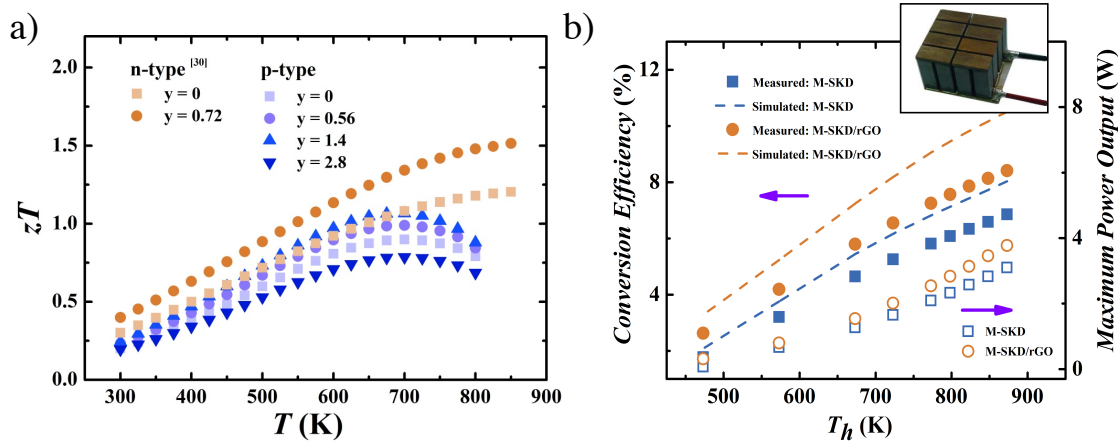


Figure 6.7: a) Temperature-dependent  $zT$  for  $\text{Ce}_{0.85}\text{Fe}_3\text{CoSb}_{12}/y$  vol% rGO ( $y = 0, 0.56, 1.4, 2.8$ ) samples from 300–800 K and  $\text{Yb}_{0.27}\text{Co}_4\text{Sb}_{12}/y$  vol% ( $y = 0, 0.72$ ) samples from 300–850 K from Ref. [167]. b) Inset: Thermoelectric module with dimension of 20 mm x 20 mm x 16 mm using  $\text{Ce}_{0.85}\text{Fe}_3\text{CoSb}_{12}/1.4$  vol% rGO and  $\text{Yb}_{0.27}\text{Co}_4\text{Sb}_{12}/0.72$  0.72 vol% rGO composite as p and n-type legs, respectively. Maximum conversion efficiency and power output as a function of the hot side temperature  $T_h$  for the skutterudite/rGO based modules (M-SKD/rGO) and the reference device made of pure SKD (M-SKD). The dash lines represent the theoretical conversion efficiency of M-SKD/rGO with a maximum value of 10.5 %, and M-SKD with a maximum value of 8.0 %, when ignoring electrical and thermal contact resistances.

### 6.1.5 $zT$ and module performance

Fig. 6.7 shows the temperature dependence of  $zT$  for p-type  $\text{Ce}_{0.85}\text{Fe}_3\text{CoSb}_{12}/y$  vol% rGO ( $y = 0, 0.56, 1.4, 2.8$ ) samples and n-type  $\text{Yb}_{0.27}\text{Co}_4\text{Sb}_{12}/y$  vol% rGO ( $y = 0, 0.72$ ) samples from Ref. [167]. For all p-type sample, the  $zT$  first increases with temperature and then drops after reaching a peak at 700 K. This is due to the decrease of power factor and rapid increase of thermal conductivity when  $T \geq 650$  K, which is attributed to bipolar conduction. Compared to samples without graphene,  $zTs$  for p-type samples with  $y \leq 1.4$  exhibit a robust increase due to the increased thermal resistance of the grain boundaries. The  $y = 1.4$  p-type sample attains a peak  $zT$  of 1.06 at 700 K, while n-type rGO sample attains a peak of 1.51 at 850 K.

The p-type  $\text{Ce}_{0.85}\text{Fe}_3\text{CoSb}_{12}/1.4$  vol% rGO and n-type  $\text{Yb}_{0.27}\text{Co}_4\text{Sb}_{12}/0.72$  vol% rGO composites were used to fabricate a thermoelectric module with dimension of 20 mm x 20 mm x 16 mm as shown in the inset of Fig. 6.7b. A module consisting of 8 n-p couples were assembled via SPS, spark cutting, and welding by the L. Chen research group at the Chinese Academy of Sciences [172]. For comparison, a reference thermoelectric module was also fabricated by using pristine n-type  $\text{Yb}_{0.27}\text{Co}_4\text{Sb}_{12}$  and p-type  $\text{Ce}_{0.85}\text{Fe}_3\text{CoSb}_{12}$  bulk materials without rGO. Based on PEM-3 measurements with hot/cold-side temperature 873K/296K, a high conversion efficiency of 8.4 % and maximum power output of 3.8 W were obtained, which is significantly higher than 6.8

% and 3.1 W of the pristine skutterudite module, further verifying that the skutterudite/rGO nanocomposite has improved performance. It is the first time that a module with n and p-type legs both made of skutterudite nanocomposite was fabricated. The measured conversion efficiency of 8.4 % ( $\Delta T = 577\text{K}$ ) is among the highest of all reported values not only for skutterudite based modules [173, 174], but also other TE material systems [175, 176]. The ANSYS-simulated ideal, theoretical conversion efficiency [176] (dash line in Fig. 6.7b) of the skutterudite/rGO module is 10.5 %, based on the measured thermoelectric properties. The 25% discrepancy between measured and predicted device efficiency can be attributed to interfacial thermal and electrical resistance between the thermoelectric material and the metallized ceramic substrate, as well as convection and radiation losses and is typical for such devices.

### 6.1.6 Discussion

Not all grain boundaries scatter phonons equivalently. Here, thermal transport modeling revealed that introducing multilayer graphene into grain boundaries of thermoelectric skutterudite dramatically increases the thermal boundary resistance. When this three dimensional rGO network in the GBs is kept thin (2 to 6 nm for 1.4 vol% rGO),  $\kappa_{\text{lat}}$  is reduced by 20% and the electrical properties are essentially unchanged, resulting in improved  $zTs$ . Additionally, thermal shorting via thermal conduction through the high  $\kappa_{\text{lat}}$  graphene layers is also avoided. This effect has been seen in both n and p-type SKD/rGO composites and a TE module consisting of 8 n-p couples was made and characterized to demonstrate the improved efficiency. It is the first time a module using n and p-type skutterudite nanocomposite has been made, and its conversion efficiency of 8.4% is among the highest of any value reported for TE modules [173, 174, 175, 176].

## 6.2 A chemical understanding of the electronic band structure in $\text{CoSb}_3$ skutterudites<sup>2</sup>

N-type skutterudites, such as  $\text{Yb}_x\text{Co}_4\text{Sb}_{12}$ , have recently been shown to exhibit high valley degeneracy with possible band convergence, explaining the excellent thermoelectric efficiency in these materials. Using a combined theoretical and experimental approach involving temperature-dependent synchrotron diffraction, molecular orbital diagrams and computational studies, the chemical nature of critical features in the band structure are highlighted. We identify how n-type doping on the filler site induces structural changes that are observed in both the diffraction data and computational results. Additionally, we show how chemical n-type doping slightly alters the electronic band structure moving the high valley degeneracy secondary conduction band closer to the primary conduction

---

<sup>2</sup>The content contained in this section was published by Hanus *et al.* in Ref. [177].

band and thus inducing band convergence.

Skutterudite CoSb<sub>3</sub> is a well-known thermoelectric material, but only recently has it been shown that, when heavily doped [168], it exhibits a complex Fermi surface with multiple valleys. Indeed, the extraordinary electronic properties of n-type thermoelectric CoSb<sub>3</sub> originates from the presence of a multi-valley secondary conduction band (CB<sub>2</sub>) located between the  $\Gamma$  and N points, which is somewhat higher in energy compared to the primary,  $\Gamma$ -point conduction band (CB <sub>$\Gamma$</sub> ). For highly doped samples and at elevated temperatures ( $\sim 700$  K), CB<sub>2</sub> appears to contribute substantially to the thermoelectric performance possibly even converging with (having the same energy as) the primary conduction band at  $\Gamma$ .

In this work, we use a combination of temperature dependent synchrotron diffraction and density functional theory calculations, in which the obtained structural data is used as an input for the theoretical calculations. The diffraction data reveals differences in the coefficient of thermal expansion of local bonds within the structure (*local*-CTE). These structural parameters are employed in the calculations to assess changes in the band structure due to structural changes. These experimental and computational efforts identify the chemical nature of the primary (CB <sub>$\Gamma$</sub> ) and secondary (CB<sub>2</sub>) conduction bands. We then show both experimentally and computationally how Yb doping changes the CoSb<sub>3</sub> structure beyond simple lattice expansion. Furthermore, a slight structure change observed with increasing Fermi level demonstrates a coupling of these conduction band states to the atom positions. It is also shown that this increase in Fermi level induces band convergence in CoSb<sub>3</sub> at room temperature and above. Here, we show that band convergence can be chemically induced through population of conduction band states not expected from a rigid band model.

### 6.2.1 Experimental and computational methods

The combined experimental and computational approach is described in detail below. Synthesis of the samples was performed using the method given by Tang *et al.* [178].

#### Powder Diffraction

X-ray powder diffraction was conducted at Argonne National Lab Advanced Photon Source (APS) on the designated powder diffraction beam line, 11-BM. Standard Debye-Scherrer geometry with a 1D detector was used for the experiment and the calibrated X-ray wavelength was 0.414208 Å. An Al<sub>2</sub>O<sub>3</sub>/Si reference sample was used for alignment and an instrument parameter file was obtained using a LaB<sub>6</sub> standard (specifications about profile parameters are given below in the refinement section). Sample absorption was calculated using the ABSORB web utility [179] (which uses the Cromer & Liberman algorithm to compute X-ray scattering cross sections). After optimizing the absorption factor, quartz capillary diameters of 0.4 mm and 0.3 mm were used for powder samples of CoSb<sub>3</sub>.

and  $\text{Yb}_{0.3}\text{Co}_4\text{Sb}_{12}$ , respectively (no diluting media was necessary). The same anomalous scattering parameters,  $f'$  and  $f''$ , used for the absorption calculation were also used in the Rietveld refinements. Room temperature scans of both samples were conducted using a high-speed sample spinner ( $\sim 90$  Hz). High temperature scans from  $100^\circ\text{C}$  to  $500^\circ\text{C}$  with  $100^\circ\text{C}$  steps were conducted using the Cyberstar hot air blower with its corresponding sample spinner ( $\sim 20\text{Hz}$ ). A typical intensity for the primary diffraction peak was  $\sim 300,000$  counts for the  $300\text{ K}$  scans and  $\sim 200,000$  counts for the scans at elevated temperature, confirming the quality of the data.

## Refinements

To examine structural changes of  $\text{CoSb}_3$  with temperature and doping, Rietveld refinements were conducted on the temperature dependent, high-resolution, powder diffraction data of filled and unfilled  $\text{CoSb}_3$ . Refinements were conducted using the General Structure Analysis System (GSAS [180, 181]) for  $\text{CoSb}_3$  in the  $\text{Im}\bar{3}$  space group with Co atoms at  $(0.25, 0.25, 0.25)$ , and Sb atoms at  $(0, y, z)$ . In this representation, the filler atom is located at  $(0, 0, 0)$ . Note that the origin in Figure 6.1 is shifted to effectively show both Sb-Sb long and short bonds in one figure.  $\text{LaB}_6$  powder was used to construct an instrument parameter file and a pseudo-Voigt peak profile was used (CW profile function 3 in GSAS). The peak profile parameters from this  $\text{LaB}_6$  parameter file were fixed throughout the refinement procedure until the last refinement step in which all refinement parameters were unfixed and refined together. To account for peak anisotropy seen in the  $\text{Yb}_{0.3}\text{Co}_4\text{Sb}_{12}$  sample, anisotropic peak broadening parameters were included through the  $\gamma$ -profile function (L11, L22, etc. parameters in GSAS) in these refinements. Refinements of  $\text{Yb}_{0.3}\text{Co}_4\text{Sb}_{12}$  without the anisotropic profile parameters were also conducted and the same trends were concluded for structural changes with temperature and doping, however the peak positions were more accurately represented when anisotropic profile parameters were included and these results are reported here. In all diffraction histograms, the electron density on the Co site  $(0.25, 0.25, 0.25)$  was slightly larger relative to that on the Sb site  $(0, y, z)$ . Several defect mechanisms were tested and statistically equivalent refinements were achieved for anti-site disorder of Sb on the Co site as well as Sb vacancies. As Sb vacancies would introduce electrons, and since the undoped samples are slightly n-type [178], a slight Sb deficiency is assumed. To include Sb vacancies in the refinement, the Co occupancy was set to 100% and the Sb occupancy was refined along with the scaling parameter. Note that a high frequency sample spinner was used for the room temperature scans resulting in better counting statistics than the scans at elevated temperatures in which a lower frequency sample spinner was used. This is reflected in the refinement statistics, in which the room temperature refinements have a higher  $\chi^2$  due to better counting statistics. Refinement uncertainties are given in the tabulated diffraction data in the Supporting Information of Ref. [177] and the experimental uncertainty of the lattice parameters of beam line 11-BM is  $0.0001\text{ \AA}$ .

## Computational methods

Density-functional theory (DFT) calculations for both doped and undoped CoSb<sub>3</sub> were conducted to determine how changes in structure and Fermi level will affect the electronic band structure.

We performed all DFT calculations as implemented in the Vienna ab initio simulation package (VASP) code. The projector-augmented wave (PAW) method [159] with Perdew-Burke-Ernzerhof (PBE) exchange-correlation functional were used for calculations on the primitive unit cell and the Yb-doped supercell [160]. The unit cell structure was fully relaxed with a plane wave cutoff energy of 550 eV with a Gamma centered 7x7x7 Monkhorst-Pack uniform k-point reciprocal space sampling. The 0.01 eV/Å Hellmann-Feynman forces were adopted for geometry optimization. The optimized lattice parameter is found to be 9.11 Å, which is consistent with the previous theoretical value of 9.115 Å using PBE [182], and the internal parameters u=0.3333, v=0.1595. The calculated direct band gap of CoSb<sub>3</sub> is 0.1665 eV, which agrees well with the gap of 0.17 eV reported earlier [183]. Sofo et al. reported a slightly higher value of 0.22 eV [184]. After our calculations of the fully relaxed CoSb<sub>3</sub> were validated with previous calculations and literature values, a systematic study on how crystal structure and doping effect the band structure was conducted.

The structural parameters of CoSb<sub>3</sub> and Yb<sub>0.3</sub>Co<sub>4</sub>Sb<sub>12</sub> from 300 to 800 K, as determined via synchrotron diffraction, were used to calculate band structures. In this way, a ‘0 K’ calculation is conducted with structural parameters set to their values at a given temperature (300 to 800 K) and we refer to this, here, as the band structure at that specific temperature. This method neglects the contribution of lattice vibrations, meaning that the computations with temperature only probe the influence of structure change on the band structure. In reality, there is an additional contribution from lattice vibrations through electron-phonon interactions (e.g. see Figure 1 of Gibbs et. al. [185]). The room temperature band gap of CoSb<sub>3</sub> calculated by this method is 0.1625 eV, which agrees with room temperature optical absorption measurements [165].

Here, all calculations of Yb-doped CoSb<sub>3</sub> were performed in a 2x2x2 supercell which contains 130 atoms. The chemical composition of this supercell is Yb<sub>0.25</sub>Co<sub>4</sub>Sb<sub>12</sub>. The nominal composition of the doped CoSb<sub>3</sub> is Yb<sub>0.3</sub>Co<sub>4</sub>Sb<sub>12</sub> and the occupancy from refinements show that the Yb content is slightly lower than the nominal content, suggesting that this composition is close to that observed experimentally [165]. Again, the atomic positions were fixed to that measured from synchrotron diffraction. Typically, the atomic positions are relaxed in supercell calculations as the positions near an impurity atom will be different than the atomic positions away from one. Synchrotron diffraction and Rietveld analysis give a spatial average of the atomic positions. Because of this, fixing the atomic positions to the spatial average may be unphysical and skew the computational results. DFT calculations, where the lattice parameter was set and the ion positions are relaxed, were conducted to ensure that the observed trends were not artifacts of the method in which the supercell calculations were conducted. Additionally, calculations in which the Fermi level was

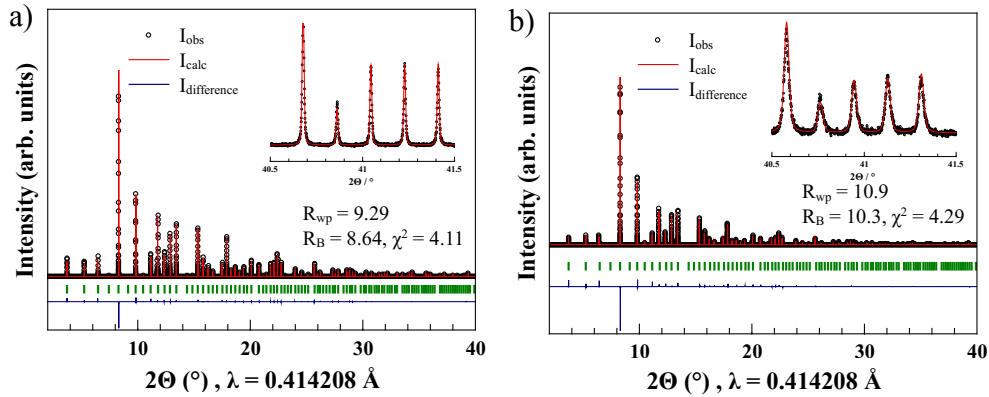


Figure 6.8: Exemplary refinement of (a)  $\text{CoSb}_3$  and (b)  $\text{Yb}_{0.3}\text{Co}_4\text{Sb}_{12}$  at 300 K with the corresponding profile residuals. The black circles are the experimental data, the red line is the calculated histogram, and the line below is the difference profile between the observed and calculated values. The insets show a zoomed in view on high angle reflections and the high quality fit of the refinement at the corresponding low d-spacing.

intentionally shifted were conducted to deduce how changing the carrier concentration will affect the band structure (summary provided in Supplemental Information of Ref. [177]) in addition to the calculations discussed in Section 6.2.2. This was achieved by manually increasing the number of electrons of  $\text{CoSb}_3$ , as well as conducting charged impurity calculations where  $\text{Yb}_i^{2+}$  was included and compared to the calculation with  $\text{Yb}_i^0$ . A compensating background charge was included, in these, to prevent divergence of the total energy of the charged system.

The COHP were generated by transferring the PAW wave functions to properly chosen local basis with Local Orbital Basis Suite Towards Electronic-Structure Reconstruction (LOBSTER) code [186], and the band unfolding procedure for Yb-doped  $\text{CoSb}_3$  supercell was performed using the BandUP code [187].

### 6.2.2 Results and discussion

#### Temperature dependent structural changes in CoSb<sub>3</sub>

The skutterudite structure can be completely defined by its lattice parameter,  $a$ , and the position of the Sb atom  $(0, y, z)$ . The different bond lengths illustrated in Figure 6.1 are then given as

$$d(\text{Co} - \text{Sb}) = a \left[ \left( \frac{1}{4} \right)^2 + \left( y - \frac{1}{4} \right)^2 + \left( z - \frac{1}{4} \right)^2 \right]^{1/2} \quad (6.3)$$

$$d_1(\text{Sb} - \text{Sb}) = 2az \quad (6.4)$$

$$d_2(\text{Sb} - \text{Sb}) = a(1 - 2y) \quad (6.5)$$

with  $d$  being the Co-Sb bond,  $d_1$  the Sb-Sb short bond, and  $d_2$  the Sb-Sb long bond [164]. As mentioned above, the Sb<sub>4</sub> ring contains two bond lengths and a fixed bond angle of 90°. When  $d_2 = d_1$  the Oftedal relation of  $y + z = 0.5$  is met (named after the discoverer of the structure [188]), the ring is a perfect square. In addition, the CoSb<sub>6</sub> octahedra do not exhibit perfect  $O_h$  symmetry either. All bond lengths are equal but the bond angles are distorted from 90°. One of the most defining characteristics of this structure is the large cage centered at (0,0,0). This interstitial site is commonly referred to as the filler site and can be used for chemical doping. The solubility limit of doping atoms on this filler site can be a limiting factor when optimizing the electron chemical potential of thermoelectrics, and it was recently highlighted that this solubility limit is temperature and composition dependent [168, 189]. Interstitial doping atoms are weakly bonded to the cage structure and much effort has been devoted to understanding how lattice dynamics of this rattling atom affect the thermal properties of filled skutterudites [190, 191, 192].

**Thermal expansion.** In this work, temperature dependent synchrotron X-ray diffraction has been performed to study the structural evolution of Yb filled and unfilled CoSb<sub>3</sub> at higher temperatures. Exemplary results obtained via Rietveld refinements of the synchrotron data for both CoSb<sub>3</sub> and Yb<sub>0.3</sub>Co<sub>4</sub>Sb<sub>12</sub> at 300 K can be found in Figure 6.8. The samples are all phase pure and good profile residuals can be obtained, indicating a high quality of the fit. All the relevant temperature dependent refinement data is tabulated in Table S1 and S2 of Ref. [177].

Figure 6.9 shows the refined lattice parameter of CoSb<sub>3</sub>, which increases linearly with increasing temperature. Introduction of the filler atom further increases the lattice and corresponds well with the expectation of Vegard's law within a CoSb<sub>3</sub> system, in which an increasing Yb content increases the lattice parameter linearly [189]. Figure 6.10 shows the changes of the structural motif with increasing temperature. The  $y$  and  $z$  positions of Sb change with temperature (see Supporting Information of Ref. [177]), resulting in an increasing octahedral angle shifting towards a more symmetric regular  $O_h$  symmetry (Figure 6.10a). While the octahedra become more symmetric

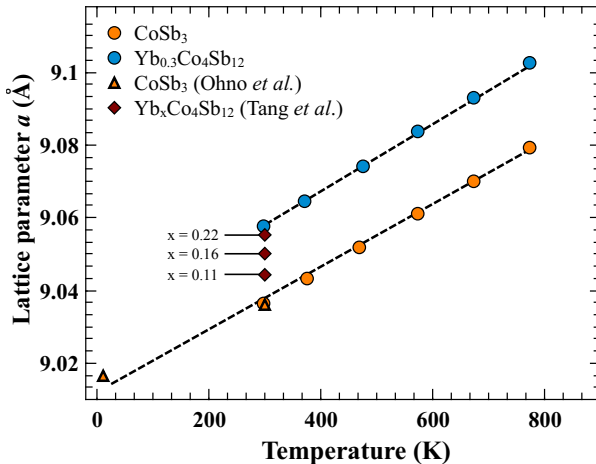


Figure 6.9: Temperature dependent lattice parameter of CoSb<sub>3</sub> obtained from the Rietveld refinements, showing the positive thermal expansion of the unit cell. Introduction of the filler atom further increases the unit cell. For comparison, data for increasing amounts of Yb are shown from Tang *et al.* [189]. Literature data from Ohno *et al.* [193] show that the linear temperature dependence of  $a$  in CoSb<sub>3</sub> is maintained down to 10 K.

(90° angle), the increasing temperature drives the Sb<sub>4</sub> ring away from a square towards a more rectangular arrangement (Figure 6.10b). In addition to the temperature effects, the filler atom itself changes these relations. Filling the structure partially with Yb increases the octahedral distortion and increases the ( $y + z$ ) relation towards a perfect square arrangement of the Sb<sub>4</sub> ring. Similar effects of substitution induced changing of bond angles have recently been reported in the YbZn<sub>2</sub>Sb<sub>2</sub> Zintl phases [194].

The atomic displacement parameters,  $\langle u^2 \rangle$ , obtained (Table S1 and S2 of Ref. [177]) agree with what has been previously reported for CoSb<sub>3</sub> [195], and other filled skutterudites [196]. The Yb atom has significantly larger values for  $\langle u^2 \rangle$  than the Co and Sb atoms, which has been cited as evidence of the rattling nature of the Yb atom on this cage site [197]. The temperature dependence of  $\langle u^2 \rangle$  gave an Einstein temperature for this localized mode of  $\theta_E = 65(5)\text{K}$ , which is similar to Yb in YbFe<sub>4</sub>Sb<sub>12</sub> [198].

**Local thermal expansion coefficients.** The changing Sb positions clearly affect the Oftedal relation, therefore the local chemical bonds, in particular the Sb-Sb bonds within the Sb<sub>4</sub> ring must be changing as well. Figure 6.11 shows the temperature dependent evolution of the different bond lengths; the Co-Sb bond and the short and long Sb-Sb bonds,  $d_1$  and  $d_2$ , respectively. At room temperature, the results correspond well with the structural data by Ohno *et al.* [193]. While all bond lengths increase with temperature, as expected due to thermal expansion, differences in the slopes between the different bonds can be detected. In addition, differences in the bond lengths of the substituted samples can be seen as well. To assess these differences, the coefficient of

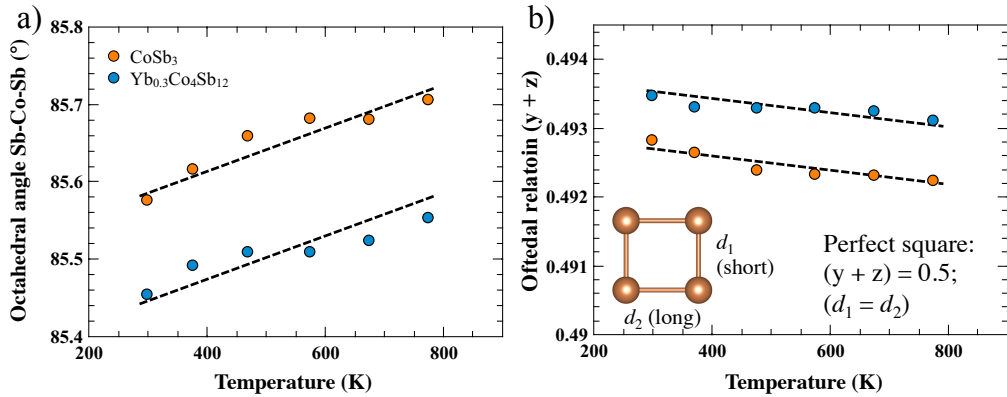


Figure 6.10: Changes in the CoSb<sub>6</sub> octahedral angle (a) and the Oftedal relation (b) with temperature. With increasing temperature, the structure shifts towards a more symmetric octahedron and away from a perfect square. Note that the doping with a filler atom leads to a distortion of the octahedral away from a symmetric 90° angle and a more square Sb<sub>4</sub> ring arrangement.

thermal expansion (CTE) is calculated for each bond separately and is treated as a linear expansion coefficient defined as

$$\alpha_{300K}^L = \frac{\Delta l}{\Delta T} \frac{1}{l_{300K}}. \quad (6.6)$$

where  $\Delta l$  is the change in length,  $\Delta T$  is the change in temperature, and  $l_{300K}$  is the length at 300 K. For a better understanding of the changes we will define  $\alpha_{300K}^L$  for bond lengths as a *local*-CTE and the evolution of the lattice parameter as CTE. Temperature dependence ( $\Delta l/\Delta T$ ) of the obtained structural parameters were successfully fit, giving  $\alpha_{300K}^L$  through Eq. 6.6 and are shown in Figure 6.11. The values for the CTE and the *local*-CTE are tabulated in Table 6.1. The obtained values of the thermal expansion coefficients of the unit cell correspond well with other literature values. For instance, Rogl *et al.* [199] measured a CTE of CoSb<sub>3</sub> to be  $9.1 \times 10^{-6} \text{ K}^{-1}$  via dilatometer measurements agreeing with our value in Table 6.1.

Figure 6.11 and Table 6.1 show that the local-CTE of the long Sb-Sb bond in CoSb<sub>3</sub> is significantly larger than that of the Co-Sb and the short Sb-Sb bond. In other words, with increasing temperature the long Sb-Sb bond ( $d_2$ ) expands much faster than the other two bonds. This faster increase of bond length of  $d_2$  and the corresponding slower increase of the short Sb-Sb bond ( $d_1$ ) leads to the observed behavior of a structural shift towards a more rectangular Sb<sub>4</sub> ring.

Upon doping of CoSb<sub>3</sub> with Yb, the  $\alpha_{300K}^L$  of the Sb-Sb short bond increases by nearly 50% while the  $\alpha_{300K}^L$  for the Co-Sb and the Sb-Sb long bond remains essentially unchanged (Figure 6.11a). In addition, the length of the short Sb-Sb bond is significantly increased upon doping, while the length of Co-Sb bond is only slightly increased and that of the long Sb-Sb bond remains unchanged (see Figure 6.11). The size of the filler atom and the resulting change in lattice parameter cannot account for the different changes of the local bonding nature, as a typical Vegard behavior is supposed to

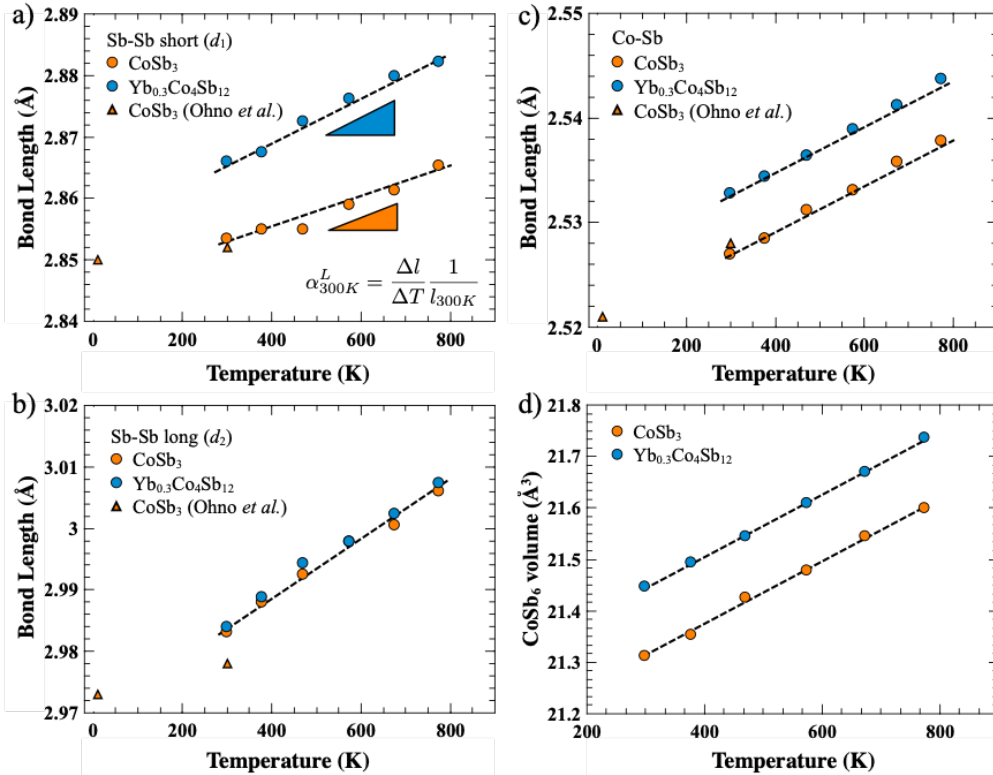


Figure 6.11: Temperature dependence of the Co-Sb (c) and Sb-Sb bond lengths (a) and (b). Lines correspond to linear fits used to calculate the local thermal expansion coefficient  $\alpha_{300K}^L$ . Literature values from Ohno *et al.* [193] are shown by triangles, showing the good fit of the data with literature values at room temperature and at 10 K. While all bonds expand with increasing temperature in the undoped CoSb<sub>3</sub>, the longer bond exhibits a larger slope and faster thermal expansion. Substitution with the filler atom increases the bond lengths as well. d) Temperature dependence of the octahedral volume, showing the linear thermal expansion of the CoSb<sub>6</sub> octahedra.

change the lattice and the atomic positions in a similar manner. These data clearly show the qualitative differences in the chemical nature of the two Sb-Sb bonds in CoSb<sub>3</sub>. Differences of these two chemical bonds has already been reported by Ohno *et al.* [193] using the maximum entropy method to reveal differences in the electron density between the Sb-Sb long and Sb-Sb short bonds. The electron density between the short bond was larger (by about 30%) than that between the long bond. This agrees well with the data presented here; less electron density results in a weaker bond, which should have a larger thermal expansion coefficient than a bond with more electron density between the atoms. In addition, calculations via density functional theory on the CoSb<sub>3</sub> lattice under strain showed that the Sb-Sb long bond was the first to break under a shear stress, which also support these experimental results [182]. From these structural data one may speculate the reason for the differences in the local-CTE behavior between the doped and undoped CoSb<sub>3</sub>. The filler atom leads to an elongation of the short Sb-Sb bond and hence less bonding interaction and

Table 6.1: Linear thermal expansion coefficients of the Sb-Sb, Co-Sb and Yb-Sb bonds in unfilled and filled skutterudite (normalized to the bond lengths at 300 K). The thermal expansion of the Sb-Sb short bond is significantly higher in  $\text{Yb}_{0.3}\text{Co}_4\text{Sb}_{12}$  than in  $\text{CoSb}_3$ .

Structural parameter	$\alpha_{300K}^L (10^{-6}\text{K}^{-1})$	
	$\text{CoSb}_3$	$\text{Yb}_{0.3}\text{Co}_4\text{Sb}_{12}$
lattice parameter, $a$	9.9	10.5
Sb-Sb long ( $d_2$ )	15.6	15.9
Sb-Sb short ( $d_1$ )	8.6	12.6
Co-Sb ( $d$ )	9.2	9.1
Yb-Sb	-	8.6

lower bond order, and with it a much faster thermal expansion similar to the long Sb-Sb bond.

The differences in the bonds local thermal expansion coefficients as well as the differently affected bond length after substitution with the filler atom are somewhat unexpected results. To provide an explanation, we will consider the inherent bonding interactions using a molecular orbital theory approach and the changes in the electronic band structure are examined via density functional theory.

### Band structure of doped and undoped $\text{CoSb}_3$

**A chemical understanding of the electronic band structure.** As recently shown for Zintl compounds [200], a combined approach using molecular orbital (MO) diagrams and density function theory can help gain a better understanding of the underlying chemical nature of the bands and how changes in structure and Fermi level may affect the bonding and electronic band situation. To interpret the observed thermal expansion behavior, we first attempt to understand the bonding qualitatively using a molecular orbital approach to determine the character of the valence and conduction bands. We then compare these conclusions to Crystal Orbital Hamilton Population (COHP) and density of states calculations.

Figure 6.12a shows the molecular orbitals for a  $\text{CoSb}_6$  octahedron in which the Sb lone pairs of the  $\text{Sb}_4$  ring coordinate to  $\text{Co}^{3+}$  forming an octahedral crystal field. The molecular orbital shows the octahedral crystal field splitting between the  $t_{2g}$  and  $e_g$  orbitals.  $\text{Co}^{3+}$  exhibits six d-electrons ( $d^6$  configuration) and therefore, the filled non-bonding  $t_{2g}$  orbitals express themselves as heavy states in the density of states of the valence band [200]. The filled deeper energy levels ( $a_{1g}$ ,  $t_{1u}$  and  $e_g$ ) in the valence band are of bonding nature and the empty anti-bonding states form the conduction band, with  $e_g^*$  representing the conduction band minimum [201]. Figure 6.12b shows the COHP of

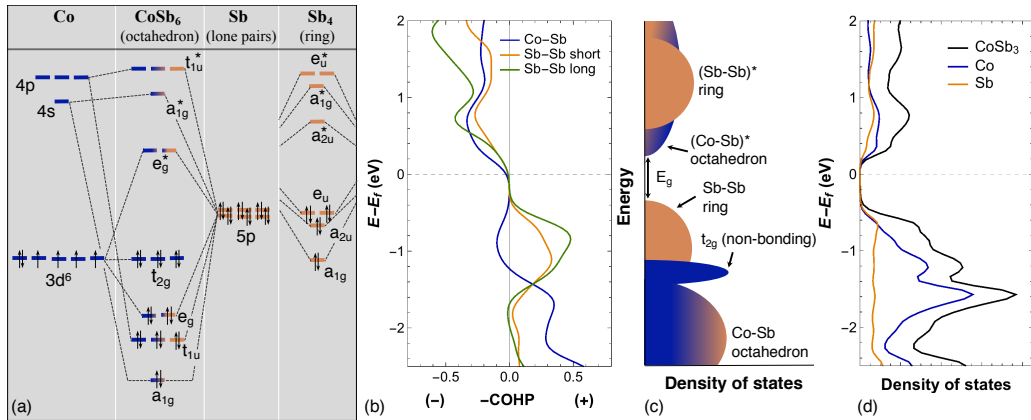


Figure 6.12: In all panels, blue corresponds to contributions from Co and orange to contributions from Sb. a) Molecular orbital diagrams of the CoSb<sub>6</sub> octahedron and the Sb<sub>4</sub> ring. Atomic orbitals are not shown for the Sb<sub>4</sub> ring. The octahedral crystal field splitting is visible and gives, in combination with the bonding, anti-bonding separation of the Sb-Sb bonds the band gap. b) Crystal Orbital Hamilton Population (COHP) calculated from the DFT data, showing the bonding nature of the Sb-Sb bonds in the valence bands and Sb-Sb anti-bonding states in the conduction band. The Co-Sb bonds in the valence band are predominantly non-bonding ( $t_{2g}$ ) in nature, whereas the conduction band has anti-bonding Co-Sb contributions. c) Schematic DOS estimated from MO diagrams in (a). d) Partial, atom projected DOS calculated from DFT data.

the different bonds and confirms the nature of low lying bonding Co-Sb states, the non-bonding  $t_{2g}$  closer to the valence band maximum and anti-bonding states at the conduction band edge. Figure 6.12a shows the molecular orbital diagram of a hypothetical Sb<sup>-1</sup> – Sb<sup>-1</sup> 4-member ring in  $D_{4h}$  symmetry (square arrangement), with the electronic configuration of a Sb with two bonds, *i.e.* valence of -1 using Zintl valence counting.

This molecular orbital diagram represents an oversimplification of the real electronic arrangement; for one the Sb<sub>4</sub> ring is rectangular and therefore  $D_{2h}$  symmetry. Also a rigorous description of the molecular orbitals of the Sb<sub>4</sub><sup>-</sup> unit would need to account for all four states per atom not only the two shown here. For simplicity, we have chosen this single Sb-Sb bond in which the symmetry of the square and the corresponding electronic energy levels [202], as well as the electron count for Sb<sup>-</sup> with two bonds and two lone pairs is incorporated. A deeper discussion regarding the contribution of the polyanionic ring to the skutterudite band structure, as well as a full tight-binding calculation, can be found in reference [203]. For a more in depth discussion on the bands and energetic configurations in solids with square arrangements, the reader is referred to Tremel and Hoffmann [202]. While the difference in symmetry between  $D_{4h}$  to  $D_{2h}$  will shift (and potentially split) the energy levels, the qualitative nature of the bonding states in the valence and anti-bonding states in the conduction band will be unaltered as can be seen in the COHP simulation results. In brief, the Sb-Sb bonding arrangement will result in bands with square-ring bonding character at the top of the valence band and bands with square-ring anti-bonding character near, but not exactly at, the bottom of the conduction band.

While the  $s$  and  $p_z$  orbitals of  $\text{Sb}^-$  can mix with the  $s$ ,  $p_z$ ,  $d_{z^2}$  and  $d_{x^2-y^2}$  of the metal at the  $\Gamma$  point (i.e. the lone pairs coordinate to Co to form  $\text{CoSb}_6$  octahedra) the bonding orbitals of the  $\text{Sb}_4$  ring cannot significantly mix with the  $\text{CoSb}_6$  octahedron as they do not have the correct topology with the Co 3d-orbitals in the  $D_{3d}$  point group [202, 203]. In other words, at the  $\Gamma$  point we can neglect the interaction of the  $\text{Sb}_4^{4-}$  ring molecular orbitals with the  $\text{CoSb}_6$  octahedron and the electronic structure of  $\text{Sb}_4^{4-}$  will superimpose on top of this  $\text{CoSb}_6$  molecular orbital diagram. The bonding states of the  $\text{Sb}_4$  ring are at a similar energy level as the  $t_{2g}$  nonbonding orbitals of Co character requiring DFT calculations to place them in the correct order. This makes the valence band edge of  $\text{CoSb}_3$  primarily Sb-Sb bonding character. The  $\text{Sb}_4$  anti-bonding states are located slightly above the  $e_g^*$  anti-bonding states of Co character, as confirmed by the calculated partial density of states (Figure 6.12d). Following this, we conclude that the primary conduction band  $\text{CB}_\Gamma$  can be attributed to the Co-Sb anti-bonding states, as has previously been established by Luo *et al.* [201]. The secondary conduction band,  $\text{CB}_2$ , could then be of Sb-Sb anti-bonding character.

**Band convergence with n-type doping.** Using the structural data of the reported refinements, the electronic band structures were calculated and the results at 300 K are given in Figure 6.13. Results at higher temperatures are shown in Figure S3 of Ref. [177] and reveal how lattice expansion influences the band structure (neglecting lattice vibrations and the electron-phonon interaction). The band structure shows a direct band gap at the  $\Gamma$  point and an additional secondary conduction band ( $\text{CB}_2$ ) at higher energies. The extraordinary thermoelectric properties of n-type filled  $\text{CoSb}_3$  have recently been attributed to contributions from this secondary conduction band. At higher temperatures and when n-type doped, carrier transport seems to occur in both bands, resulting in a higher valley degeneracy and higher thermopower [178]. An understanding of the chemical nature of the bands and how they change with temperature and chemical doping are of critical importance when optimizing n-type  $\text{CoSb}_3$ . To elucidate the effect of the doping on the  $\text{CoSb}_3$  band structure, DFT calculations were conducted on supercell structures with Yb atoms included on the filler site representing a composition of  $\text{Yb}_{0.25}\text{Co}_4\text{Sb}_{12}$ .

Because the calculations were conducted on supercell structures the Brillouin zone size was reduced, resulting in a folding of the bands. To compare these band structures to that of undoped  $\text{CoSb}_3$  (primitive cell), the band structures were unfolded and are shown in Figure 6.13b (effective primitive cell band structure). The two conduction bands become closer in energy with Yb doping as observed in Figure 6.13, where by aligning energy scales at the bottom of  $\text{CB}_\Gamma$ , a decrease in the energy of the band offset ( $\text{CB}_2 - \text{CB}_\Gamma$ ) is shown. This band convergence was also observed in the calculations of Shi *et al.* [204] in which a different, higher conduction band (at  $\Gamma$  in the supercell), was highlighted as opposed to the  $\text{CB}_2$  discussed here. It can also be seen that the Fermi level is increased to just above the  $\text{CB}_2$  minimum, confirming the contribution of this band to electrical transport in n-type doped  $\text{CoSb}_3$ . The band between the  $\Gamma$  and P point also moves quickly upon the addition of filler atoms [204], which is associated with the movement of the  $\text{CB}_2$  and addition of Yb.

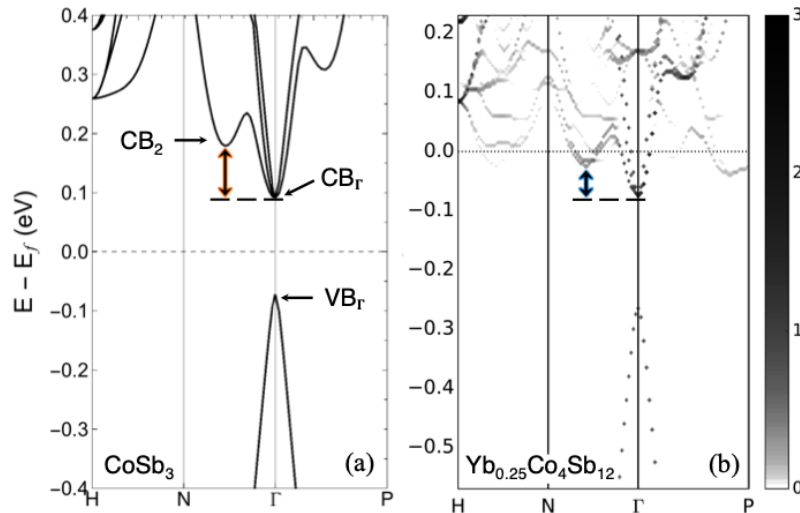


Figure 6.13: a) Calculated band structure of undoped  $\text{CoSb}_3$  at 300 K with the relevant band extrema labeled. The valence band maximum and conduction band minimum are at the  $\Gamma$  point (3-fold degenerate), making  $\text{CoSb}_3$  a direct band gap semiconductor. At higher energies, there is a second conduction band with 12 carrier pockets ( $\text{CB}_2$ ). b) Effective primitive cell band structure of Yb-doped  $\text{CoSb}_3$  calculated using a supercell (with fixed structural parameters). Dashed lines and color-coded arrows are guides to the eye, showing that in the doped structure the conduction bands are shifted compared to the undoped  $E(\mathbf{k})$ . The scale bar represents the weighting function

The introduction of Yb on the filler cage site can influence the band structure in several ways. When introduced, the Yb atom will simultaneously change the potential field set by the nuclei of the lattice (lattice potential effect) and increase the number of electrons in the system (carrier density effect). Therefore, to truly know the origin of band convergence, one needs to determine which of these effects is most responsible for the changes in band structure observed from Figure 6.13a to Figure 6.13b, namely the decrease of  $(\text{CB}_2 - \text{CB}_\Gamma)$ . To achieve this, an additional calculation was conducted on  $\text{CoSb}_3$  with additional electrons introduced to simulate the electrons donated with Yb doping, but without the associated change in the lattice potential field.

The result of this calculation is shown in Table 6.2, and reveals that a decrease in  $(\text{CB}_2 - \text{CB}_\Gamma)$ , an increase in  $E_g$ , and a slight increase of the Sb-Sb short bond all occur when the Fermi level is increased. Charged impurity calculations of  $\text{Yb}_{0.25}\text{Co}_4\text{Sb}_{12}$  with  $\text{Yb}_i^{2+}$  on the interstitial site, simulating a removal of the conduction electrons donated by Yb, show similar trends. In Table 6.2  $\text{CoSb}_3$ :doped refers to the addition of four electrons (per  $2 \times 2 \times 2$  supercell) and  $\text{Yb}_{0.25}\text{Co}_4\text{Sb}_{12}$ :doped refers to  $\text{Yb}_i^0$  as the interstitial defect, undoped refers to  $\text{Yb}_i^{2+}$ . The position-relaxed calculations show that upon doping with Yb, Sb-Sb short and Co-Sb bonds increase while the Sb-Sb long bond is essentially unchanged, agreeing with the diffraction data (see Figure 6.11). Through this analysis, we suggest that the filler atom changes the local structure leading to changes in bonding interactions resulting in what may have been unexpected trends in bond lengths and local-CTE, as discussed

Table 6.2: DFT calculations with different Fermi levels, and computational parameters. Similar changes in the band structure and structural parameters are observed with ‘doping’ regardless of computational method. \*Indicates that this calculation is shown in Figure 7. †Indicates that the values are average bond distances within the supercell..

Description				Band structure		Structural parameters		
Composition	doped/ undoped	a	positions	E (eV)	$\text{CB}_2-\text{CB}_\Gamma$ (eV)	Sb-Sb short ( $\text{\AA}$ )	Sb-Sb long ( $\text{\AA}$ )	Co-Sb ( $\text{\AA}$ )
$\text{CoSb}_3^*$	undoped	fixed	fixed	0.163	0.089	2.854	2.983	2.527
$\text{CoSb}_3$	doped	fixed	fixed	0.215	0.077	2.854	2.983	2.527
$\text{CoSb}_3$	undoped	fixed	relaxed	0.242	0.105	2.882	3.014	2.518
$\text{CoSb}_3$	doped	fixed	relaxed	0.292	0.093	2.884	3.013	2.518
$\text{Yb}_{0.25}\text{Co}_4\text{Sb}_{12}^*$	doped	fixed	fixed	0.191	0.050	2.866	2.984	2.533
$\text{Yb}_{0.25}\text{Co}_4\text{Sb}_{12}$	undoped	fixed	relaxed	0.221	0.088	2.898†	3.012†	2.524†
$\text{Yb}_{0.25}\text{Co}_4\text{Sb}_{12}$	doped	fixed	relaxed	0.727	0.075	2.900†	3.012†	2.523†

above. Additionally, the slight change in crystal structure with increased  $E_f$  demonstrates a coupling of it with these electronic states.

While the addition of Yb leads to the observed structural changes and with it changes in the band structure, the increasing Fermi level due to a donation of electrons into the conduction band and occupation of anti-bonding states (see Figure 6.12) further lowers the secondary energy gap,  $(\text{CB}_2 - \text{CB}_\Gamma)$ . These results suggest that band convergence in n-type  $\text{CoSb}_3$  can be induced by increasing the carrier density, and therefore should happen with all types of n-type dopants (e.g. other rare earth fillers, alkaline earth and alkali metal fillers, as well as Te or Ni doping). Tang *et al.* [178] constructed a three-band model within the rigid band approximation, with a band offset of  $(\text{CB}_2 - \text{CB}_\Gamma) = 0.08\text{eV}$ , which is between the values we obtained for  $\text{CoSb}_3$  and  $\text{Yb}_{0.25}\text{Co}_4\text{Sb}_{12}$ . This model successfully predicted the experimentally observed change in density of states effective mass (obtained via Seebeck measurements). The change in  $(\text{CB}_2 - \text{CB}_\Gamma)$  observed here is a higher order effect that would not alter the qualitative conclusions of Tang *et al.*

### 6.2.3 Discussion

The thermal expansion behavior of bonds (*local*-CTE) within Yb-filled and unfilled  $\text{CoSb}_3$  has been studied with temperature-dependent synchrotron diffraction, revealing a difference in the chemical nature of the Sb-Sb long and short bonds. Specifically, the Sb-Sb long bond is found to have a significantly larger thermal expansion than the Sb-Sb short and Co-Sb bonds. By combining

these structural results with systematic density functional theory calculations and molecular orbital diagrams, the chemical nature of band structure features was determined. It was identified that upon n-type doping, the charge carriers introduced populate anti-bonding states and change the electronic structure, leading to band convergence at room temperature in electron doped CoSb<sub>3</sub>. Computational results on Yb-doped CoSb<sub>3</sub> agree with synchrotron diffraction data showing that occupying the filler site changes the local structure in addition to simple lattice expansion. This work shows that the introduction of charge carriers, from presumably any n-type dopant, can influence the electronic structure and lead to band convergence.

We show the importance of combining accurate structure determination with systematic density functional theory calculations to understand band convergence and structural changes in thermo-electric materials. This combined approach is a powerful tool that can provide new strategies and approaches in optimizing energy materials.

## Bibliography

- [1] U.S. Energy Flow Chart (2017). Lawrence Livermore National Lab. ([flowcharts.llnl.gov](http://flowcharts.llnl.gov)), 2018.
- [2] Guang-Bo Gao, Ming-Zhu Wang, Xiang Gui, and Hadis Morkoc. Thermal design studies of high-power heterojunction bipolar transistors. *IEEE Transactions on Electron Devices*, 36(5):854–863, 1989.
- [3] Eric Pop. Energy dissipation and transport in nanoscale devices. *Nano Research*, 3(3):147–169, 2010.
- [4] Christian Monachon, Ludger Weber, and Chris Dames. Thermal Boundary Conductance: A Materials Science Perspective. *Annual Review of Materials Research*, 46:433–463, 2016.
- [5] S Mei, C J Foss, L N Maurer, O Jonasson, Z Aksamija, and I Knezevic. Boundaries, interfaces, point defects, and strain as impediments to thermal transport in nanostructures. *IEEE*, pages 1–10, 2017.
- [6] G. Jeffrey Snyder and Alemayouh H Snyder. Figure of merit ZT of a thermoelectric device defined from materials properties. *Energy and Environmental Science*, 10(11):2280–2283, 2017.
- [7] Stephen Dongmin Kang and G. Jeffrey Snyder. Transport property analysis method for thermoelectric materials: material quality factor and the effective mass model. *arXiv:1710.06896v2*, pages 1–5, 2017.
- [8] Zachary M. Gibbs, Francesco Ricci, Guodong Li, Hong Zhu, Kristin Persson, Gerbrand Ceder, Geoffroy Hautier, Anubhav Jain, and G. Jeffrey Snyder. Effective mass and Fermi surface complexity factor from ab initio band structure calculations. *npj Computational Materials*, 3(1):8, 2017.
- [9] Alan J. H. McGaughey, Ankit Jain, and Hyun-young Kim. Phonon properties and thermal conductivity from first principles, lattice dynamics, and the Boltzmann transport equation. *Journal of Applied Physics*, 125(1):011101, 2019.

- [10] P. B. Allen, J. L. Feldman, J. Fabian, and F. Wooten. Diffusons, locons and propagons: Character of atomic vibrations in amorphous Si. *Philosophical Magazine B*, 79(11/12):1715–1731, 1999.
- [11] Robert J. Hardy. Energy-Flux Operator for a Lattice. *Physical Review*, 132(1):168–177, 1963.
- [12] Philip B. Allen and Joseph L. Feldman. Thermal conductivity of disordered harmonic solids. *Physical Review B*, 48(17):12581–12588, 1993.
- [13] Saikat Mukhopadhyay, David S. Parker, Brian C. Sales, Alexander A. Puretzky, Michael A. McGuire, and Lucas Lindsay. Two-channel model for ultralow thermal conductivity of crystalline  $Tl_3VSe_4$ . *Science*, 360(6396):1455–1458, 2018.
- [14] Freddy DeAngelis, Murali Gopal Muraleedharan, Jaeyun Moon, Hamid Reza Seyf, Austin J Minnich, Alan J. H. McGaughey, and Asegun Henry. Thermal Transport in Disordered Materials. *Nanoscale and Microscale Thermophysical Engineering*, 0(0):1–36, 2018.
- [15] VASP. <https://www.vasp.at/>.
- [16] QuantumEspresso. <https://www.quantum-espresso.org/>.
- [17] Phonopy. <https://atztogo.github.io/phonopy/index.html>.
- [18] Phonopy database. <http://phonondb.mtl.kyoto-u.ac.jp/ph20180417/index.html>.
- [19] almaBTE database. <http://www.almabte.eu/index.php/database/>.
- [20] Navaneetha K. Ravichandran and David Broido. Unified first-principles theory of thermal properties of insulators. *Physical Review B*, 98(8):085205, 2018.
- [21] A. Debernardi, F. de Geuser, J. Kulda, M. Cardona, and E. E. Haller. Anharmonic Self-Energy of Phonons: Ab Initio Calculations and Neutron Spin Echo Measurements. *arXiv*, 2002.
- [22] Shobhana Narasimhan and David Vanderbilt. Anharmonic self-energies of phonons in silicon. *Physical Review B*, 43(5):4541–4544, 1991.
- [23] Benoit Latour and Yann Chalopin. Distinguishing between spatial coherence and temporal coherence of phonons. *Physical Review B*, 95(21):214310, 2017.
- [24] I. Pomeranchuk. On the thermal conductivity of dielectrics. *Physical Review*, 60(11):820–821, 1941.
- [25] André Herpin. Contribuition à létude de la théorie cinétique des solides. *Annales de Physique*, 12(7):91–139, 1952.

- [26] P.G. Klemens. The thermal conductivity of dielectric solids at low temperatures (Theoretical). *Proceedings of the Royal Society of London. Series A. Mathematical and Physical Sciences*, 208(1092):108–133, 1951.
- [27] Conyers Herring. Role of Low-Energy Phonons in Thermal Conduction. *Physical Review*, 95(4):954–965, 1954.
- [28] B. C. Daly, K. Kang, Y. Wang, and David G. Cahill. Picosecond ultrasonic measurements of attenuation of longitudinal acoustic phonons in silicon. *Physical Review B - Condensed Matter and Materials Physics*, 80(17):1–5, 2009.
- [29] J. M. Ziman. *Electrons and Phonons: The Theory of Transport Phenomena in Solids*. Oxford University Press, 1960.
- [30] P G Klemens. The Scattering of Low-Frequency Lattice Waves by Static Imperfections. *Proceedings of the Physical Society. Section A*, 68(12):1113–1128, 1955.
- [31] Shin-ichiro Tamura. Isotope scattering of dispersive phonons in Ge. *Physical Review B*, 27(2):858–866, 1983.
- [32] L A Turk and P G Klemens. Phonon Scattering by impurity platlet precipitates in diamond. *Phys. Rev. B*, 9(10):4422–4428, 1974.
- [33] John Nye. *Physical Properties of Crystals: Their Representation by Tensors and Matrices*. Clarendon Press, 1985.
- [34] Duane C. Wallace. *Thermodynamics of Crystals*. John Wiley and Sons, Inc., New York, 1972.
- [35] R Brown. The effect of dislocations on thermal conductivity. *Jounal de Physique Colloques*, 42(C6):C6–271–C6–273, 1981.
- [36] Peter Carruthers. Scattering of Phonons by Elastic Strain Fields and the Thermal Resistance of Dislocations. *Physical Review*, 114(4), 1959.
- [37] R Landauer. Spatial Variation of Currents and Fields Due to Localized Scatterers. *IBM Journal*, -(July):223–231, 1957.
- [38] E. T. Swartz and R. O. Pohl. Thermal boundary resistance. *Reviews of Modern Physics*, 61(3):605–668, 1989.
- [39] Riley Hanus, Anupam Garg, and G Jeffery Snyder. Phonon diffraction and dimensionality crossover in phonon-interface scattering. *Communications Physics*, 1(1):78, 2018.

- [40] David G. Cahill, Paul V. Braun, Gang Chen, David R. Clarke, Shanhui Fan, Kenneth E. Goodson, Pawel Kebinski, William P. King, Gerald D. Mahan, Arun Majumdar, Humphrey J. Maris, Simon R. Phillpot, Eric Pop, and Li Shi. Nanoscale thermal transport. II. 2003-2012. *Applied Physics Reviews*, 1(1):1–45, 2014.
- [41] W. A. Little. Transport of heat between dissimilar solids at low temperatures. *Canadian Journal of Physics*, 37:334–349, 1959.
- [42] H. B. G. Casimir. Note on the conduction of heat in crystals. *Physica*, 5(6):495–500, 1938.
- [43] Zhaojie Wang, Joseph E. Alaniz, Wanyoung Jang, Javier E. Garay, and Chris Dames. Thermal conductivity of nanocrystalline silicon: Importance of grain size and frequency-dependent mean free paths. *Nano Letters*, 11(6):2206–2213, 2011.
- [44] Koji Watari, Hiromi Nakano, Kazuyori Urabe, Kozo Ishizaki, Shixun Cao, and Katsunori Mori. Thermal conductivity of AlN ceramic with a very low amount of grain boundary phase at 4 to 1000 K. *Journal of Materials Research*, 17(11):2940–2944, nov 2002.
- [45] R Berman. The Thermal Conductivity of some Polycrystalline Solids at Low Temperatures. *Proceedings of the Physical Society. Section A*, 65(12):1029–1040, 1952.
- [46] Takuma Hori, Junichiro Shiomi, and Chris Dames. Effective phonon mean free path in polycrystalline nanostructures. *Applied Physics Letters*, 106(17):1–6, 2015.
- [47] Chengyun Hua and Austin J. Minnich. Importance of frequency-dependent grain boundary scattering in nanocrystalline silicon and silicon-germanium thermoelectrics. *Semiconductor Science and Technology*, 29(124004):1–17, 2014.
- [48] Takafumi Oyake, Lei Feng, Takuma Shiga, Masayuki Isogawa, Yoshiaki Nakamura, and Junichiro Shiomi. Ultimate Confinement of Phonon Propagation in Silicon Nanocrystalline Structure. *Physical Review Letters*, 120(4):45901, 2018.
- [49] Chengyun Hua, Xiangwen Chen, Navaneetha K. Ravichandran, and Austin J. Minnich. Experimental metrology to obtain thermal phonon transmission coefficients at solid interfaces. *Physical Review B*, 95(20):205423, 2017.
- [50] R. W. Balluffi, Y. Komem, and T. Schober. Electron microscope studies of grain boundary dislocation behavior. *Surface Science*, 31:68–103, 1971.
- [51] T. Schober. Observation of misfit dislocation arrays in high angle (110) twist grain boundaries in gold. *Philosophical Magazine*, 22(179):1063–1068, 1970.

- [52] T. Schober and R. W. Balluffi. Quantitative observation of misfit dislocation arrays in low and high angle twist grain boundaries. *Philosophical Magazine*, 21(169):109–123, 1970.
- [53] S. von Alfthan, P. D. Haynes, K. Kaski, and A. P. Sutton. Are the structures of twist grain boundaries in silicon ordered at 0 K? *Physical Review Letters*, 96(5):1–4, 2006.
- [54] Sebastian von Alfthan, Nicole A. Benedek, Lin Chen, Alvin Chua, David Cockayne, Karleen J. Dudeck, Christian Elsässer, Michael W. Finnis, Christoph T. Koch, Behnaz Rahmati, Manfred Rühle, Shao-Ju Shih, and Adrian P. Sutton. The Structure of Grain Boundaries in Strontium Titanate: Theory, Simulation, and Electron Microscopy. *Annual Review of Materials Research*, 40(1):557–599, 2010.
- [55] W. T. Read and W. Shockley. Dislocation Models of Crystal Grain Boundaries. *Physical Review*, 78(3):275–289, 1950.
- [56] Louisette Priester. *Grain Boundaries From Theory to Engineering*. Springer, 2006.
- [57] Dieter Wolf. Structure and Energy of Grain Boundaries. In *Handbook of Materials Modelling*, chapter 6.9, pages 1953–1983. Springer Netherlands, 2005.
- [58] J. Hirth and J. Lothe. *Theory of Dislocations*. Wiley, New York, New York, 2nd edition, 1982.
- [59] Taku Watanabe, Boris Ni, Simon R. Phillpot, Patrick K. Schelling, and Pawel Kebinski. Thermal conductance across grain boundaries in diamond from molecular dynamics simulation. *Journal of Applied Physics*, 102(6), 2007.
- [60] S. H. Huang, G. Balakrishnan, A. Khoshakhlagh, A. Jallipalli, L. R. Dawson, and D. L. Huffaker. Strain relief by periodic misfit arrays for low defect density GaSb on GaAs. *Applied Physics Letters*, 88(13):131911, 2006.
- [61] O. Yastrubchak, T. Wosinski, T. Figielksi, E. Lusakowska, B. Pecz, and A. L. Toth. Misfit dislocations and surface morphology of lattice-mismatched GaAs/InGaAs heterostructures. *Physica E: Low-Dimensional Systems and Nanostructures*, 17(1-4):561–563, 2003.
- [62] R. W. Balluffi, S. L. Sass, and T. Schober. Grain boundary dislocation networks as electron diffraction gratings. *Philosophical Magazine*, 26(3):585–592, 1972.
- [63] V. M. Kaganer, R. Köhler, M. Schmidbauer, R. Opitz, and B. Jenichen. X-ray diffraction peaks due to misfit dislocations in heteroepitaxial structures. *Physical Review B*, 55(3):1793–1810, 1997.
- [64] M. Omini and A. Sparavigna. Role of grain boundaries as phonon diffraction gratings in the theory of thermal conductivity. *Physical Review B*, 61(10):6677–6688, 2000.

- [65] Hyun-Sik Kim, Stephen D. Kang, Yinglu Tang, Riley Hanus, and G. Jeffrey Snyder. Dislocation strain as the mechanism of phonon scattering at grain boundaries. *Mater. Horiz.*, 3(3):234–240, 2016.
- [66] J H Van Der Merwe. On the Stresses and Energies associated with Inter-Crystalline Boundaries. *Proceedings of the Physical Society. Section A*, 63:616–637, 2002.
- [67] Qingping Meng, Lijun Wu, and Yimei Zhu. Phonon scattering of interfacial strain field between dissimilar lattices. *Physical Review B - Condensed Matter and Materials Physics*, 87(6):1–9, 2013.
- [68] R. A. Brown. The scattering of phonons by the strain and rotation fields of crystal defects. *Journal of Physics C: Solid State Physics*, 16:1009–1029, 1983.
- [69] B.D. Cullity and S.R. Stock. *Elements of X-Ray Diffraction*. Pearson Education, Cambridge, 3rd edition, 2014.
- [70] C. Dames and G. Chen. Theoretical phonon thermal conductivity of Si/Ge superlattice nanowires. *Journal of Applied Physics*, 95(2):682–693, 2004.
- [71] Riley Hanus. GitHub repository: <https://github.com/rileyhanus/Phonon-scattering-and-transport-in-polycyrstals>.
- [72] Glen A. Slack and S. Galginaitis. Thermal conductivity and phonon scattering by magnetic impurities in CdTe. *Physical Review*, 133(1A), 1964.
- [73] C. J. Glassbrenner and Glen a. Slack. Thermal conductivity of silicon and germanium from 3K to the melting point. *Physical Review*, 134(4A), 1964.
- [74] Hadis Morkoç. General Properties of Nitrides. In *Nitride Semiconductor Devices*, volume 1, pages 1–61. Wiley-VCH, Weinheim, Germany, 2013.
- [75] Louis R. Rossi and Willis G. Lawrence. Elastic Properties of Oxide Solid Solutions: The System Al<sub>2</sub>O<sub>3</sub>-Cr<sub>2</sub>O<sub>3</sub>. *Journal of American Ceramic Society*, 53(11):604–608, 1970.
- [76] H. Rücker and M. Methfessel. Anharmonic Keating model for group-IV semiconductors with application to the lattice dynamics in alloys of Si, Ge, and C. *Physical Review B*, 52(15):11059–11072, 1995.
- [77] H. Iwanaga, a. Kunishige, and S. Takeuchi. Anisotropic thermal expansion in wurtzite-type crystals. *Journal of Materials Science*, 35(10):2451–2454, 2000.

- [78] S García-Revilla, F Rodríguez, R. Valiente, and M. Pollnau. Optical spectroscopy of  $\text{Al}_2\text{O}_3:\text{Ti}^{3+}$  single crystal under hydrostatic pressure. The influence on the Jahn-Teller coupling. *Journal of Physics: Condensed Matter*, 14(3):447–459, 2002.
- [79] J. J. Wortman and R. A. Evans. Young’s modulus, shear modulus, and poisson’s ratio in silicon and germanium. *Journal of Applied Physics*, 36(1):153–156, 1965.
- [80] P. K. Schelling, S. R. Phillipot, and P. Kebbinski. Kapitza conductance and phonon scattering at grain boundaries by simulation. *Journal of Applied Physics*, 95(11 I):6082–6091, 2004.
- [81] Carlos A. Polanco, Rouzbeh Rastgarkashgarkolaei, Jingjie Zhang, Nam Q. Le, Pamela M. Norris, Patrick E. Hopkins, and Avik W. Ghosh. Role of crystal structure and junction morphology on interface thermal conductance. *Physical Review B - Condensed Matter and Materials Physics*, 92(14):1–10, 2015.
- [82] Sridhar Sadashivam, Yuhang Che, Zhen Huang, Liang Chen, Satish Kumar, and T S Fisher. The Atomistic Green’s Function Method for Interfacial Phonon Transport. *Annual Review of Heat Transfer*, 17, 2014.
- [83] K. Sääskilahti, J. Oksanen, J. Tulkki, and S. Volz. Role of anharmonic phonon scattering in the spectrally decomposed thermal conductance at planar interfaces. *Physical Review B - Condensed Matter and Materials Physics*, 90(13):1–8, 2014.
- [84] B. Deng, A. Chernatynskiy, P. Shukla, S.B. Sinnott, and S.R. Phillipot. Effects of edge dislocations on thermal transport in  $\text{UO}_2$ . *Journal of Nuclear Materials*, 434(1-3):203–209, mar 2013.
- [85] Tao Wang, Jesús Carrete, Ambroise Van Roekeghem, Natalio Mingo, and Georg K H Madsen. Ab initio phonon scattering by dislocations. *Physical Review B*, 95:1–7, 2017.
- [86] J. Moore and D. Kuhlmann-Wilsdorf. Theory of Dislocation Cells. II. Dislocation Multipoles. *Journal of Applied Physics*, 42(3):953–961, 1971.
- [87] J. Friedel. *Dislocations*. Pergamon, Oxford, New York, 1964.
- [88] Masayoshi Sato and Koji Sumino. Effect of Dislocations on the Low Temperature Thermal Conductivity in Germanium. *Journal of the Physical Society of Japan*, 36(4):1075–1083, 1974.
- [89] Da-ming Zhu and A C Anderson. Scattering of Phonons by Sessile Dislocations in Deformed Germanium. *Journal of Low Temperature Physics*, 82:37–47, 1991.
- [90] D. Xu, Riley Hanus, Y. Xiao, S. Wang, G.J. Snyder, and Q. Hao. Thermal boundary resistance correlated with strain energy in individual Si film-wafer twist boundaries. *Materials Today Physics*, 6:53–59, 2018.

- [91] Akira Otsuki. Misorientation dependence of energies of Si(001) twist grain boundaries. *Interface Science*, 9(3-4):293–296, 2001.
- [92] H. K. Liu, Y. Lin, and S. N. Luo. Grain boundary energy and grain size dependences of thermal conductivity of polycrystalline graphene. *Journal of Physical Chemistry C*, 118(42):24797–24802, 2014.
- [93] Sheng-Hong Ju and Xin-Gang Liang. Investigation on interfacial thermal resistance and phonon scattering at twist boundary of silicon. *Journal of Applied Physics*, 113(5):053513, 2013.
- [94] Lisa J. Porter, Joao F. Justo, and Sidney Yip. The importance of Grüneisen parameters in developing interatomic potentials. *Journal of Applied Physics*, 82(11):5378–5381, 1997.
- [95] Gangjian Tan, Shiqiang Hao, Riley C. Hanus, Xiaomi Zhang, Shashwat Anand, Trevor P. Bailey, Alexander J. E. Rettie, Xianli Su, Ctirad Uher, Vinayak P. Dravid, G. Jeffrey Snyder, Chris Wolverton, and Mercouri G. Kanatzidis. High Thermoelectric Performance in SnTe–AgSbTe<sub>2</sub> Alloys from Lattice Softening, Giant Phonon–Vacancy Scattering, and Valence Band Convergence. *ACS Energy Letters*, 3(3):705–712, 2018.
- [96] John Androulakis, Robert Pcionek, Eric Quarez, Jun Huang Do, Huijun Kong, Oleg Palchik, C. Uher, Jonathan James D’Angelo, Jarrod Short, Tim Hogan, and Mercouri G. Kanatzidis. Coexistence of large thermopower and degenerate doping in the nanostructured material Ag<sub>0.85</sub>SnSb<sub>1.15</sub>Te<sub>3</sub>. *Chemistry of Materials*, 18(20):4719–4721, 2006.
- [97] Takeshi Ishihara. Lattice Thermal Conductivity in AgSbTe<sub>2</sub>–SnTe as Deduced from the Calculation of Electronic Thermal Conductivity. *J. Phys. Soc. Japan*, 17:719–720, 1962.
- [98] DH Damon. Thermal Conductivity of SnTe between 100 and 500K. *Journal of Applied Physics*, 37(8):3181–3190, 1966.
- [99] C. A. Ratsifaritana and P. G. Klemens. Scattering of phonons by vacancies. *International Journal of Thermophysics*, 8(6):737–750, 1987.
- [100] Riley Hanus, Matthias T. Agne, Alexander J. E. Rettie, Zhiwei Chen, Gangjian Tan, Duck Young Chung, Mercouri G. Kanatzidis, Yanzhong Pei, Peter W. Voorhees, and G. Jeffrey Snyder. Lattice Softening Significantly Reduces Thermal Conductivity and Leads to High Thermoelectric Efficiency. *Advanced Materials*, 1900108:1900108, 2019.
- [101] Gangjian Tan, Fengyuan Shi, Shiqiang Hao, Li-Dong Zhao, Hang Chi, Xiaomi Zhang, Ctirad Uher, Chris Wolverton, Vinayak P. Dravid, and Mercouri G. Kanatzidis. Non-equilibrium processing leads to record high thermoelectric figure of merit in PbTe-SrTe. *Nature Communications*, 7(1):12167, dec 2016.

- [102] Zhiwei Chen, Zhengzhong Jian, Wen Li, Yunjie Chang, Binghui Ge, Riley Hanus, Jiong Yang, Yue Chen, Mingxin Huang, Gerald Jeffrey Snyder, and Yanzhong Pei. Lattice Dislocations Enhancing Thermoelectric PbTe in Addition to Band Convergence. *Advanced Materials*, 29(23):1606768, jun 2017.
- [103] Yanzhong Pei, Aaron LaLonde, Shiho Iwanaga, and G. Jeffrey Snyder. High thermoelectric figure of merit in heavy hole dominated PbTe. *Energy and Environmental Science*, 4(6):2085, 2011.
- [104] Zhiwei Chen, Binghui Ge, Wen Li, Siqi Lin, Jiawen Shen, Yunjie Chang, Riley Hanus, G. Jeffrey Snyder, and Yanzhong Pei. Vacancy-induced dislocations within grains for high-performance PbSe thermoelectrics. *Nature Communications*, 8:13828, 2017.
- [105] Eric S. Toberer, Alex Zevalkink, and G. Jeffrey Snyder. Phonon engineering through crystal chemistry. *Journal of Materials Chemistry*, 21(40):15843, 2011.
- [106] Zihang Liu, Jun Mao, Te-Huan Liu, Gang Chen, and Zhifeng Ren. Nano-microstructural control of phonon engineering for thermoelectric energy harvesting. *MRS Bulletin*, 43(03):181–186, 2018.
- [107] Yee Kan Koh, C. J. Vineis, S. D. Calawa, M. P. Walsh, and David G. Cahill. Lattice thermal conductivity of nanostructured thermoelectric materials based on PbTe. *Applied Physics Letters*, 94(15):2007–2010, 2009.
- [108] Song Yi Back, Hyunyong Cho, Young-Kwang Kim, Seokyeong Byeon, Hyungyu Jin, Kunihito Koumoto, and Jong-Soo Rhyee. Enhancement of thermoelectric properties by lattice softening and energy band gap control in Te-deficient InTe<sub>1- $\delta$</sub> . *AIP Advances*, 8(11):115227, 2018.
- [109] Sangyeop Lee, Keivan Esfarjani, Tengfei Luo, Jiawei Zhou, Zhiting Tian, and Gang Chen. Resonant bonding leads to low lattice thermal conductivity. *Nature communications*, 5:3525, 2014.
- [110] C. Mion, J. F. Muth, E. A. Preble, and D. Hanser. Accurate dependence of gallium nitride thermal conductivity on dislocation density. *Applied Physics Letters*, 89(9), 2006.
- [111] David R Clarke. Materials selection guidelines for low thermal conductivity thermal barrier coatings. *Surface and Coatings Technology*, 163-164:67–74, 2003.
- [112] Ho Soon Yang, G. R. Bai, L. J. Thompson, and J. a. Eastman. Interfacial thermal resistance in nanocrystalline yttria-stabilized zirconia. *Acta Materialia*, 50(9):2309–2317, 2002.
- [113] Cristian Pantea, Dwight G. Rickel, Albert Migliori, Robert G. Leisure, Jianzhong Zhang, Yusheng Zhao, Sami El-Khatib, and Baosheng Li. Digital ultrasonic pulse-echo overlap system

- and algorithm for unambiguous determination of pulse transit time. *Review of Scientific Instruments*, 76(11):114902, 2005.
- [114] Cormac Toher, Jose J. Plata, Ohad Levy, Maarten de Jong, Mark Asta, Marco Buongiorno Nardelli, and Stefano Curtarolo. High-throughput computational screening of thermal conductivity, Debye temperature, and Grüneisen parameter using a quasiharmonic Debye model. *Physical Review B*, 90(17):174107, 2014.
  - [115] Samuel A. Miller, Prashun Gorai, Brenden R. Ortiz, Anuj Goyal, Duanfeng Gao, Scott A. Barnett, Thomas O. Mason, G. Jeffrey Snyder, Qin Lv, Vladan Stevanović, and Eric S. Toberer. Capturing Anharmonicity in a Lattice Thermal Conductivity Model for High-Throughput Predictions. *Chemistry of Materials*, 29(6):2494–2501, 2017.
  - [116] Bland Houston, R. E. Strakna, and Henry S. Belson. Elastic constants, thermal expansion, and Debye temperature of lead telluride. *Journal of Applied Physics*, 39(8):3913–3916, 1968.
  - [117] Jan W. Jaeken and Stefaan Cottenier. Solving the Christoffel equation: Phase and group velocities. *Computer Physics Communications*, 207:445–451, 2016.
  - [118] K. Brugger. Generalized Grüneisen Parameters in the Anisotropic Debye Model. *Physical Review*, 137(6A):A1826–A1827, 1965.
  - [119] T. Ungár. Microstructural parameters from X-ray diffraction peak broadening. *Scripta Materialia*, 51(8 SPEC. ISS.):777–781, 2004.
  - [120] Tamil Many K Thandavan, Siti Meriam Abdul Gani, Chiow San Wong, and Roslan Md Nor. Evaluation of Williamson-Hall Strain and Stress Distribution in ZnO Nanowires Prepared Using Aliphatic Alcohol. *Journal of Nondestructive Evaluation*, 34(2):1–9, 2015.
  - [121] A. Khorsand Zak, W. H. Abd. Majid, M. E. Abrishami, and Ramin Yousefi. X-ray analysis of ZnO nanoparticles by Williamson-Hall and size-strain plot methods. *Solid State Sciences*, 13(1):251–256, 2011.
  - [122] Vitalij K. Pecharsky and Peter Y. Zavalij. *Fundamentals of Powder Diffraction and Structural Characterization of Materials*. Springer US, Boston, MA, 2nd edition, 2009.
  - [123] Mingda Li, Zhiwei Ding, Qingping Meng, Jiawei Zhou, Yimei Zhu, Hong Liu, M S Dresselhaus, and Gang Chen. Nonperturbative Quantum Nature of the Dislocation - Phonon Interaction. *Nano Letters*, 17(3):1587–1594, 2017.
  - [124] C. Zener. Relation between residual strain energy and elastic moduli. *Acta Crystallographica*, 2(3):163–166, 1949.

- [125] A. Granato and K. Lücke. Theory of mechanical damping due to dislocations. *Journal of Applied Physics*, 27(6):583–593, 1956.
- [126] Agnès Maurel, Vincent Pagneux, Felipe Barra, and Fernando Lund. Wave propagation through a random array of pinned dislocations: Velocity change and attenuation in a generalized Granato and Lücke theory. *Physical Review B - Condensed Matter and Materials Physics*, 72(17):1–15, 2005.
- [127] P.G. Klemens. Thermal Conductivity and Lattice Vibrational Modes. In *Solid State Physics*, volume 7, pages 1–98. 1958.
- [128] A. Gibin, G.G. Devyatkh, A.V. Gusev, R.K. Kremer, M. Cardona, and H.-J. Pohl. Heat capacity of isotopically enriched  $^{28}\text{Si}$ ,  $^{29}\text{Si}$ , and  $^{30}\text{Si}$  in the temperature range  $4\text{K} < T < 100\text{K}$ . *Solid State Communications*, 133(9):569–572, 2005.
- [129] Tania Claudio, Niklas Stein, Daniel G Stroppa, Benedikt Klobes, Michael Marek Koza, Petra Kudejova, Nils Petermann, Hartmut Wiggers, Gabi Schierning, and Raphaël P Hermann. Nanocrystalline silicon: lattice dynamics and enhanced thermoelectric properties. *Phys. Chem. Chem. Phys.*, 16(47):25701–25709, 2014.
- [130] Xin-Ke Wang, Igor Veremchuk, Matej Bobnar, Jing-Tai Zhao, and Yuri Grin. Solid solution  $\text{Pb}_{1-x}\text{Eu}_x\text{Te}$ : constitution and thermoelectric behavior. *Inorganic Chemistry Frontiers*, 3(9):1152–1159, 2016.
- [131] Matthias T. Agne, Riley Hanus, and G. Jeffrey Snyder. Minimum thermal conductivity in the context of diffuson-mediated thermal transport. *Energy and Environmental Science*, 11(3):609–616, 2018.
- [132] Pierre M Kibasomba, Simon Dhlamini, Malik Maaza, Chuan-pu Liu, Mohamed M Rashad, Diaa A Rayan, and Bonex W Mwakikunga. Strain and grain size of  $\text{TiO}_2$  nanoparticles from TEM, Raman spectroscopy and XRD: The revisiting of the Williamson-Hall plot method. *Results in Physics*, 9:628–635, 2018.
- [133] Gwénaël Gouadec and Philippe Colombe. Raman Spectroscopy of nanomaterials: How spectra relate to disorder, particle size and mechanical properties. *Progress in Crystal Growth and Characterization of Materials*, 53(1):1–56, 2007.
- [134] Yi Zhang, Xuezhi Ke, Changfeng Chen, J. Yang, and P. R.C. Kent. Thermodynamic properties of  $\text{PbTe}$ ,  $\text{PbSe}$ , and  $\text{PbS}$ : First-principles study. *Physical Review B - Condensed Matter and Materials Physics*, 80(2):1–12, 2009.

- [135] Ronan M. Murphy, Éamonn D. Murray, Stephen Fahy, and Ivana Savić. Broadband phonon scattering in PbTe-based materials driven near ferroelectric phase transition by strain or alloying. *Physical Review B*, 93(10):104304, 2016.
- [136] Gerda Rogl, Daria Setman, Erhard Schaffler, Jelena Horky, Michael Kerber, Michael Zehetbauer, Matthias Falmbigl, Peter Rogl, Esmaeil Royanian, and Ernst Bauer. High-pressure torsion, a new processing route for thermoelectrics of high ZTs by means of severe plastic deformation. *Acta Materialia*, 60(5):2146–2157, 2012.
- [137] L. P. Hu, X. H. Liu, H. H. Xie, J. J. Shen, T. J. Zhu, and X. B. Zhao. Improving thermoelectric properties of n-type bismuth-telluride-based alloys by deformation-induced lattice defects and texture enhancement. *Acta Materialia*, 60(11):4431–4437, 2012.
- [138] Tania Claudio, Niklas Stein, Nils Petermann, Daniel G. Stroppa, Michael Marek Koza, Hartmut Wiggers, Benedikt Klobes, Gabi Schierning, and Raphaël P. Hermann. Lattice dynamics and thermoelectric properties of nanocrystalline silicon-germanium alloys. *Physica Status Solidi (A) Applications and Materials Science*, 213(3):515–523, 2016.
- [139] B. Klobes, D. Bessas, F. Juranyi, H. Görlitz, V. Pacheco, and R. P. Hermann. Effect of nanocrystallinity on lattice dynamics in Bi<sub>2</sub>Te<sub>3</sub> based thermoelectrics. *Physica Status Solidi - Rapid Research Letters*, 9(1):57–61, 2015.
- [140] Fariborz Kargar, Elias H. Penilla, Ece Aytan, Jacob S. Lewis, Javier E. Garay, and Alexander A. Balandin. Acoustic phonon spectrum engineering in bulk crystals via incorporation of dopant atoms. *Applied Physics Letters*, 112(19):191902, 2018.
- [141] C Mathioudakis and P.C Kelires. Softening of elastic moduli of amorphous semiconductors. *Journal of Non-Crystalline Solids*, 266-269:161–165, 2000.
- [142] Dariusz Oleszak and Paul H. Shingu. Nanocrystalline metals prepared by low energy ball milling. *Journal of Applied Physics*, 79(6):2975–2980, 1996.
- [143] Brian H. Toby and Robert B. Von Dreele. GSAS-II: The genesis of a modern open-source all purpose crystallography software package. *Journal of Applied Crystallography*, 46(2):544–549, 2013.
- [144] Sebastian Christensen, Niels Bindzus, Mattia Sist, Masaki Takata, and Bo Brummerstedt Iversen. Structural disorder, anisotropic micro-strain and cation vacancies in thermo-electric lead chalcogenides. *Phys. Chem. Chem. Phys.*, 18(23):15874–15883, 2016.
- [145] Orson L. Anderson. A simplified method for calculating the Debye temperature from elastic constants. *J. Phys. Chem. Solids*, 24:909–917, 1963.

- [146] ASTM Standard. E112-13, Standard Test Method for Determin ing Average Grain Size.” West Conshohocken, PA. pages 1–28, 2013.
- [147] B. Abeles. Lattice Thermal Conductivity of Disordered Semiconductor Alloys at High Temperatures. *Physical Review*, 131(5):1906–1911, 1963.
- [148] Sabah K. Bux, Richard G. Blair, Pawan K. Gogna, Hohyun Lee, Gang Chen, Mildred S. Dresselhaus, Richard B. Kaner, and Jean Pierre Fleurial. Nanostructured bulk silicon as an effective thermoelectric material. *Advanced Functional Materials*, 19(15):2445–2452, 2009.
- [149] Wei Lv and Asegun S. Henry. Examining the validity of the phonon gas model in amorphous materials. *Scientific reports*, page (under review), 2016.
- [150] Hamid Reza Seyf, Luke Yates, Thomas L. Bougner, Samuel Graham, Baratunde A. Cola, Theeradetch Detchprohm, Mi Hee Ji, Jeomoh Kim, Russell Dupuis, Wei Lv, and Asegun Henry. Rethinking phonons: The issue of disorder. *npj Computational Materials*, 3(1), 2017.
- [151] David G. Cahill, S. K. Watson, and R. O. Pohl. Lower limit to the thermal conductivity of disordered crystals. *Physical Review B*, 46(10):6131–6140, 1992.
- [152] Zhe Cheng, Alex Weidenbach, Tianli Feng, M. Brooks Tellekamp, Sebastian Howard, Matthew J. Wahila, Bill Zivasatiengraj, Brian Foley, Sokrates T. Pantelides, Louis F. J. Piper, William Doolittle, and Samuel Graham. Diffuson-driven ultralow thermal conductivity in amorphous  $Nb_2O_5$  thin films. *Physical Review Materials*, 3(2):025002, feb 2019.
- [153] Joseph L. Feldman, Mark D. Kluge, Philip B. Allen, and Frederick Wooten. Thermal conductivity and localization in glasses: Numerical study of a model of amorphous silicon. *Physical Review B*, 48(17):12589–12602, 1993.
- [154] Shawna R. Brown, Susan M. Kauzlarich, Franck Gascoin, and G. Jeffrey Snyder.  $Yb_{14}MnSb_{11}$  : New High Efficiency Thermoelectric Material for Power Generation. *Chemistry of Materials*, 18(7):1873–1877, 2006.
- [155] Eric S. Toberer, Shawna R. Brown, Teruyuki Ikeda, Susan M. Kauzlarich, and G. Jeffrey Snyder. High thermoelectric efficiency in lanthanum doped  $Yb_{14}MnSb_{11}$ . *Applied Physics Letters*, 93(6):062110, 2008.
- [156] Jason H. Grebenkemper, Yufei Hu, Dashiell Barrett, Pawan Gogna, Chen-Kuo Huang, Sabah K. Bux, and Susan M. Kauzlarich. High Temperature Thermoelectric Properties of  $Yb_{14}MnSb_{11}$  Prepared from Reaction of MnSb with the Elements. *Chemistry of Materials*, 27(16):5791–5798, 2015.

- [157] M. B. Stone, V. O. Garlea, B. Gillon, A. Cousson, A. D. Christianson, M. D. Lumsden, S. E. Nagler, D. Mandrus, and B. C. Sales. Excitations and magnetization density distribution in the dilute ferromagnetic semiconductor  $\text{Yb}_{14}\text{MnSb}_{11}$ . *Physical Review B*, 95(2):1–5, 2017.
- [158] E. Blochl, P. Projector-Augmented Plane-Wave Method. *Physical Review B*, 50(24d):17953, 1994.
- [159] G. Kresse and D. Joubert. From ultrasoft pseudopotentials to the projector augmented-wave method. *Physical Review B*, 59(3):1758–1775, 1999.
- [160] John P. Perdew, Kieron Burke, and Matthias Ernzerhof. Generalized Gradient Approximation Made Simple. *Physical Review Letters*, 77(18):3865–3868, 1996.
- [161] Atsushi Togo, Fumiyasu Oba, and Isao Tanaka. First-principles calculations of the ferroelastic transition between rutile-type and  $\text{CaCl}_2$ -type  $\text{SiO}_2$  at high pressures. *Physical Review B - Condensed Matter and Materials Physics*, 78(13):1–9, 2008.
- [162] Atsushi Togo and Isao Tanaka. First principles phonon calculations in materials science. *Scripta Materialia*, 108:1–5, 2015.
- [163] Richard Tumanjong Azuah, Larry R. Kneller, Yiming Qiu, Philip L. W. Tregenna-Piggott, Craig M. Brown, John R. D. Copley, and Robert M. Dimeo. DAVE: A Comprehensive Software Suite for the Reduction, Visualization, and Analysis of Low Energy Neutron Spectroscopic Data. *Journal of Research of the National Institute of Standards and Technology*, 114(6):341, 2009.
- [164] Ctirad Uher. Skutterudites : Prospective Novel Thermoelectrics. *Semiconductors and Semimetals*, 69:139–253, 2001.
- [165] Yinglu Tang, Zachary M Gibbs, Luis a Agapito, Guodong Li, Hyun-Sik Kim, Marco Buongiorno Nardelli, Stefano Curtarolo, and G Jeffrey Snyder. Convergence of multi-valley bands as the electronic origin of high thermoelectric performance in  $\text{CoSb}_3$  skutterudites. *Nature materials*, 14(October):6–12, 2015.
- [166] Peng-an Zong, Riley Hanus, Maxwell Dylla, Yunshan Tang, Jingcheng Liao, Qihao Zhang, G. Jeffrey Snyder, and Lidong Chen. Skutterudite with graphene-modified grain-boundary complexion enhances zT enabling high-efficiency thermoelectric device. *Energy Environ. Sci.*, 10(1):183–191, 2017.
- [167] Peng-an Zong, Xihong Chen, Yanwu Zhu, Ziwei Liu, Yi Zeng, and Lidong Chen. Construction of a 3D-rGO network-wrapping architecture in a  $\text{Yb}_y\text{Co}_4\text{Sb}_{12}$  /rGO composite for enhancing the thermoelectric performance. *J. Mater. Chem. A*, 00:1–7, 2015.

- [168] Yinglu Tang, Riley Hanus, Sinn-wen Chen, and G. Jeffrey Snyder. Solubility design leading to high figure of merit in low-cost Ce-CoSb<sub>3</sub> skutterudites. *Nature Communications*, 6(May):7584, 2015.
- [169] Michael K Miller, Kaye F Russell, Keith Thompson, Roger Alvis, and David J Larson. Review of atom probe FIB-based specimen preparation methods. *Microscopy and microanalysis : the official journal of Microscopy Society of America, Microbeam Analysis Society, Microscopical Society of Canada*, 13(6):428–436, 2007.
- [170] E Pop, V Varshney, and Ak Roy. Thermal properties of graphene: Fundamentals and applications. *Mrs Bulletin*, 1273(December):1–28, 2012.
- [171] D. D L Chung. Review: Graphite. *Journal of Materials Science*, 37(8):1475–1489, 2002.
- [172] Yun-Shan Tang, Sheng-Qiang Bai, and Du-Di Ren. Interface Structure and Electrical Property of Yb<sub>0.3</sub>Co<sub>4</sub>Sb<sub>12</sub>/Mo-Cu Element Prepared by Welding Using Ag-Cu-Zn Solder. *JOURNAL OF INORGANIC MATERIALS-BEIJING*, 30(3):256–260, 2015.
- [173] T. Ochi, G. Nie, S. Suzuki, M. Kikuchi, S. Ito, and J. Q. Guo. Power-generation performance and durability of a skutterudite thermoelectric generator. *Journal of Electronic Materials*, 43(6):2344–2347, 2014.
- [174] James R. Salvador, Jung Y. Cho, Zuxin Ye, Joshua E. Moczygemb, Alan J. Thompson, Jeffrey W. Sharp, Jan D. Koenig, Ryan Maloney, Travis Thompson, Jeffrey Sakamoto, Hsin Wang, and Andrew A. Wereszczak. Conversion efficiency of skutterudite-based thermoelectric modules. *Physical chemistry chemical physics : PCCP*, 16(1):12510–20, 2014.
- [175] Xiaokai Hu, Priyanka Jood, Michihiro Ohta, Masaru Kunii, Kazuo Nagase, Hirotaka Nishiate, Mercouri G. Kanatzidis, and Atsushi Yamamoto. Power generation from nanostructured PbTe-based thermoelectrics: comprehensive development from materials to modules. *Energy Environ. Sci.*, 9:1–11, 2015.
- [176] Chenguang Fu, Shengqiang Bai, Yintu Liu, Yunshan Tang, Lidong Chen, Xinbing Zhao, and Tiejun Zhu. Realizing high figure of merit in heavy-band p-type half-Heusler thermoelectric materials. *Nature communications*, 6:8144, 2015.
- [177] Riley Hanus, Xingyu Guo, Yinglu Tang, Guodong Li, G. Jeffrey Snyder, and Wolfgang G. Zeier. A Chemical Understanding of the Band Convergence in Thermoelectric CoSb<sub>3</sub> Skutterudites: Influence of Electron Population, Local Thermal Expansion, and Bonding Interactions. *Chemistry of Materials*, 29(3):1156–1164, feb 2017.

- [178] Yinglu Tang, Zachary M. Gibbs, Luis A. Agapito, Guodong Li, Hyun-Sik Kim, Marco Buon-giorno Nardelli, Stefano Curtarolo, and G. Jeffrey Snyder. Convergence of multi-valley bands as the electronic origin of high thermoelectric performance in CoSb<sub>3</sub> skutterudites. *Nature Materials*, 14(12):1223–1228, 2015.
- [179] Robert Von Dreele, Matthew Suchomel, and Brian Toby. Advanced Photon Source: Compute X-ray Absorption. <http://11bm.xray.aps.anl.gov/absorb/absorb.php>, 2013.
- [180] A. C. Larson and R. B. Von Dreele. General Structure Analysis System (GSAS). *Los Alamos National Laboratory Report*, LAUR 86-74, 2004.
- [181] B. H. Toby. 'EXPGUI', a graphical user interface for GSAS. *Journal of Applied Crystallography*, 34:210–213, 2001.
- [182] Guodong Li, Saurabh Bajaj, Umut Aydemir, Shiqiang Hao, Hai Xiao, William A. Goddard, Pengcheng Zhai, Qingjie Zhang, and G. Jeffrey Snyder. p-Type Co Interstitial Defects in Thermoelectric Skutterudite CoSb<sub>3</sub> Due to the Breakage of Sb<sub>4</sub>-Rings. *Chemistry of Materials*, 28(7):2172–2179, 2016.
- [183] Yinglu Tang, Yuting Qiu, Lili Xi, Xun Shi, Wenqing Zhang, Lidong Chen, Ssu-Ming Tseng, Sinn-wen Chen, and G. Jeffrey Snyder. Phase diagram of In–Co–Sb system and thermoelectric properties of In-containing skutterudites. *Energy Environ. Sci.*, 7(2):812–819, 2014.
- [184] J. O. Sofo and G. D. Mahan. Electronic structure of CoSb<sub>3</sub>: A narrow-band-gap semiconductor. *Physical Review B*, 58(23):15620–15623, 1998.
- [185] Zachary M. Gibbs, Hyun Sik Kim, Heng Wang, and G. Jeffrey Snyder. Band gap estimation from temperature dependent Seebeck measurement - Deviations from the  $2e|S|\max T_{\max}$  relation. *Applied Physics Letters*, 106(2):0–5, 2015.
- [186] Richard Dronskowski and Peter E. Bloechl. Crystal orbital Hamilton populations (COHP): energy-resolved visualization of chemical bonding in solids based on density-functional calculations. *The Journal of Physical Chemistry*, 97(33):8617–8624, 1993.
- [187] Paulo V C Medeiros, Sven Stafstrom, and Jonas Bjork. Effects of extrinsic and intrinsic perturbations on the electronic structure of graphene: Retaining an effective primitive cell band structure by band unfolding. *Physical Review B - Condensed Matter and Materials Physics*, 89(4), 2014.
- [188] I. Oftedal. The crystal structure of skutterudite and related minerals. *Norsk Geologisk Tidsskrift*, 8:250–257, 1926.

- [189] Yinglu Tang, Sinn-wen Chen, and G. Jeffrey Snyder. Temperature dependent solubility of Yb in Yb–CoSb<sub>3</sub> skutterudite and its effect on preparation, optimization and lifetime of thermoelectrics. *Journal of Materomics*, 1(1):75–84, 2015.
- [190] A. Mochel, I. Sergueev, N. Nguyen, Gary J. Long, Fernande Grandjean, D. C. Johnson, and R. P. Hermann. Lattice dynamics in the FeSb<sub>3</sub> skutterudite. *Physical Review B - Condensed Matter and Materials Physics*, 84(6):1–9, 2011.
- [191] V Keppens, D Mandrus, B C Sales, B C Chakoumakos, P Dai, R Coldea, M B Maple, D a Gajewski, E J Freeman, and S Bennington. Localized vibrational modes in metallic solids. *Nature*, 395(6705):876–878, 1998.
- [192] G. P. Meisner, D. T. Morelli, S. Hu, J. Yang, and C. Uher. Structure and Lattice Thermal Conductivity of Fractionally Filled Skutterudites: Solid Solutions of Fully Filled and Unfilled End Members. *Physical Review Letters*, 80(16):3551–3554, 1998.
- [193] Atsuko Ohno, Satoshi Sasaki, Eiji Nishibori, Shinobu Aoyagi, Makoto Sakata, and Bo Brummerstedt Iversen. X-ray charge density study of chemical bonding in skutterudite CoSb<sub>3</sub>. *Physical Review B*, 76(6):064119, 2007.
- [194] Alex Zevalkink, Wolfgang G. Zeier, Ethan Cheng, Jeffrey Snyder, Jean-Pierre Fleurial, and Sabah Bux. Nonstoichiometry in the Zintl Phase Yb<sub>1-x</sub>Zn<sub>2</sub>Sb<sub>2</sub> as a Route to Thermoelectric Optimization. *Chemistry of Materials*, 26(19):5710–5717, 2014.
- [195] M. Puyet, B. Lenoir, A. Dauscher, P. Weisbecker, and S.J. Clarke. Synthesis and crystal structure of Ca<sub>x</sub>Co<sub>4</sub>Sb<sub>12</sub> skutterudites. *Journal of Solid State Chemistry*, 177(6):2138–2143, 2004.
- [196] I. Sergueev, K. Glazyrin, I. Kantor, M. A. McGuire, A. I. Chumakov, B. Klobes, B. C. Sales, and R. P. Hermann. Quenching rattling modes in skutterudites with pressure. *Physical Review B - Condensed Matter and Materials Physics*, 91(22):2–8, 2015.
- [197] B C Sales, B C Chakoumakos, and D Mandrus. Thermoelectric properties of thallium-filled skutterudites. *Physical Review B*, 61(4):2475, 2000.
- [198] A. Mochel, I. Sergueev, H. C. Wille, J. Voigt, M. Prager, M. B. Stone, B. C. Sales, Z. Guguchia, A. Shengelaya, V. Keppens, and R. P. Hermann. Lattice dynamics and anomalous softening in the YbFe<sub>4</sub>Sb<sub>12</sub> skutterudite. *Physical Review B - Condensed Matter and Materials Physics*, 84(18), 2011.
- [199] G. Rogl, L. Zhang, P. Rogl, A. Grytsiv, M. Falmbigl, D. Rajs, M. Kriegisch, H. Muller, E. Bauer, J. Koppensteiner, W. Schranz, M. Zehetbauer, Z. Henkie, and M. B. Maple. Thermal expansion of skutterudites. *Journal of Applied Physics*, 107(4):043507, 2010.

- [200] Wolfgang G. Zeier, Jennifer Schmitt, Geoffroy Hautier, Umut Aydemir, Zachary M. Gibbs, Claudia Felser, and G. Jeffrey Snyder. Engineering half-Heusler thermoelectric materials using Zintl chemistry. *Nature Reviews Materials*, 1(6):16032, 2016.
- [201] Huixia Luo, Jason W. Krizan, Lukas Muechler, Neel Haldolaarachchige, Tomasz Klimczuk, Weiwei Xie, Michael K. Fuccillo, Claudia Felser, and Robert J. Cava. A large family of filled skutterudites stabilized by electron count. *Nature Communications*, 6:6489, 2015.
- [202] Wolfgang Tremel and Roald Hoffmann. Square Nets of Main Group Elements in Solid Materials. *Journal of American Chemical Society*, 109:124–140, 1987.
- [203] Dongwoon Jung, Myung Hwan Whangbo, and Santiago Alvarez. Importance of the  $X_4$  ring orbitals for the semiconducting, metallic, or superconducting properties of skutterudites  $MX_3$  and  $RM_4X_{12}$ . *Inorganic Chemistry*, 29(12):2252–2255, 1990.
- [204] Xiaoya Shi, Jiong Yang, Lijun Wu, James R Salvador, Cheng Zhang, William L Villaire, Daad Haddad, Jihui Yang, Yimei Zhu, and Qiang Li. Band Structure Engineering and Thermoelectric Properties of Charge-Compensated Filled Skutterudites. *Scientific Reports*, 5(October):14641, 2015.
- [205] Massoud Kaviany. *Heat Transfer Physics*. Cambridge University Press, New York, 1st edition, 2008.
- [206] N. W. Ashcroft and N. D. Mermin. *Solid State Physics*. Thomson Learning, Inc., 1976.
- [207] Micheline Roufosse and P. G. Klemens. Thermal Conductivity of Complex Dielectric Crystals. *Physical Review B*, 7(12):5379–5386, 1973.
- [208] Rohn Truell, Charles Elbaum, and Bruce B. Chick. *Ultrasonic Methods in Solid State Physics*. Academic Press Inc., New York, New York, 1969.
- [209] Matthias T Agne, Kazuki Imasato, Shashwat Anand, Kathleen Lee, Sabah K Bux, Alexander J E Rettie, Duck Young Chung, Mercouri G Kanatzidis, and G. Jeffrey Snyder. Heat capacity of  $Mg_3Sb_2$ ,  $Mg_3Bi_2$  and their alloys at high temperature. *Materials Today Physics*, 6:DOI 10.1016/j.mtphys.2018.10.001, 2018.
- [210] Jesús Carrete, Bjorn Vermeersch, Ankita Katre, Ambroise van Roekeghem, Tao Wang, Georg K.H. Madsen, and Natalio Mingo. almaBTE : A solver of the space-time dependent Boltzmann transport equation for phonons in structured materials. *Computer Physics Communications*, 220:351–362, 2017.

- [211] A. Ward, D. A. Broido, Derek A. Stewart, and G. Deinzer. Ab initio theory of the lattice thermal conductivity in diamond. *Physical Review B - Condensed Matter and Materials Physics*, 80(12):1–8, 2009.
- [212] Z. Chen, Z. Wei, Y. Chen, and C. Dames. Anisotropic Debye model for the thermal boundary conductance. *Physical Review B - Condensed Matter and Materials Physics*, 87(12):1–14, 2013.

## Appendix A

### Reciprocal space and the first Brillouin zone

It is rather intuitive that information contained in a sound wave is more easily interpreted in the frequency domain, rather than the time domain. Transforming the pressure versus time information of a sound wave into frequency, or the inverse of time, essentially amounts to a Fourier transform. Similarly, much information about quasiparticles in crystals, such as (nearly free) electrons and phonons, is more easily interpreted in reciprocal space rather than real space.

We now take a moment to define a crystalline lattice, reciprocal lattice, and the first Brillouin zone. A primitive unit cell is defined by lattice vectors  $\mathbf{a}_1$ ,  $\mathbf{a}_2$ , and  $\mathbf{a}_3$ , which are sometimes broken down into at lattice basis multiplied by a lattice constant. The volume of the primitive unit cell is given by

$$V_{\text{PUC}} = (\mathbf{a}_1 \times \mathbf{a}_2) \cdot \mathbf{a}_3. \quad (\text{A.0.1})$$

We define the reciprocal lattice vectors as

$$\mathbf{b}_1 = \frac{\mathbf{a}_2 \times \mathbf{a}_3}{V_{\text{PUC}}} \quad (\text{A.0.2})$$

$$\mathbf{b}_2 = \frac{\mathbf{a}_3 \times \mathbf{a}_1}{V_{\text{PUC}}} \quad (\text{A.0.3})$$

$$\mathbf{b}_3 = \frac{\mathbf{a}_1 \times \mathbf{a}_2}{V_{\text{PUC}}} \quad (\text{A.0.4})$$

There may be more than one atom per unit cell. Each atom is designated by an atomic position vector  $\mathbf{r}$  which locates it relative to the origin of the unit cell. When there is one atom per primitive unit cell,  $\mathbf{r}$  is commonly taken to be 0. For multi-atomic unit cells there will be non-zero  $\mathbf{r}$ 's. In this way all atoms in a crystal are defined mathematically, and this information is typically contained in a POSCAR file. A reciprocal lattice is defined by applying translational symmetry to the reciprocal lattice vectors. If we were to pick a reciprocal lattice point and call it the origin  $\Gamma$ , the first Brillouin zone is defined as the locus of points in the reciprocal lattice that are closer to  $\Gamma$  than they are to any other reciprocal lattice point.

Imagine you have a linear chain of atoms spaced by  $a$ . The minimum wavelength of a vibration you can induce is  $\lambda = 2a$ , making the maximum wavevector in this linear chain  $\pi/a$ . This principle extends to 3 dimensions, and as a result all of information can be displayed in the first Brillouin zone (FBZ). This makes the maximum  $\mathbf{k}$ -vector pointing, for example, in the  $\mathbf{b}_1$  direction  $\mathbf{k} = \mathbf{b}_1/2$ , when we consider transport properties.

The definition for the reciprocal lattice and FBZ given above naturally contains information about crystal structure and is therefore anisotropic. However many models, in particular ones that focus on the specular treatment of  $\kappa$  (i.e. and integral over frequency), will make the isotropic approximation. This means that the model will only consider the magnitude of the  $\mathbf{k}$ -vector,  $k$ , and not its direction. Therefore, we define a maximum  $k$  by defining a sphere that has the same volume as the FBZ, and obtain

$$k_{\max} = \left( \frac{6\pi^2}{V_{\text{PUC}}} \right)^{1/3}, \quad (\text{A.0.5})$$

where  $V_{\text{PUC}} = NV$ ,  $N$  is the number of atoms in the primitive unit cell and  $V$  is the volume per atom. If one were to consider three phonon branches which span from  $k = 0$  to  $k = k_{\max}$ , then only acoustic phonons are considered. However, if  $V$  is substituted for  $V_{\text{PUC}}$  in Eq. A.0.5, and  $N > 1$  then optical modes are being included in the transport model, in essence. This point is often overlooked in the literature.

## Appendix B

### Lattice dynamics

The mathematical description of atomic vibrations of a crystal starts by Taylor expanding the potential energy of the crystal

$$U = U_0 + \sum_{\alpha} \sum_i (-F_i^{\alpha}) u_i^{\alpha} + \frac{1}{2!} \sum_{\alpha\beta} \sum_{ij} \Phi_{ij}^{\alpha\beta} u_i^{\alpha} u_j^{\beta} + \frac{1}{3!} \sum_{\alpha\beta\gamma} \sum_{ijk} \Phi_{ijk}^{\alpha\beta\gamma} u_i^{\alpha} u_j^{\beta} u_k^{\gamma} + \dots \quad (\text{B.0.1})$$

$i, j, k$  designate Cartesian directions and  $\alpha, \beta, \gamma$  designate atoms in the crystal.  $U_0$  is the reference potential energy and is set to zero. The linear term is also zero since we are Taylor expanding  $U$  about its equilibrium energy. At equilibrium, the bottom of this potential energy landscape, the slope is zero (think the bottom of a parabola). The slope of the potential energy with atomic displacement give the negative of the force on the atom

$$-F_i^{\alpha} = \frac{\partial U}{\partial u_i^{\alpha}}. \quad (\text{B.0.2})$$

Physically this means there is no net force on the atoms when they are all in their equilibrium positions,  $-F_i^{\alpha} = 0$ . Therefore, the first non-zero term in this expansion is the 2nd order, Harmonic term. The interatomic force constants contained in the 2nd and 3rd order terms are defined as derivatives of the potential energy with respect to atomic displacements

$$\Phi_{ij}^{\alpha\beta} = \frac{\partial^2 U}{\partial u_i^{\alpha} \partial u_j^{\beta}} \quad (\text{B.0.3})$$

$$\Phi_{ijk}^{\alpha\beta\gamma} = \frac{\partial^3 U}{\partial u_i^{\alpha} \partial u_j^{\beta} \partial u_k^{\gamma}}. \quad (\text{B.0.4})$$

If we truncate  $\mathcal{H}$  at  $U_{2\text{nd}}$  then we can write the equation of motion given in Eq. 2.15. To solve this differential equation we exploit the lattice translational invariance of a perfect infinite crystal to

tak the solution as a Fourier decomposed plane wave,

$$u_i^\alpha = \frac{1}{\sqrt{m_\alpha}} \sum_{\mathbf{k}} A_{\mathbf{k}} \epsilon_{i,\mathbf{k}}^\alpha e^{i(\mathbf{k} \cdot \mathbf{R}_\alpha - \omega t)}. \quad (\text{B.0.5})$$

Note that  $A_{\mathbf{k}}$  is the mode amplitude (scalar),  $\epsilon_{i,\mathbf{k}}^\alpha$  is the polarization vector (denoted by the Cartesian index  $i$ ) of atom  $\alpha$ , and  $\mathbf{R}_\alpha$  is the lattice vector pointing to the unit cell in which atom  $\alpha$  resides.  $\mathbf{k}$  is the wavevector,  $2\pi$  over the wavelength,  $\mathbf{k} = 2\pi/\lambda$ , and is confined to the first Brillouin zone (FBZ), defined in Appendix A. The acceleration vector can be found by differentiating this twice with respect to time  $t$

$$\ddot{u}_i^\alpha = \frac{-\omega^2}{\sqrt{m_\alpha}} \sum_{\mathbf{k}} A_{\mathbf{k}} \epsilon_{i,\mathbf{k}}^\alpha e^{i(\mathbf{k} \cdot \mathbf{R}_\alpha - \omega t)}. \quad (\text{B.0.6})$$

Substituting these into Eq. 2.15 we have

$$\sum_{\mathbf{k}} \omega^2 A_{\mathbf{k}} \epsilon_{i,\mathbf{k}}^\alpha e^{i\mathbf{k} \cdot \mathbf{R}_\alpha} = \sum_{j\beta} \sum_{\mathbf{k}} \Phi_{ij}^{\alpha\beta} \frac{A_{\mathbf{k}} \epsilon_{j,\mathbf{k}}^\beta}{\sqrt{m_\alpha m_\beta}} e^{i\mathbf{k} \cdot \mathbf{R}_\beta}, \quad (\text{B.0.7})$$

where we have moved the factors of mass to the right side and cancelled the factor  $e^{-i\omega t}$ . Switching the  $\mathbf{k}$  to  $\mathbf{k}'$  and multiplying by  $e^{-i\mathbf{k} \cdot \mathbf{R}_\alpha}$  we have

$$\sum_{\mathbf{k}'} \omega^2 A_{\mathbf{k}'} \epsilon_{i,\mathbf{k}'}^\alpha e^{i\mathbf{k}' \cdot \mathbf{R}_\alpha} e^{-i\mathbf{k} \cdot \mathbf{R}_\alpha} = \sum_{j\beta} \sum_{\mathbf{k}'} \Phi_{ij}^{\alpha\beta} \frac{A_{\mathbf{k}'} \epsilon_{j,\mathbf{k}'}^\beta}{\sqrt{m_\alpha m_\beta}} e^{i\mathbf{k}' \cdot \mathbf{R}_\beta} e^{-i\mathbf{k} \cdot \mathbf{R}_\alpha}. \quad (\text{B.0.8})$$

Since the plane wave states are orthogonal only the cases in the summations where  $\mathbf{k} = \mathbf{k}'$  survive, and the amplitudes cancel

$$\omega^2 \epsilon_{i,\mathbf{k}}^\alpha = \sum_{j\beta} \frac{\Phi_{ij}^{\alpha\beta}}{\sqrt{m_\alpha m_\beta}} e^{i\mathbf{k} \cdot (\mathbf{R}_\beta - \mathbf{R}_\alpha)} \epsilon_{j,\mathbf{k}}^\beta. \quad (\text{B.0.9})$$

As one can see the solution only depends on the relative placement of the unit cells in the lattice ( $\mathbf{R}_\beta - \mathbf{R}_\alpha$ ), i.e. it does not matter what unit cell you call the origin.  $\mathbf{R}_\alpha$  is therefore taken to be zero. Additionally, the atomic index  $\alpha$  loses its dependence on unit cell and therefore becomes and simply an atomic site index, which spans the number of atoms in the primitive unit cell  $N$ . We define the dynamical matrix as

$$\Phi_{ij}^{\alpha\beta}(\mathbf{k}) = \frac{\Phi_{ij}^{\alpha\beta}}{\sqrt{m_\alpha m_\beta}} e^{i\mathbf{k} \cdot \mathbf{R}_\beta}, \quad (\text{B.0.10})$$

which is a  $3N \times 3N$  matrix. When this matrix is diagonalized, there will be  $3N$  eigenvalues and eigenvectors labeled by a branch index  $s$ . The eigenvalues are the phonon frequency squared  $\omega^2(\mathbf{k}s)$

and eigenvectors are the phonon mode shapes  $\epsilon_i^\alpha(\mathbf{k}s)$

$$\omega^2(\mathbf{k}s)\epsilon_i^\alpha(\mathbf{k}s) = \sum_{j\beta} \Phi_{ij}^{\alpha\beta}(\mathbf{k})\epsilon_j^\beta(\mathbf{k}s). \quad (\text{B.0.11})$$

By this procedure, the phonon frequency can be computed at any  $\mathbf{k}$  if the crystal structure and 2nd order IFCs  $\Phi_{ij}^{\alpha\beta}$  are known.

## Appendix C

### Phonon Boltzmann transport equation

Most of this derivation follows Kaviany [205], pg. 189. Aschroft and Mermin also cover this from a kinetic theory of gases type perspective, [206] pg. 499.

Let us consider a system which conducts heat through independent conduction channels. If we consider phonons in a crystal as the heat carriers, then the conduction channels are non-interacting phonon modes denoted by their wavevector  $\mathbf{k}$  and branch index  $s$ ,  $\mathbf{ks}$ . These non-interacting modes are sometimes referred to as normal modes or eigenstates, each of which has an eigenvector (mode shape) and eigenvalue (mode energy or frequency). At a given temperature, every channel will have an equilibrium number of carriers. Since phonons are bosons, this equilibrium number is given by the Bose-Einstein distribution function,

$$n_{\text{BE}}(\mathbf{ks}, T) = \frac{1}{e^x - 1}, \quad x = \frac{\hbar\omega(\mathbf{ks})}{k_B T}, \quad (\text{C.0.1})$$

where  $\hbar$  is the reduced Planck's constant ( $h/2\pi$ ),  $\omega(\mathbf{ks})$  is the frequency of phonon mode  $\mathbf{ks}$ ,  $k_B$  is Boltzmann's constant, and  $T$  is the temperature. If thermal energy is injected into the system at a particular location  $\mathbf{r}$ , the occupation number of phonons  $n$  will be pushed away from its equilibrium number  $n_{\text{BE}}$ . We express  $n$  as the sum of the equilibrium occupation number (time  $t$  independent) and its deviation from this equilibrium ( $t$  dependent),  $n(\mathbf{ks}, T, t) = n_{\text{BE}}(\mathbf{ks}, T) + n'(\mathbf{ks}, t)$ . This deviation from  $n_{\text{BE}}$  will induce a thermal heat flux, denoted by the vector  $j^i$  (or equivalently  $\mathbf{j}$ ). In the phonon-gas model, this vector is given simply by the product of the phonon modes energy  $E(\mathbf{ks}) = \hbar\omega(\mathbf{ks})$ , the phonon group velocity  $v_g^i$  at which the carrier travels, and the number of phonons contributing to transport  $n(\mathbf{ks}, t)$ ,

$$j_{\text{ph}}^i = \frac{1}{V_{\mathbf{k}}} \sum_{\mathbf{ks}} E(\mathbf{ks}) v_g^i(\mathbf{ks}) n(\mathbf{ks}, T, t). \quad (\text{C.0.2})$$

$1/V_{\mathbf{k}}$  is the volume in  $\mathbf{k}$ -space that a phonon mode in the sum occupies and is defined as volume

of the FBZ ( $1/V_{\text{PUC}}$ ) divided by the number of  $\mathbf{k}$ -vectors in the sum ( $N_{\mathbf{k}}$ ),  $1/V_{\mathbf{k}} = 1/(N_{\mathbf{k}}V_{\text{PUC}})$ , when a uniform  $\mathbf{k}$ -grid is used. For example, when a  $30 \times 30 \times 30$  uniform  $\mathbf{k}$ -mesh is used  $N_{\mathbf{k}} = 30^3$ . Therefore the sum accounts for all phonon modes in the first Brillouin zone. Note, that if  $n = n_{\text{BE}}$  in Eq. C.0.2 then  $j^i = 0$  after the sum over  $\mathbf{k}s$  is performed. Or stated more simply, when the system is in equilibrium ( $n = n_{\text{BE}}$ ) there is no net thermal flux ( $j^i = 0$ ). Therefore,  $n$  can be replaced by  $n'$  in this equation without consequence, and both forms are seen in literature.

In order to determine a functional expression of the thermal conductivity,  $\kappa^{ij}$ , we seek a form of (C.0.2) that we can directly compare to Fourier's law in Eq. 2.1. While the form of Eqs. C.0.2 and 2.1 can be applied to other heat carriers (e.g. electrons), here we will focus on heat conduction by phonons,  $\kappa^{ij} = \kappa_{\text{ph}}^{ij}$ .

An equation for  $n'(\mathbf{k}s, t)$  can be found through the Boltzmann transport equation (BTE) simplified by recognizing that the external forces will be zero for phonons ( $F^i \nabla^i n = 0$ ),

$$v^i \nabla^i n = \left. \frac{dn}{dt} \right|_{\text{coll}}, \quad (\text{C.0.3})$$

where the velocity here is the group velocity of the phonon,  $v^i = v_g^i$ . This is one instance where we assert the phonon-gas model. If the length scale of the gradient in temperature is longer than the phonon mean free path, the phonons are able to relax to their equilibrium occupation. In this case  $n$  obtains spatial dependence only through the spatial dependence of  $T$ ,

$$v_g^i (\nabla^i n) = v_g^i \left( \frac{dn}{dT} \nabla^i T \right). \quad (\text{C.0.4})$$

Note that if  $n'$  is not a function of  $T$  then  $dn/dT = dn_{\text{BE}}/dT$ . Now we apply the relaxation-time approximation (RTA), which can be viewed as assuming the form of the time varying portion of  $n'$  as an exponential decay with the time constant  $\tau$ ,

$$n'(\mathbf{k}s, t) \propto e^{-t/\tau(\mathbf{k}s)} \quad (\text{C.0.5})$$

which allows us to evaluate the collision term in (C.0.3) as

$$\left. \frac{dn(\mathbf{k}s, t)}{dt} \right|_{\text{coll}} = -\frac{n'(\mathbf{k}s, t)}{\tau(\mathbf{k}s)}. \quad (\text{C.0.6})$$

Therefore, using Eqs. C.0.3, C.0.4, and C.0.6 our expression for  $n'$  is

$$n'(\mathbf{k}s) = -\tau(\mathbf{k}s) v_g^i(\mathbf{k}s) \frac{dn_{\text{BE}}(\mathbf{k}s, T)}{dT} \nabla^i T. \quad (\text{C.0.7})$$

Applying this to (C.0.2) we have

$$j_{\text{ph}}^i = -\frac{1}{V_{\mathbf{k}}} \sum_{\mathbf{k}s} E \frac{dn_{\text{BE}}}{dT} v_g^i v_g^j \tau \nabla^j T. \quad (\text{C.0.8})$$

Now we recall that heat capacity per unit volume of a specific phonon mode  $C$  (at constant volume) is the change in energy of the phonons in this mode with a change in temperature. If the phonon frequencies are assumed to stay constant with temperature when volume is unchanged (the quasi-harmonic approximation) we can define

$$C(\mathbf{k}s) = \frac{1}{V_{\mathbf{k}}} \left. \frac{d(E n_{\text{BE}})}{dT} \right|_V = \frac{E(\mathbf{k}s)}{V_{\mathbf{k}}} \frac{dn_{\text{BE}}}{dT} = \frac{k_B}{V_{\mathbf{k}}} \frac{x^2 e^x}{(e^x - 1)^2}. \quad (\text{C.0.9})$$

Incorporating (C.0.9) into (C.0.8) gives

$$j_{\text{ph}}^i = - \sum_{\mathbf{k}s} C(\mathbf{k}s) v_g^i(\mathbf{k}s) v_g^j(\mathbf{k}s) \tau(\mathbf{k}s) \nabla^j T. \quad (\text{C.0.10})$$

Now by comparing this with Fourier's law in (2.1), we find an expression for the phonon-gas channel thermal conductivity tensor which is given in Eq. 2.17.

## Appendix D

### Analytical models for phonon properties

#### D.1 Dispersion relation approximations

The Debye approximation simply assumes all phonons have a group velocity equal to the material's speed of sound  $v_s$ . It is also customary to also make the isotropic approximation, such that the speed of sound used is the isotropic speed of sound and  $\omega$  is therefore only a function of the magnitude of  $\mathbf{k}$ ,  $k$

$$\omega(k) = v_s k, \text{ for } 0 < k < k_{\max}. \quad (\text{D.1.1})$$

Another common dispersion approximation is the Born-von Karman dispersion relation

$$\omega(k) = \omega_{\max} \sin \left( \frac{\pi k}{2k_{\max}} \right) \quad (\text{D.1.2})$$

where  $k_{\max} = (6\pi^2/(NV))^{1/3}$  and  $\omega_{\max} = 2v_s k_{\max}/\pi$ . Since  $k_{\max}$  is determined using the volume of the primitive unit cell  $V_{\text{PUC}} = NV$  (rather than the volume per atom  $V$ ) this thermal transport model only considers acoustic phonons, in concordance with Wang *et al.* [85].

#### D.2 Heat capacity

The heat capacity of phonon mode  $\mathbf{k}_s$  is given in Eq. C.0.9. For spectral theories we consider the heat capacity carried by phonons as a function of frequency and are therefore interested in the quantity

$$C(\omega) = \frac{1}{V_{\text{PUC}}} \sum_{\mathbf{k}s} \frac{\hbar^2 \omega^2}{k_B T^2} \frac{e^{\hbar\omega/k_B T}}{(e^{\hbar\omega/k_B T} - 1)^2} \delta(\omega - \omega(\mathbf{k}s)). \quad (\text{D.2.1})$$

Note that Eq. C.0.9 contains a factor  $1/V_{\mathbf{k}} = 1/(N_{\mathbf{k}} V_{\text{PUC}})$ , since that expression is intended to be applied computationally where the FBZ sum is approximated by computing phonon properties at

$N_{\mathbf{k}}$  discrete points in  $\mathbf{k}$  space. In this analytical treatment we send  $N_{\mathbf{k}}$  to infinity such that there are an infinite number of terms in the sum over  $\mathbf{k}$ . Therefore, here we lose the dependence on  $N_{\mathbf{k}}$ , which arises from the use of a discrete  $\mathbf{k}$ -mesh and simply pull the factor of  $V_{\text{PUC}}$  out of the sum.

Since we desire an analytical expression we convert the sum over  $\mathbf{k}$  to an integral

$$C(\omega) = \sum_s \int \frac{d^3\mathbf{k}}{(2\pi)^3} \frac{\hbar^2 \omega^2}{k_B T^2} \frac{e^{\hbar\omega/k_B T}}{(e^{\hbar\omega/k_B T} - 1)^2} \delta(\omega - \omega(\mathbf{k}s)), \quad (\text{D.2.2})$$

where the factor of  $V_{\text{PUC}}$  that comes along with switching a sum over  $\mathbf{k}$  to an integral, and the one in Eq. D.2.1 cancel. Now by switching to spherical coordinates, making the isotropic dispersion approximation, taking the integral over  $\theta$  and  $\phi$ , and converting the integral over  $k$  to one over  $\omega$  we have

$$C(\omega) = \frac{4\pi}{(2\pi)^3} \sum_s \int \frac{d\omega}{v_g v_p^2} \frac{\omega^2}{k_B T^2} \frac{\hbar^2 \omega^2}{(e^{\hbar\omega/k_B T} - 1)^2} \delta(\omega - \omega(k, s)). \quad (\text{D.2.3})$$

The  $\delta$ -function makes the integral over  $\omega$  trivial and we obtain

$$C(\omega) = \frac{1}{2\pi^2} \sum_s \frac{\omega^4}{v_g v_p^2} \frac{\hbar^2}{k_B T^2} \frac{e^{\hbar\omega/k_B T}}{(e^{\hbar\omega/k_B T} - 1)^2}. \quad (\text{D.2.4})$$

Now, if we make the single mode approximation where all phonon branches  $s$  are replaced by 3 degenerate acoustic branches we obtain

$$C(\omega) = \frac{3}{2\pi^2} \frac{\omega^4}{v_g v_p^2} \frac{\hbar^2}{k_B T^2} \frac{e^{\hbar\omega/k_B T}}{(e^{\hbar\omega/k_B T} - 1)^2}. \quad (\text{D.2.5})$$

The phonon velocities in this single mode approximation expression should be computed using Eq. E.1.1.

### D.3 Phonon thermal conductivity at high- $T$

Here we solve for an analytical expression for the phonon thermal conductivity at high- $T$ . The spectral heat capacity given in Eq. D.2.5, at high temperatures ( $T > \theta_D$ ) becomes

$$C_{\text{ph}}(\omega) = \frac{3k_B \omega^2}{2\pi^2 v_g v_p^2}, \quad (\text{D.3.1})$$

A widely used expression for phonon-phonon scattering at high temperatures is [105, 72, 127, 207]

$$\tau_{\text{pp}} = \left( \frac{6\pi^2}{V} \right)^{1/3} \frac{\bar{M} v_g v_p^2}{2k_B \gamma^2 \omega^2 T}, \quad (\text{D.3.2})$$

where  $\bar{M}$  and  $V$  are the average atomic mass and volume, and  $\gamma$  is the Grüneisen parameter. With Eqs. D.3.1 and D.3.2, assuming phonon-phonon scattering dominates ( $\tau = \tau_{\text{pp}}$ ) Eq. 2.22 becomes

$$\kappa_{\text{ph}} = \left( \frac{6\pi^2}{V} \right)^{1/3} \frac{\bar{M}}{4\pi^2\gamma^2 T} \int_0^{\omega_{\text{max}}} v_g^2 d\omega. \quad (\text{D.3.3})$$

Notice that the factors of  $v_g v_p^2$  in Eqs. D.3.1 and D.3.2 cancel, leaving only  $v_g^2$  in the integral over  $\omega$ . By switching the variable of integration from  $\omega$  to  $k$  we can observe the cubic dependence of  $\kappa_L$  on the phonon velocity

$$\int_0^{\omega_{\text{max}}} v_g^2 d\omega = \int_0^{k_{\text{max}}} v_g^3 dk. \quad (\text{D.3.4})$$

Therefore, it is useful to define an average  $v_g^3$  through the Brillouin zone

$$\langle v_g^3 \rangle = \frac{1}{k_{\text{max}}} \int_0^{k_{\text{max}}} v_g^3 dk, \quad (\text{D.3.5})$$

where  $k_{\text{max}} = (6\pi^2/V)^{1/3}$ . With this definition Eq. D.3.3 becomes

$$\kappa_{\text{ph}} = \left( \frac{6\pi^2}{V} \right)^{2/3} \frac{\bar{M}}{4\pi^2\gamma^2} \frac{\langle v_g^3 \rangle}{T}. \quad (\text{D.3.6})$$

Next, we show that  $\int_0^{k_{\text{max}}} v_g^3 dk \propto v_s^3$  is rigorously true within the Born von Karman approximation for the phonon dispersion relation, where

$$\omega = v_s \frac{2}{\pi} k_{\text{max}} \sin \left( \frac{\pi}{2} \frac{k}{k_{\text{max}}} \right) \quad (\text{D.3.7})$$

and

$$v_g = v_s \cos \left( \frac{\pi}{2} \frac{k}{k_{\text{max}}} \right). \quad (\text{D.3.8})$$

Inserting Eq. D.3.8 in Eq. D.3.4 one obtains

$$\int_0^{k_{\text{max}}} v_g^3 dk = v_s^3 \frac{2k_{\text{max}}}{\pi} \propto v_s^3. \quad (\text{D.3.9})$$

Thus, since in practice the pre-factor,  $A$ , in  $\kappa_{\text{ph}}$  is normalized to a control sample and held constant for a given materials system (i.e.  $\bar{M}$ ,  $V$ , and  $\gamma$  are unchanged), the use of  $v_s$  in  $\kappa_L = Av_s^3 T^{-1}$  only assumes that the a change in a material's speed of sound accurately reflects the average change in the group velocity throughout the Brillouin zone.

From Eq. 4.4 we can see that  $A$  is defined as

$$A = \left( \frac{6\pi^2}{V} \right)^{2/3} \frac{\bar{M}}{4\pi^2\gamma^2}, \quad (\text{D.3.10})$$

which we can incorporate into Eq. D.3.2 and obtain

$$\tau_{\text{pp}} = A \left( \frac{V}{6\pi^2} \right)^{1/3} \frac{2\pi^2 v_g v_p^2}{k_B \omega^2 T}. \quad (\text{D.3.11})$$

## Appendix E

### Measurements of the speed of sound and Debye temperature

#### E.1 Pulse-echo ultrasound

The speeds of sound can be easily and accurately measured by the pulse-echo method where a piezo-electric transducer coupled to the sample first sends the initial stress-wave pulse, and then acts as receiver measuring the echoed ultrasound reflection, Figure E.1 [208]. When no preferred orientation is observed in the X-Ray analysis, randomly oriented polycrystals can be treated as elastically isotropic. The time-delay,  $t_d$ , between subsequent reflections must be determined by maximizing the cross-correlation (Figure E.1c) of the two reflections as follows. If  $A_n(t)$  is the amplitude of reflection  $n$ , then  $\sum_t A_n(t)A_{n+1}(t - t_d)$  is maximized by varying  $t_d$ . This corresponding value of  $t_d$  along with the sample thickness,  $h$ , is then used to calculate the speed of sound,  $v_{L,T} = 2h/t_d$ . Our specific instrument uses a longitudinal transducer (measuring  $v_L$ ) with a principle frequency of 5 MHz (Olympus V1091) and a transverse transducer (measuring  $v_T$ ) at 5 MHz (Olympus V157-RM) with a Panametrics 5072PR pulser/receiver. Table honey with low water content acts as a nice coupling agent for both longitudinal and transverse acoustic waves. Its viscoelastic properties make it surprisingly effective at transferring acoustic energy. Crystalbond or superglue can also be used. A Tektronix TBS 1072B-EDU oscilloscope is used to record the waveforms. A typical waveform contains over four reflections (3 time-delay measurements), and the measurements from a minimum of three waveforms (corresponding to 9 individual speed of sound measurements) are averaged. Measurements having a standard deviation of less than 1% of the mean are common. The largest error in this measurement technique is the measurement of the sample thickness, and if care is taken to ensure the sample faces are parallel and a micrometer is used to measure the sample thickness, < 1% analysis related error is achievable. A single crystal of yttrium aluminum garnet (YAG) with known elastic properties was used to determine that measurements of the speed of sound on this home built system have an accuracy of better than 0.6%. The average speed of sound which is

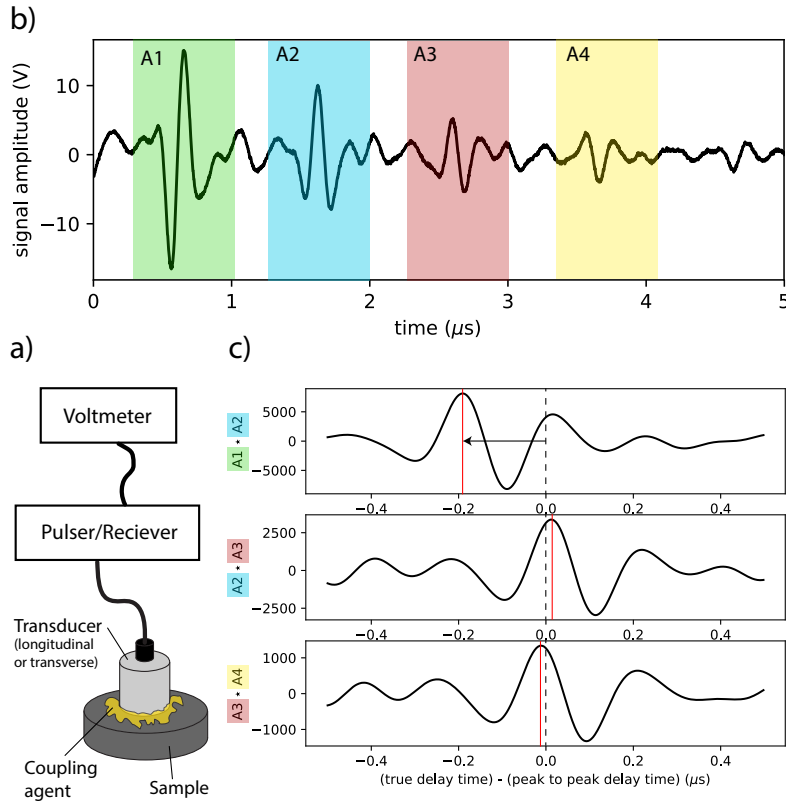


Figure E.1: Overview of pulse-echo ultrasound. a) The experimental setup. b) Example waveform. c) Cross-correlation between successive reflections in the waveform.

commonly used for transport modeling is calculated as [145]

$$v_s = \left( \frac{1}{3} \left[ \frac{1}{v_L^3} + \frac{2}{v_T^3} \right] \right)^{-1/3}. \quad (\text{E.1.1})$$

The Debye temperature can be calculated using  $v_s$  and the volume per atom  $V$  by Eq. 2.16.

## E.2 Low temperature heat capacity

To verify speed of sound measurements via pulse-echo ultrasound, low-T heat capacity can be used. A Quantum Design Dynacool Physical Property Measurement System was utilized for such measurements. Apiezon N grease was used to couple samples to the heat capacity option stage. A semi-adiabatic thermal relaxation method was used and data were collected on warming.

It is possible to determine the so-called Debye level which is defined as  $\beta \rightarrow C_p/T^3$  in the  $T \rightarrow 0$

K limit, where  $C_p$  is the heat capacity at constant pressure.  $\beta$  is the horizontal plateau that is observed when the low frequency linear dispersion (i.e. speed of sound) makes up the vibrational density of states (i.e.,  $g(\omega) \propto \omega^2$ ), and is related to the Debye temperature through the relation

$$\theta_D = \left( \frac{12}{5} \pi^4 N R \right)^{1/3} \beta^{-1/3}, \quad (\text{E.2.1})$$

where  $\beta$  has units of  $\text{J mol}^{-1} \text{K}^{-4}$ ,  $N$  is the number of atoms per formula unit and  $R$  is the gas constant. The results of low-T heat capacity have provided excellent verification of the pulse-echo experiments in many systems including PbTe [100], SnTe [95], and the  $\text{Mg}_2(\text{Sb,Bi})_3$  system [209].

## Appendix F

### Grüneisen parameters and tensors

There are many different formulations and definitions of Grüneisen parameter. One thing all parameters have in common is that they in someway, capture a materials anharmonicity. Here we rigorously define several commonly used forms, and relate thermodynamic and lattice dynamics based definitions.

We can define a thermodynamic-Grüneisen parameter which is related to Eq. 2.43. Starting with the change in Helmholtz free energy (at constant composition, charge carrier concentration etc.)

$$dF_V = \sigma_{ij} d\epsilon_{ij} - S_V dT, \quad (\text{F.0.1})$$

where  $F_V$  is the Helmholtz free energy per unit volume,  $\sigma_{ij}$  and  $\epsilon_{ij}$  are the 3x3 stress and strain tensors, and  $S_V$  is the entropy per unit volume. From Eq. F.0.1 we can obtain the Maxwell relation

$$\left( \frac{\partial S_V}{\partial \epsilon_{ij}} \right)_T = - \left( \frac{\partial \sigma_{ij}}{\partial T} \right)_\epsilon. \quad (\text{F.0.2})$$

Now the thermodynamic-Grüneisen parameter is defined as

$$\gamma_{ij} = \frac{1}{c_V} \left( \frac{\partial S_V}{\partial \epsilon_{ij}} \right)_T = - \frac{1}{c_V} \left( \frac{\partial \sigma_{ij}}{\partial T} \right)_\epsilon. \quad (\text{F.0.3})$$

When only hydrostatic stains and stresses are considered, we take the trace of this 3x3 tensor

$$\gamma = \frac{V}{c_V} \left( \frac{\partial S_V}{\partial V} \right)_T = - \frac{1}{c_V} \left( \frac{\partial P}{\partial T} \right)_\epsilon. \quad (\text{F.0.4})$$

Now we can arrive at Gruneisen's initial result, which in the midst of all of these definitions I explicitly name the hydrostatic thermodynamic Grüneisen parameter (Note: you have to use the

triple product rule<sup>1</sup> to manipulate  $\partial\sigma/\partial T$ )

$$\gamma = \frac{B_T \alpha_P}{c_V}, \quad (\text{F.0.6})$$

where  $B_T$  is the bulk modulus at constant temperature,  $\alpha_P$  is the thermal expansion at constant pressure, and  $c_V$  is the heat capacity per unit volume.

### F.0.1 Relating phonon and thermodynamic Gruneisen parameters

Returning to Eq. F.0.1 we recall that

$$\sigma_{ij} = \frac{\partial F_V}{\partial \epsilon_{ij}}. \quad (\text{F.0.7})$$

Now in the quasi-harmonic approximation the free energy of the solid can be written as the sum of a bond enthalpy term  $\Phi$  and vibrational entropy of harmonic oscillators, both zero point energy and energy from thermal phonons, such that

$$F_V = \Phi + \frac{1}{2} \sum_{\mathbf{k}s} \hbar\omega(\mathbf{k}s) + \sum_{\mathbf{k}s} n_{\text{BE}}(\omega, T) \hbar\omega(\mathbf{k}s), \quad (\text{F.0.8})$$

taking the partial derivative of this with respect to a component of the strain tensor,  $\epsilon_{ij}$ , we have

$$\frac{\partial F_V}{\partial \epsilon_{ij}} = \frac{\partial \Phi}{\partial \epsilon_{ij}} + \frac{1}{2} \sum_{\mathbf{k}s} \hbar \frac{\partial \omega(\mathbf{k}s)}{\partial \epsilon_{ij}} + \sum_{\mathbf{k}s} n(\omega, T) \hbar \frac{\partial \omega(\mathbf{k}s)}{\partial \epsilon_{ij}}, \quad (\text{F.0.9})$$

where under the quasi-harmonic approximation we assume that the strain does not change the number of phonons at a given frequency,  $\partial n(\omega, T)/\partial \epsilon_{ij} = 0$ . Now we take the partial derivative with respect to temperature and obtain the following

$$\frac{\partial \sigma_{ij}}{\partial T} = \sum_{\mathbf{k}s} \frac{\partial n(\omega, T)}{\partial T} \hbar \frac{\omega(\mathbf{k}s)}{\omega(\mathbf{k}s)} \frac{\partial \omega(\mathbf{k}s)}{\partial \epsilon_{ij}}, \quad (\text{F.0.10})$$

since the bond enthalpy and thus phonon frequencies don't change with a change in temperature under the quasi-harmonic approximation. Recognizing that

$$c_V(\mathbf{k}s) = \hbar\omega(\mathbf{k}s) \frac{\partial n(\omega, T)}{\partial T} \quad (\text{F.0.11})$$

---

<sup>1</sup>The triple product rule is

$$\left( \frac{\partial x}{\partial y} \right)_z \left( \frac{\partial y}{\partial z} \right)_x \left( \frac{\partial z}{\partial x} \right)_y = -1. \quad (\text{F.0.5})$$

is the heat capacity for a given phonon mode ( $\mathbf{ks}$ ) and the definition of the mode-specific Grüneisen tensor  $\gamma_{ij}(\mathbf{ks})$  in Eq. 2.43, we write

$$\frac{\partial \sigma_{ij}}{\partial T} = - \sum_{\mathbf{ks}} c_V(\mathbf{ks}) \gamma_{ij}(\mathbf{ks}). \quad (\text{F.0.12})$$

Now with Eqs. F.0.12 and F.0.3 we can relate the phonon-Grüneisen tensor to the thermodynamic-Grüneisen tensor

$$\gamma_{ij} = \frac{\sum_{\mathbf{ks}} c_V(\mathbf{ks}) \gamma_{ij}(\mathbf{ks})}{\sum_{\mathbf{ks}} c_V(\mathbf{ks})} z = \frac{1}{c_V} \sum_{\mathbf{ks}} c_V(\mathbf{ks}) \gamma_{ij}(\mathbf{ks}). \quad (\text{F.0.13})$$

The trace of the thermodynamic-Grüneisen tensor gives the hydrostatic thermodynamic Grüneisen parameter, which is commonly referred to simply as the Grüneisen parameter

$$\gamma = \gamma_{ii}. \quad (\text{F.0.14})$$

## Appendix G

### Phonon scattering theory

Here, we derived the phonon relaxation time due to the introduction of a perturbation  $\mathcal{H}'$  to the harmonic lattice Hamiltonian  $\mathcal{H} = \mathcal{T} + U_{\text{2nd}}$ . For intrinsic phonon-phonon scattering this perturbation comes from another phonon when anharmonicity is included. For phonon defect scattering, this perturbation can be described by a spatially varying scattering potential  $V(\mathbf{r})$ . The probability of scattering per unit time of a phonon is given by Fermi's Golden Rule as [206]

$$W_{\mathbf{k},\mathbf{k}'} = \frac{2\pi}{\hbar} |\langle f | \mathcal{H}' | i \rangle|^2 \delta(\Delta E). \quad (\text{G.0.1})$$

#### G.1 Three phonon scattering

The intrinsic lifetime of a phonon depends on its interaction with other phonons in the system. The largest contributor is a three phonon interaction of which there are two types, emission (Type I) and absorption (Type II). These interactions must conserve wavevector, and energy which is given for Type I

$$\mathbf{k}_1 = \mathbf{k}_2 + \mathbf{k}_3 + \mathbf{b} \quad (\text{G.1.1})$$

$$\hbar\omega_1 = \hbar\omega_2 + \hbar\omega_3 \quad (\text{G.1.2})$$

and for Type II

$$\mathbf{k}_1 + \mathbf{k}_{2(3)} = \mathbf{k}_{3(2)} + \mathbf{b} \quad (\text{G.1.3})$$

$$\hbar\omega_1 + \hbar\omega_{2(3)} = \hbar\omega_{3(2)}. \quad (\text{G.1.4})$$

$\mathbf{b}$  is zero for Normal processes and a reciprocal lattice vector (Eq. A.0.2 to A.0.4) for Umklapp processes. Since Normal processes conserve the phonon momentum and energy they do not directly

contribute to thermal resistance. However, they do serve to populate phonon modes which can undergo Umklapp processes, which are resistive. The relaxation time approximation which is asserted in Eq. C.0.6, in practice assumes that both Normal and Umklapp processes are resistive. Therefore, the RTA is known to under-predict  $\kappa_{\text{ph}}$ . An iterative solution of the phonon BTE captures the appropriate behavior of Normal versus Umklapp processes and is therefore more accurate.

To examine the errors introduced by adopting the RTA, we return to our example problem of Si shown in Figure 2.2.  $\kappa_{\text{ph}}$  was computed using both the RTA and an iterative solution to the phonon BTE, using the almaBTE suite [210]. The RTA calculated  $\kappa_{\text{ph}}$  was 2.5% lower than the iterative solution at 300K and 1.3% lower at 50K. Experimental error in the measurement of thermal diffusivity by LFA is 3%. Therefore, in this work we find the RTA to be sufficiently accurate. We therefore do not distinguish between Normal and Umklapp process, and simply refer to intrinsic phonon scattering as phonon-phonon scattering, which is meant to include both Umklapp and Normal processes. Cases where the RTA fails seem to be in materials with very high thermal conductivity [211] and/or in materials where there are phase space restrictions which prohibit a phonon mode from easily reaching its equilibrium occupation number. The RTA seems to work well in low thermal conductivity materials.

## G.2 Elastic defect scattering

For elastic defect scattering, an incident phonon  $\mathbf{k}$  interacts with the defect and scatters into  $\mathbf{k}'$  of the same energy. Therefore the initial state in Eq. G.0.1 is simply a phonon in state  $\mathbf{k}$ ,  $|i\rangle = |\mathbf{k}\rangle$ , and the final is one in state  $\mathbf{k}'$ ,  $|i\rangle = |\mathbf{k}'\rangle$ . The change in energy of the system is then given by  $\Delta E = E_{\mathbf{k}} - E_{\mathbf{k}'}$ , where  $E_{\mathbf{k}} = \hbar\omega_{\mathbf{k}}$  is the energy of a phonon with wavevector  $\mathbf{k}$ . For simplicity, we suppress phonon branch index, since that does not affect the central point of our argument, which can be seen by thinking of the perturbation in terms of a scattering potential  $V(\mathbf{r})$ . It is convenient to think of the crystal as a rectilinear brick with sides  $L_x$ ,  $L_y$ ,  $L_z$  and in the  $x$ ,  $y$ , and  $z$  directions, and to write the volume of the crystal as  $L_x L_y L_z$ . The matrix element is then given by

$$\langle \mathbf{k}' | \mathcal{H}' | \mathbf{k} \rangle = \frac{1}{L_x L_y L_z} \iiint d^3 \mathbf{r} V(\mathbf{r}) e^{-i(\mathbf{k}' - \mathbf{k}) \cdot \mathbf{r}}. \quad (\text{G.2.1})$$

It is also convenient to introduce the scattering vector

$$\mathbf{q} = \mathbf{k}' - \mathbf{k}. \quad (\text{G.2.2})$$

The object of ultimately greater interest than the scattering probability to us is the relaxation time of a phonon,  $\tau(\mathbf{k})$ , and its inverse the phonon scattering rate  $\Gamma(\mathbf{k}) = \tau(\mathbf{k})^{-1}$ . To find this, we must integrate  $W_{\mathbf{k}, \mathbf{k}'}$  over all possible final phonon wavevectors. At the same time, we imagine that the

inverse of this life time is defined via a Boltzmann equation formulation, on the basis of which we incorporate in this integral, a forward scattering suppression factor  $(1 - \hat{\mathbf{k}} \cdot \hat{\mathbf{k}}')$  with  $\hat{\mathbf{k}}$  and  $\hat{\mathbf{k}}'$  being unit vectors parallel to  $\mathbf{k}$  and  $\mathbf{k}'$ . That is to say [206],

$$\Gamma(\mathbf{k}) = L_x L_y L_z \iiint \frac{d^3 \mathbf{k}'}{(2\pi)^3} W_{\mathbf{k}, \mathbf{k}'} (1 - \hat{\mathbf{k}} \cdot \hat{\mathbf{k}}'). \quad (\text{G.2.3})$$

The role of the dimensionality of the scattering defect can now be addressed. It is useful to discuss the different dimensionalities separately, and begin in the middle with a linear defect,  $d_d = 1$ .

### G.2.1 One-dimensional defects

Suppose the defect is a linear object parallel to the  $z$  direction, so that

$$V(\mathbf{r}) = V(x, y) \quad (\text{G.2.4})$$

is a function only of  $x$  and  $y$ , independent of  $z$ . The position integral in the matrix element then simplifies to

$$\iiint d^3 \mathbf{r} V(x, y) e^{-i\mathbf{q} \cdot \mathbf{r}} = 2\pi \delta(q_z) \times \iint dx dy V(x, y) e^{-i(q_x x + q_y y)}, \quad (\text{G.2.5})$$

and invoking well established rules for interpreting the square of a  $\delta$ -function (the square of the  $\delta$ -function needs to be rewritten as  $\delta^2(q_i) = L_i \delta(q_i)/(2\pi)$ ), we find a scattering probability

$$W_{\mathbf{k}, \mathbf{k}'} = \frac{2\pi}{\hbar} \frac{L_z}{(L_x L_y L_z)^2} \left| \iint dx dy V(x, y) e^{-i(q_x x + q_y y)} \right|^2 \times (2\pi) \delta(q_z) \delta(E_{\mathbf{k}'} - E_{\mathbf{k}}). \quad (\text{G.2.6})$$

We now define a reduced matrix element,

$$M_{2d} = \iint dx dy V(x, y) e^{-i(q_x x + q_y y)}, \quad (\text{G.2.7})$$

where the subscript ‘2d’ indicates that the integral is two-dimensional. Then,

$$W_{\mathbf{k}, \mathbf{k}'} = \frac{(2\pi)^2}{\hbar} \frac{L_z}{(L_x L_y L_z)^2} |M_{2d}|^2 \delta(q_z) \delta(E_{\mathbf{k}'} - E_{\mathbf{k}}), \quad (\text{G.2.8})$$

and, with  $n_{2d} = (L_x L_y)^{-1}$  defined as the areal density of linear defects,

$$\Gamma(\mathbf{k}) = \frac{n_{2d}}{2\pi\hbar} \iiint d^3 k' |M_{2d}(q_x, q_y)|^2 (1 - \hat{\mathbf{k}} \cdot \hat{\mathbf{k}}') \delta(q_z) \delta(E_{\mathbf{k}'} - E_{\mathbf{k}}). \quad (\text{G.2.9})$$

The essential point now is that the two  $\delta$ -functions in the integral, which express conservation of energy and wavevector parallel to the defect, constrain us to a one-dimensional curve in  $k$ -space,

and thus render the integral effectively one-dimensional. We can see this very clearly by assuming an isotropic phonon spectrum,  $E_{\mathbf{k}} = E_k = \hbar\omega_k$ , in which the energy  $E_{\mathbf{k}}$  depends on  $k = |\mathbf{k}|$  only. With the phonon group and phase velocities defined as

$$v_g(k) = \frac{\partial\omega_k}{\partial k}, \quad v_p(k) = \frac{\omega_k}{k}, \quad (\text{G.2.10})$$

we get

$$\delta(E_{k'} - E_k) = \frac{1}{\hbar|v_g(k)|} \delta(k - k'). \quad (\text{G.2.11})$$

Beginning here, we will omit the absolute value sign around  $v_g$  as the group velocity is always positive for our treatment. However, real phonon dispersion relations can have a negative  $v_g$  and in this case the absolute value is required. We stress that the assumption of isotropy in no way diminishes the generality of the dimensional arguments, and is made so as to not encumber the analysis with inessential detail. In spherical polar coordinates, the second  $\delta$ -function (in conjunction with  $\delta(k - k')$ ) reads

$$\delta(q_z) = \delta(k \cos \vartheta - k' \cos \vartheta') = \frac{1}{k} \delta(\cos \vartheta - \cos \vartheta'). \quad (\text{G.2.12})$$

The conservation laws are equivalent to  $k' = k$  and  $\vartheta' = \vartheta$ . Further,  $d^3k' = k'^2 \sin \vartheta' dk' d\vartheta' d\varphi'$ . The integrals over  $k'$  and  $\vartheta'$  can be done trivially because of the  $\delta$ -functions, and we get

$$\Gamma(\mathbf{k}) = \frac{n_{2d}\omega_k}{2\pi v_g v_p \hbar^2} \int_0^{2\pi} d\varphi' |M_{2d}(q_x, q_y)|^2 (1 - \hat{\mathbf{k}} \cdot \hat{\mathbf{k}}'). \quad (\text{G.2.13})$$

The two-dimensional phonon density of states is

$$g_{2d}(\omega) = \frac{\omega}{2\pi v_g(\omega) v_p(\omega)}, \quad (\text{G.2.14})$$

and if we define the average squared matrix element as

$$\overline{|M_{2d}|^2} = \frac{1}{\hbar^2} \int_0^{2\pi} d\varphi' |M_{2d}(q_x, q_y)|^2 (1 - \hat{\mathbf{k}} \cdot \hat{\mathbf{k}}'), \quad (\text{G.2.15})$$

we get the result quoted in Eq. 1, i.e.,

$$\Gamma(\mathbf{k}) = n_{2d} g_{2d}(\omega_k) \overline{|M_{2d}|^2} \quad (\text{linear defect}). \quad (\text{G.2.16})$$

For the evaluation of  $\overline{|M_{2d}|^2}$  it is useful to keep in mind that

$$\begin{aligned} q_x &= k \sin \vartheta (\cos \varphi' - \cos \varphi), \\ q_y &= k \sin \vartheta (\sin \varphi' - \sin \varphi), \\ (1 - \hat{\mathbf{k}} \cdot \hat{\mathbf{k}}') &= 2 \sin^2 \vartheta \sin^2 \frac{1}{2}(\varphi' - \varphi). \end{aligned} \quad (\text{G.2.17})$$

### G.2.2 Zero-dimensional defects

For a zero-dimensional or point defect, the potential

$$V(\mathbf{r}) = V(x, y, z) \quad (\text{G.2.18})$$

depends on all three coordinates, and there is no simplification in the matrix element. We write this matrix element as

$$M_{3d}(\mathbf{q}) = \iiint d^3 r V(\mathbf{r}) e^{-i\mathbf{q} \cdot \mathbf{r}}, \quad (\text{G.2.19})$$

where the subscript indicates a three-dimensional integral. Then,

$$W_{\mathbf{k}, \mathbf{k}'} = \frac{2\pi}{\hbar} \frac{1}{(L_x L_y L_z)^2} |M_{3d}|^2 \delta(E_{\mathbf{k}'} - E_{\mathbf{k}}), \quad (\text{G.2.20})$$

and, with  $n_{3d} = (L_x L_y L_z)^{-1}$  defined as the (volumetric) density of point defects,

$$\Gamma(\mathbf{k}) = \frac{n_{3d}}{(2\pi)^2 \hbar} \iiint d^3 k' |M_{3d}(\mathbf{q})|^2 (1 - \hat{\mathbf{k}} \cdot \hat{\mathbf{k}}') \delta(E_{\mathbf{k}'} - E_{\mathbf{k}}). \quad (\text{G.2.21})$$

If we once again take an isotropic phonon spectrum for simplicity, and employ spherical polar coordinates, the integral over the magnitude  $k = |\mathbf{k}|$  can be done, and we get

$$\Gamma(\mathbf{k}) = \frac{n_{3d} \omega_k^2}{4\pi^2 v_g v_p^2 \hbar^2} \int d\Omega' |M_{3d}(\mathbf{q})|^2 (1 - \hat{\mathbf{k}} \cdot \hat{\mathbf{k}}'), \quad (\text{G.2.22})$$

where  $d\Omega' = \sin \vartheta' d\vartheta' d\varphi'$ . The three-dimensional phonon density of states is

$$g_{3d}(\omega) = \frac{\omega^2}{2\pi^2 v_g(\omega) v_p^2(\omega)}, \quad (\text{G.2.23})$$

and if we define the average squared matrix element as

$$\overline{|M_{3d}|^2} = \frac{1}{2\hbar^2} \int d\Omega' |M_{3d}(\mathbf{q})|^2 (1 - \hat{\mathbf{k}} \cdot \hat{\mathbf{k}}'), \quad (\text{G.2.24})$$

we get the result cast into the form of Eq. 2.27,

$$\Gamma(\mathbf{k}) = n_{3d} g_{3d}(\omega_k) \overline{|M_{3d}|^2}. \quad (\text{point defect}) \quad (\text{G.2.25})$$

This time, there is no useful simplification for the arguments of the functions in the integrand for  $|M_{3d}|^2$ , and one must remember the full expressions,

$$\begin{aligned} \mathbf{q} &= \mathbf{k}' - \mathbf{k}, \\ \mathbf{k} &= k(\sin \vartheta \cos \varphi, \sin \vartheta \sin \varphi, \cos \vartheta), \\ \mathbf{k}' &= k(\sin \vartheta' \cos \varphi', \sin \vartheta' \sin \varphi', \cos \vartheta'). \end{aligned} \quad (\text{G.2.26})$$

### G.2.3 Two-dimensional defects

We now consider a two-dimensional or planar defect parallel to the  $yz$  plane. Then

$$V(\mathbf{r}) = V(x) \quad (\text{G.2.27})$$

depends on  $x$  only. As a result, both  $k_y$  and  $k_z$  are conserved in addition to  $E_k$ , and there are only two possibilities for the final state wavevector:

$$k'_x = \pm k_x, \quad k'_y = k_y, \quad k'_z = k_z, \quad (\text{G.2.28})$$

corresponding to forward scattering and specular reflection. Only the latter contributes to the life time, and we get

$$\Gamma(\mathbf{k}) = \frac{n_{1d}}{\hbar^2 v_g} [ |M_{1d}(q_x)|^2 (1 - \hat{\mathbf{k}} \cdot \hat{\mathbf{k}}') ]_{q_x = -2k_x}. \quad (\text{G.2.29})$$

Here  $n_{1d} = L_x^{-1}$  is the density of planar defects,

$$g_{1d} = \frac{1}{\pi v_g} \quad (\text{G.2.30})$$

is the one-dimensional phonon density of states, and

$$M_{1d}(q_x) = \int dx V(x) e^{-iq_x x}. \quad (\text{G.2.31})$$

To cast the answer into the form of Eq. 2.27,

$$\Gamma(\mathbf{k}) = n_{1d} g_{1d}(\omega_k) \overline{|M_{1d}|^2}, \quad (\text{planar defect}) \quad (\text{G.2.32})$$

we must define,

$$\overline{|M_{1d}|^2} = \frac{\pi}{\hbar^2} [ |M_{1d}(q_x)|^2 (1 - \hat{\mathbf{k}} \cdot \hat{\mathbf{k}}') ]_{q_x = -2k_x}. \quad (\text{G.2.33})$$

In this equation, one can also write the forward scattering suppression factor as

$$(1 - \hat{\mathbf{k}} \cdot \hat{\mathbf{k}}') = \frac{2k_x^2}{k^2}. \quad (\text{G.2.34})$$

### G.3 Defining $\tau(\omega)$ for non-isotropic defect scattering

The phonon scattering rate for linear and planar defects depends on the direction of incidence, due to conservation of components of  $\mathbf{k}$ . Naturally an expression for the spectral phonon relaxation time,  $\tau(\omega)$  as implemented into Eq. 2.22, will need to contain information about the direction of thermal transport with respect to the direction of the defect. We seek the appropriate definition of  $\tau(\omega)$  for phonon scattering events which depend on direction of incidence.

For a dislocation line pointing in the  $z$ -direction, or grain boundary in the  $yz$  plane, the component of the thermal conductivity tensor which is most commonly of interest is the  $(i,j) = 1, 1$  or  $xx$  component. From standard transport theory for an isotropic solid, we have

$$\kappa_{\text{ph},xx} = 3 \iiint \frac{d^3\mathbf{k}}{8\pi^3} \frac{k_B(\hbar\omega_k/k_B T)^2 e^{\hbar\omega_k/k_B T}}{(e^{\hbar\omega_k/k_B T} - 1)^2} \frac{1}{\Gamma(\mathbf{k})} \frac{v_g^2 k_x^2}{k^2} \quad (\text{G.3.1})$$

where  $\Gamma(\mathbf{k})$  is the scattering rate for phonons of wavevector  $\mathbf{k}$ ,  $v_g$  is the group velocity, and the integral runs over the first Brillouin zone. It is useful to perform the integrations over the magnitude and orientation of  $\mathbf{k}$  separately. We therefore define the phonon lifetime as a weighted orientational average of the inverse of the orientation-specific scattering rate,

$$\tau(\omega) = \frac{\iint \Gamma^{-1}(\mathbf{k}) k_x^2 d\Omega}{\iint k_x^2 d\Omega} = \frac{3}{4\pi} \iint \Gamma^{-1}(\mathbf{k}) \frac{k_x^2}{k^2} d\Omega, \quad (\text{G.3.2})$$

with  $d\Omega = \sin\theta d\theta d\phi$ . In terms of this quantity, we then have

$$\kappa_{\text{ph},xx} = \frac{1}{2\pi^2} \int \frac{k_B(\hbar\omega_k/k_B T)^2 e^{\hbar\omega_k/k_B T}}{(e^{\hbar\omega_k/k_B T} - 1)^2} \tau(\omega) v_g^2 k^2 dk. \quad (\text{G.3.3})$$

By defining a spectral heat capacity in Eq. D.2.5 and switching the variable of integration to  $\omega$ , we

arrive at the expression quoted in Eq. 2.22. There, we omit the tensor subscripts and write just  $\kappa_{\text{ph}}$  instead of  $\kappa_{\text{ph},xx}$ .

## G.4 Scattering from an infinite array of linear defects

We extend the analysis of the previous sections to a scattering potential

$$V(x, y) = \sum_{n=-\infty}^{\infty} V_0(x, y - nD), \quad (\text{G.4.1})$$

which describes an array of one-dimensional defects all parallel to the  $z$  axis, lying in the  $yz$  plane. The potential  $V_0$  is associated with a single line defect. For convenience this single line defect is centered about the origin ( $x = y = 0$ ). With

$$\tilde{V}_0(q_x, q_y) = \iint dx dy V_0(x, y) e^{-i(q_x x + q_y y)}, \quad (\text{G.4.2})$$

the reduced matrix element for the array becomes

$$\begin{aligned} M_{2d} &= \iint dx dy \sum_{n=-\infty}^{\infty} V_0(x, y - nD) e^{-i(q_x x + q_y y)} \\ &= \sum_{n=-\infty}^{\infty} e^{-iq_y n D} \tilde{V}_0(q_x, q_y). \end{aligned} \quad (\text{G.4.3})$$

If we now apply the Poisson summation formula,

$$\sum_{n=-\infty}^{\infty} e^{-iq_y n D} = \frac{2\pi}{D} \sum_{m=-\infty}^{\infty} \delta(q_y + q_m), \quad \left( q_m = \frac{2\pi m}{D} \right), \quad (\text{G.4.4})$$

square the matrix element, and interpret the squared delta function as before, we obtain

$$|M_{2d}|^2 = \frac{2\pi L_y}{D^2} \sum_{m=-\infty}^{\infty} \delta(q_y + q_m) \left| \tilde{V}_0(q_x, q_y) \right|^2. \quad (\text{G.4.5})$$

If we substitute this into Eq. G.2.3 and Eq. G.2.8, we obtain

$$\Gamma(\mathbf{k}) = n_{1d} \sum_m \iiint d^3 \mathbf{k}' \frac{\left| \tilde{V}_0(q_x, q_y) \right|^2}{\hbar^2 D^2} (1 - \hat{\mathbf{k}} \cdot \hat{\mathbf{k}'}) \delta(q_z) \delta(q_y + q_m) \delta(\omega_{k'} - \omega_k). \quad (\text{G.4.6})$$

### G.4.1 Conservation laws

To evaluate the integral over  $\mathbf{k}'$ , it is necessary to reexpress the  $\delta$ -functions in terms of  $\mathbf{k}'$  directly. We first note that

$$\delta(\omega_{k'} - \omega_k) = \frac{\delta(k' - k)}{v_g} = \frac{2k}{v_g} \delta(k'^2 - k^2). \quad (\text{G.4.7})$$

We then observe that along with the constraints  $k'_z = k_z$ ,  $k'_y = k_y - q_m$ ,

$$k'^2 - k^2 = k_x'^2 - (k_x^2 + 2k_y q_m - q_m^2). \quad (\text{G.4.8})$$

It is useful to define

$$k'_{x,m\pm} = \pm(k_x^2 + 2k_y q_m - q_m^2)^{1/2}, \quad q_{x,m\pm} = -k_x \pm (k_x^2 + 2k_y q_m - q_m^2)^{1/2}. \quad (\text{G.4.9})$$

We thus obtain the replacement rule

$$\delta(q_z) \delta(q_y + q_m) \delta(\omega_{k'} - \omega_k) = \frac{1}{v_g} \sum_{\sigma=\pm} J(\mathbf{k}, m) \delta(q_z) \delta(q_y + q_m) \delta(q_x - q_{x,m\sigma}), \quad (\text{G.4.10})$$

where  $J$  is a dimensionless Jacobian or volume rescaling factor,

$$J(\mathbf{k}, m) = \frac{k}{|k'_{x,m\sigma}|} = \frac{k}{(k_x^2 + 2k_y q_m - q_m^2)^{1/2}}. \quad (\text{G.4.11})$$

For practical purposes, it is also useful to rewrite the forward scattering suppression factor (keeping in mind that  $k' = k$ ),

$$1 - \hat{\mathbf{k}} \cdot \hat{\mathbf{k}}' = -\frac{\mathbf{q} \cdot \mathbf{k}}{k^2} = \frac{1}{k^2} (k_x^2 \mp k_x (k_x^2 + 2k_y q_m - q_m^2)^{1/2} + k_y q_m). \quad (\text{G.4.12})$$

Hence,

$$\Gamma(\mathbf{k}) = \frac{n_{1d}}{\hbar^2 v_g D^2} \sum_{m=-\infty}^{\infty} \sum_{\sigma=\pm} \frac{(k_x^2 \mp k_x (k_x^2 + 2k_y q_m - q_m^2)^{1/2} + k_y q_m)}{k(k_x^2 + 2k_y q_m - q_m^2)^{1/2}} \left| \tilde{V}_1(q_{x,m\sigma}, -q_m) \right|^2. \quad (\text{G.4.13})$$

This is the working formula that we use for numerical calculation.

### G.4.2 Specular scattering: long wavelength limit

In this section we derive what is essentially the acoustic mismatch model (AMM) by solving Eq. 3.13 analytically in the low-frequency limit. As mentioned in Section 3.1.2, at low frequencies the only scattering is specular reflection due to rotation, i.e., the  $m = 0$  term. This term leads to a

scattering rate,

$$\Gamma_{\text{spec}}(\mathbf{k}) = \frac{2n_{1d}v_s\gamma_R^2 b^2}{D^2} \frac{k}{|k_x|}. \quad (\text{G.4.14})$$

The corresponding contribution to the phonon lifetime, after averaging over incident phonon direction is

$$\tau_{\text{spec}}(k) = \frac{D^2}{2n_{1d}v_s\gamma_R^2 b^2} \times \frac{3}{4\pi} \iint \frac{|k_x|^3}{k^3} d\Omega = \frac{3D^2}{8n_{1d}v_s\gamma_R^2 b^2}, \quad (k < \pi/D). \quad (\text{G.4.15})$$

The reciprocal of this analytic expression is precisely the first term in 3.14, and provides a check on our numerical evaluation.

### G.4.3 Phonon-dislocation strain scattering: short wavelength limit

Similar to the how the AMM was derived by evaluating Eq. 3.13 in the low-frequency limit, phonon scattering from independent dislocations can be derived by evaluating it in the high-frequency limit. When the phonon frequency is high there are many diffracted beams, and the Poisson sum can be approximated by an integral. The resulting expression for the scattering rate simplifies to

$$\Gamma(\mathbf{k}) = \frac{n_{1d}\gamma^2\omega^2}{2\pi v_s D} \iiint d^3\mathbf{k}' \sum_a |\tilde{\epsilon}_a(\mathbf{q})|^2 (1 - \hat{\mathbf{k}} \cdot \hat{\mathbf{k}'}) \delta(q_z) \delta(k' - k). \quad (\text{G.4.16})$$

To evaluate this integral, we employ spherical polar coordinates with  $k'_z$  as the pole, and the azimuth measured from  $k'_x$ . Using  $\theta$  and  $\phi$  as the polar and azimuthal angles for  $\mathbf{k}$ , and  $\theta'$  and  $\phi'$  for  $\mathbf{k}'$ , we get

$$\Gamma(\mathbf{k}) = \frac{n_{1d}\gamma^2\omega^2 k}{2\pi v_s D} \sum_a F_a(\mathbf{k}), \quad (\text{G.4.17})$$

with

$$F_a(\mathbf{k}) = 2 \sin^2 \theta \int_0^{2\pi} |\tilde{\epsilon}_a(\mathbf{q})|^2 \sin^2 \frac{1}{2}(\phi' - \phi) d\phi'. \quad (\text{G.4.18})$$

In evaluating the  $F_a$ 's, it is useful to observe that

$$\begin{aligned} q_x &= -2k \sin \theta \sin \frac{1}{2}(\phi' + \phi) \sin \frac{1}{2}(\phi' - \phi), \\ q_y &= 2k \sin \theta \cos \frac{1}{2}(\phi' + \phi) \sin \frac{1}{2}(\phi' - \phi), \\ q_x^2 + q_y^2 &= 4k^2 \sin^2 \theta \sin^2 \frac{1}{2}(\phi' - \phi). \end{aligned} \quad (\text{G.4.19})$$

Hence,

$$\begin{aligned} F_R(\mathbf{k}) &= 4b^2 \frac{1}{2k^2} \int_0^{2\pi} \sin^2 \frac{1}{2}(\phi' + \phi) d\phi' = \frac{2\pi}{k^2} b^2, \\ F_\Delta(\mathbf{k}) &= \left[ \frac{b(1-2\nu)}{1-\nu} \right]^2 \frac{1}{2k^2} \int_0^{2\pi} \cos^2 \frac{1}{2}(\phi' + \phi) d\phi' = \frac{\pi}{2k^2} \left[ \frac{b(1-2\nu)}{1-\nu} \right]^2, \quad \text{and} \\ F_S(\mathbf{k}) &= \frac{b^2}{(1-\nu)^2} \frac{1}{2k^2} \int_0^{2\pi} \sin^2 \frac{1}{2}(\phi' + \phi) \cos^4 \frac{1}{2}(\phi' + \phi) d\phi' = \frac{\pi}{16k^2} \frac{b^2}{(1-\nu)^2}. \end{aligned} \quad (\text{G.4.20})$$

We see that all three  $F_a$ 's are independent of the direction of  $\mathbf{k}$ . So, consequently, is the scattering rate. This rate is therefore equal to its orientational harmonic mean, and thus directly equal to the inverse of the phonon lifetime defined in Section G.3. That is,

$$\frac{1}{\tau(k)} = \Gamma(\mathbf{k}) = \frac{n_{1d}\gamma^2\omega^2 k}{2\pi v_s D} \times \frac{1}{k^2} \left[ \frac{\pi}{2} \frac{b^2(1-2\nu)^2}{(1-\nu)^2} + 2\pi b^2 + \frac{\pi}{16} \frac{b^2}{(1-\nu)^2} \right], \quad (k \gg \pi/D). \quad (\text{G.4.21})$$

Using  $\omega = v_s k$  and  $n_{1d}/D = n_{2d}$ , we can write this more compactly as

$$\frac{1}{\tau(\omega)} = K_\nu n_{2d} \gamma^2 b^2 \omega, \quad (k \gg \pi/D), \quad (\text{G.4.22})$$

with  $K_\nu$  defined in Eq. 3.16.

## G.5 Useful Fourier transforms and identities

This section provides Fourier transforms that are used throughout this thesis.

- The integral definition of a Dirac  $\delta$ -function is essentially the Fourier transform of 1

$$\int e^{-ik_x x} dx = 2\pi\delta(k_x). \quad (\text{G.5.1})$$

- Care must be taken when handling the square of a Dirac  $\delta$ -function

$$\delta(k_x)^2 = \delta(k_x) \frac{1}{2\pi} \int e^{-ik_x x} dx = \delta(k_x) \frac{L_x}{2\pi}, \quad (\text{G.5.2})$$

where  $L_x$  is the length integrated over in the  $x$ -direction (length of crystal). In practice  $L_x$  typically ends up contributing to the dimensions contained in the spatial density of defects  $n_{nd}$ , see for example Eq. G.2.8.

- The Fourier transform of  $1/r$ , with  $r = (x^2 + y^2)^{1/2}$  and  $q = (q_x^2 + q_y^2)^{1/2}$ , is

$$\iint \left(\frac{1}{r}\right) e^{-i(q_x x + q_y y)} dx dy = \frac{2\pi}{q}. \quad (\text{G.5.3})$$

- The Fourier transform of a step function defined as

$$\begin{aligned} \Theta(x) &= -1/2 \text{ when } x < 0 \\ \Theta(x) &= 1/2 \text{ when } x > 0, \end{aligned} \quad (\text{G.5.4})$$

is

$$\int \Theta(x) e^{-iq_x x} dx = \frac{i}{q_x}. \quad (\text{G.5.5})$$

## Appendix H

### Thermal boundary conductance

The thermal conductance due to phonon transport across an interface, or the thermal boundary conductance  $h_B$ , can be derived by accounting for the amount of heat impinging upon an interface and defining a transmission probability,  $t(\mathbf{ks})$ , which has values between 0 and 1

$$h_B = \sum_{\mathbf{ks}} h_B(\mathbf{ks}) \quad (\text{H.0.1})$$

$$h_B(\mathbf{ks}) = \frac{1}{4} C(\mathbf{ks}) v_g(\mathbf{ks}) \frac{t(\mathbf{ks})}{1 - t(\mathbf{ks})}, \quad (\text{H.0.2})$$

where  $C(\mathbf{ks})$  is defined in Eq. C.0.9. This formalism was first proposed by Landauer [37] for electron transport, and has been extended to phonons by Dames *et al.* [70, 212, 46, 4]. Occasionally in literature the factor  $t/(1 - t)$  is replaced by  $t$ . While both treatments agree at small  $t$ , when  $t$  approaches 1, this will introduce a fictitious thermal resistance. This can be observed by setting  $t(\mathbf{ks}) = 1$  at which  $h_B(\mathbf{ks})$  should go to infinity (resistance go to 0). If the factor  $t/(1 - t)$  were simply  $t$  in Eq. H.0.2,  $h_B(\mathbf{ks})$  would be finite. A discussion regarding the physical differences between the two formulations is given in Appendix C of Ref. [212] and Ref. [37].

Now we will relate this mode specific Landauer model to a mode specific model utilizing perturbation theory and relaxation times. We set the interface plane normal to be the  $z$ -direction and examine the  $(i, j) = (z, z)$  component of  $\kappa_{\text{ph},ij}$  as shown in Figure 2.5. The phonon thermal conductivity of mode  $\mathbf{ks}$  in Landauer theory is given by

$$\kappa_{\text{ph}}(\mathbf{ks})^{-1} = \kappa_{\text{bulk}}(\mathbf{ks})^{-1} + (L h_B(\mathbf{ks}))^{-1} \quad (\text{H.0.3})$$

where  $\kappa_{\text{bulk}}(\mathbf{ks}) = C(\mathbf{ks}) v_g(\mathbf{ks})^2 \cos^2 \theta \tau_{\text{pp}}(\mathbf{ks})$ , recalling that  $v_{g,z}(\mathbf{ks}) = v_g(\mathbf{ks}) \cos \theta$ .

The phonon thermal conductivity using a interfacial relaxation time and perturbation theory is

given by

$$\kappa_{\text{ph}}(\mathbf{k}s)^{-1} = \kappa_{\text{bulk}}(\mathbf{k}s)^{-1} + \kappa_{\text{B}}(\mathbf{k}s)^{-1} \quad (\text{H.0.4})$$

where  $\kappa_{\text{B}}(\mathbf{k}s) = C(\mathbf{k}s)v_g(\mathbf{k}s)^2 \cos^2 \theta \tau_{\text{B}}(\mathbf{k}s)$ . By equating Eqs. H.0.3 and H.0.4 we find

$$t(\mathbf{k}s) = \frac{\tau_{\text{B}}(\mathbf{k}s)}{\frac{L}{4v_g(\mathbf{k}s)\cos^2 \theta} + \tau_{\text{B}}(\mathbf{k}s)}. \quad (\text{H.0.5})$$

If phonon mode  $\mathbf{k}s$  is travels in a direction perpendicular to the plane normal vector,  $\theta = 90^\circ$  and  $t(\mathbf{k}s) = 0$ , as expected.

## List of Figures

1.1	The general ranges of thermal ( $\kappa$ ) and electrical ( $\sigma$ ) conductivity for solids. Thermal conductivity spans approximately 5 orders of magnitude while electrical conductivity spans approximately 26. Within a material system, such as silicon (Si), thermal and electrical conductivity can be changed by approximately 1.5 and 6 orders of magnitude, respectively. . . . .	13
2.1	An illustration of a solid in which heat is flowing. A source has injected heat on the left side, and on the right side there exists a sufficiently large heat sink. When steady state is reached a thermal gradient $\nabla^i T$ has been established. The magnitude of the heat current $j^i$ is set by the materials thermal conductivity $\kappa^{ij}$ through Fourier's law, Eq. 2.1. . . . .	19

2.2 Phonons and phonon thermal conductivity of perfect, single crystalline Si computed using <i>ab initio</i> based lattice dynamics and the phonon Boltzmann transport equation at 300K. The green lines show analytical expressions which hold at low- $\omega$ , and highlight numerical artifacts which commonly accompany this type of mode specific simulation. a) The phonon dispersion relation along $\Gamma - X$ calculated from 2nd order interatomic force constants (Appendix B). b) The spectral heat capacity (Eq. 2.18). c) Mode dependent phonon group velocity, $v_g(\mathbf{k}s)$ (dots) and the isotropic average group velocity at a given frequency $v_g(\omega)$ (line, Eq. 2.19). d) The phonon dispersion relation with phonon line broadening defined by the phonon-phonon scattering relaxation time. The discrete behavior in $\mathbf{k}$ is not physical and represents the discrete nature of the uniform $\mathbf{k}$ -mesh. Note that we use a relatively dense mesh of 30 x 30 x 30. e) The mode dependent relaxation time due to phonon-phonon scattering $\tau(\mathbf{k}s)$ (dots), and the isotropic average relaxation time at a given frequency $\tau(\omega)$ (line, Eq. 2.20). The inset shows a $\tau \propto \omega^{-2}$ fit to the computational data at low- $\omega$ . f) The spectral thermal conductivity computed using the data points shown in panels a, c, and e. The peak at 5 meV is artificial and is due to poor sampling of $\mathbf{k}$ -space below 10 meV. From analytical consideration (green lines), $\kappa(\omega)$ should converge to a constant value as $\omega \rightarrow 0$ rather than go to zero. . . . .	21
2.3 Schematic representations of phonon scattering and lattice softening. a) A real space depiction of phonon scattering and lattice softening. b) The phonon dispersion and linewidth of a pristine crystal. c) Phonon scattering due to the introduction of crystal defects. d) Lattice softening, reduced elastic moduli and speed of sound due to the introduction of crystal defects. . . . .	30
2.4 Phonon scattering diagrams for defects with different dimensionality. a) A phonon scattered elastically by a point defect scatters into the 3d phonon density of states (pDOS). b) A phonon scattered by a linear defect (scattering potential, $V(x, y)$ ) conserves phonon momentum in the $z$ -direction and thus scatters into the 2d pDOS, contributing $\omega$ to the phonon scattering rate. c) A phonon scattered by planar defect ( $V(x)$ ) conserves phonon momentum within the defect plane ( $yz$ -plane) and scatters into the 1d pDOS which is $\omega$ -independent. $v_g$ and $v_p$ are the phonon group and phase velocities. The bottom panel shows this dimensionality argument for the $\omega$ power law applied to the scattering rate due to mass fluctuation scattering. . . . .	33

- 2.5 a) A schematic illustration of two common models used to describe heat conduction in materials with interfaces. The vertical can be interpreted as temperature of a specific conduction channel, which can be either a specific phonon mode  $\mathbf{k}s$  or frequency  $\omega$  depending on the level of detail of the model. The blue line depicts the Landauer based model where a thermal boundary resistance arising from the conduction channel having a interfacial transmission probability  $t(\mathbf{k}s) > 1$  (or  $t(\omega) > 0$ ), induces an instantaneous drop in temperature. The red line depicts a model based on phonon scattering theory and Matthiessen's rule, where each scattering mechanism contributes a scattering rate ( $\tau(\mathbf{k}s)^{-1}$  or  $\tau(\omega)^{-1}$ ) and thermal resistance to the conduction channel. b) A comparison between the transmissivity calculated using classical acoustic mismatch (AMM) theory and quantum perturbation theory (Eq. 2.50 and 2.59). The two differ no more than 5% across the entire range. . . . . 40
- 3.1 The low temperature lattice thermal conductivity ( $\kappa_L$ ) of polycrystalline samples compared to that of single crystals. In polycrystals where the phonon scattering is dominated by grain boundary interactions,  $\kappa_{\text{ph}}$  scales as  $T^2$ . In single crystals where scattering is dominated by phonon sample surface interactions,  $T^3$  behavior is observed. The  $\kappa_{\text{ph}}$  and  $T$  values are normalized for comparison. Un-normalized data are shown in Figure 3.7. . . . . 43
- 3.2 Kinematics and conservation laws leading to diffraction conditions and dimensionality crossover. a) An illustration of the array of linear defects which scatters a phonon  $\mathbf{k}$  into a state  $\mathbf{k}'$ . b) Scattering from linear defects requires the conservation of momentum in the  $k_z$  direction,  $k_z = k'_z$ . This results in a scattering circle that lies parallel to the  $xy$ -plane. c) Because of further conservation laws arising from the periodic nature of the scattering potential (given in Eq. 3.3 in the text), only intersections of this circle with the dashed lines are valid. For small  $|\mathbf{k}|$ , only the  $m = 0$  line will give valid solutions (and a phonon density of states (pDOS),  $g_{1d}$ ). When  $|\mathbf{k}|$  is large, the entire circle is essentially accessible (pDOS  $g_{2d}$ ). . . . . 46
- 3.3 A periodic array of edge dislocations describing the structure of a symmetric tilt grain boundary. a) Schematic illustration of an array of edge dislocations ( $\perp$ ) periodically spaced by  $D$  with Burger's vector  $b\hat{\mathbf{x}}$  forming a grain boundary of angle  $\theta_{\text{GB}}$ . Careful examination of the atoms highlighted in red reveals that they are displaced. b) Grain boundary strain maps of hydrostatic strain  $\epsilon_{\Delta}$ , pure shear strain  $\epsilon_S$ , and rotation  $\epsilon_R$ , calculated via Eq. 3.11 with parameters given in Table 3.1. Scale bar shows the percent strain ( $10^{-2}$ ). . . . . 48

3.4 Phonon diffraction peaks arising from the periodic nature of a grain boundary strain field. The scattering rate is calculated from Eq. 3.13 for a phonon at normal incidence ( $\mathbf{k} \parallel \hat{\mathbf{x}}$ ) at different magnitudes of the phonon wavevector, $k =  \mathbf{k} $ . Scattering at low $k$ is non-zero as shown in the inset, and diffraction peaks are observed as singularities at $2\pi m/D$ , where $m$ is an integer. . . . .	50
3.5 Dimensionality crossover effects observed in phonon-GB strain field scattering in diffuse heat conduction. a) The vertical dashed line denotes the crossover frequency, below which the phonon scatters off the GB as a 2d defect ( $\omega$ independent, $\tau \propto \omega^0$ ), and above which scatters off the grain boundary as an array of 1d defects ( $\tau \propto \omega^{-1}$ ). $D$ is the linear defect spacing (Figure 3.3a), and $\theta_{\text{GB}}$ can be interpreted as the magnitude of angular deviation from a special boundary [57]. b) The spectral scattering rate is shown where the dashed line compares the approximate formula given in the main text (Eq. 3.14) to the exact formula (solid line). c) Phonon-GB strain field scattering cast in terms of a spectral transmissivity function (Eq. 3.17) shows a frequency independent transmissivity at low- $\omega$ and a decrease above the crossover frequency. . . . .	52
3.6 General features of the influence of phonon-grain boundary (GB) strain-field scattering on low temperature lattice thermal conductivity. The figure is based on parameters appropriate for Si with a Debye dispersion as described in the text. Curves are shown for several values of GB dislocation spacing ( $D$ ), corresponding to GB angles ( $\theta_{\text{GB}}$ shown in the legend). When $D$ is small, phonons see the grain boundary as a planar defect ( $\bar{n} = 1$ ) resulting in $\omega$ -independent scattering and $\kappa_{\text{ph}} \propto T^3$ . When $D$ is large the phonons see the grain boundary as an array of independently scattering line defects ( $\bar{n} = 2$ ) which gives $\tau_{\text{gbs}}^{-1} \propto \omega$ , leading to $\kappa_{\text{ph}} \propto T^2$ behavior at low- $T$ . The full and dashed lines are calculated using the full summation (Eq. 3.13 and G.4.13) and the semi-empirical formula (Eq. 3.14), respectively. . . . .	55
3.7 Thermal transport modeling of polycrystalline (pc) a) Si, b) AlN, and c) Al <sub>2</sub> O <sub>3</sub> . Data for these materials is taken from Refs. [43, 44, 45]. The intrinsic scattering parameters are fit to single crystals (sc) and have the values shown in Table 3.1. The solid lines follow from the theoretical modeling as described in the text. The data for polycrystals shows a clear $T^2$ power law in accord with our GB strain field scattering theory and defect dimensionality arguments. The dashed lines show a comparison of the data with the gray model. The error in the literature data is smaller than size of the data points on this logarithmic scale. . . . .	57

- 3.8 Transition electron microscopy images of Si twist GBs. a) Image of the GB with the electron beam perpendicular to the GB plane normal vector  $<001>$ . The GB structure seems to be amorphous when observed from this angle. b) Image of GBs with the electron beam parallel to the GB plane normal vector. When viewed from this angle the GB dislocation structure can be observed, confirming that this procedure produces clean GBs in their low energy configuration. Notice that the GB strain field thickness (3nm) shown in panel a is approximately equal to GB dislocation spacing in panel b. c) A lower magnification image of panel b. . . . . 60
- 3.9 Experimental data of the GB energy ( $\gamma_{\text{GB}}$ ) and thermal boundary resistance ( $R_{\kappa}$ ) of Si twist GBs. Open circles (left axis) are data from Otsuki [91]. Blue squares (right axis) are  $R_{\kappa}$  data from this study for samples after annealing. The lines are associated with the left axis and show the extended Read-Shockley model for GB energies, where the core energy ( $\gamma_{\text{core}}$ ) and the strain energy ( $\gamma_{\text{strain}}$ ) sum to give  $\gamma_{\text{GB}}$ . 61
- 4.1 (a) Room temperature lattice parameters of SnTe as a function of AgSbTe<sub>2</sub> content. The linear change in lattice parameter through the entire composition range suggests a full solid solution. (b) Backscattered electron image, (c) corresponding elemental maps obtained from energy dispersive X-ray spectroscopy. (d) Transmission electron microscopy image as well as selective area diffraction pattern (lower left inset image in (d)) for the sample AgSn<sub>5</sub>SbTe<sub>7</sub>. There is no evident phase separation at either the micro- or nano scale, which suggests a solid solution behavior between SnTe and AgSbTe<sub>2</sub>. . . . . 65
- 4.2 a) Schematic diagram summarizing the results of the DFT defect energy study. Ag and Sb prefer to reside as nearest neighbors on the metal sublattice and promote Sn-vacancy formation. Each Sn-vacancy contributes two holes to the valence band. b) Experimental measurements of the average speed of sound. The measured Hall carrier concentration for the end members are labeled. Ag and Sb promote cation vacancy formation which increases the carrier concentration and decreases the average speed of sound. . . . . 66

- 4.3 (a) Lattice thermal conductivity modeling. Data from a SnTe single crystal from Damon [98] was modeled along with the polycrystalline SnTe sample and m = 5 sample, AgSn<sub>5</sub>SbTe<sub>7</sub> of this study. The gray shaded region shows the reduction in  $\kappa_{\text{lat}}$  from SnTe to AgSn<sub>5</sub>SbTe<sub>7</sub> solely due to lattice softening because of decreased sound velocity, which is measured using ultrasound. The further reduction from gray to blue (blue shaded region) is due to increased [V<sub>Sn</sub>] and phonon-vacancy scattering. (b) ZT values as a function of temperature for AgSn<sub>m</sub>SbTe<sub>2+m</sub> system. (ZT here is the material figure of merit.) . . . . . 68
- 4.4 Milestone improvements in the figure of merit ( $zT$ ) of Na-doped PbTe due to reductions in lattice thermal conductivity ( $\kappa_L$ ) (a) The improved  $zT$  was previously attributed solely to phonon scattering from micro/nanostructural defects. Data for (Na,Sr)-PbTe (Pb<sub>0.98</sub>Na<sub>0.02</sub>Te-10%SrTe) are from [101], (Na,Eu)-PbTe (Na<sub>0.025</sub>Eu<sub>0.03</sub>Pb<sub>0.945</sub>Te) from [102], and Na-PbTe from [103]. (b) A reduction of  $\kappa_L$  upon the introduction of micro/nanostructural defects. The lines show the  $\kappa_L = Av_s^3T^{-1}$  model describing phonon thermal conductivity in the high-T limit where the only scattering mechanism is phonon-phonon scattering.  $A$  is normalized to the Na-PbTe sample and fixed. The shaded region shows the reduction in  $\kappa_L$  expected from lattice softening alone, without assuming an increase in phonon-defect scattering centers. Phonon scattering mechanisms could account for the remaining reduction in  $\kappa_L$ , depicted by the cross-hatched region. The speed of sound ( $v_s$ ) reduction, measured in this study, is given in the legend. The circles are data for a Na-doped (0.75% Na) sample synthesized and measured in this study. The square data points are a low dislocation density sample from Ref. [104] (Na<sub>0.015</sub>Eu<sub>0.03</sub>Pb<sub>0.955</sub>Te). . . . . 71
- 4.5 Lattice thermal conductivity of PbTe samples with different amounts of internal strain and average speeds of sound ( $v_s$ ). (a)  $\kappa_L$  vs.  $T$  of three characteristic samples. The lines are applications of the  $\kappa_L = Av_s^3T^{-1}$  model where, since the coefficient  $A = 1.09 \times 10^{-7} \text{Ws}^3\text{m}^{-4}$  is normalized to the unstrained sample (squares) and held constant, there are no adjustable parameters and only difference in the model between samples is the measured  $v_s$ . (b) A different representation of Eq. 4.4, showing the data in panel (a) in comparison to a reproducibility study containing three independently synthesized samples (Figure S4 of [100]). The dashed lines show a 5% error in  $\kappa_L$ . This data shows that the reduction in lattice thermal conductivity in stoichiometric PbTe is fully accounted for by lattice softening. (c) The measured grain size (filled data points) and density (empty data points) of each sample versus its room temperature  $\kappa_L$  showing that all samples have a density between 97 and 99% of the theoretical density, are large grained, and that there is no systematic trend of  $\kappa_L$  with grain size or density. . . . . 74

4.6 Experimentally measured heat capacity plotted as $C_p/T^3$ vs $T$ in order to illustrate the horizontal Debye level, $\beta$ , in the $T \rightarrow 0$ K limit. Corresponding Debye model fits of $\beta$ , from which Debye temperature $\theta_D$ can be calculated, are shown for each data set. Inside parenthesis, $\theta_D$ and $v_s$ are shown as a percentage of the nominally unstrained sample (green). The reduction in $\theta_D$ is in excellent agreement with the reduction measured by pulse-echo ultrasound. . . . .	75
4.7 Speed of sound decreases linearly with increasing internal-strain in PbTe based materials. a) Williamson-Hall strain analysis of stoichiometric PbTe, as well as Na-doped, high $zT$ , compositions (colors are consistent with Figure 4.4 and 4.5). $\beta$ is the integral breadth (peak area/height) of a diffraction peak at $\theta$ . The slope of the plots ( $C\epsilon_{XRD}$ ) are proportional to the average internal-strain in the material (details in Section 4.2.4). b) Example peak fits of a low and high internal-strain samples (circled in panel (c)). Diffraction peaks in samples with large amounts of internal-strain show peak shape asymmetry where the peak has a larger broadening on the low $2\theta$ (larger d-spacing) side of the peak maximum. c) The speed of sound ( $v_s$ ) measured by pulse-echo ultrasound versus the internal-strain ( $C\epsilon_{XRD}$ ) as measured in panel (a). The increase in internal-strain is correlated with a linear decrease in the speed of sound, a reduction in the lattice thermal conductivity, and improved thermoelectric efficiency. . . . .	77
4.8 A schematic transport model demonstrating the characteristics features of defect scattering and lattice softening mechanisms in the reduction of lattice thermal conductivity ( $\kappa_L$ ). a) The $\kappa_L$ of a pristine sample ( $\kappa_o$ ) compared to the $\kappa_L$ of defective samples where the reduction in $\kappa_L$ is induced by phonon-defect scattering and lattice softening. In the pristine sample ( $\kappa_o$ ), and the case of lattice softening (dark red), $\tau^{-1} = \tau_{pp}^{-1} \propto T$ . For the case of phonon-defect scattering (dashed), $\tau^{-1} = \tau_{pp}^{-1} + \tau_{defect}^{-1} \propto T + \text{constant}$ . b) The ratio of $\kappa_L$ for the defective sample over that for the pristine sample. A positive slope of $\kappa/\kappa_o$ indicates significant phonon scattering effects, and no slope indicates softening effects. . . . .	79



4.12 Scanning electron microscopy images of fracture surfaces, with the average grain size determined via the linear intercept method indicated. Data points are consistent with Figures 4.5 and S4 of [100], and the scale is the same for all six images. The thermal conductivity measured does not systematically trend with the materials grain size. . . . .	88
5.1 Brillouin zone folding promotes phonon conduction through the diffuson channel. Schematic illustration of the folding of one phonon branch when the number of atoms per unit cell is increased from one to two and four. A commonly cited effect of zone folding is that it reduces the average phonon group velocity, $v_g = d\omega/dk$ , of the phonon-gas channel. However, when the diffuson conduction channel is considered, in addition to the phonon-gas, one recognizes that zone folding increases the number of branches $s$ and decreases their energy separation. Upon the broadening of these phonon branches this will promote normal mode mixing, and in turn increase thermal conduction through the diffuson channel. . . . .	92
5.2 a) The body centered $\text{Yb}_{14}MSb_{11}$ tetrahedral crystal structure containing 208 atoms ( $I4_1/acd$ , no. 142). There are 104 in the primitive unit cell. Yb is shown in blue, Sb in green and $M = \text{Mn}, \text{Mg}$ are contained in the red $\text{Sb}_4$ tetrahedra. b) The reciprocal lattice and first Brillouin zone. The harmonic vibrational band structure is shown along the $\Gamma - \text{N}$ and $\Gamma - \text{X}$ high symmetry lines. . . . .	93
5.3 The dynamic structure factor (scattering function) shown as a function the magnitude of the scattering wave-vector ( $ \mathbf{Q} $ ) and energy ( $E$ ), $S( \mathbf{Q} , E)$ . Polycrystalline samples of $\text{Yb}_{14}\text{MgSb}_{11}$ with 104 atoms per primitive unit cell, and Al with one atom per primitive unit cell are shown for comparison. In polycrystalline Al, clear phonon branches are observed that originate from the diffraction peaks at $E = 0 \text{ meV}$ . These isolated phonon branches are not easily observed in $\text{Yb}_{14}\text{MgSb}_{11}$ , and through this qualitative comparison one may suspect that the character of atomic vibrations in $\text{Yb}_{14}\text{MgSb}_{11}$ is not consistent with the phonon-gas picture. The isolated and distinguished branches in Al indicate that the phonon-gas picture holds. . . . .	95
5.4 The phonon band structure, and vibrational density of states (DOS) computed from DFT-based lattice dynamics for a) $\text{Yb}_{14}\text{MgSb}_{11}$ and b) $\text{Yb}_{14}\text{MnSb}_{11}$ . For the DOS, an $8 \times 8 \times 8$ uniform $\mathbf{k}$ -mesh and the tetrahedron method was used to approximate the integration over the Brillouin zone. Additionally the DOS was convoluted with a 1.5 meV full width half max Gaussian function which is consistent with the instrument resolution seen in the inelastic neutron experiments. . . . .	97

5.5 Neutron weighted density of states in a) Yb <sub>14</sub> MgSb <sub>11</sub> and b) Yb <sub>14</sub> MnSb <sub>11</sub> measured via inelastic neutron scattering at 300K on the ARCS spectrometer at the SNS. The experimental data and computational predictions have been normalized and the energy axis has been shifted for comparison. The computation predictions shown here are based on the results shown in Figure 5.4. As can be seen the simulations agree well experimental results, particularly for phonon modes below 20 meV. . . . .	98
6.1 Structural representation of Yb-filled CoSb <sub>3</sub> (shown with the origin shifted by - 1/4[111]) with Co in blue, Sb atoms in gold, and Yb atoms (filler) in light blue. Sb forms Sb <sub>4</sub> rings that coordinate to Co. (b) Structural motif of CoSb <sub>3</sub> . Two octahedra share either one Sb or an edge of an Sb-Sb ring. Star labeled atoms represent the motif (b) in context within the structure (a). . . . .	101
6.2 High angle annular dark-field, scanning transmission electron microscopy (HAADF-STEM) image of the p-type Ce <sub>0.85</sub> Fe <sub>3</sub> CoSb <sub>12</sub> /0.56 vol% rGO sample. Right Insets: local energy spectrum analysis for Sb, Fe, Ce, Co and C respectively. . . . .	103
6.3 Atom probe tomography (APT) analysis of the most heavily doped sample Ce <sub>0.2</sub> Co <sub>4</sub> Sb <sub>12</sub> . (a) 3D reconstruction of microtip containing a grain boundary. Ce atoms are displayed in red; Sb and Co atoms omitted for clarity. (b) Concentration profile across the grain boundary and in the grain. The black dashed lines show values measured by electron probe micro analysis (EPMA), and the error bars represent the standard error, $\sqrt{c(1 - c)/n}$ , where c is the concentration and n is the number of atoms detected in each data point bin. . . . .	104
6.4 Temperature dependence of the (a) electrical conductivity, (b) carrier mobility, (c) Seebeck coefficients, (d) power factors of p-type Ce <sub>0.85</sub> Fe <sub>3</sub> CoSb <sub>12</sub> /y vol% rGO samples (y = 0, 0.56, 1.4, 2.8) and n-type Yb <sub>0.27</sub> Co <sub>4</sub> Sb <sub>12</sub> /y vol% samples (y = 0, 0.72) from Ref. [167] . . . . .	105
6.5 Determination of interfacial thermal resistance ( $R_\kappa$ ) from grain boundaries in polycrystalline skutterudite samples (without rGO). The uncertainty in the grain-size is 20%. (a) and (c) show room temperature lattice thermal conductivity with varying grain size. $R_\kappa$ is in units of $10^{-7} \text{ m}^2 \text{ K W}^{-1}$ ; (b) and (d) show $\kappa_{\text{lat}}$ with temperature for n and p-type skutterudite samples. Lines in all figures are calculated from Eq. 6.1. 106	

6.6 a) Diagram of the thermal circuit representing the thermal resistance of grain boundaries wrapped in graphene with the resistance elements labeled by their respective thermal conductivities. b) Lattice thermal conductivity ( $\kappa_{\text{lat}}$ ) at 300 K with varying amounts of rGO for both n and p-type skutterudite/rGO composite (solid symbols). Data for n-type material are from Ref. [167]. The solid lines represent the model (Eq. 6.2) when thermal boundary resistance is unchanged $R_\kappa = 3.8 \times 10^{-7} \text{ m}^2 \text{ KW}^{-1}$ . The dashed lines represent the model when the thermal boundary resistance is increased to $17 \times 10^{-7} \text{ m}^2 \text{ KW}^{-1}$ for n-type and $11 \times 10^{-7} \text{ m}^2 \text{ KW}^{-1}$ for p-type, due to graphene modification. . . . .	107
6.7 a) Temperature-dependent $zT$ for $\text{Ce}_{0.85}\text{Fe}_3\text{CoSb}_{12}/y$ vol% rGO ( $y = 0, 0.56, 1.4, 2.8$ ) samples from 300-800 K and $\text{Yb}_{0.27}\text{Co}_4\text{Sb}_{12}/y$ vol% ( $y = 0, 0.72$ ) samples from 300-850 K from Ref. [167]. b) Inset: Thermoelectric module with dimension of 20 mm x 20 mm x 16 mm using $\text{Ce}_{0.85}\text{Fe}_3\text{CoSb}_{12}/1.4$ vol% rGO and $\text{Yb}_{0.27}\text{Co}_4\text{Sb}_{12}/0.72$ 0.72 vol% rGO composite as p and n-type legs, respectively. Maximum conversion efficiency and power output as a function of the hot side temperature $T_h$ for the skutterudite/rGO based modules (M-SKD/rGO) and the reference device made of pure SKD (M-SKD). The dash lines represent the theoretical conversion efficiency of M-SKD/rGO with a maximum value of 10.5 %, and M-SKD with a maximum value of 8.0 %, when ignoring electrical and thermal contact resistances. . . . .	108
6.8 Exemplary refinement of (a) $\text{CoSb}_3$ and (b) $\text{Yb}_{0.3}\text{Co}_4\text{Sb}_{12}$ at 300 K with the corresponding profile residuals. The black circles are the experimental data, the red line is the calculated histogram, and the line below is the difference profile between the observed and calculated values. The insets show a zoomed in view on high angle reflections and the high quality fit of the refinement at the corresponding low d-spacing. . . . .	113
6.9 Temperature dependent lattice parameter of $\text{CoSb}_3$ obtained from the Rietveld refinements, showing the positive thermal expansion of the unit cell. Introduction of the filler atom further increases the unit cell. For comparison, data for increasing amounts of Yb are shown from Tang <i>et al.</i> [189]. Literature data from Ohno <i>et al.</i> [193] show that the linear temperature dependence of $a$ in $\text{CoSb}_3$ is maintained down to 10 K. . . . .	115
6.10 Changes in the $\text{CoSb}_6$ octahedral angle (a) and the Oftedal relation (b) with temperature. With increasing temperature, the structure shifts towards a more symmetric octahedron and away from a perfect square. Note that the doping with a filler atom leads to a distortion of the octahedral away from a symmetric $90^\circ$ angle and a more square $\text{Sb}_4$ ring arrangement. . . . .	116

- 6.11 Temperature dependence of the Co-Sb (c) and Sb-Sb bond lengths (a) and (b). Lines correspond to linear fits used to calculate the local thermal expansion coefficient  $\alpha_{300K}^L$ . Literature values from Ohno *et al.* [193] are shown by triangles, showing the good fit of the data with literature values at room temperature and at 10 K. While all bonds expand with increasing temperature in the undoped  $\text{CoSb}_3$ , the longer bond exhibits a larger slope and faster thermal expansion. Substitution with the filler atom increases the bond lengths as well. d) Temperature dependence of the octahedral volume, showing the linear thermal expansion of the  $\text{CoSb}_6$  octahedra. . . 117
- 6.12 In all panels, blue corresponds to contributions from Co and orange to contributions from Sb. a) Molecular orbital diagrams of the  $\text{CoSb}_6$  octahedron and the  $\text{Sb}_4$  ring. Atomic orbitals are not shown for the  $\text{Sb}_4$  ring. The octahedral crystal field splitting is visible and gives, in combination with the bonding, anti-bonding separation of the Sb-Sb bonds the band gap. b) Crystal Orbital Hamilton Population (COHP) calculated from the DFT data, showing the bonding nature of the Sb-Sb bonds in the valence bands and Sb-Sb anti-bonding states in the conduction band. The Co-Sb bonds in the valence band are predominantly non-bonding ( $t_{2g}$ ) in nature, whereas the conduction band has anti-bonding Co-Sb contributions. c) Schematic DOS estimated from MO diagrams in (a). d) Partial, atom projected DOS calculated from DFT data. 119
- 6.13 a) Calculated band structure of undoped  $\text{CoSb}_3$  at 300 K with the relevant band extrema labeled. The valence band maximum and conduction band minimum are at the  $\Gamma$  point (3-fold degenerate), making  $\text{CoSb}_3$  a direct band gap semiconductor. At higher energies, there is a second conduction band with 12 carrier pockets ( $\text{CB}_2$ ). b) Effective primitive cell band structure of Yb-doped  $\text{CoSb}_3$  calculated using a supercell (with fixed structural parameters). Dashed lines and color-coded arrows are guides to the eye, showing that in the doped structure the conduction bands are shifted compared to the undoped  $E(\mathbf{k})$ . The scale bar represents the weighting function . . . 121
- E.1 Overview of pulse-echo ultrasound. a) The experimental setup. b) Example waveform. c) Cross-correlation between successive reflections in the waveform. . . . . 156

## List of Tables

3.1	Intrinsic scattering parameters entering $\tau_{\text{pp}}^{-1}$ , $\tau_{\text{pd}}^{-1}$ , and $\tau_{\text{Casimir}}^{-1}$ obtained by fitting to single crystal data [73, 44, 45]. For each material, parameters are given based on both Debye and Born von Karman (BvK) phonon dispersions. . . . .	54
3.2	Material parameters used for grain boundary strain scattering, $\tau_{\text{gbs}}^{-1}$ . *Grain size distribution having a standard deviation of 48% of the average grain size, $0.55\mu\text{m}$ . . . . .	56
4.1	Parameters for $\kappa_{\text{lat}}$ modeling. . . . .	70
4.2	Elasticity data for the samples shown in Figure 4.5. Samples can be identified by the labeled $v_s$ values. . . . .	87
4.3	Material parameters used in the thermal transport model shown in Figure 4.9a, based on Eqs. 2.22, 2.18, 4.15, and 3.14. . . . .	89
6.1	Linear thermal expansion coefficients of the Sb-Sb, Co-Sb and Yb-Sb bonds in un-filled and filled skutterudite (normalized to the bond lengths at 300 K). The thermal expansion of the Sb-Sb short bond is significantly higher in $\text{Yb}_{0.3}\text{Co}_4\text{Sb}_{12}$ than in $\text{CoSb}_3$ . . . . .	118
6.2	DFT calculations with different Fermi levels, and computational parameters. Similar changes in the band structure and structural parameters are observed with ‘doping’ regardless of computational method. *Indicates that this calculation is shown in Figure 7. †Indicates that the values are average bond distances within the supercell..	122